

# **Interleaflet and Substrate Coupling in Phospholipid Bilayers**

James Andrew Goodchild

Submitted in accordance with the requirements for the degree of  
Doctor of Philosophy

The University of Leeds  
School of Physics and Astronomy

September 2018

The candidate confirms that the work submitted is his own, except where work which has formed part of jointly authored publications has been included. The contribution of the candidate and the other authors to this work has been explicitly indicated below. The candidate confirms that appropriate credit has been given within the thesis where reference has been made to the work of others.

Data from Chapter 4 of this thesis obtained by JAG is used in the book chapter;

*Connell S.D., Heath G.R., **Goodchild J.A.** (2019\*) Quantitative Analysis of Structure and Dynamics in AFM Images of Lipid Membranes. In. Santos N., Carvalho F. (eds) Atomic Force Microscopy. Methods in Molecular Biology, vol 1886. Humana Press, New York, NY \*published online 30 October 2018*

Book chapter was written by SDC. Data was acquired by SDC, GRH and JAG.

Chapter 4 is based on a manuscript in preparation for submission to Biophysical Journal;

***Goodchild J.A.**, Connell S.D., Anti-Registration in Supported Lipids Bilayers*

All data was acquired by JAG and manuscript is being written by JAG.

Chapter 7 is based on a manuscript in preparation for submission to Langmuir;

***Goodchild J.A.**, Walsh D.L., Connell S.D., Substrate Roughness Significantly Affects Bilayer Phase Separation: A Comparison of Mica and Glass*

All data was acquired by JAG except Fluorescence Microscopy data that was jointly acquired with DLW. Manuscript was written by JAG.

Chapter 8 is based on a manuscript in preparation (journal undecided);

***Goodchild J.A.**, Walsh D.L., Laurent H, Connell S.D., PDMS as a substrate for Lipid Bilayer Phase Separation*

All data was acquired by JAG except Fluorescence Microscopy data that was jointly acquired with DLW, PDMS stretching data that was acquired by HL, and PDMS microsphere data that was jointly acquired by HL and JAG. Manuscript was written by JAG.

This copy has been supplied on the understanding that it is copyright material and that no quotation from the thesis may be published without proper acknowledgement.

The right of James Andrew Goodchild to be identified as Author of this work has been asserted by him in accordance with the Copyright, Designs and Patents Act 1988.

© 2018 The University of Leeds and James Andrew Goodchild

## Acknowledgements

Firstly, thanks to my supervisor Dr Simon Connell who allowed me the freedom to make this PhD my own, but was full of ideas, enthusiasm and AFM/bilayer expertise when I needed it. Thank you for staying calm when I was panicking about deadlines. Thank you for reading the majority of my thesis in under 3 days!

I would also like to thank Dr Anders Aufderhorst-Roberts, who in my first two years taught me how to make SLBs and how to do AFM. He was a patient teacher who always had time to lend a hand whether it be with AFM, presentations or project ideas. I know he will be a great academic.

Thanks to Dr Danielle Walsh, who worked as a postdoc on the substrate effects project for my final year. As well as contributing massively to the millions of experiments done over my final year, she was always great at stopping me from having a complete final year melt down. Thank you.

Thanks to Dr Peng Bao for training our group in fluorescence microscopy, lending us flow cells, and for always having time to fix the numerous issues we encountered.

Thanks to Harrison Laurent, who started the substrate effects work when he developed a device for wrinkling PDMS to form bilayers on. When I took on his project, we thought it would take a few weeks. It took nearly a year and a half, and forms two chapters and soon two papers!

I would also like to thank every member of MNP past and present, too many to mention by name. Without the lively office, jokes, cakes, dinners, Fenton Friday etc. I believe parts of my PhD would have been truly miserable.

Thank you Jonny Bairstow for all the runs you scored and all the hours of procrastination I spent watching you bat. Thank you for hitting a century in Sri Lanka on the morning of my viva!

I would like to give a massive thanks to my Mum, Dad and brother Simon for supporting me through every stage of my life and education, and for always helping me to see the bigger picture.

Most of all I would like to thank Becky. Thank you for your support through these four years, thank you for moving to Leeds for me, and thank you for those times you brought me dinners to work when I had to stay late in the lab.



## Abstract

Since the existence of lateral organisation in the cell membrane was first proposed by Erwin London in 1997, much has been discovered about the complex behaviour of lipid bilayers. Whilst some membrane proteins involved in signalling are almost as mobile as lipid molecules, such as the photoreceptor protein rhodopsin, others such as the peripheral glycoprotein fibronectin are virtually static. This has been linked to the existence of phase separated micro-domains, sometimes known as lipid rafts, in model systems. However, there are still many open questions, including the effect of asymmetry and curvature on bilayers. Domains in the two leaflets of a model bilayer always align, or register. Conversely, the plasma membrane is asymmetric in composition, which implies that different phases can exist across the bilayer midplane, known as anti-registration. Hydrophobic mismatch at phase boundaries should favour a fully anti-registered bilayer in model systems, implying an interleaflet coupling force drives registration. In this thesis, hydrophobic mismatch between phases is controlled, with anti-registered domains forming at a mismatch of 8 carbons per leaflet. A coupling free energy of  $0.021 \text{ k}_B\text{T}/\text{nm}^2$  was determined, in close agreement with the only other experimental study using a different methodology, and refining the values found via simulation. Methods are explored to induce anti-registration with lower mismatch, and to characterise the orientation of the anti-registered states.

Arising from this work is a greater understanding of how substrate choice for supported bilayers greatly affects phase behaviour. Glass, used in fluorescence microscopy experiments, and PDMS (Polydimethylsiloxane), used to create flexible and curved bilayer substrates, result in nanoscale domain formation compared to micro-scale domains on atomically flat mica. This difference is investigated and it is found that the hydrodynamic motion of domains is hindered by rougher substrates, having great implications for the study and understanding of supported lipid bilayers.

## Abbreviations

**DPPC** - 1,2-dipalmitoyl-*sn*-glycero-3-phosphocholine / 16:0 PC

**DSPC** - 1,2-distearoyl-*sn*-glycero-3-phosphocholine / 18:0 PC

**20:0PC** - 1,2-diarachidoyl-*sn*-glycero-3-phosphocholine

**22:0PC** - 1,2-dibehenoyl-*sn*-glycero-3-phosphocholine

**DOPC** - 1,2-dioleoyl-*sn*-glycero-3-phosphocholine

**14:1PC** - 1,2-dimyristoleoyl-*sn*-glycero-3-phosphocholine

**Chol** - Cholesterol

**TR-DHPE** - Texas Red 1,2-Dihexadecanoyl-*sn*-Glycero-3-Phosphoethanolamine, Triethylammonium Salt

**16:0 NBD PC** - 1,2-dipalmitoyl-*sn*-glycero-3-phosphoethanolamine-N-(7-nitro-2-1,3-benzoxadiazol-4-yl) (ammonium salt)

**PC** - Phosphocholine

**SM** - Sphingomyelin

**PE** - Phosphoethanolamine

**PS** - Phosphoserine

**PDMS** - Polydimethylsiloxane

**CHCl<sub>3</sub>** - Chloroform

**MeOH** - Methanol

**IPA** - Isopropyl Alcohol / Isopropanol

**L<sub>o</sub>** - Liquid Ordered Phase

**L<sub>d</sub>** - Liquid Disordered Phase

**L<sub>β</sub>** - Gel Phase

**T<sub>m</sub>** - Transition Temperature

**R** – Registered (domains) / Registration

**AR** - Anti-Registered (domains) / Anti-Registration

**SUV/LUV/GUV** - Small/Large/Giant Unilamellar Vesicles

**MLV** - Multilamellar Lamellar Vesicle

**SLB** - Supported Lipid Bilayer

**LB/LS** - Langmuir-Blodgett / Langmuir-Schaefer Bilayer

**AFM** - Atomic Force Microscopy

**PFT** - Peak Force Tapping

**DMT** - Derjaguin-Muller-Toporov Model

**QNM** - Quantitative Nanomechanical Mapping

**DSC** - Differential Scanning Calorimetry

**FRAP** - Fluorescence Recovery after Photobleaching

## Table of Contents

<b>Acknowledgements</b> .....	<b>iv</b>
<b>Abstract</b> .....	<b>v</b>
<b>Abbreviations</b> .....	<b>vi</b>
<b>Table of Contents</b> .....	<b>viii</b>
<b>List of Tables</b> .....	<b>xiii</b>
<b>List of Figures</b> .....	<b>xiv</b>
<b>Chapter 1. Introduction</b> .....	<b>1</b>
1.1 Project Overview .....	1
1.2 Lipid Bilayers.....	3
1.2.1Lipids.....	3
1.2.2Self-Assembly .....	7
1.2.3Intermolecular Interactions .....	8
1.2.4Phase Separation.....	9
1.2.5Phase Diagrams.....	11
1.2.6Lipid Raft Theory.....	13
1.2.7Model Bilayers.....	16
1.2.7.1 Supported Lipid Bilayers .....	17
1.2.7.2 Substrates for Supported Lipid Bilayers .....	17
1.2.7.3 Formation of Supported Lipid Bilayers .....	18
1.3 Asymmetry in Lipid Bilayers .....	20
1.3.1Natural Asymmetry in biology.....	20
1.3.2Symmetry in Model Bilayers.....	21
1.3.3Registration and Anti-Registration.....	22
1.3.4Inter-leaflet Coupling .....	22
1.3.5Computational Modelling.....	23
1.3.6Inter-leaflet Coupling Mechanisms .....	24
1.3.7Asymmetry in Model Bilayers .....	27
1.3.8Increasing Hydrophobic Mismatch .....	32
1.4 Thesis Aims and Structure .....	35
<b>Chapter 2. Background to Experimental Techniques</b> .....	<b>36</b>
2.1 Atomic Force Microscopy .....	36
2.2 AFM Probes .....	37
2.3 Piezo Scanner .....	38
2.4 Feedback Control.....	38

2.5	Imaging .....	39
2.6	Tip-Sample Forces .....	40
2.7	Imaging Modes.....	40
2.7.1	Contact Mode .....	40
2.7.2	Tapping Mode .....	40
2.7.3	Imaging bilayers .....	41
2.8	AFM Force Spectroscopy.....	42
2.8.1	Cantilever Calibration.....	42
2.8.1.1	Deflection sensitivity .....	42
2.8.1.2	Spring Constant .....	43
2.8.2	Contact Mechanics.....	43
2.8.3	AFM Force Spectroscopy on Bilayers .....	46
2.8.4	Force Volume, Peak Force Tapping (PFT) and Quantitative Nano-mechanical Mapping (QNM).....	47
2.9	Fluorescence Microscopy.....	47
2.10	Differential Scanning Calorimetry.....	50
<b>Chapter 3.</b>	<b>Experimental Methods.....</b>	<b>51</b>
3.1	Chemicals .....	51
3.1.1	Lipid Storage .....	51
3.1.2	Making Lipid Mixtures .....	51
3.2	Substrate Preparation .....	52
3.2.1	Mica Preparation .....	52
3.2.2	HF Mica Etch.....	52
3.2.3	Glass Preparation .....	52
3.2.4	PDMS Preparation .....	52
3.2.5	Wrinkled PDMS.....	53
3.2.6	PDMS Microspheres .....	54
3.3	Bilayer Formation .....	54
3.3.1	Anti-Registration Project .....	54
3.3.1.1	Preparation of Lipid Vesicles.....	54
3.3.1.2	Supported Lipid Bilayer Formation.....	55
3.3.2	Substrate Effects Project.....	55
3.3.2.1	Preparation of Lipid Vesicles.....	55
3.3.2.2	Supported Lipid Bilayers for AFM .....	56
3.3.2.3	Supported Lipid Bilayers for Fluorescence .....	56

3.3.2.4	Temperature measurements of Supported Lipid Bilayers .....	57
3.3.2.5	Bilayer Formation on PDMS Microspheres .....	57
3.4	Atomic Force Microscopy .....	58
3.4.1	Anti-Registration Project.....	58
3.4.2	Substrates Effects Project.....	58
3.4.3	Quantitative Nanomechanical Mapping AFM Tip Calibration .....	58
3.4.4	AFM Image Analysis .....	59
3.4.4.1	Bilayer Heights and Area Fractions.....	59
3.4.4.2	Power Spectral Density.....	60
3.4.4.3	Roughness.....	60
3.4.4.4	Domain Size.....	61
3.4.4.5	Correlation Length.....	61
3.5	Fluorescence Microscopy.....	62
3.5.1	Domain Fitting .....	63
3.5.2	Correlation Length.....	63
3.5.3	FRAP (Fluorescence Recovery after Photobleaching).....	64
3.5.3.1	FRAP for Transition Temperature Determination.....	65
3.6	Differential Scanning Calorimetry.....	66
3.6.1	Lipid Sample Preparation .....	66
3.6.2	Filling the DSC Cells .....	67
3.6.3	DSC Measurements .....	68
3.6.4	DSC Thermogram Processing and Analysis .....	69
3.7	Contact Angle.....	69
<b>Chapter 4.</b>	<b>Registration and Anti-Registration .....</b>	<b>71</b>
4.1	Introduction .....	71
4.2	Atomic Force Microscopy of DPPC/14:1PC/Chol.....	73
4.3	Reproducibly Forming Supported Lipid Bilayers .....	76
4.4	Increasing Hydrophobic Mismatch .....	77
4.4.1	Further DSPC and 20:0 PC Registered Examples.....	79
4.4.2	22:0 PC Heights and Morphologies.....	81
4.4.3	Hydrophobic Mismatch.....	84
4.4.4	Absolute Bilayer Heights .....	87
4.5	Anti-Registration.....	88

4.6	Summary.....	90
<b>Chapter 5.</b>	<b>Determining Anti-Registration Orientation .....</b>	<b>92</b>
5.1	Introduction .....	92
5.2	Tapping Mode Phase Imaging .....	93
5.3	Quantitative Nanomechanical Mapping.....	95
5.3.1	Calibrating Peak Force Quantitative Nanomechanical Mapping .....	96
5.3.2	Test samples.....	98
5.3.3	Symmetric two phase bilayers.....	98
5.3.4	Anti-Registered 3 phase bilayers .....	101
5.3.5	Summary.....	105
<b>Chapter 6.</b>	<b>Attempting to form Anti-Registered Bilayers in Shorter Chain Mixtures.....</b>	<b>108</b>
6.1	Introduction .....	108
6.2	Critical Compositions in DPPC/14:1PC/Chol.....	111
6.4	AFM with Temperature.....	120
6.4.1	Bruker Fastscan Built-in Temperature Stage .....	121
6.4.2	Peltier Heater and Cooler.....	123
6.4.3	Asylum MFP3D Heater Stage .....	125
6.4.4	Temperature Work Summary.....	127
6.5	Mismatch Free Energy .....	127
6.6	Chapter Summary .....	131
<b>Chapter 7.</b>	<b>Substrate Coupling in Supported Lipid Bilayers - Glass 133</b>	
7.1	Introduction .....	133
7.2	Brief Overview of Substrate Coupling in Bilayers .....	133
7.3	Phase Separation is Different on Mica and Glass .....	135
7.4	Single Lipid Gel Phase Structure is also different on Mica and Glass.....	139
7.5	Difference in Phase Separation between Mica and Glass is not due to Molecular Diffusion Rate .....	141
7.6	Molecular Ordering is affected by Different Substrates .....	144
7.7	Substrate Roughness is linked to Domain Size.....	147
7.8	Glass as a substrate for bilayer formation.....	149
7.9	Formation of Optically Visible Domains on Glass.....	150
7.10	Summary.....	152

<b>Chapter 8. Substrate Coupling in Supported Lipid Bilayers - PDMS 154</b>	
8.1 Introduction .....	154
8.2 Overview of PDMS as a Substrate for Supported Lipids Bilayers .....	155
8.3 Curved PDMS .....	156
8.4 Phase Separation on PDMS .....	157
8.5 Phase Separation on PDMS shown by AFM.....	158
8.6 Lipid Mobility .....	159
8.7 Molecular Ordering of Bilayers on PDMS.....	160
8.7.1 Lipid-Coated PDMS microspheres .....	161
8.8 Hydrophobic Recovery .....	163
8.8.1 Attempting to slow down hydrophobic recovery .....	165
8.9 PDMS Surface Structure and Roughness.....	167
8.10 Implications for Phase Separation on PDMS Substrates in Published Literature .....	171
8.11 Summary of PDMS Substrate Coupling .....	173
8.12 Overall Substrate Discussion Points .....	174
8.12.1 Roughness affects Bilayer Structure .....	174
8.12.2 Substrate Roughness affects Hydrodynamic Lipid Flow and Domain Formation .....	175
8.12.3 Leaflet Decoupling due to Substrate .....	178
8.12.4 Cytoskeleton .....	179
8.12.5 Summary of Substrate Coupling Chapters.....	180
<b>Chapter 9. Conclusions and Future Work .....</b>	<b>182</b>
9.1 Conclusions.....	182
9.2 Future Work .....	187
9.2.1 Anti-Registration.....	187
9.2.2 Substrates .....	190
<b>References.....</b>	<b>193</b>



## List of Tables

<b>Table 1.1 The chemical structures of lipids that are used in this thesis.....</b>	<b>5</b>
<b>Table 1.2 The chemical structures of lipid headgroups for the most common lipid types in the plasma membrane. SM = sphingomyelin, PS = phosphoserine, PE = phosphoethanolamine, PI = phosphatidyinositol .....</b>	<b>6</b>
<b>Table 1.3 Table showing intermolecular interactions that are relevant for lipid systems and their interactions energies.....</b>	<b>8</b>
<b>Table 2.1 Chemical structures of the fluorescent lipid dyes used in this thesis .....</b>	<b>49</b>
<b>Table 6.1 Table showing free energy values calculated for lipid bilayer systems of different hydrophobic mismatch .....</b>	<b>129</b>
<b>Table 7.1 Domain Sizes and Correlation Lengths for Mica and Glass bilayers at different cooling rates.....</b>	<b>137</b>
<b>Table 7.2 Contact Angle Measurements of glass cover slips after successive cleaning steps. ....</b>	<b>147</b>
<b>Table 8.1 Domain Sizes and Correlation Lengths for DPPC/DOPC(60:40) domains on Mica and PDMS, at different cooling rates from incubation temperature down to room temperature. ....</b>	<b>160</b>

## List of Figures

Figure 1.1 Schematic showing the two leaflets of a bilayer consisting of two coexisting phases in both leaflets. A shows domain registration (R) and B shows domain anti-registration (AR).....	2
Figure 1.2 Schematic lipid showing the hydrophilic head and the hydrophobic head superimposed onto a lipid chemical structure.....	3
Figure 1.3 Schematic of lipids in self-assembled structures A) Micelle B) Vesicle .....	7
Figure 1.4 Schematic showing phase separation between two lipid species, an ordered phase with a filled-in black head ( $L_o$ or $L_\beta$ ) and a less ordered phase with a clear head ( $L_d$ ) .....	9
Figure 1.5 Generic ternary phase diagram for a Saturated Lipid, Unsaturated Lipid and Cholesterol mixture at room temperature. ....	10
Figure 1.6 Domain growth in 1:1 DOPC/DPPC + 25% Chol GUVs Top) Domains formed by nucleation which then grow by domain ripening (also called coalescence). Bottom) Domains formed by spinodal decomposition.....	12
Figure 1.7 Schematic showing the complex and heterogeneous plasma membrane as described by the modern interpretation of the lipid raft theory. ....	15
Figure 1.8 Schematic of a Supported Lipid Bilayer (SLB) on a substrate .....	16
Figure 1.9 Methods of SLB Formation. A) Langmuir-Blodgett Deposition, which involves SLB deposition by moving a substrate through a monolayer at an air-water interface B) Vesicle Fusion, which involves the absorption of vesicles to a substrate followed by rupturing and spreading. ....	19
Figure 1.10 Example showing the asymmetry in the erythrocyte (red blood cell) membrane. ....	20
Figure 1.11 A model example showing how acyl chain composition can influence interleaflet coupling. ....	24
Figure 1.12 Snapshots from coarse-grain molecular dynamics simulations illustrating cholesterol flip-flop.....	25
Figure 1.13 Examples from literature of LB/LS bilayers with the same lipid compositions in both leaflets, showing $L_o/L_d$ domains not in registration.....	28
Figure 1.14 Shear applied to bilayers to de-register domains.....	29
Figure 1.15 AFM image and line scan height section of three heights in a DLPC/DSPC SLB formed on mica, showing potential AR. ....	31

Figure 1.16 Snapshots from coarse-grained molecular dynamics simulations showing registration (R) and anti-registration (AR). .....	32
Figure 1.17 Local 3D free energy landscape shown for set values of $J$ , which represents line tension and promotes anti-registration, and $B$ , which represents the mismatch free energy or interleaflet coupling parameter and promotes registration. ....	34
Figure 2.1 Schematic of an Atomic Force Microscope (AFM) setup.....	36
Figure 2.2 AFM Probes Schematic and Image .....	37
Figure 2.3 Lennard-Jones potential showing tip-sample forces in AFM. ....	39
Figure 2.4 Schematic of AFM tip scanning across phase separated bilayer and an example AFM image.....	41
Figure 2.5 Schematic showing the deformation of samples using AFM tips A) Spherical tip B) Conical Tip.....	44
Figure 2.6 Force curves on a DPPC/14:1PC/Chol bilayer. ....	45
Figure 2.7 Example force curve showing Peak Force as well as the physical properties that can be obtained from the curve.....	46
Figure 2.8 A) Jablonski diagram showing excitation and emission of a photon. B) Texas Red excitation and emission wavelengths.....	48
Figure 3.1 Home-built device for stretching and wrinkling PDMS .....	53
Figure 3.2 Photos of the home-built flow cell for forming SLBs.....	56
Figure 3.3 Example Depth and Area Analysis of a Flattened Phase Separated Bilayer AFM image.....	60
Figure 3.4 Example Correlation Length Analysis.....	62
Figure 3.5 Example Domain Fitting to Fluorescence Image.....	63
Figure 3.6 Example FRAP Bleach and Recovery on a DOPC SLB.....	66
Figure 3.7 Schematic showing the filling of DSC cells .....	67
Figure 3.8 DSC Thermogram for DPPC/14:1PC (80:20) showing the calculation of $T_m$ , $T_{on}$ and $T_{off}$ . ....	68
Figure 3.9. Contact Angle Measurement Example. ....	70
Figure 4.1 Chemical Structures for Saturated Lipids DPPC(16:0PC), DSPC (18:0PC), 20:0PC and 22:0PC at the top, 14:1PC in the middle and Cholesterol at the bottom.....	72
Figure 4.2. DPPC/14:1PC/Chol Ternary Phase Diagram with AFM Images.....	74
Figure 4.3 AFM images showing five bilayers made on five different AFM stubs subsequently using the same hydrated DPPC/14:1PC/Chol (1:1:1) lipid mixture.....	76

Figure 4.4 Increasing hydrophobic mismatch in ternary lipid mixtures. ....	78
Figure 4.5 More example AFM images of increasing hydrophobic mismatch. ....	79
Figure 4.6 Examples of different DSPC/14:1PC/Chol compositions, all showing two heights and registered phases. ....	80
Figure 4.7 Examples of different 20:0PC/14:1PC/Chol compositions, all showing two heights and registered phases. ....	81
Figure 4.8 Example Images of 22:0PC/14:1PC/Chol Bilayers, showing a range of morphologies. ....	82
Figure 4.9 Examples of other morphologies observed in 22:0PC/14:1PC/Chol ternary mixtures. ....	83
Figure 4.10 Change in height mismatch between bilayer phases with increase in saturated chain length. ....	84
Figure 4.11 Change in height mismatch with composition across a phase diagram. ....	85
Figure 4.12 Line profiles of Defect Bilayers. ....	87
Figure 4.13 Schematic showing the two possible orientations of an AR Bilayer. Black headgroups are gel phase, white headgroups are fluid phase. ....	88
Figure 5.1 Tapping Mode Phase Imaging of three height AR bilayers. ....	94
Figure 5.2 Example QNM Force Curve showing how physical properties can be obtained. ....	95
Figure 5.3 QNM AFM images on a test sample with a mix of Polystyrene (PS) and Low Density Polyethylene (LDPE). ....	98
Figure 5.4 QNM images of two-phase DPPC/14:1PC/Chol bilayers .....	99
Figure 5.5 Increasing imaging force increases Hydrophobic Mismatch. ....	100
Figure 5.6 QNM channels with increasing force on a three Phase 22:0PC/14:1PC/Chol bilayer. ....	101
Figure 5.7 QNM DMT modulus and deformation with increasing force on a three phase 22:0PC/14:1PC/Chol bilayer. ....	102
Figure 5.8 Tapping Mode Height, Tapping Mode Phase and QNM of the same three phase AR 22:0PC/14:1PC/Chol bilayer area. ....	103
Figure 5.9 Graph showing the change in height mismatch between the three phase AR heights for a 22:0PC/14:1PC/Chol bilayer with increasing force. ....	105
Figure 6.1. DPPC/14:1PC/Chol Ternary Phase Diagram with AFM Images. ....	110

Figure 6.2 Schematic showing the maximum possible anti-registration (AR) bilayer area for two different bilayers of different compositions of Phase 1 and Phase 2.....	110
Figure 6.3 DSC of DPPC/14:1PC Mixtures.....	112
Figure 6.4 Estimating the transition temperature ( $T_m$ ) of 14:1PC.....	114
Figure 6.5 DSC of DPPC/14:1PC/Chol mixtures.....	115
Figure 6.6 DSC of the binary DPPC/Chol axes. ....	116
Figure 6.7 Ternary phase Diagrams with transition temperature colour contour plots. ....	118
Figure 6.8 Images of AFM temperature stages.....	120
Figure 6.9 AFM with Controlled temperature on a DPPC/14:1PC/Chol (42.5:25:32.5) bilayer using the built in heat stage on the Bruker Dimension Fastscan AFM. ....	122
Figure 6.10 AFM with controlled temperature on a DPPC/14:1PC/Chol bilayer (45:25:30) using a peltier stage built for the Dimension Fastscan AFM. ....	124
Figure 6.11 AFM with controlled temperature on a DPPC/14:1PC/Chol bilayer (42.5:25:32.5) using a temperature stage on an Asylum MFP3D AFM. ....	126
Figure 6.12 Mismatch Free Energy of a bilayer plotted against hydrophobic mismatch.....	130
Figure 7.1 DPPC/DOPC (60:40) SLBs imaged with AFM (B,D,F,H) and DPPC/DOPC (60:40) + 0.5%TR SLBs imaged with fluorescence (A,C,E,G). A,B,E,F are on mica and C,D,G,H are on glass. ....	135
Figure 7.2 DPPC/DOPC (60:40) SLBs on mica, imaged using both fluorescence (A and B) and AFM (C) on the same area using a combined AFM/Fluorescence microscope. ....	136
Figure 7.3 DPPC/DOPC (60:40) SLBs on mica (A) and glass (B), highlighting the discrepancy in size and morphology of domains. ....	138
Figure 7.4 Using a gaussian blur on an AFM image of nanoscale domains on glass, to mimic the diffraction limit of an optical microscope.....	139
Figure 7.5 Room Temperature Images of DPPC with 0.5mol% NBD or 0.5mol% TR on mica and glass. ....	140
Figure 7.6 DPPC + 0.5mol% TR DHPE cooling from through DPPC's transition temperature. ....	141
Figure 7.7 Example AFM images of DPPC/DOPC (60:40) on glass at different cooling rates. ....	143
Figure 7.8 Transition Temperature Determination for DPPC with DSC and temperature FRAP studies. ....	144

Figure 7.9 FRAP on DPPC+ 0.5mol% NBD bilayer on mica (A,B,C) and glass (D,E,F) as the bilayer cools.....	146
Figure 7.10 AFM images and roughness of mica after cleavage (A) and Glass after Piranha and UV ozone clean (B).....	148
Figure 7.11 AFM images of A) Mica etched in 40% HF for 30 min, and B) DPPC/DOPC(60:40) bilayer on HF etched mica.....	149
Figure 7.12 Variability and Nanoholes on glass substrates .....	149
Figure 7.13 AFM images of A) Glass substrate before Piranha/UV Ozone with nanoholes B) and C) DPPC/DOPC (60:40) bilayer on glass, where nanoholes are visible in the bilayer at the same size as holes in the substrate. ....	150
Figure 8.1 AFM images showing curved PDMS.....	156
Figure 8.2 AFM images of plasma oxidised PDMS with and without DPPC/DOPC (60:40) bilayers, and comparison to bilayers on Glass and mica.....	158
Figure 8.3 AFM images of a patch of DPPC/DOPC (60:40) bilayer on PDMS.....	159
Figure 8.4 FRAP on a DPPC+ 0.5mol% NBD bilayer on PDMS as the bilayer cools. ....	161
Figure 8.5 Images of PDMS Microspheres with and without DPPC+ 0.5 mol% TR-DHPE bilayer coating.....	162
Figure 8.6 The effect of PDMS hydrophobic recovery on DPPC/DOPC (60:40)bilayers.....	164
Figure 8.7 Attempting to slow down hydrophobic recovery of PDMS using solvent washes, shown by contact angle measurements with time.....	166
Figure 8.8 AFM images of PDMS structure and roughness measurements pre and post oxygen plasma treatment. ....	168
Figure 8.9 AFM images of mica, glass and PDMS substrates with no bilayers.....	169
Figure 8.10 AFM images of PDMS structure cast against mica, silicon and spin coated.....	170
Figure 8.11 Comparison of Hindered Domain Formation to Domains formed by pinning of a cytoskeleton to the bilayer.....	179
Figure 9.1 Local 3D free energy landscape and leaflet-leaflet phase diagram showing asymmetry within phase separated bilayers. ....	188

## Chapter 1. Introduction

### 1.1 Project Overview

Since the proposal of the highly controversial 'lipid raft theory' in 1997,<sup>1</sup> the understanding of lateral lipid organisation within phospholipid bilayers has improved dramatically.<sup>2-5</sup> Lipid rafts are proposed heterogeneities in cell membranes caused by the aggregation of cholesterol and saturated lipids and they have been implicated in important cellular mechanisms such as signalling and protein clustering.<sup>3</sup> Model bilayer systems designed to mimic lipid rafts, consisting of a saturated lipid, an unsaturated lipid and cholesterol, form bilayers with two coexisting phases, the liquid-ordered ( $L_o$ ) and liquid-disordered ( $L_d$ ) phases.<sup>6</sup> In the laboratory, complete symmetry between the two bilayer leaflets, both in terms of composition and lateral phase organisation, is observed.<sup>7,8</sup> The transmembrane symmetry between phase separated domains observed in model bilayers is known as registration (R) (Figure 1.1A).<sup>9</sup> Biological plasma membranes, however, show compositional asymmetry between the leaflets, with model bilayers formed from outer leaflet lipids showing phase separation and those formed from inner leaflet lipids forming a single homogeneous phase.<sup>10,11</sup> Due to this asymmetry between the two leaflets of the biological membrane, it is likely that lipid phases can align asymmetrically in plasma membranes.

There is a line tension at the interface between  $L_o$  and  $L_d$  domains, caused in part by the exposure of the hydrophobic lipid tails of the thicker phase to water. This line tension would be at a minimum for a bilayer that showed domain anti-registration (AR) (Figure 1.1B), which is the asymmetric configuration with  $L_o$  phases opposing  $L_d$  phases and vice versa. The line tension would be lower as there is no hydrophobic mismatch between the lipid phases and therefore this should be the equilibrium state. Model bilayers however show registration between domains implying the existence of an interleaflet-force that favours R. It has been shown under certain conditions that a phase separated leaflet can induce phase separation in the opposing leaflet.<sup>12</sup> This observation also implies that there is an inter-leaflet coupling force between the two leaflets of

a bilayer. This could also be a mechanism by which cells can send signals across the bilayer membrane.

One question which remains unanswered is the identity of the interleaflet coupling forces which drive domains of similar lipid phases to register symmetrically across the two leaflets of a bilayer. There is significant debate over the origins and magnitude of the forces involved.<sup>9,10</sup> Theoretical studies have suggested that chain interdigitation, electrostatic coupling, cholesterol flip-flop and curvature coupling could be driving domain registration but experimental evidence is severely lacking.<sup>9,10</sup> A deeper understanding of the forces between the two opposing leaflets of a bilayer is now needed. This will help to bridge the gap between simplified symmetric model membranes, and the complex, heterogeneous and asymmetric plasma cell membrane, and help to understand the mechanisms by which signals can be transmitted into and out of a cell.

Mean field theoretical studies and coarse-grained molecular dynamics simulations have shown that high line tension can overcome the interleaflet coupling forces causing domains to register, and cause asymmetric AR domains to form.<sup>13,14</sup> As the difference in height between the two phases increases, the line tension increases.<sup>15</sup> This project intends to investigate experimentally whether the interleaflet coupling forces that favour registration

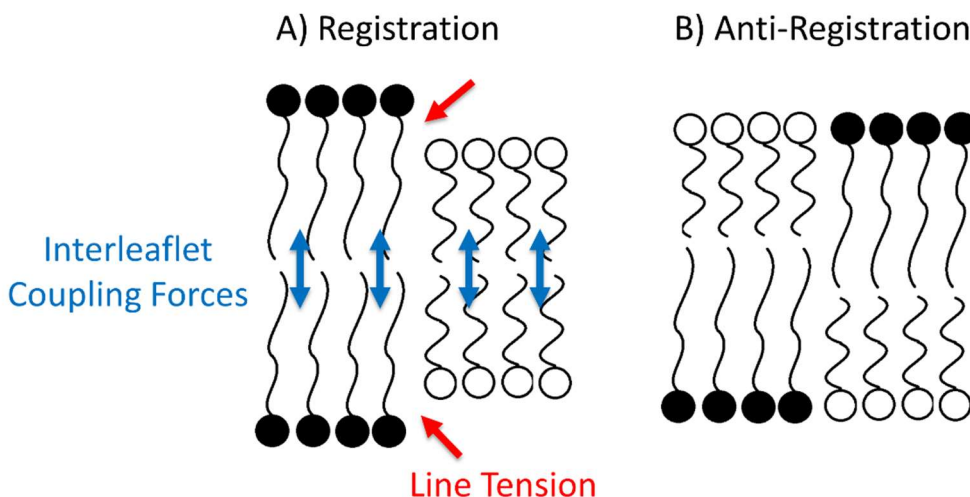


**Figure 1.1 Schematic showing the two leaflets of a bilayer consisting of two coexisting phases in both leaflets. A shows domain registration (R) and B shows domain anti-registration (AR).**



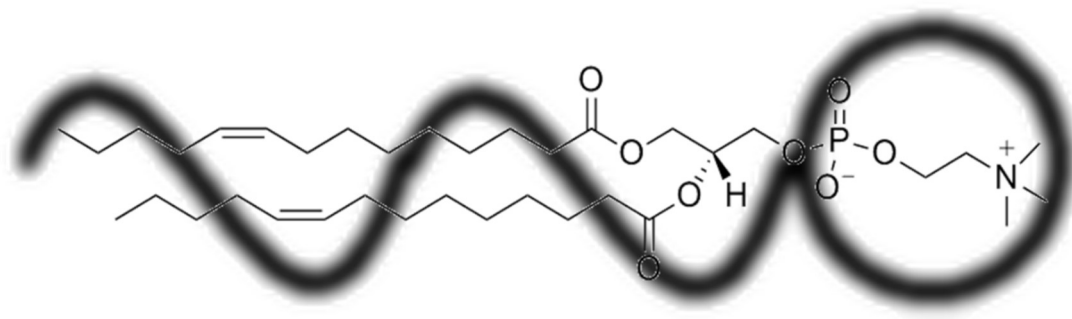
can be overcome, by increasing the hydrophobic mismatch and line tension between two lipid phases, to form AR domains.

## 1.2 Lipid Bilayers

### 1.2.1 Lipids

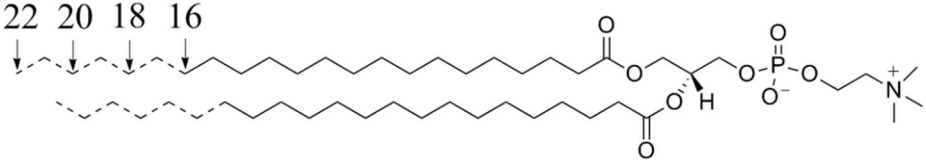
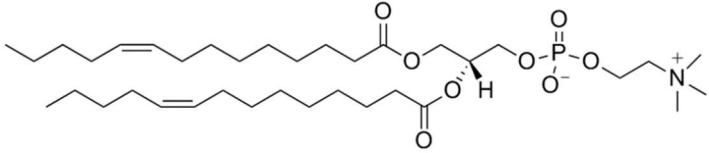
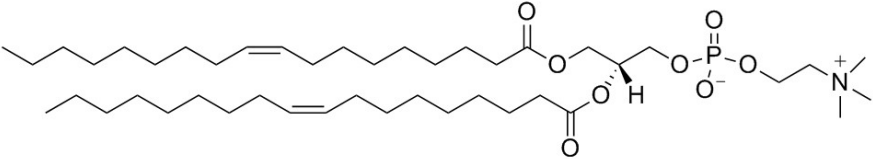
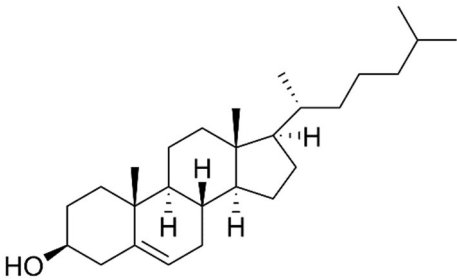
Lipids are amphiphilic molecules, meaning that they possess both a hydrophilic and a hydrophobic moiety. The names and structures of the lipids used in this thesis are shown in Table 1.1. The lipids used here have PC (phosphocholine) headgroups, one of the most common lipids species in the mammalian cell membrane.<sup>16,17</sup> The PC headgroups consists of a positively charged tertiary amine and a negatively charged phosphate group, making the lipid zwitterionic. The charge separation across the headgroup makes it polar. The headgroup is linked to two hydrophobic hydrocarbon tail chains. Figure 1.2 shows an example of the simplified lipid schematics used in this thesis with a round headgroup and tail, superimposed onto the lipid chemical structure it represents.

There are a wide variety of lipid types present in the biological plasma membrane.<sup>16,17</sup> The most common lipid headgroups, SM (sphingomyelin), PS (phosphoserine), PE (phosphoethanolamine) and PI (phosphatidylinositol), are shown Table 1.2, along with PC in Table 1.1. These are present in varying amounts within different cell types. The chemical structure of the headgroups can affect their properties such as the overall charge on the PS headgroup and the sugar moiety on the PI headgroups. All of the lipids in Table 1.2 are

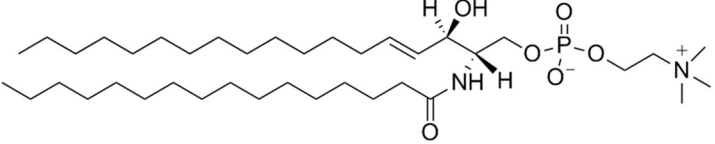
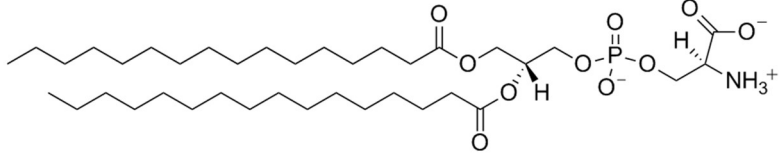
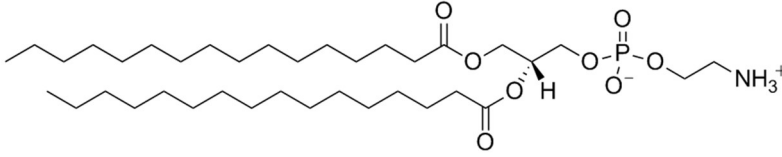
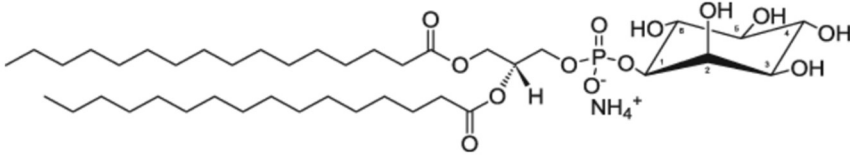


**Figure 1.2 Schematic lipid showing the hydrophilic head and the hydrophobic tail superimposed onto a lipid chemical structure**

shown with both tail chains having fully saturated 16 carbon chains but in reality there is also a variety of chains. The lipid tails can be fully saturated, mono-unsaturated with the double bond at different positions along the tail chain, and poly-unsaturated. DOPC and 14:1PC are examples of mono-unsaturated lipids (Table 1.1). Lipids can also be asymmetric in terms of the two tail chains. The two chains can vary in carbon length and degree of unsaturation. All of these types of lipid make for a diverse membrane which results in lateral inhomogeneity as well as asymmetry between the two leaflets of the plasma membrane bilayer. The lateral inhomogeneity, or phase separation, arising from coexisting lipid types is discussed in sections 1.2.4, 1.2.5 and 1.2.6. Asymmetry between different types of lipids in the two leaflets of the plasma membrane bilayer is discussed in section 1.3.

Lipid	Structure
DPPC/16:0PC DSPC/18:0PC 20:0PC 22:0PC	
14:1PC	
DOPC	
Cholesterol	

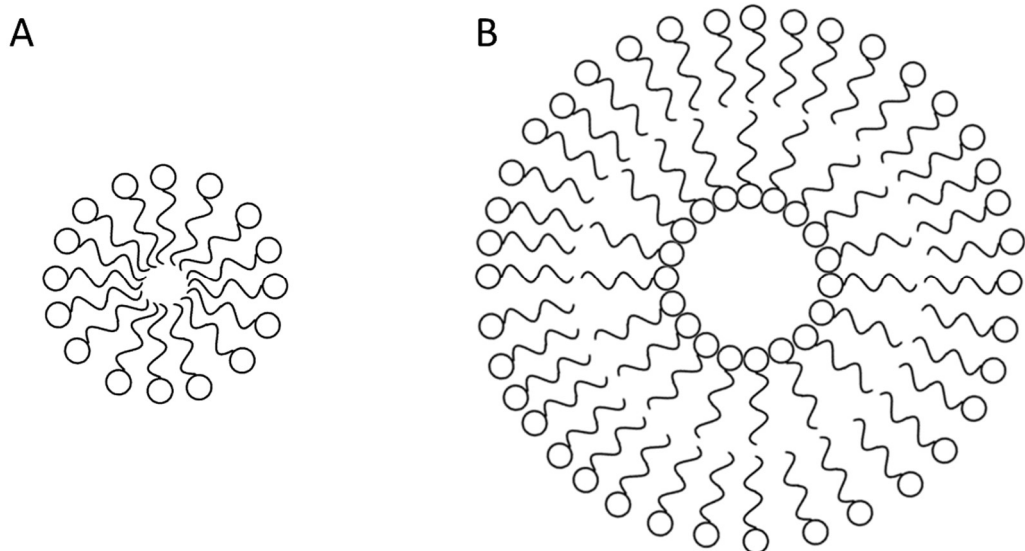
**Table 1.1 The chemical structures of lipids that are used in this thesis**

Lipid Headgroup	Structure
SM	
PS	
PE	
PI	

**Table 1.2 The chemical structures of lipid headgroups for the most common lipid types in the plasma membrane. SM = sphingomyelin, PS = phosphoserine, PE = phosphoethanolamine, PI = phosphatidylinositol**

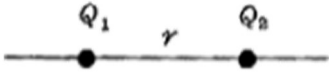
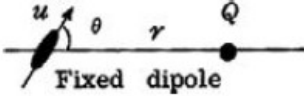
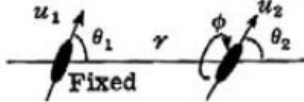
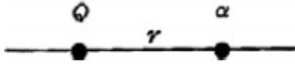
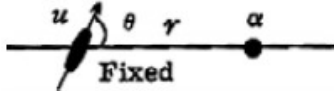
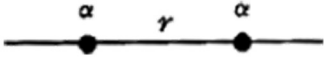
### 1.2.2 Self-Assembly

The amphiphilic nature of lipids causes them to self-assemble in water due to the hydrophobic effect. Water is able to form hydrogen bonds between molecules to lower the free energy of the system. If a hydrophobic molecule such as an alkane chain is introduced into water, the non-polarised hydrocarbon backbone cannot form any hydrogen bonds with water. Water forms a cage-like structure around the hydrophobic molecule, reducing the entropy of the system and increasing the free energy. If more than one hydrophobic molecule is present, the two hydrophobic molecules will prefer to make contact in order to reduce the overall contact area with water and the amount of water hydrogen bond network that is disrupted. For an amphiphilic molecule such as a lipid, with a polarised hydrophilic head group and a hydrophobic tail, the hydrophilic head groups align in such a way as to maximise their exposure with water and the tails bury themselves inside to minimise their contact with the water. In the simplest case this results in a micelle, but can also result in vesicles with a bilayer structure (Figure 1.3), as well as more unusual phases like hexagonal and cubic phases.



**Figure 1.3 Schematic of lipids in self-assembled structures A) Micelle  
B) Vesicle**

### 1.2.3 Intermolecular Interactions

Type of Interaction	Schematic of Interaction	Interaction Free Energy (J)
Charge-Charge		$+ \frac{Q_1 Q_2}{4\pi\epsilon_0 r}$
Charge-Dipole		$- \frac{Qu \cos \theta}{4\pi\epsilon_0 r^2}$
Dipole-Dipole		$- \frac{u_1 u_2 [2 \cos \theta_1 \cos \theta_2 - \sin \theta_1 \sin \theta_2 \cos \phi]}{4\pi\epsilon_0 r^3}$
Charge-non-polar		$- \frac{Q^2 \alpha}{2(4\pi\epsilon_0)^2 r^4}$
Dipole-non-polar		$- \frac{u^2 \alpha (1 + 3 \cos^2 \theta)}{2(4\pi\epsilon_0)^2 r^6}$
Two non-polar molecules		$- \frac{3h\nu\alpha^2}{4(4\pi\epsilon_0)^2 r^6}$

**Table 1.3** Table showing intermolecular interactions that are relevant for lipid systems and their interactions energies. Q = electric charge (C), u = electric dipole moment (Cm),  $\alpha$  = electric polarizability ( $C^2m^2J^{-1}$ ), r = distance between centres of interacting atoms or molecules (m), k = Boltzmann constant, T = temperature,  $\epsilon_0$  = dielectric permittivity of free space, h = Planck's constant,  $\nu$  = electronic absorption frequency ( $s^{-1}$ ) For dipoles they are assumed to be fixed in this table but there are added directionality terms when dipoles can move and rotate. Table recreated from reference<sup>18</sup>

As well as the hydrophobic forces driving self-assembly and bilayer formation, there are many intermolecular interactions that are important within lipid bilayers. The relevant interactions that may occur between lipids in a bilayer are summarised in Table 1.3. Intermolecular interactions act laterally between lipid headgroups and between tails, but can also act between the two leaflets of the bilayer across the bilayer midplane. These interactions can form the basis for interleaflet coupling, which is discussed further in Sections 1.3.4 and 1.3.6. Each interaction has a different length scale dependence, as highlighted by the interaction energy equations.

### 1.2.4 Phase Separation

Single component bilayers form two phases predominantly; the gel phase ( $L_{\beta}$ ) in which the lipid hydrocarbon tail chains are solid-like with high molecular packing and low lateral mobility, and the liquid disordered phase ( $L_d$ ) in which the tails are liquid-like with less dense molecular packing and higher lateral mobility.<sup>19</sup> The temperature at which the  $L_{\beta}$  phase melts to the  $L_d$  phase is called the melting transition temperature ( $T_m$ ).

Mixtures of lipids can show coexistence between multiple phases (Figure 1.4), for example a mixture of a saturated and a unsaturated lipid. Saturated lipids, such as DPPC (Table 1.1), have complete saturation in their tails and at room temperature pack tightly together to form a  $L_{\beta}$  phase. Unsaturated lipids, such

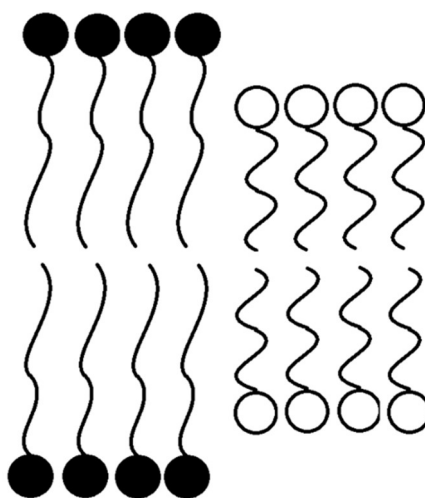


**Figure 1.4 Schematic showing phase separation between two lipid species, an ordered phase with a filled-in black head ( $L_o$  or  $L_{\beta}$ ) and a less ordered phase with a clear head ( $L_d$ )**

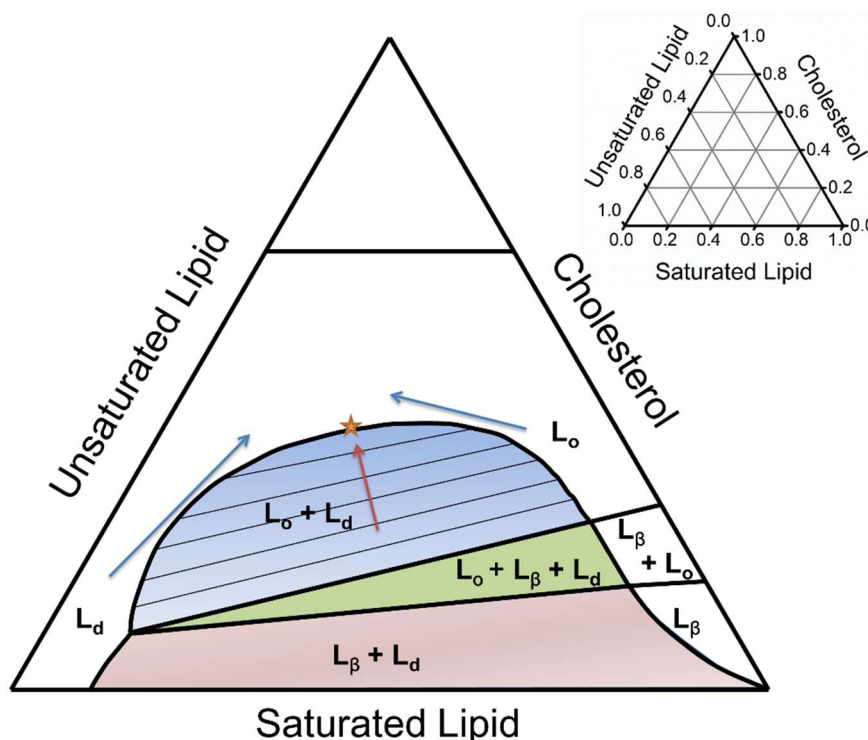


**Figure 1.5 Generic ternary phase diagram for a Saturated Lipid, Unsaturated Lipid and Cholesterol mixture at room temperature. Yellow star is critical composition at room temperature. Black lines within blue region are tie-lines. Picture adapted from reference.<sup>20</sup>**

as DOPC, have unsaturated bonds in their tails creating a kink that disrupts packing and a  $L_d$  phase is formed at room temperature. For certain compositions of saturated and unsaturated lipids mixed together, there is phase separation. The tightly packed  $L_\beta$  phase is thicker than the less densely packed fluid  $L_d$  phase. There is a line tension at the interface between the different lipids due to their different heights, caused by the unfavourable interaction of the hydrophobic tails in the  $L_\beta$  phase to water. This drives the two phases to separate laterally into distinct phase domains, to reduce the perimeter of the high energy interface between them.

One of the most commonly used lipid mixtures is a saturated lipid, an unsaturated lipid and cholesterol. When cholesterol is added to a bilayer, it can induce an intermediate phase between the  $L_\beta$  and  $L_d$  called the liquid ordered phase ( $L_o$ ), which still has high molecular chain packing but is liquid-like in terms of its lateral mobility. Ternary mixtures of a saturated lipid, an unsaturated lipid and cholesterol are regularly used to model biological



membranes, as they show complex phase behaviour which has been linked to the lipid raft theory in biological membranes (described in section 1.2.6).

### 1.2.5 Phase Diagrams

The phase behaviour of ternary lipid mixtures can be described using a ternary phase diagram. Figure 1.5 shows a general phase diagram for a ternary lipid mixture adapted from published data.<sup>20</sup> Each vertex of the triangle represents 100% of one of the components, and then following a line from the vertex to the midpoint of the side opposite the tip proportionately reduces the quantity of that component to zero. Specific mixtures can be found by following the grid lines from the three compositions on each axes and finding where they intersect.

Within the  $L_o$ - $L_d$  coexistence region, tie lines (black lines within blue region in Figure 1.5) can be used to calculate the ratio of the two phases using the lever rule.<sup>21</sup> For a given composition, following the tie line to both boundaries will give the individual compositions of the two coexisting phases. The ratio of the two phases is defined by the composition's position along the tie line in regards to both axes. Tie lines must be experimentally determined. The single  $L_o$  phase and  $L_d$  phase regions (white) do not have a clear distinction between them in the phase diagram. As the compositions move along the two blue lines the  $L_o$  and  $L_d$  phases become similar in structure and therefore there is a composition at which the two phases should have the same structure. At the critical point (star), the composition is such that the two coexisting phases should be identical, but in fact there is not a smooth transition, and critical fluctuations are observed as thermally driven local compositional fluctuations lead to the phase flipping back and forth between the distinct (but *more* similar)  $L_o$  and  $L_d$  phases. As the critical point is approached (along the red line) the two coexisting phases, determined from following the tie lines, become closer in structure and height. Close to the critical point the energy barrier between the two phases is low enough due to low hydrophobic mismatch, that there is a low energy penalty for long interconnected domain boundaries.

The phase diagram shown in Figure 1.5 shows just the phase behaviour at room temperatures. When a ternary lipid mixture bilayer is heated up within

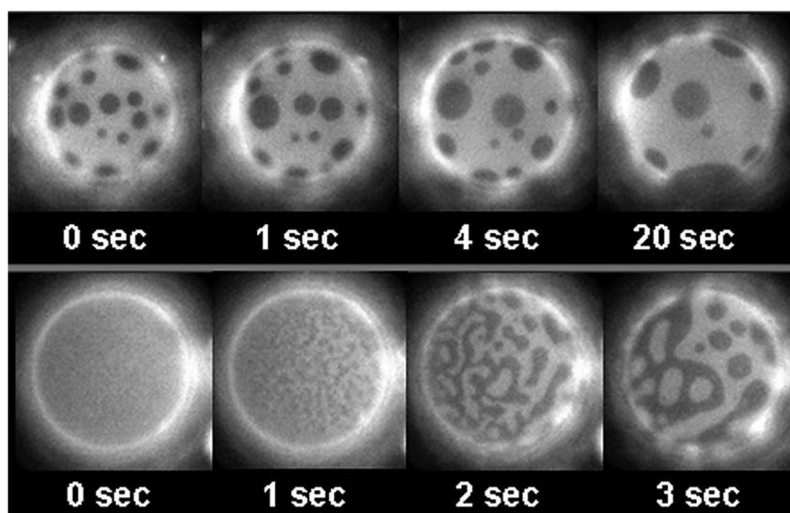


**Figure 1.6 Domain growth in 1:1 DOPC/DPPC + 25% Chol GUVs Top) Domains formed by nucleation which then grow by domain ripening (also called coalescence). Bottom) Domains formed by spinodal decomposition. From reference<sup>6</sup>**

the  $L_o$ - $L_d$  coexistence region, at the miscibility transition temperature the composition will move into the single phase region. Isolated  $L_o$  phase domains will appear to melt, forming a single  $L_d$  phase bilayer. This picture is, however, very misleading. If the two phase structure happened to be predominantly  $L_o$  phase, then upon increasing temperature the disordered  $L_d$  phase would appear to diminish until all of the bilayer becomes a single  $L_o$  phase. This is counter-intuitive as it appears that increasing temperature induces the system to become more ordered. The transition should really be termed a mixing or de-mixing transition, rather than a melting transition, the composition now lies in a single phase region that is either  $L_d$  or  $L_o$  phase. Stacks of ternary phase diagrams for each temperature on top of each other would create a 3D phase boundary surface. The miscibility transition temperature varies based on the lipids used and varies within the  $L_o$ - $L_d$  coexistence region. As the bilayer is cooled down though the miscibility transition temperature,  $L_o$  domains can reform in two ways. Close to the critical point where the energy barrier between the two phases is low, the  $L_o$  domains form via spinodal decomposition, forming long domain boundaries due to low line tension (Figure 1.6, bottom line). Away from the critical point, the  $L_o$  domains form via a nucleation and growth mechanism (Figure 1.6, top line). High line tension causes the domain edges to reduce and smaller circular structured domains are formed.

### 1.2.6 Lipid Raft Theory

Lipid bilayers provide the base structure for the plasma cell membrane, as well as key cell organelles such as the Golgi Apparatus and the Endoplasmic Reticulum. Lipid bilayer membranes are responsible for all compartmentalisation within the cell,<sup>22</sup> providing a semi-permeable barrier controlling the passage of biomolecules in and out of the cell, and they also enable chemical and electrical potentials within the cell.

In 1972, Singer and Nicholson presented the fluid mosaic model in which the lipid bilayer is presented as a homogenous structure for the more biologically active proteins to embed and diffuse in.<sup>23</sup> Observations of phase separation between mixtures of lipids were responsible for lipids re-emergence as an active not a passive membrane component.

In 1997 Kai Simons published work that introduced the term 'lipid raft', bringing together the ideas of the time regarding membrane structure and lipid phase separation.<sup>1</sup> The Lipid Raft theory claims that there are dynamic clustered domains enriched in SM and cholesterol in the cell membrane that show increased order and reduced diffusion. Lipid rafts are proposed to be responsible for biological processes such as protein clustering, due to membrane spanning proteins hydrophobic matching to the thicker raft phases, and signalling, due in part to the proposed ability of these rafts to align opposite to each other between the extracellular outer leaflet and the intracellular inner leaflet of a bilayer.

The L<sub>o</sub>-L<sub>d</sub> coexistence region of a ternary phase diagram (blue region in Figure 1.5), where there is lateral phase separation between the two phases, is thought to provide a good model for the biologically relevant lipid rafts.<sup>6</sup> The liquid ordered phase (L<sub>o</sub>) seen in model bilayers which is enriched in saturated lipid and cholesterol, shows similar properties to the proposed raft domains with higher chain packing and order. By contrast the liquid disordered phase (L<sub>d</sub>), which is enriched in unsaturated lipid and depleted of cholesterol, shows lower order and higher lateral mobility.

Phase separation into lateral coexisting liquid-liquid phases has now been observed in model systems with techniques such as fluorescence microscopy,<sup>6</sup> Atomic Force Microscopy (AFM),<sup>19,24</sup> scattering techniques,<sup>25</sup>

Nuclear Magnetic Resonance (NMR)<sup>26</sup> and many others. The raft hypothesis has proved controversial however due to the lack of evidence for macroscopic phase separation in biological membranes. This has led to the idea that rafts are transient, dynamic and of nm length scales, beyond the typical resolution of many techniques and in particular the ubiquitous diffraction limited fluorescence microscopy. With the advent of super resolution microscopy, sub-diffraction limit imaging can be now theoretically be achieved in cells. Issues with quantitative imaging, fluorescence probe development, temporal resolution of a dynamic system and the potential for phase separated domains to be below even the resolution of super resolution, mean that the search for evidence proving or disproving the existence of phase separated rafts in vivo continues.<sup>27</sup>

A modern raft theory has emerged recently which implicates lipids, proteins and the cytoskeleton, which is a dense layer of polymeric actin protein filaments pinned to the membrane, in membrane organisation.<sup>3-5</sup> Figure 1.7 shows the modern view of the complex and heterogenous structure of the plasma membrane. It consists of different types of lipids separated into domains with different amounts of cholesterol, proteins anchored to the membrane, transmembrane proteins spanning the membranes and an actin meshwork pinned to the bilayer surface.

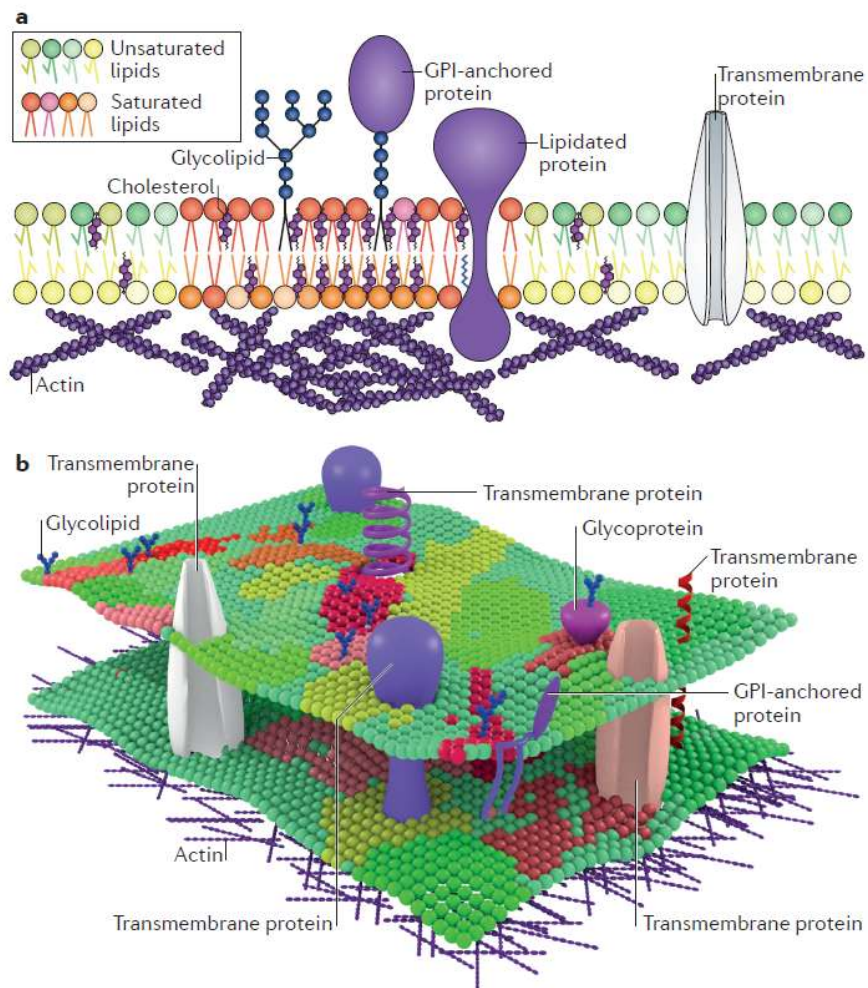


**Figure 1.7 Schematic showing the complex and heterogeneous plasma membrane as described by the modern interpretation of the lipid raft theory. Lipid rafts are shown as enriched in saturated phospholipids, sphingolipids, glycolipids, cholesterol and lipidated proteins. These rafts are defined as small, dynamic and transient, with increased lipid packing and order, and decreased fluidity. Cortical actin is an active part of domain maintenance. From reference<sup>5</sup>**

### 1.2.7 Model Bilayers

Model lipid membranes have been studied extensively to investigate the fundamental structure and physics of the cell membrane in an attempt to elucidate the complex questions surrounding lipid rafts and phase separation.<sup>28-30</sup> They have also been used to investigate protein and drug interactions with the membrane,<sup>31</sup> and to develop biotechnological applications such as drug delivery systems.<sup>32</sup>

The simplest form of model system is lipid vesicles (Figure 1.3B). Multilamellar lipid vesicles (MLVs) consisting of multiple bilayers will form when a dried lipid film is hydrated. MLVs can be useful in scattering techniques, Differential Scanning Calorimetry (DSC) and NMR, which are bulk measurements needing many repeated bilayer motifs. Small Unilamellar Vesicles (SUVs) that are typically 20-100 nm can be formed by tip sonicating MLVs. Different sizes of SUVs and LUVs (Large Unilamellar Vesicles) ranging from 50-400 nm can be formed by extruding MLVs through a pore of defined diameter. Giant Unilamellar Vesicles (GUVs) are formed by electroformation, which involves applying a sinusoidal AC field across a lipid film. GUVs are typically 1-100 $\mu$ m. Vesicles are used commonly in fluorescence microscopy techniques.<sup>33</sup>

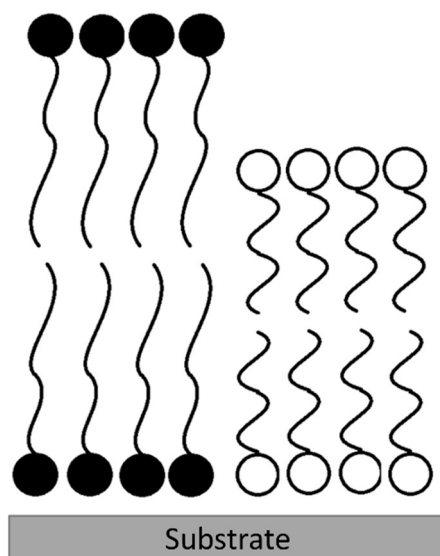


**Figure 1.8 Schematic of a Supported Lipid Bilayer (SLB) on a substrate**

### **1.2.7.1 Supported Lipid Bilayers**

The ability to form Supported Lipid Bilayers (SLBs) (Figure 1.8) on solid substrates renders them experimentally accessible to surface sensitive techniques, such as AFM,<sup>24</sup> Quartz Crystal Microbalance with Dissipation (QCM-D),<sup>34</sup> and fluorescence techniques such as Fluorescence Correlation Spectroscopy (FCS)<sup>35,36</sup> and Fluorescence Recovery After Photobleaching (FRAP).<sup>37,38</sup> This has yielded information about lipid diffusion, lipid ordering, bilayer structure, and phase behaviour.<sup>24,36,39,40</sup> In particular, the height and height mismatch between phases can be obtained in supported systems that is difficult to obtain in free-floating systems. Free-floating GUVs have the advantage of not being coupled to a substrate surface so provide a simpler physical model, but as a consequence cannot be easily immobilised in aqueous conditions and are therefore difficult to image using surface sensitive techniques. In AFM the interaction between the tip and the vesicles would cause them to move and they would be impossible to image.

Fascinatingly solid supports also provide the potential to tune bilayer properties to those of a biological cell membrane. The cell membrane is not isolated but sits between the cytoskeleton and the extracellular matrix networks.<sup>41,42</sup> Substrates can potentially be designed to replicate these rough, elastic and porous polymer networks. SLBs can also be used in biotechnological applications such as pharmaceutical or protein biosensor assays.<sup>31</sup>

### **1.2.7.2 Substrates for Supported Lipid Bilayers**

Many substrates can be used to support lipid bilayers including mica, glass and silicon, the choice usually driven by the signal being measured. AFM predominantly uses mica, a mineral that is easily cleaved to be atomically flat, enabling high z resolution of SLBs and their phases.<sup>43,44</sup> Fluorescence microscopy techniques are best utilised using glass, which is optically transparent.<sup>38,45</sup> Other bilayer substrates include silicon, gold and Polydimethylsiloxane (PDMS). Substrates can effect bilayer properties compared to free vesicles, for example lipid diffusion is reduced.<sup>29,46</sup> However, how different substrates affect bilayer properties is not well understood. There has also been very little work investigating how phase separation is affected

by different substrates. The literature regarding the effect of substrates on bilayer properties, specifically phase separation, is reviewed in more detail within Chapters 7 and 8.

### **1.2.7.3 Formation of Supported Lipid Bilayers**

The most common method to form SLBs is the vesicle fusion method (Figure 1.9).<sup>47,48</sup> Vesicle fusion involves incubation of SUVs, approximately 20-200 nm diameter, on a substrate. The process involves absorption of the vesicles to the surface, followed by rupturing and then spreading to form a planar bilayer across the surface.<sup>34,49</sup>

Another common method for forming SLBs is Langmuir-Blodgett (LB) or Langmuir-Schaefer (LS) Deposition (Figure 1.9).<sup>47</sup> This involves forming a lipid monolayer at the air-water interface in a Langmuir trough, and then pulling a substrate through the interface. This results in the deposition of a monolayer from the interface to the substrate, if a specified lateral pressure is applied to the monolayer using a compression barrier. Pulling the substrate through the interface twice deposits two monolayers to make a bilayer. The bilayer film must then be hydrated. LB/LS deposition is particularly useful for creating asymmetric bilayers, by replacing the lipid monolayer before the second deposition.



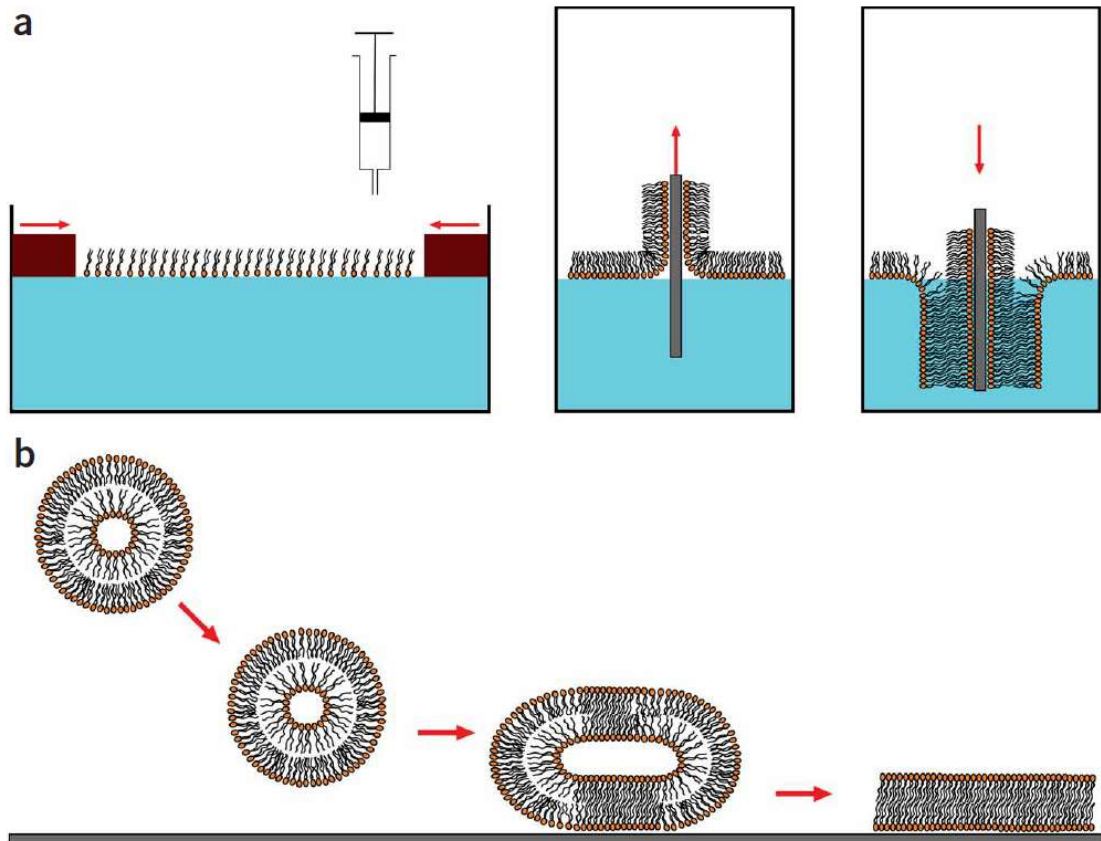


**Figure 1.9 Methods of SLB Formation. A) Langmuir-Blodgett Deposition, which involves SLB deposition by moving a substrate through a monolayer at an air-water interface B) Vesicle Fusion, which involves the absorption of vesicles to a substrate followed by rupturing and spreading. Image from reference<sup>47</sup>**

## 1.3 Asymmetry in Lipid Bilayers

### 1.3.1 Natural Asymmetry in biology

The cell membrane has a diverse range of different lipid types and shows asymmetry in terms of lipid composition.<sup>50</sup> In a healthy mammalian cell membrane, the extracellular (outward facing) leaflet comprises mainly PC and SM, the cytoplasmic leaflet (inward facing) contains mainly PS, PE and PI lipids (Figure 1.10).<sup>16,17,51</sup> Model bilayers formed from outer leaflet lipids show phase separation and those formed from inner leaflet lipids form only a single homogeneous phase.<sup>10,11</sup> Asymmetry can be maintained by translocase enzymes that can catalyse the transport of lipids between the two leaflets.<sup>52</sup> Asymmetry in terms of lipid compositions leads logically to the possibility of asymmetry in phase behaviour. Two different lipid phases could align opposite each other across the bilayer midplane.

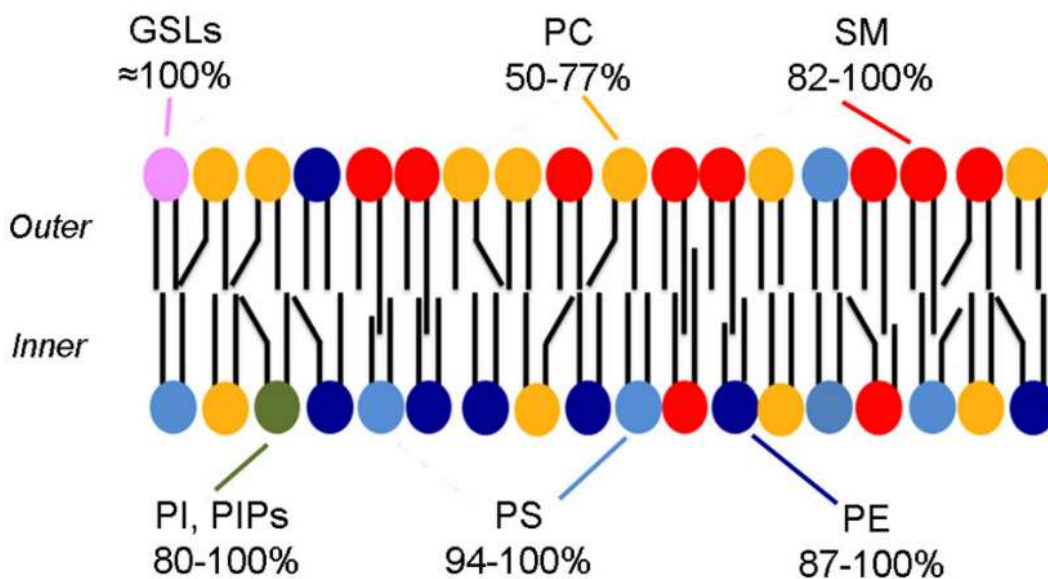


**Figure 1.10 Example showing the asymmetry in the erythrocyte (red blood cell) membrane. The colours indicate the type of lipid headgroup and shows the asymmetry between the inner and outer leaflet. The range in percentages indicates the amounts present in the preferred leaflet, but most lipids are likely to be present in the less favoured leaflet also, but in smaller amounts. Cholesterol is a major component of both leaflets but is not included in this figure. GSLs are glycosphingolipids. From reference<sup>16</sup>**

### 1.3.2 Symmetry in Model Bilayers

Model bilayers formed in the laboratory do not show the same asymmetry as natural cell membranes. In fact they form symmetrically as indicated by their phase behaviour. In 1999 Korlach et al. noted that for GUVs consisting of DLPC and DPPC, there was only one measured fluorescence intensity for the  $L_o$  and  $L_d$  regions.<sup>8</sup> The fluorescent dye is in both leaflets, so both leaflets are observed. There was no intermediate fluorescence value, which would occur if there were regions of one leaflet in the  $L_o$  phase and the opposing leaflet in the  $L_d$  phase. The domains in opposing leaflets superimpose across the two leaflets. This finding was backed up by Dietrich et al. in 2001 in GUVs,<sup>53</sup> and has been backed up hundreds of times since in free-floating vesicle systems. Figure 1.6 shows example GUVs with just two fluorescence intensities for  $L_o$ - $L_d$  phase separated systems.

SLBs formed from vesicle fusion on mica also show just two fluorescence intensities for DPPC/DOPC systems imaged using fluorescence.<sup>54</sup> The dye used DiI-C<sub>18</sub> (1,1'-Dioctadecyl-3,3',3',3'-tetramethylindocarbocyanin perchlorate), has been shown in separate studies using Fluorescence Interference Contrast Microscopy (FLIC) to partition  $36\pm 17\%$ <sup>55</sup> and  $54\pm 4\%$ <sup>56</sup> into the distal (top) bilayer leaflet of supported bilayers. Despite these numbers not matching particular well, what they prove is that the dye is definitely in both bilayer leaflets for SLBs. Relating back to the two fluorescence signals with no intermediate for self-assembled phase separated SLBs formed via vesicle fusion, this is evidence that the domains are symmetric between the two leaflets. For reference, results from this thesis also show just two fluorescence signals for  $L_\beta$ - $L_d$  phase separated SLBs (Figure 7.1). The height mismatch between phases measured by AFM, also provides evidence for domain symmetry. First of all as only two heights are observed, no intermediate height, but also as the height mismatch matches to the expected difference between the co-aligned heights of the individual lipids. This is discussed thoroughly in Chapter 4.

There is a clear difference between the domain symmetry observed in simplified symmetric model bilayers, and the complex, heterogeneous and asymmetric plasma cell membrane.

### 1.3.3 Registration and Anti-Registration

Bilayers that are symmetric are called registered (R), where  $L_o$  domains in one leaflet align with  $L_o$  domains in the opposing leaflet and  $L_d$  domains align opposite  $L_d$  domains (Figure 1.1A).<sup>7</sup> As the  $L_o$  phase lipids have more tightly packed tails in more extended conformations, the phase is usually thicker than the  $L_d$  phase. This causes an unfavourable interaction between the exposed hydrophobic tail chains of the  $L_d$  phase and external water. It has been shown that bilayers will rearrange their phase morphology and size, and even deform and bend to minimise this line tension.<sup>6,15</sup> The line tension caused by the hydrophobic mismatch between the  $L_o$  phase and the thinner  $L_d$  phase should make the anti-registered (AR) state more energetically favourable (Figure 1.1B). In the AR state,  $L_o$  domains align opposite  $L_d$  domain. As R is observed for model systems, this implies the presence of favourable interactions between similar phases in the two leaflets at the bilayer midplane.

Researchers have attempted to quantify these favourable interactions and the term 'mismatch free energy' is used to describe the energy penalty for anti-registration.<sup>57</sup> Mismatch free energy is the free-energy penalty for creating an asymmetric mismatch region per unit area at the expense of a symmetric region.<sup>57</sup> It is the difference between the initial fully R state and the final fully AR state (From A to B in Figure 1.1).

Mismatch free energy has been estimated theoretically ; 0.01-0.03  $k_B T/nm^2$  (<sup>57</sup>), 0.1-0.2  $k_B T/nm^2$  (<sup>9</sup>), 0.146  $k_B T/nm^2$  (<sup>58</sup>), 0.15±0.05  $k_B T/nm^2$  (<sup>59</sup>) and 0.5  $k_B T/nm^2$  (<sup>10</sup>). The estimates vary largely and this can be attributed to compositional dependence as well as the different models used to estimate the value. Line tension estimates vary in the literature but it is generally thought to be 1-10 pN<sup>15,60,61</sup> The large variance of the value is due to different lipids types, composition and height mismatch used to calculate it. The competition between the mismatch free energy and line tension likely determines whether domains register or anti-register. It could be possible to increase line tension to overcome the mismatch free energy.

### 1.3.4 Inter-leaflet Coupling

The registration of domains in vesicles and SLBs, indicates that there is interleaflet coupling between the two leaflets. There is a force or forces that

make it energetically more favourable for the same type of phase domain to face each other across the bilayer midplane. Biological membranes may be able to maintain asymmetry using translocase enzymes that mediate the exchange of lipids between the two leaflets,<sup>52</sup> but this must be overcoming the interleaflet coupling forces driving registration. The same forces must be present in both model systems and plasma membranes.

To date most investigations into the interleaflet bilayer forces which make up the mismatch free energy are theoretical calculations or simulations.

### **1.3.5 Computational Modelling**

Simulations have advanced sufficiently towards the realistic modelling of phase separation in bilayers, with properties that agree well with experimental data, such as AFM and NMR experiments.<sup>13,59</sup> The parameters that can be accurately modelled include correct lipid compositions in each phase, order parameters of lipid acyl chains, area per lipid values, membrane thickness and lateral diffusion coefficients. Coarse-grained molecular dynamic simulations, in which a bead represents a group of 4 non-hydrogen atoms, are a common method for modelling lipids in bilayers.<sup>13,59</sup> This reduction in complexity loses atomic detail but enables larger length and time scales, for example 40 x 40 nm for 10  $\mu$ s.<sup>62</sup> For a fully atomistic simulation, where each atom of the lipids is modelled individually, a more realistic length scale is 15 x 15 nm for 500 ns.<sup>58</sup>

Bilayers can be simulated to force compositional asymmetry and phase asymmetry by creating a single component  $L_d$  forming top leaflet opposite a ternary phase separated  $L_o/L_d$  bottom leaflet. This forces a  $L_o$  phase to form opposite a  $L_d$  phase, an AR state. One group's simulations<sup>13</sup> support experimental findings,<sup>63</sup> by showing that  $L_o$  domains in the ternary leaflet can potentially increase the lipid chain order of lipids in the opposite leaflet, forming a more ordered  $L_o$ -like phase in a lipid composition that would not normally phase separate. If the plasma membrane is in fact asymmetric and the inner leaflet does not have phase separating lipid compositions, then these findings go a long way to answering the question of how the proposed signalling rafts in cells transmit signals from the upper leaflet to lower leaflet.<sup>11</sup> For example an induced  $L_o$  phase, caused by outer membrane interactions

with a signalling molecule, could induce a more ordered phase in the inner leaflet causing a specific protein to fold into the membrane which forms a pore to allow another protein into the membrane.

### 1.3.6 Inter-leaflet Coupling Mechanisms

Several studies suggest the presence of a surface tension at the midplane between bilayer leaflets which is minimised by having lipids with similar tail ordering opposite each other.<sup>10,59,64</sup> This may be caused by a preference for lipid tails vibrations and fluctuations to exist next to a set of lipid tails with similar vibrations. One study compares the surface tension at the midplane to the line tension between  $L_o$  and  $L_d$  domains where the different ordered chains meet.<sup>10</sup> Assuming that the midplane surface tension per area is the same as the line tension per contact area of  $L_o$  and  $L_d$  phase, an estimate of  $0.5 \text{ k}_B\text{T}/\text{nm}^2$  can be made.<sup>10</sup> This could be driving registration but another study argues that the interfacial tension is not large enough to account for all of the mismatch free energy and that there are probably several contributing factors.<sup>64</sup> This argument is dependent on the magnitude of mismatch free energy however, which as shown earlier is not agreed upon.

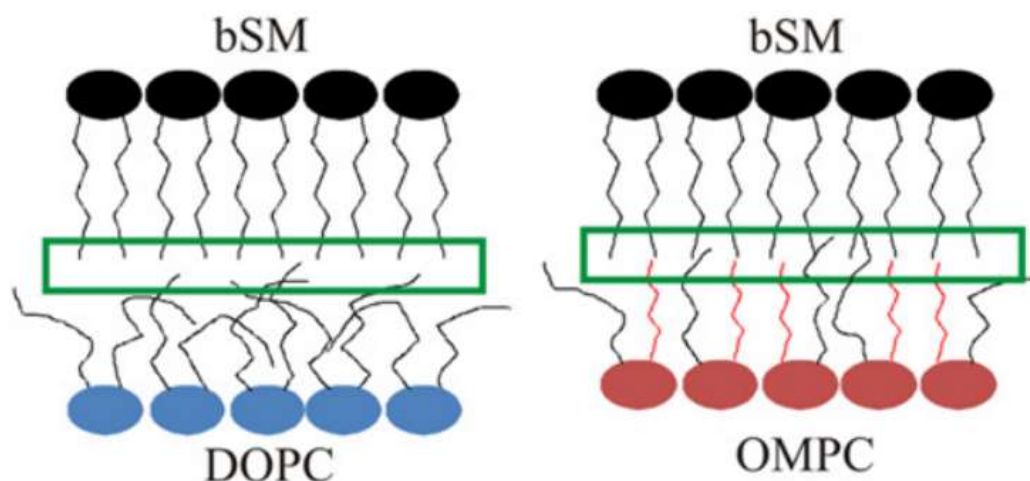


**Figure 1.11** A model example showing how acyl chain composition can influence interleaflet coupling. Schematic models of asymmetric bilayers with outer leaflets of brainSM and inner leaflets of DOPC (left) and OMPC (1-oleoyl-2-myristoyl-sn-glycero-3-phosphocholine/18:1-14:0PC)(right). The green rectangles indicate region near the bilayer midplane, where acyl chains from an opposing leaflet might interact. Red lines represent the saturated PC acyl chains in OMPC. The figure shows greater interdigitation for OMPC than for DOPC. From reference<sup>181</sup>



A progression of the idea of surface tension at the midplane is the idea of dynamic chain interdigitation, when lipid tails can cross the midplane of the bilayers and increase their entropy.<sup>9</sup>  $L_d$  chains can penetrate more easily into opposing  $L_d$  chains than they can to opposing  $L_o$  chains. The lower chain packing and density of the  $L_d$  chains enables this, whereas the more densely packed  $L_o$  chains hinder this. Therefore the alignment of  $L_d$  phases opposite  $L_d$  phases causes the entropy to increase relative to having  $L_d$  phases opposite  $L_o$  phases. Again the significance of this coupling mechanism is disputed with one study calculating it to be of the same order of magnitude as the estimated mismatch free energy.<sup>9</sup> Another study however, suggests that chain interdigitation is only significant if the lipids have different tail lengths and if there is a low level of cholesterol.<sup>10</sup> Figure 1.11 shows a schematic representation of how the extent of interdigitation can depend on lipid type.

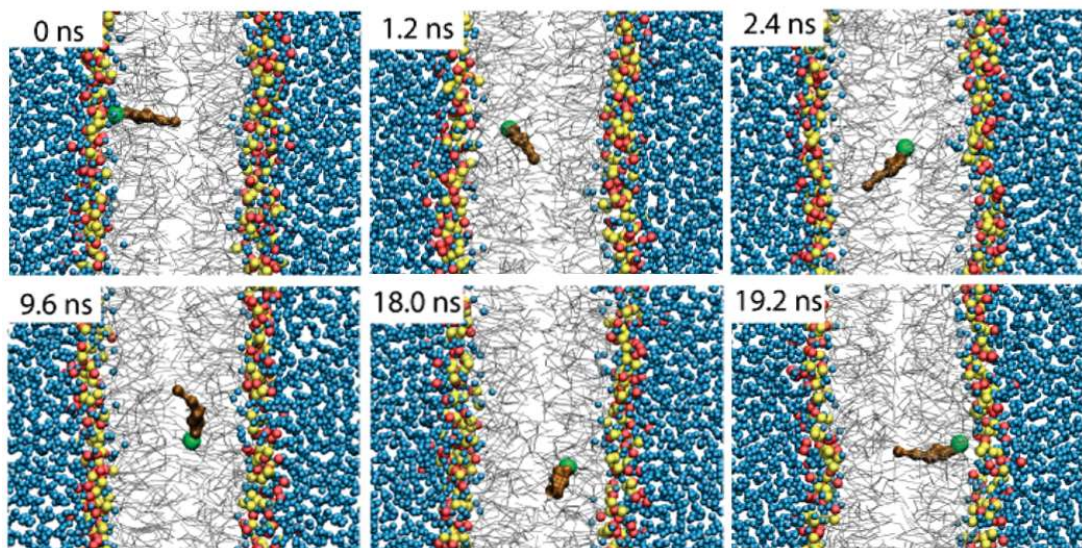


**Figure 1.12 Snapshots from coarse-grain molecular dynamics simulations illustrating cholesterol flip-flop. The bilayer is made from coarse-grain DPPC. Water particles are blue spheres. For DPPC the choline parts of the headgroups are red spheres, the phosphate parts of the headgroups are yellow spheres and the tails are grey lines. The body of cholesterol is brown and the hydroxyl groups are green spheres. 0 ns corresponds to the time point immediately preceding the hydroxyl of cholesterol entering the hydrophobic interior of the bilayer (1.2  $\mu$ s of whole simulation). The figure shows a cholesterol molecule flipping from one leaflet to the adjacent leaflet. The timescale of flip-flop can be dependent on bilayer composition and can vary between different simulations and experiments. Cholesterol flip-flop between different phases has been proposed as an interleaflet coupling mechanism. From reference<sup>182</sup>**

The DOPC example shows no interdigitation and the OMPC example shows slight interdigitation.

Cholesterol flip-flop is the movement of cholesterol between the two bilayer leaflets (Figure 1.12).<sup>9</sup> There is evidence in coarse-grain simulations to show that cholesterol has a higher relative diffusion rate in the  $L_d$  phase,<sup>59</sup> likely due to the less densely packed chains in this phase. Therefore it is proposed that cholesterol can flip-flop faster when two  $L_d$  domains align across leaflets. For non-matching domains there are lower rates of flip-flop and there is a free energy cost of confining cholesterol to one leaflet. Some consider this to be too small to significantly contribute to mismatch free energy,<sup>57</sup> one study calculating it to be just  $0.003 k_B T/nm^2$ . One study describes cholesterol flip flop as enabling the system to be driven towards the equilibrium state faster where the chemical potential of cholesterol in the two leaflets is the same.<sup>10</sup> Another coarse-grain simulation study shows that with cholesterol flip-flop there is registration of domains, and without it there is anti-registration.<sup>65</sup>

Intermolecular interactions may also contribute to interleaflet coupling, such as those detailed in Table 1.3. Different intermolecular interactions act over different length scales and this is important for interleaflet coupling. Electrostatic interactions between two charged polar headgroups (dipoles) have a  $1/r^3$  distance dependence and must act across the 4/5 nm bilayer. Van der Waals interactions however, which have a shorter range  $1/r^6$  dependence, can act between lipids in opposite leaflets directly at the midplane. Electrostatic coupling of charged lipid headgroups based on a Boltzmann model has been calculated and there is determined to be a stronger repulsion across R domains than AR domains, but this is not considered large enough to significantly contribute towards the mismatch free energy.<sup>9</sup> Simple Van der Waals attraction between non-polar tails has also been discussed as a coupling mechanism but not significantly researched.<sup>9</sup> It is clear that more research is needed on how intermolecular interactions may contribute to interleaflet coupling and how headgroup charge, headgroup size, tail length, electron density of tail chains and temperature may affect this coupling.

Although several coupling interactions have been proposed it is still unclear which is dominant and what the magnitudes might be. Dynamic chain



interdigitation and cholesterol flip-flop are considered to be the highest contributors to the mismatch free energy but other mechanisms and interactions have been considered. Mismatch free energy is likely to be the sum of several contributing forces, a compromise to find the lowest free energy. There is much debate in the literature<sup>9,10</sup> but what is needed is experimental evidence. Computational modelling has taken the field forward but there is a lack of experimental evidence proving or disproving any of the inter-leaflet coupling findings in simulations.

One group suggest that interleaflet coupling forces are not required for domain registration, but instead shifting domains in opposing leaflets relative to each other by a few nm can reduce line tension.<sup>66</sup> This is controversial, with a comment to this paper published claiming that an asymmetric slip region of domains in opposing leaflets with no direct leaflet coupling would in fact cause AR.<sup>67</sup>

It is clear that despite many simulations and theoretical studies, what is needed is experimental evidence to prove which interleaflet coupling mechanisms are responsible for domain registration.

### **1.3.7 Asymmetry in Model Bilayers**

Researchers have developed numerous techniques for forming asymmetric model bilayers, and the key methods are outlined below.

Chemical methods can be employed to create asymmetry. Enzymes can be added to pre-formed symmetric vesicles to modify the headgroups of the outer lipids,<sup>68</sup> and pH differences can be applied across the vesicle bilayer containing charged lipids.<sup>68,69</sup> Catalysed lipid exchange uses lipid carriers such as bovine serum albumin or cyclodextrins to mix together two symmetric vesicle populations.<sup>68</sup> For example methyl- $\beta$ -cyclodextrin (m $\beta$ CD), a ring-shaped oligosaccharide, can extract and create a complex with a single lipid form a vesicle, due to its hydrophobic core.<sup>68,70</sup> If m $\beta$ CD is incubated with donor vesicles, and then acceptor vesicles with different lipid are added, there is an exchange of the acceptor vesicle outer leaflet with donor lipid, resulting in an asymmetric vesicle. Catalysed lipid exchange is a powerful technique, but currently only LUVs have been formed via this method, which make it hard to observe phase separation and asymmetry thereof.

Asymmetric vesicles can be formed using the phase transfer technique.<sup>71</sup> This technique starts by forming water-in-oil droplets. The oil is saturated with lipid (Lipid A) and the water-in-oil droplets are stabilised by the formation of monolayers at the air-water interface. These monolayer-stabilised water-in-oil droplets are then passed through an oil-water interface with a second oil containing a second lipid (Lipid B). At this oil-air interface, monolayers of Lipid B are present. As the water-in-oil droplets stabilised by Lipid A pass across the interface they are encapsulated by the monolayer of Lipid B, forming an asymmetric vesicle in water with Lipid A on the inside and Lipid B on the outside. Phase transfer can also be performed on a microfluidic chip.<sup>72</sup>

Another method that can combine two monolayers of different lipids is Langmuir-Blodgett/Langmuir-Shaefer Deposition (Section 1.2.7.3).<sup>55</sup> Once the substrate has been moved through the air-water interface once, the lipid monolayer is replaced with a monolayer of a second lipid, and the substrate is moved through the interface a second time. Crane et al. used LB/LS deposition to form SLBs with two different phase separating mixtures in each leaflet.<sup>55</sup> Using fluorescence microscopy with dye in both leaflets, these bilayers clearly show asymmetric phase behaviour between the two leaflets i.e. areas of AR with misaligned domains. This is observed via two clear sets

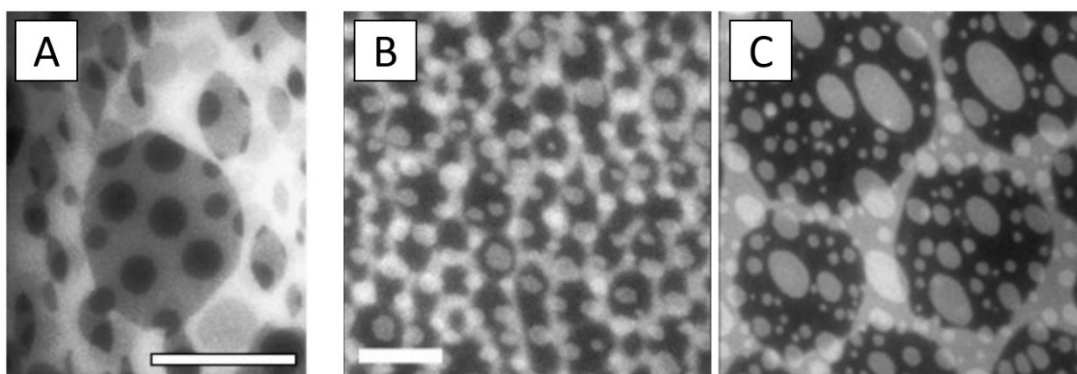


**Figure 1.13** Examples from literature of LB/LS bilayers with the same lipid compositions in both leaflets, showing  $L_o/L_d$  domains not in registration. **A)** LB/LS bilayer of 2:2:1 DOPC/BSM(BrainSM)/Chol +TR-DPPE in both leaflets on glass. Scale bar is 20  $\mu\text{m}$ . From reference<sup>40</sup> **B)** LB/LS bilayer of 1:1:1 POPC(1-palmitoyl-2-oleoyl-glycero-3-phosphocholine)/DPPC/Chol +0.5% Rhodamine-DPPE dye in both leaflets **C)** LB/LS bilayer of 1:1:1 bPC(Brain PC)/bSM/Chol + 0.5% Rhodamine-DPPE in both leaflets. Both B and C were formed on quartz and are the same size image. The scale bar in B is 10  $\mu\text{m}$ . Both B and C are from reference<sup>55</sup>

of contrasting domains size that are not registered. Also, there are three different fluorescence intensities. The dye partitions preferentially into the  $L_d$  phase and therefore these three intensities are; highest for  $L_d$ - $L_d$ , half intensity for  $L_d$ - $L_o$ / $L_o$ - $L_d$  and no intensity or background intensity for  $L_o$ - $L_o$ . LB/LS bilayers formed with the same composition in both leaflets also show asymmetric domain formation i.e. domains are not in registration (Figure 1.13).<sup>40,55</sup> This is despite self-assembled vesicles and SLBs with the same compositions forming symmetric registered bilayers. This questions the validity of the LB/LS technique for forming bilayers, which seems to produce a different structure to one that self-assembles.

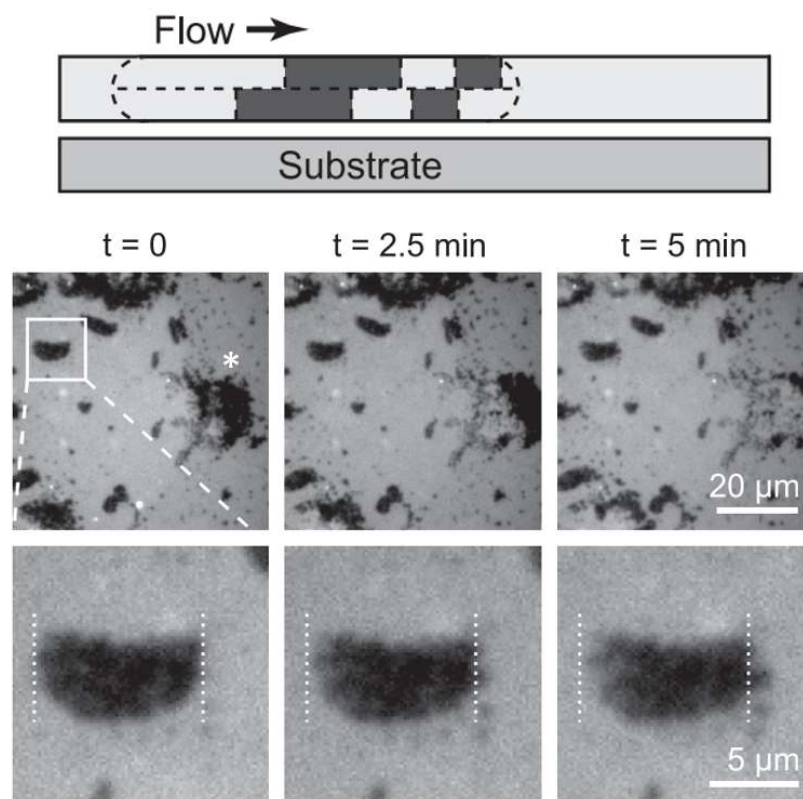


**Figure 1.14 Shear applied to bilayers to de-register domains. The top schematic shows how the flow of water in a microfluidic device across a supported bilayer can cause domains to de-register. The supported bilayers are formed by rupturing  $L_o$ - $L_d$  GUVs onto glass and then using vesicle fusion of  $L_d$  SUVs to form a full SLB. The fluorescence microscopy images show the movement of domains from left to right under a solvent flow rate of 0.66 mL/min corresponding to 25 Pa shear at the centre of the image. The large starred domains moves drastically under the flow conditions, whereas the smaller domain shown on the bottom row moves less. Threshold movement shear is proportional to domain size. At a lower shear of 17Pa the large domain moved but the small domain did not (data not shown). From reference<sup>73</sup>**

Although there are many ways of forming asymmetric vesicles, none of the methods outlined above enable the measurement of interleaflet coupling forces and mismatch free energy. There are issues with domains not being large enough to observe, or there not appearing to be any coupling between the leaflets, as with LB/LS bilayers. Another issue with these methods is that they are not in equilibrium and through lipid flip-flop between the leaflets should eventually return to the equilibrium state of symmetric composition and phases. Without translocases, as in the plasma cell membrane, it is hard to hold bilayers out of equilibrium.

An inventive method to force asymmetry used flow to apply shear stress to the top leaflet of a vesicle ruptured onto a surface (Figure 1.14).<sup>73</sup> This resulted in misaligned domains between the two leaflets, which were large enough to be measured optically using fluorescence. This enabled the only mismatch free energy estimate from directly from experimental data,  $0.016 \pm 0.004 \text{ k}_B\text{T}/\text{nm}^2$ . This compares well with one estimate from theoretical calculations and not with others;  $0.01\text{-}0.03 \text{ k}_B\text{T}/\text{nm}^2$  <sup>(57)</sup>,  $0.1\text{-}0.2 \text{ k}_B\text{T}/\text{nm}^2$  <sup>(9)</sup>,  $0.146 \text{ k}_B\text{T}/\text{nm}^2$  <sup>(58)</sup>,  $0.15 \pm 0.05 \text{ k}_B\text{T}/\text{nm}^2$  <sup>(59)</sup> and  $0.5 \text{ k}_B\text{T}/\text{nm}^2$  <sup>(10)</sup>.

Lin et al. show the only experimental evidence showing potential anti-registration purely from allowing vesicles to fuse onto a surface and then allowing domains to grow, in DLPC/DPSC SLBs (Figure 1.15).<sup>74</sup> Three heights are observed using AFM, explained as the coexistence of R gel, R fluid and an intermediate height AR state. The authors claim that by varying the method of SUV formation, different levels of the gel phase lipid DSPC can be found between the two leaflets of SUVs before deposition, a result of the different lipid packing parameters and high curvature in the small vesicles. The domains also changed over time with the tallest R gel phase eroding over time to make way for a higher area fraction of the AR state. This is explained as flip-flop of lipids to alleviate the large hydrophobic mismatch between DLPC and DPSC, six carbon difference in acyl chain length.

The large hydrophobic mismatch between the two phases is likely very significant in the work of Lin et al.<sup>74</sup> Not only is it likely the driving force behind the flip-flop towards a larger AR area fraction, it is also likely the only reason AR states form in the first place. There have been no other reports of three phase bilayers forming naturally from a mixture, without the monolayer leaflets being forced in some manner, and the next section details simulations and theory that can explain why the only observed case appears in a system of high hydrophobic mismatch.

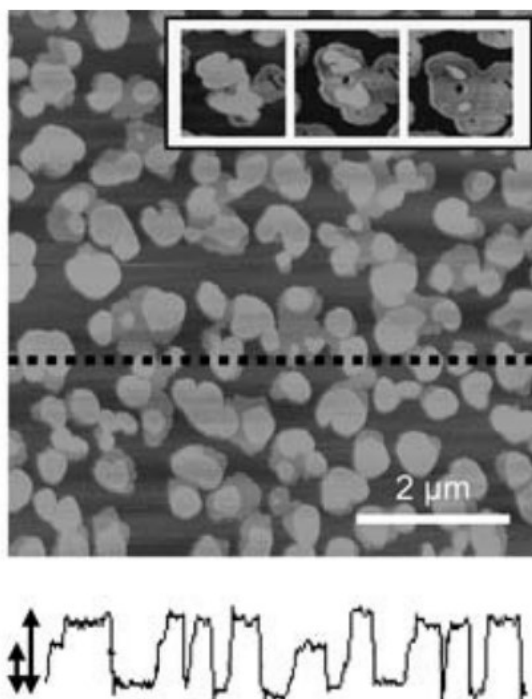


**Figure 1.15 AFM image and line scan height section of three heights in a DLPC/DSPC SLB formed on mica, showing potential AR. Lighter colour represents higher phases. AFM image was acquired over minutes with the SLB domains stationary over this timescale. The line scan below the AFM image is taken from the black dotted line on the AFM image. The domains have heights extending 1.8 nm and 1.1 nm above the surrounding lower height DLPC phase and these heights are indicated with arrows beside the line scan. The top right inset shows 1.8 nm height domains convert into 1.1 nm domains. The inset images are taken at 30 min, 1.5 h and 4 h after SLB formation. From reference<sup>74</sup>**

### 1.3.8 Increasing Hydrophobic Mismatch

Coarse-grained molecular dynamics simulations shows the effect of increasing hydrophobic mismatch on domain registration.<sup>13</sup> The length of the saturated  $L_o$  chain is lengthened to increase the height mismatch and the line tension. When the height mismatch is increased to a carbon chain mismatch between the  $L_o$  and the  $L_d$  of 4 carbons, an AR state becomes energetically favourable (Figure 1.16). Although this is not the exact acyl chain mismatch in the AR systems observed by Lin et al.,<sup>74</sup> the absolute values from this simulation may not translate into experiments, however the simulations show that increased hydrophobic mismatch results in AR. This suggests that it could be possible to observe AR experimentally by following a similar method of increasing height mismatch and line tension. This finding is backed up by separate coarse-grained molecular dynamics simulations published more

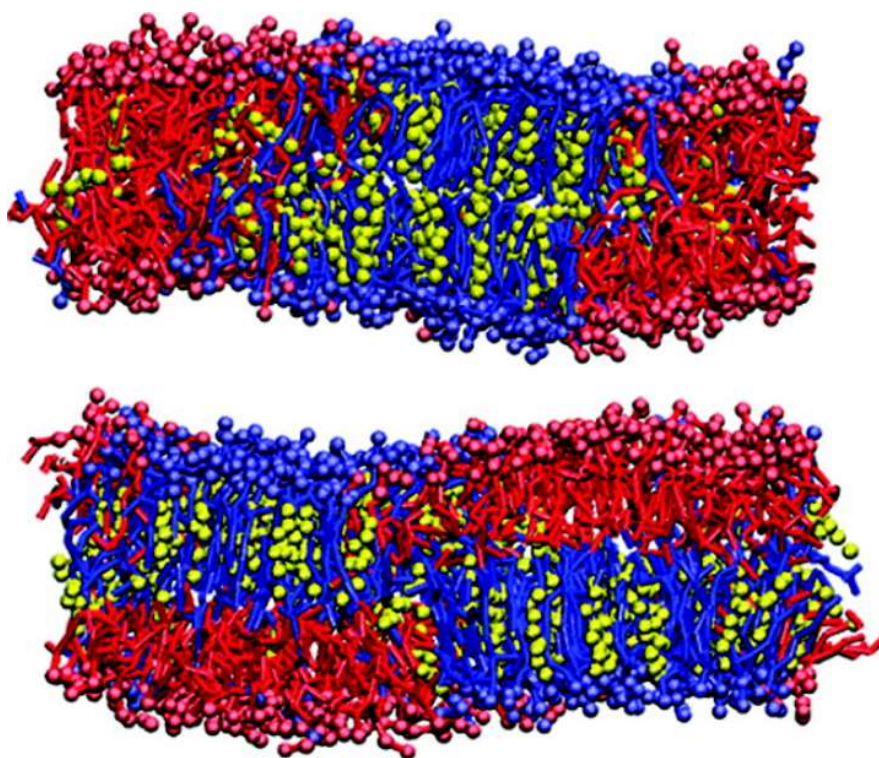


**Figure 1.16** Snapshots from coarse-grained molecular dynamics simulations showing registration (R) and anti-registration (AR). The top bilayer shows R. The length of the saturated lipid tail is then increased and the bilayer shows AR (bottom bilayer). Saturated lipids are blue, unsaturated lipids are red and cholesterol is yellow. Water has been removed from the figure for clarity. From reference<sup>13</sup>

recently, which also find that increasing hydrophobic mismatch results in AR bilayers.<sup>75,76</sup>

A mean-field model which specifically accounts for amphiphile (lipid) level structural features also shows how increasing height mismatch can lead to AR bilayers.<sup>14,77,78</sup> There are two competing couplings;  $J$  which represents line tension and promotes AR and  $B$  which represents the mismatch free energy and favours R. The competition of these two parameters leads to complex energy landscapes suggesting complex kinetics. Figure 1.17 shows a leaflet-leaflet free energy diagram where the  $z$  axis is the free energy, and the  $x$  and  $y$  axes represent the upper and lower leaflet compositions of a bilayer. The  $x=y$  plane represents a totally symmetric bilayer (representing a single tie line on the standard phase diagram which assumes full symmetry of the bilayer), and any deviation from this plane represents asymmetry. There is a clear competition between metastable AR states as well as equilibrium R states. Metastable AR states can form before reaching the equilibrium R state but only when there is a sufficient hydrophobic mismatch.

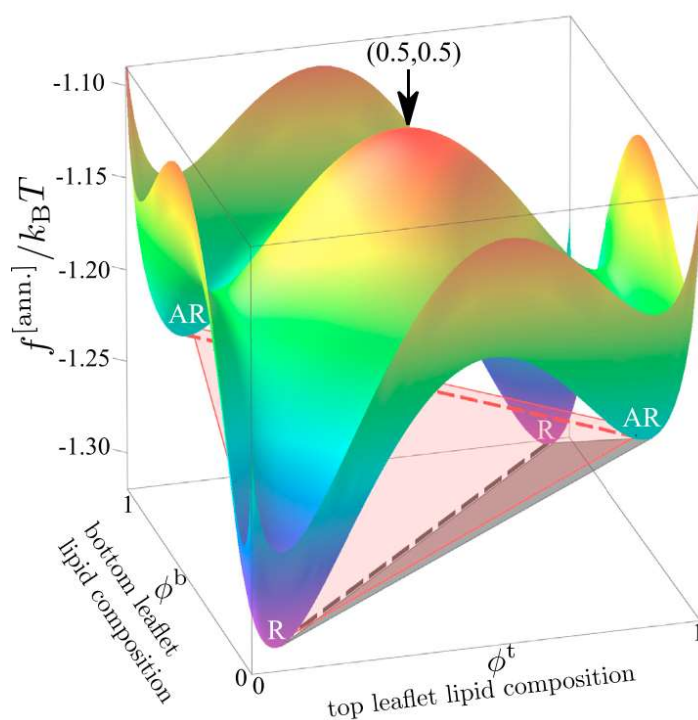


**Figure 1.17 Local 3D free energy landscape shown for set values of  $J$ , which represents line tension and promotes anti-registration, and  $B$ , which represents the mismatch free energy or interleaflet coupling parameter and promotes registration. The  $x$  and  $y$  axes are the individual compositions of the two leaflets and the  $x=y$  line corresponds to a symmetric bilayer. The black dotted line shows coexistence between two R phases, R-R. The red dotted line shows coexistence between two AR phases, AR-AR. The black and red three phase triangles correspond to the coexistence of 3 phases, R-R-AR or AR-AR-R. R-R would manifest itself as Figure 1.16 top/Figure 1.1A. AR-AR would manifest itself as Figure 1.16 bottom/Figure 1.1B. R-R-AR would manifest itself as Figure 1.15/Figure 4.13, with three heights. From reference<sup>14</sup>**



## 1.4 Thesis Aims and Structure

This thesis aims to use experimental methods to investigate interleaflet coupling forces and mismatch free energy. To be able to estimate the mismatch free energy (also called interleaflet coupling parameter in literature<sup>73</sup>) a system was designed that sequentially increases hydrophobic mismatch to see if and at what hydrophobic mismatch anti-registration becomes favoured. This will be the point at which the energy penalty for line tension becomes higher than the energy gained for R domains. This should allow the estimation of the mismatch free energy.

Chapter 1 – Introduction to Lipid Bilayers and Asymmetry.

Chapter 2 – Experimental techniques used in this thesis.

Chapter 3 – Experimental methods used in this thesis.

Chapter 4 – Hydrophobic mismatch is increased in ternary lipid supported bilayers to try to overcome interleaflet coupling forces and form AR bilayers.

Chapter 5 – Methods for forcing AR bilayers are explored including forming close to critical 50:50  $L_o:L_d$  area fraction mixtures and attempting temperature control and quenching of bilayers while AFM imaging.

Chapter 6 – AFM mechanical measurements are explored as a method for distinguishing between and isolating the effects of individual bilayer leaflets.

Chapter 7 – The effect of glass substrates on domain formation is investigated and compared to mica using fluorescence and AFM, to help explain confusing fluorescence results and the trapped nature of domains on surfaces.

Chapter 8 – The effect of PDMS on domain formation is investigated. PDMS is a substrate that allows patterning and curving of bilayers, and the aim was to link asymmetry and curvature in bilayers.

## Chapter 2. Background to Experimental Techniques

### 2.1 Atomic Force Microscopy

AFM is a type of Scanning Probe Microscopy, a class of microscopy that forms an image by scanning a probe across a surface and monitoring the probe-surface interactions. First the Scanning Tunnelling Microscope was developed in the early 1980s by Binnig and Rohrer, making use of quantum tunnelling of electrons to image conductive samples.<sup>79</sup> Then Binnig demonstrated the first use of an AFM in 1986, capable of imaging insulator samples.<sup>80</sup> A probe with a sharp tip is raster scanned across a sample surface, and a 3D topography map is obtained, giving angstrom level resolution in the Z direction. AFM is a versatile tool and has developed as a good method for imaging biological samples in aqueous environments. With the continued development of fast scan imaging, AFM has transformed from a technique that took minutes to render one image, to a technique that can image biological processes

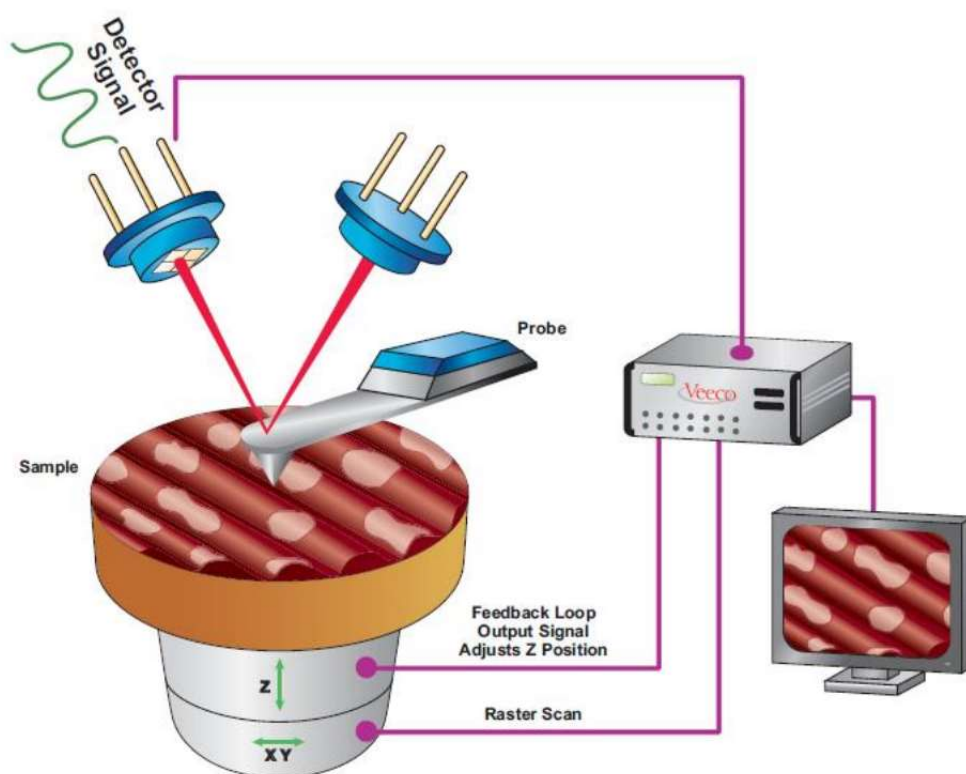


Figure 2.1 Schematic of an Atomic Force Microscope (AFM) setup.  
From reference<sup>183</sup>

happening in real time, with several frames per second. The basic components of an Atomic Force Microscope (AFM) setup are shown in Figure 2.1. AFM is regularly capable of 0.1 nm z resolution and 10-50 nm x-y resolution,<sup>81</sup> however sub-angstrom molecular resolution can be achieved using a carbon monoxide (CO) molecule absorbed onto the AFM probe in an ultrahigh vacuum.<sup>82</sup> To function at the high resolution that it does, there are several key features which are discussed below.

## 2.2 AFM Probes

Colloquially within an AFM lab, the terms 'probe', 'tip', 'cantilever' and 'lever' can often be used interchangeably. In this thesis the terms will be used to describe specific aspects of the AFM probe. A schematic of an AFM probe and an electron microscopy image of an AFM tip are shown in Figure 2.2. Probe is a general term used to describe the whole silicon/silicon nitride wafer chip, which consists of the base used to clip the probe into AFM tip holder, a cantilever and a tip.

Cantilever refers to the mechanical lever that protrudes from the probe base and deflects as it crosses across features on the scanned surface. Cantilevers come in a variety of shapes but the standard shape is triangular, as shown in Figure 2.2A. Typical cantilevers dimensions are 20-150  $\mu\text{m}$  in length and 5-

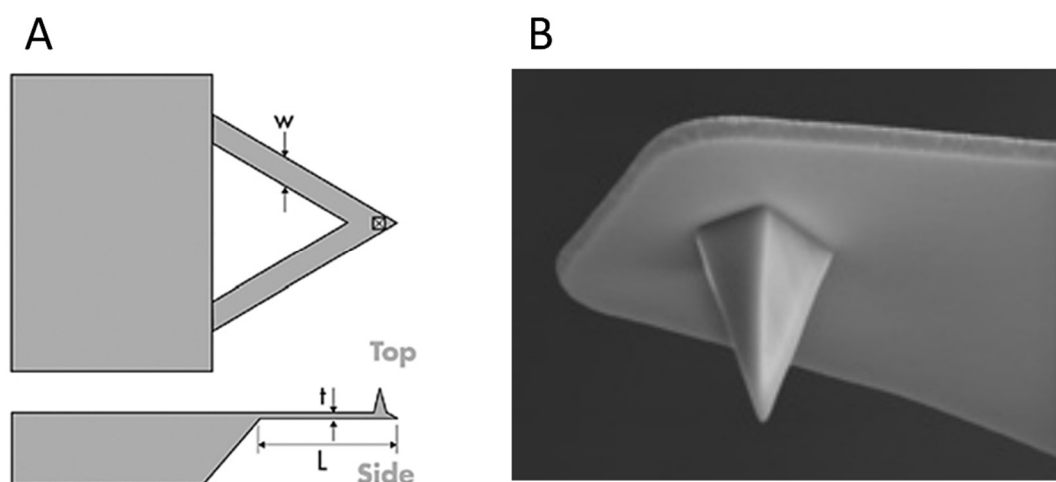


**Figure 2.2 AFM Probes Schematic and Image A) Schematic of an AFM probe showing the cantilever protruding from the probe, and the tip protruding from the cantilever. B) Electron microscopy image of an AFM tip protruding from a cantilever. From reference<sup>184</sup>**

25  $\mu\text{m}$  in width. Cantilever spring constant ( $k$ ) values can vary from 0.1 N/m for the study of soft samples such as biomolecules, to 100-200 N/m for the study of harder samples such as metal films. Softer cantilevers with lower spring constants enable a higher  $z$  resolution.

The tip is sharp and protrudes down from the cantilever with a pyramidal shape, and is the part of the AFM probe which interacts and makes contact with the surface. AFM tips typically have radius values of 5-50 nm, the sharper tips providing higher resolution.

### **2.3 Piezo Scanner**

Piezoelectric materials, usually made from ceramics, are vital for AFM as they enable voltage to be converted into mechanical motion.<sup>81</sup> When a voltage is applied across a piezo, it changes geometry. The expansion of the piezo per volt applied is typically around 1nm.<sup>81</sup> It is this property which enables AFMs to control small movements and image at high resolution. There are two different types of piezo in an AFM system. There is an X-Y scanning piezo which is responsible for moving the tip across the sample in a raster pattern. It should be noted that in Figure 2.1 the X-Y scanner is below the AFM sample stage, and thus it is actually the sample that is moved relative to the tip. There is also a Z piezo scanner which enables the force applied to the bilayer to be finely controlled.

### **2.4 Feedback Control**

Feedback electronics enable the force to be kept constant across an image so that the tip tracks the surface topography. The force on the cantilever across the sample is fed into a PID (Proportional-Integral-Derivative) controller, which uses the change in force from the desired set point, along with user input proportional and integral gains, to control the Z piezo and move the force back to the set point.

## 2.5 Imaging

The probe, piezo and feedback control work together to scan a surface. The AFM probe is used as an optical lever force sensor. A laser is aligned on the reflective top coating of the probe into a photodetector. A set point is defined by the user which is a set force, or in reality a set voltage relative to the photodetector. When the tip begins to scan across the surface, moved by a voltage signal sent to the X-Y piezo, the tip will deflect more as it hits higher surface features and less as it crosses lower surface features. This change in deflection of the cantilever, causes the reflected laser spot to move on the photodetector. The change in voltage in the photodetector is then fed through the PID feedback loop, where it is combined with user defined proportional and integral gains to send a voltage back to the Z piezo to move up or down to rectify the cantilever deflection back to the setpoint. The movement of the Z piezo therefore gives a track of the topography of the sample.

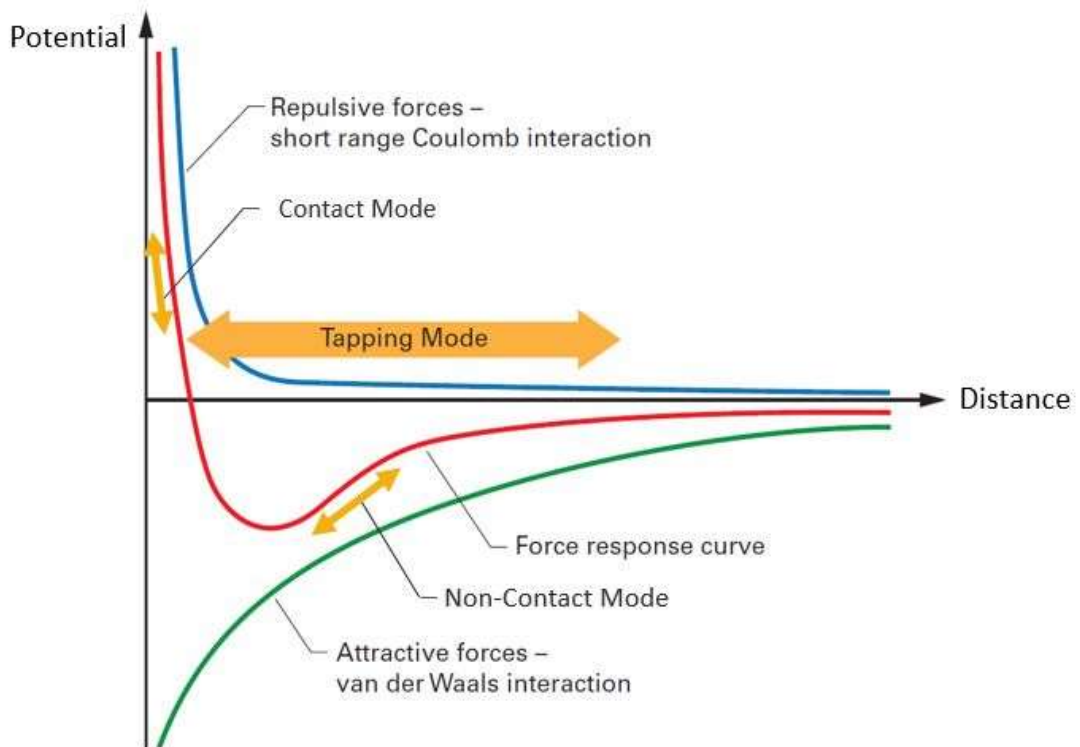


**Figure 2.3 Lennard-Jones potential showing tip-sample forces in AFM. Adapted from reference<sup>86</sup>**

## 2.6 Tip-Sample Forces

When the tip interacts with a surface, the forces involved can be shown using the Lennard Jones Potential (Figure 2.3).

$$U(r) = 4\varepsilon \left( \left( \frac{\sigma}{r} \right)^{12} - \left( \frac{\sigma}{r} \right)^6 \right) \quad (2.1)$$

Where  $U(r)$  is the potential energy between the tip and the sample,  $r$  is the tip-sample distance,  $\varepsilon$  is the minimum potential and  $\sigma$  is the tip-sample separation at zero potential. As the tip approaches the sample there is first an attractive Van der Waals force, causing the cantilever to deflect towards the surface. Then as the tip-sample separation drops there is a shorter range repulsive force due to the Pauli Exclusion principle, that equals out and then overcomes the attractive force, resulting in the cantilever deflecting away from the surface. The type of tip-sample interaction, as described by the Lennard-Jones potential, leads to different modes of AFM Imaging.

## 2.7 Imaging Modes

### 2.7.1 Contact Mode

The most basic AFM imaging mode is contact mode. For contact mode, the tip-sample interaction is in the repulsive regime so the cantilever is constantly deflected away from the surface. The cantilever tip is brought into contact with the surface to a set deflection setpoint. As the tip moves across the bilayer, the changes in height on the surface cause the cantilever to deflect. The feedback circuit maintains the cantilever deflection at a constant level by moving the Z piezo. The z piezo motion gives a map of the surface topography. As the tip is always in contact with the surface contact mode can apply high lateral forces as it is scanned across a surface. This makes it unsuitable for imaging soft biological samples as they are destroyed or displaced.

### 2.7.2 Tapping Mode

Tapping mode AFM makes intermittent contact with the surface instead of being in contact with the surface constantly. This is achieved by resonating the cantilever at its resonant frequency, at amplitudes of around 20 nm. The

full cycle of the oscillation takes the tip in and out of the attractive and repulsive regimes repeatedly. The feedback is now controlled by an amplitude set point of the oscillation. If the tip interacts with a higher surface feature the oscillation is damped, and the z piezo will retract the tip to return the amplitude to the set point. When the tip interacts with lower surface features the oscillation amplitude increase and the z piezo moves the tip down to damp it back to the set point. By being in intermittent contact with the surface the lateral forces on the sample are reduced, so this mode is safer for imaging soft samples that may be damaged.

When in tapping mode a phase image is captured simultaneously with a topographic image. This is the phase difference between the driving piezo and the cantilever.<sup>83</sup> According to Simple Harmonic Theory this lag is  $90^\circ$  at the resonant frequency.<sup>81</sup> As the resonating cantilever approaches the surface the tip interacts with the sample. Intermolecular forces between tip and surface cause the oscillation amplitude to be reduced in response to the surface topography. There is then a phase lag between the oscillation of the piezo and the oscillation of the cantilever, which is the phase measurement. Phase images can be indicative of the physical properties surface.

### 2.7.3 Imaging bilayers

AFM is a particularly good technique for imaging SLBs as the z resolution can measure height mismatch between different phases to the angstrom level (Figure 2.4).<sup>19,24</sup> The x-y resolution of AFM, which is affected by the tip radius and the sampling rate, is also far superior to diffraction limited techniques. Domains sizes of 10s of nanometres can be imaged easily. AFM images, like the image in Figure 2.4, are false colour images. Z distance is represented by

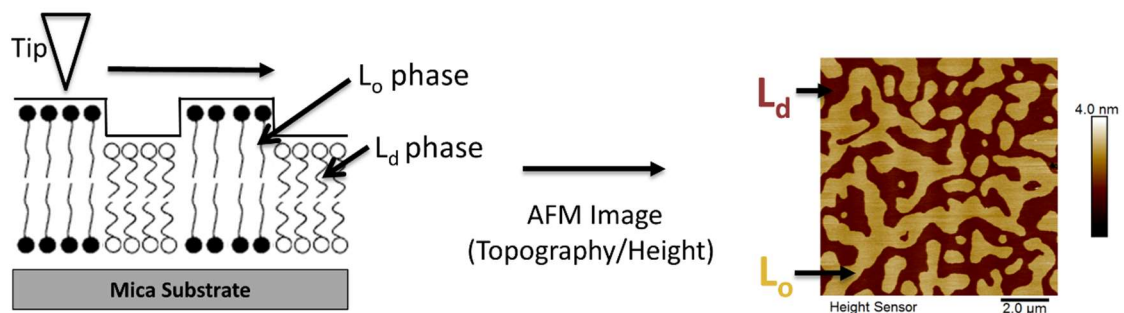


**Figure 2.4 Schematic of AFM tip scanning across phase separated bilayer and an example AFM image.**

a colour gradient with a scale bar to the right of the image. AFM can be run smoothly in liquid, which is vital for bilayer imaging as they must be kept hydrated at all times.

## **2.8 AFM Force Spectroscopy**

AFM Force spectroscopy enables the nano-mechanical properties of surfaces to be probed. By recording the deflection of a cantilever as it is extended and retracted on a surface in just the Z direction with no lateral X-Y scanning, a force curve mapping the interactions between tip and sample is produced. Example force curves are shown in Figure 2.6. These force curves are for lipid bilayers and will be discussed later in this section. For quantitative force measurements, the force exerted by the cantilever on the sample must be known. Therefore the cantilever must be calibrated so that deflection which is initially in volts, can be converted to displacement and then to force. This involves calibrating the deflection sensitivity (nm/V) and the spring constant (N/m) for the cantilever.

### **2.8.1 Cantilever Calibration**

#### **2.8.1.1 Deflection sensitivity**

First, the deflection in the photodetector measured in volts (V) must be converted to a deflection of the cantilever in distance (nm). This conversion needs the deflection sensitivity (V/nm) of the cantilever, which is the change in voltage in the photodetector per unit distance of cantilever deflection. This can be calibrated by ramping the cantilever into a surface with a modulus significantly higher than that of the tip, so that only the cantilever deflects when there is contact and there is no deformation of the surface. In this case, all of the cantilever deflection results in movement of the reflected laser in the photodetector. The deformation of the surface does not reduce the movement of the reflected laser in the photodetector and does not affect the deflection sensitivity of the cantilever which is independent of the type of surface.



### 2.8.1.2 Spring Constant

Cantilever deflection (nm) can be converted to a force (N) if the cantilever spring constant (N/m) is known. The cantilever can be modelled as a spring and Hooke's law used.

$$F = -kx \quad (2.2)$$

Where  $F$  is the force applied,  $x$  is the displacement of the cantilever and  $k$  is the spring constant. The spring constant can be measured directly using a Vibrometer. Alternatively, a thermal tune can be used which measures the mechanical response of the cantilever to thermal fluctuations. If the cantilever is considered to be in equilibrium with its surroundings, the equipartition theorem allows thermal fluctuations to be linked to the work done by the cantilever. By measuring the mean-squared displacement of the cantilever, the spring constant can be calculated. If the lever spring constant is pre-calibrated by the manufacturers, then the thermal tune can be used in reverse and the deflection sensitivity can be obtained without touching the surface.

$$k = \frac{0.971k_B T}{\chi^2 \langle Z^2 \rangle} \quad (2.3)$$

Where  $k$  is spring constant,  $T$  is temperature,  $k_B$  is the boltzmann constant,  $Z$  is cantilever displacement and  $\chi$  is the sensitivity correction factor.

### 2.8.2 Contact Mechanics

Once the cantilever is calibrated, force curves can be displayed as Force vs  $Z$  distance. These force curves can be used to calculate the modulus of the sample being measured. Young's modulus is defined as;

$$E = \frac{\sigma}{\varepsilon} = \frac{\frac{F}{A}}{\frac{\Delta L}{L}} \quad (2.4)$$

Where  $E$  is the Young's Modulus (modulus of elasticity),  $F$  is the force exerted on the sample by the tip,  $A$  is the contact area the force is applied to,  $\Delta L$  is the change in length of the sample after deformation from the tip, and  $L$  is the original length of the sample. The force can be extracted from the  $y$  axis of the force curve, as long as the cantilever is calibrated, and the change in length or indentation of the sample can be calculated by subtracting the cantilever

deflection from the movement of the Z scanner once the tip has made contact with the surface. To be able to calculate modulus, the contact area between the tip and the sample must be known.

The Hertz model treats the contact area between the tip and the sample as a sphere (Figure 2.5A) and gives the equation;

$$F_{Tip} = \frac{4}{3} \frac{E}{(1 - \nu^2)} \sqrt{R} \delta^{\frac{3}{2}} \quad (2.5)$$

Where  $F$  is the force exerted by the tip on the sample,  $E$  is the Young's modulus,  $R$  is the radius of the indenter tip,  $\delta$  is indentation and  $\nu$  is the Poisson ratio of the sample, which is the negative ratio of transverse to axial strain on an indented sample. The Poisson ratio is usually between 0.2-0.5 and is typically taken as 0.5 for MPa material. By fitting the force curve to the Hertz model, the modulus of the sample can be calculated. An updated version of the Hertz model is the DMT model (Derjaguin-Muller-Toporov) which is the same as the Hertz model but also includes the adhesion of the tip as it pulls away from the surface. For the Hertz and DMT models to be valid, the indentation depth must be much smaller than the radius of the tip. If the indentation is too large, then the contact area is no longer spherical but conical. For large deformations, the Sneddon model can be used to treat the contact area as conical (Figure 2.5B). This gives the equation;

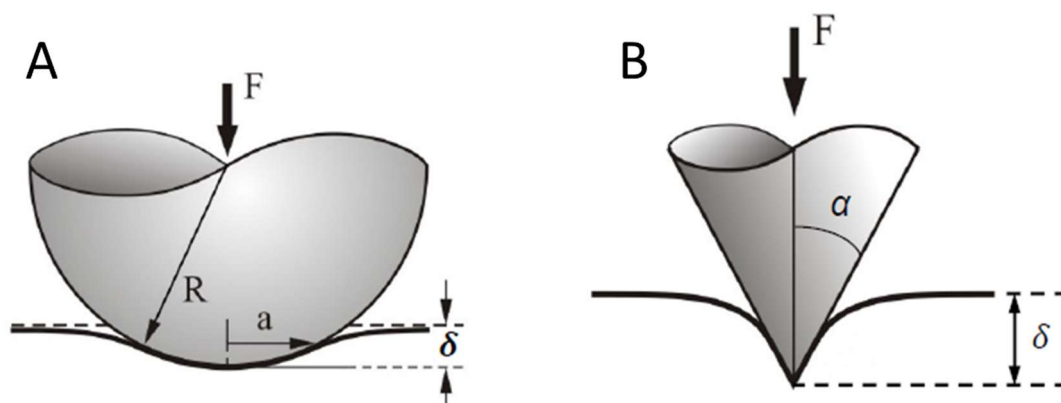


**Figure 2.5 Schematic showing the deformation of samples using AFM tips A) Spherical tip B) Conical Tip.<sup>87</sup>**

$$F = \frac{2E \tan \alpha}{\pi(1 - \nu)} \delta^{\frac{3}{2}} \quad (2.6)$$

Where all of the parameters are the same as for the Hertz model, but instead of tip radius there is tip half angle,  $\alpha$ .

The Hertz and Sneddon model require an extra stage of calibration to calculate modulus, as tip radius and tip half angle occur in the equations as a result of the contact mechanics. AFM tips generally have radii between 100-1nm. These can be measured accurately using electron microscopy, but can also be calculated or estimated using an AFM. By imaging a sample with sharp features (known as a tip checker sample), the tip can be imaged by the sample instead of vice versa. And an imprint of the end of the tip is then used to extract a tip radii. A relative calibration can also be performed on a surface of known modulus, where the tip radius is manually altered in the software until the modulus calculation gives the correct value. Probes that have the tip radius pre-calibrated by the manufacturer are beneficial as there is no need

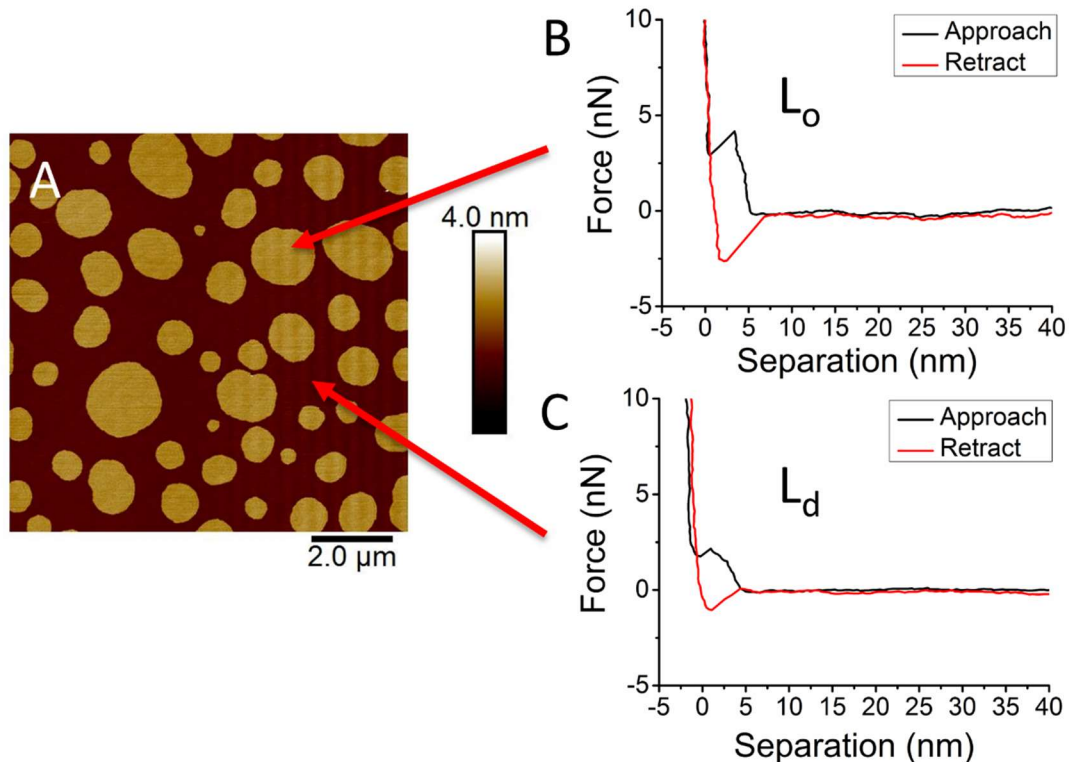


**Figure 2.6 Force curves on a DPPC/14:1PC/Chol bilayer. A force curve is shown for both the Liquid-Ordered (L<sub>o</sub>) and Liquid-Disordered (L<sub>d</sub>) phases.**

to engage a surface before imaging to calibrate it. This means there is a lower risk of tip contamination or blunting.

### 2.8.3 AFM Force Spectroscopy on Bilayers

AFM Force spectroscopy enables the nano-mechanical properties of lipid bilayers to be probed.<sup>84,85</sup> Example force curves on bilayers are shown in Figure 2.6. When the tip comes into contact with the bilayer the cantilever starts to deflect until a threshold force, where the bilayer ruptures. This rupture point can therefore be used to confirm the presence of a bilayer and calculate the force needed to break through it. This force is related to the order within the bilayer and hence the lipid phase, meaning that the bilayer phase can be determined from force curves. The more ordered  $L_o$  phase has a higher break-through force than the  $L_d$  phase. Once the bilayer has ruptured the cantilever then makes contact with the hard mica substrate and starts to deflect linearly. By measuring the point of first contact with the bilayer to the zero point where the tip contacts the substrate below, the height of the bilayer can be obtained. The force curves in Figure 2.6 show bilayer heights of 5nm, consistent with bilayer height.

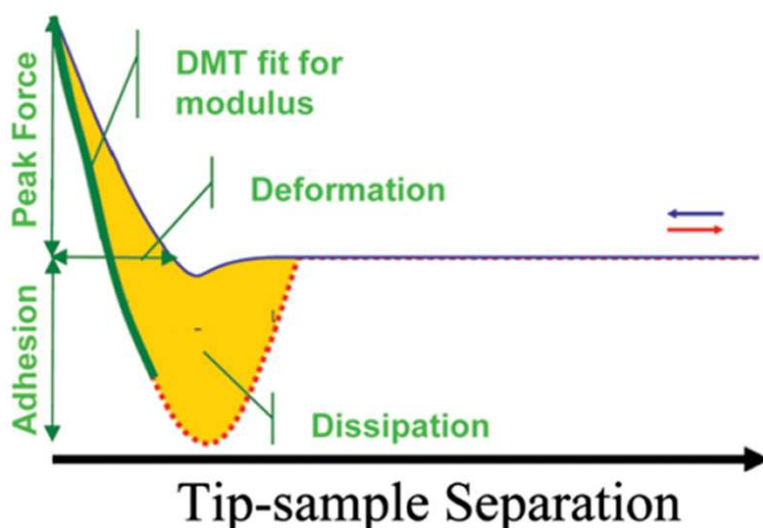


Figure 2.7 Example force curve showing Peak Force as well as the physical properties that can be obtained from the curve.<sup>87</sup>

#### **2.8.4 Force Volume, Peak Force Tapping (PFT) and Quantitative Nano-mechanical Mapping (QNM)**

Force volume mode is an AFM mode that performs a force curve at every pixel of an image using linear ramps.<sup>86</sup> This produces a force map, which is an AFM topography image with force curve data at each pixel. Peak Force tapping (PFT) also performs a force curve at every pixel, but the tip is oscillated instead of performing linear ramps.<sup>86</sup> This means that the time between each force curve is drastically reduced and the force map can be obtained much faster. Unlike tapping mode the oscillation however is well below the resonance of the lever, 1-4kHz compared to 100s kHz. The tip follows a sine wave motion, with a force curve at each trough when it makes intermittent contact with the surface. Whereas standard tapping mode feeds back on the amplitude of the oscillation, PFT feeds back on the maximum force exerted in the force curve cycle. Therefore PFT enables the imaging force on a sample to be easily calculated and controlled. Quantitative Nanomechanical Mapping (QNM) analyses the force curves from PFT mode in real time to give AFM image maps of physical properties including modulus, adhesion, deformation and dissipation.<sup>87</sup> QNM is explored further in Chapter 5.

### **2.9 Fluorescence Microscopy**

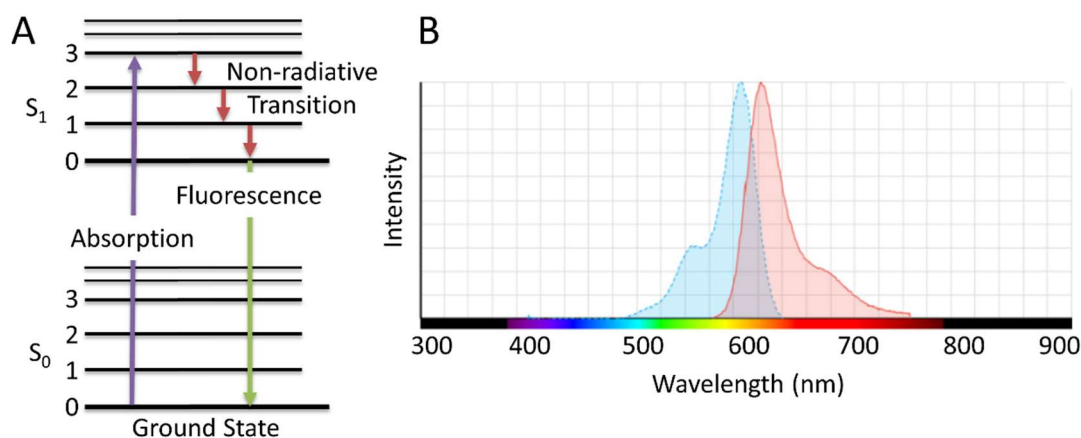
When fluorescent molecules (fluorophores) absorb light, electrons are excited from their ground state to excited states (Figure 2.8A).<sup>88</sup> When these electrons return to the ground state a fluorescent photon is emitted. When excited, energy is often lost via non radiative pathways such as energy transfer to a nearby molecule. Therefore the photon emitted when the electrons return to the ground state is often lower energy and higher wavelength than the emission photon. This is called Stokes Shift. Figure 2.8B shows the excitation and emission wavelengths for the fluorophore Texas Red (TR). The structure of Texas Red can be seen in Table 2.1 for TR-DHPE. As is the case with most dyes, TR has an extended conjugated system of unsaturated bonds. This changes the energy levels of the molecular orbitals so that the energy gap is in the visible region and photons can excite electrons. The emission

wavelength for TR is red-shifted from the excitation wavelength, showing Stokes shift.

Fluorescence can be imaged using a microscope if the appropriate filter cubes are used. Filter cubes filter the wavelength of light to the excitation wavelength needed for a specific fluorophore and then only filter out unwanted wavelengths from reaching the microscope camera.

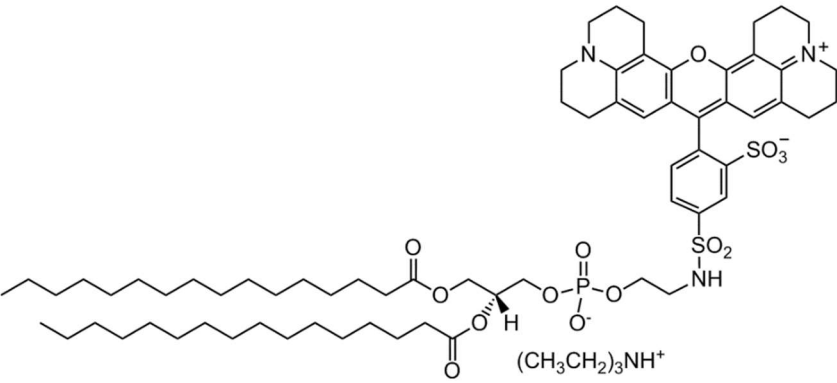
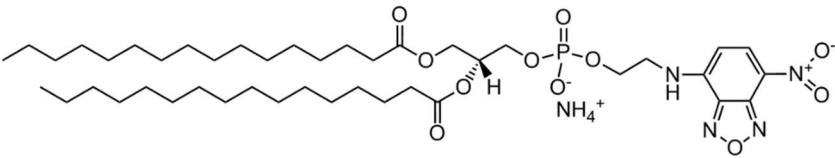
Fluorescent probes can be used to image lipid bilayers. The fluorescence probes used in this thesis are shown in Table 2.1. As can be seen, the probes consist of a conjugated dye molecule attached to a lipid. This structure enables the dye to self-assemble into the bilayer structure. Fluorescent probes are very useful as they can be designed to partition preferentially into different bilayer phases such as the  $L_o$  or  $L_d$  phases. This enables phase separation of micron scale domains to be imaged.

Lipid dyes within the bilayer also enable the measurement of diffusion, using a fluorescence technique called Fluorescence Recovery after Photobleaching (FRAP). Photobleaching occurs when a fluorophore is over exposed and it is irreversibly damaged. FRAP takes advantage of this phenomenon. A circular area of the bilayer is bleached with high intensity white light so that the lipids there are photobleached. The bilayer patch is monitored over time, as the non-bleached lipids from the rest of the bilayer diffuse back into the bleached area and fluorescence recovery is observed. By plotting and fitting the recovery of fluorescence in the bleached spot area with time to an exponential, a



**Figure 2.8 A) Jablonski diagram showing excitation and emission of a photon. B) Texas Red excitation and emission wavelengths. B adapted from reference<sup>185</sup>**

characteristic recovery constant can be obtained. This recovery constant can be converted to a half-life and then using the Axelrod Method be converted to a diffusion coefficient (D).<sup>89</sup> The only additional information needed is the radius of the bleach spot. The FRAP method and calculation is discussed in more detail in the methods section (Section 3.5.3).

Name	Structure
TR-DHPE	 <p>The structure of TR-DHPE consists of a 1,6-dipalmitoyl-sn-glycero-3-phosphoethanolamine lipid backbone. The phosphate group is linked to a 2,2',6,6'-tetrakisethylpiperidine-10-yl group, which is further substituted with a 4-sulfonatephenyl group. The sulfonate group is shown as SO<sub>3</sub><sup>-</sup>.</p>
16:0 NBD PE	 <p>The structure of 16:0 NBD PE consists of a 1,6-dipalmitoyl-sn-glycero-3-phosphoethanolamine lipid backbone. The phosphate group is linked to a 2-(diethylamino)ethyl group, which is further substituted with a 6-nitro-2-naphthyl group. The nitro group is shown as N<sup>+</sup>O<sup>-</sup>.</p>

**Table 2.1 Chemical structures of the fluorescent lipid dyes used in this thesis**

## 2.10 Differential Scanning Calorimetry

Differential Scanning Calorimetry (DSC) can be used to observe temperature phase transitions. DSCs have two separate cells, one for the sample and one for the reference solvent, and the temperature difference between the cells is kept constant. When there is a phase transition in the sample, the process can either be exothermic or endothermic. In both cases, the power to the two cells is adjusted so the temperature difference remains constant. The power difference between the two heaters ( $\text{cal}/^\circ\text{C}$ ), along with the scanning rate ( $^\circ\text{C}/\text{s}$ ) gives the heat capacity ( $\text{cal}/^\circ\text{C}$ ). At the temperature where the transition occurred a peak in the thermogram will be observed as the power difference and hence heat capacity changed.

DSC can be used to observe phase transitions in lipid bilayers. Samples of MLVs are placed in the sample cell and heated at a constant rate along with a reference solvent sample. As the bilayer melts there is a larger power difference between the cells, resulting in a larger heat capacity and a peak in the thermogram. The area under a thermogram peak is equal to the enthalpy of the transition;

$$\Delta H = \int_{T_2}^{T_1} \Delta c_p dT \quad (2.7)$$

where  $\Delta H$  is the change in enthalpy,  $T_1$  and  $T_2$  are the onset and offset temperatures of the peak and  $c_p$  is the heat capacity. The temperature of the peak ( $T_m$ ) can also be used to plot phase boundaries and phase diagrams. The transition in a single lipid mixture will represent the transition from a gel phase to a liquid phase, and the transition in a mixed phase separation system will represent the transition from a two-phase to a single-phase region.



## Chapter 3. Experimental Methods

### 3.1 Chemicals

DPPC (1,2-dipalmitoyl-*sn*-glycero-3-phosphocholine), DSPC (1,2-distearoyl-*sn*-glycero-3-phosphocholine), 20:0PC (1,2-diarachidoyl-*sn*-glycero-3-phosphocholine), 22:0PC (1,2-dibehenoyl-*sn*-glycero-3-phosphocholine), DOPC (1,2-dioleoyl-*sn*-glycero-3-phosphocholine), 14:1 PC (1,2-dimyristoleoyl-*sn*-glycero-3-phosphocholine) and 16:0 NBD PE [1,2-dipalmitoyl-*sn*-glycero-3-phosphoethanolamine-N-(7-nitro-2-1,3-benzoxadiazol-4-yl) (ammonium salt)] were purchased from Avanti Polar Lipids (Alabaster, AL). Texas Red DHPE (Texas Red 1,2-Dihexadecanoyl-*sn*-Glycero-3-Phosphoethanolamine, Triethylammonium Salt) and Magnesium Chloride ( $\text{MgCl}_2$ ) were purchased from Thermo Fisher Scientific UK. All water used was Milli-Q Ultrapure Water (18M $\Omega$ ). Chloroform ( $\text{CHCl}_3$ ), Methanol (MeOH) and Isopropanol/Isopropyl Alcohol (IPA) were purchased from VWR. Sulphuric Acid ( $\text{H}_2\text{SO}_4$ ) and Hydrogen Peroxide ( $\text{H}_2\text{O}_2$ ) for piranha cleaning were purchased from Fisher Scientific

#### 3.1.1 Lipid Storage

Lipids were received from the manufacturers in powder form or dissolved in  $\text{CHCl}_3$ . Lipids in powder form were dissolved in  $\text{CHCl}_3$  and separated into smaller aliquots in glass vials. The  $\text{CHCl}_3$  was evaporated off under  $\text{N}_2$  for 20 min, the lipid film stored under vacuum overnight and then the lipid was weighed. The vials were filled with argon, parafilm and stored at  $-20^\circ\text{C}$  until used. The same procedure was followed for lipids received in  $\text{CHCl}_3$ , without the need for the first step dissolving in  $\text{CHCl}_3$ .

#### 3.1.2 Making Lipid Mixtures

To make lipid mixtures the dried down aliquots for each individual lipid were dissolved into 5mM  $\text{CHCl}_3$  stock solutions (5mM in  $\text{CHCl}_3$ :MeOH 1:1 for 22:0PC), using the weighed mass of the lipid. Lipids could then be mixed in the desired molar ratio using the ratio of volumes. Once the lipids had been mixed together in the desired molar/volume ratios, the lipids were dried under

N<sub>2</sub> for 20min and stored under vacuum overnight. The dried down mixture was used immediately to form vesicles or stored under argon at -20 °C until needed.

## **3.2 Substrate Preparation**

### **3.2.1 Mica Preparation**

Mica (Agar Scientific) substrates were punched out in 12mm diameter circular disks and glued to 12mm magnetic AFM stubs (Agar Scientific) using epoxy. For fluorescence measurements, the mica was cut to size to fit into the fluorescence fluid cell (approx. 22mm diameter disks). Mica was cleaved using scotch tape prior to use.

### **3.2.2 HF Mica Etch**

To etch mica, stubs were cleaved and placed in PTFE beakers with 40% Hydrofluoric Acid (HF) for given lengths of time. The beaker and mica stubs were then poured into a large amount of Sodium Bicarbonate (90g in 1L), and thoroughly rinsed with de-ionised water. This method was originally developed as a calibration tool for AFM, due to the perfect 1nm height steps etched into mica.<sup>90</sup> Dr Mark Tarn, a colleague trained in the safe handling of HF, performed this procedure for us.

### **3.2.3 Glass Preparation**

Round glass coverslips (Thermo Scientific, Menzel-Glaser) were prepared by bath sonicating in Decon detergent for 15 min, followed by 10 min piranha treatment (1:3 H<sub>2</sub>O<sub>2</sub>:H<sub>2</sub>SO<sub>4</sub>), followed by 20 min exposure to UV ozone (UVOCS Inc. UV Ozone Cleaning System). These coverslips were used for the fluorescence flow cell and glued to a magnetic stub to be used on the AFM stage.

### **3.2.4 PDMS Preparation**

PDMS (polydimethylsiloxane) base and crosslinker (Sylgard 184) were purchased from Dow Corning. These were mixed in a 10:1 base to cross linker ratio and stirred thoroughly for 2 min, degassed by centrifuging at 4000 rpm for 1 min and then put in a vacuum desiccator for 15 min. For contact angle

measurements the degassed mixture was cured in a plastic petri dish at 70 °C for 30 min, cut into 1cm<sup>2</sup> pieces and glued with epoxy to glass microscope slides. PDMS substrates for AFM and fluorescence were prepared by spin-coating (Laurel technologies WS-640 MZ) the degassed PDMS mixture onto a glass cover slip. A small droplet of PDMS was placed in the centre of a glass cover slip and then spin coated at 1700rpm for 60s accelerating at 200rpm<sup>s</sup><sup>-1</sup>. The PDMS was then cured by placing the cover slip on a hot plate for 10 min at 95 °C. PDMS was oxidised using a Diener Electronic Zepto Oxygen Plasma Laboratory Unit for 2 min at 0.3-0.4mBar (100W, 40kHz). Oxidised PDMS for contact angle measurements was stored in air or in water, samples stored in water were dried under nitrogen before measurements. Oxidised PDMS for forming SLBs was used immediately.

### 3.2.5 Wrinkled PDMS

PDMS pieces were stretched using a home-built device, where the PDMS piece could be clamped in on either side and then a micrometre screw used



Figure 3.1 Home-built device for stretching and wrinkling PDMS

to pull the clamps and PDMS apart to a chosen strain (Figure 3.1). The device and PDMS was placed in the Diener Electronic Zepto Oxygen Plasma Laboratory Unit for 2 min at 0.3-0.4mBar (100W, 40kHz). Then the strain was slowly released to spontaneously form periodic sinusoidal wrinkles in the PDMS. The critical strain must be overcome and must also be below 200%, where PDMS reaches its breaking point. The wavelength and height of the wrinkles increase with oxygen plasma exposure time, height increases with pre-strain, and wavelength shows a weak dependence on pre-strain. These trends are shown in Figure 8.1 and match strongly with literature.<sup>91-94</sup>

The home-built device for stretching PDMS was developed by Harrison Laurent for a Master's Project. AFM data for wrinkled PDMS and for bilayers on wrinkled PDMS was obtained by Harrison, analysis was performed by both of us.

### **3.2.6 PDMS Microspheres**

PDMS microspheres were formed using emulsion polymerisation as described by Yin et al.<sup>95</sup> 0.6 g of degassed PDMS mixture was added to 30 mL of a 15 wt.% polyvinyl alcohol (PVA) solution, stirred overnight at room temperature to form polydisperse microspheres and then stirred at 90 °C over the following night to cure the spheres. The solution was then centrifuged at 4000 rpm for 1 minute, the excess PVA solution pipetted off the top, Milli-Q was added and then the sample was stirred using a vortex stirrer. This process was repeated several times to remove the PVA solution.

PDMS microspheres were formed by Harrison Laurent for a Masters Project. We worked together to oxidise them, incubate them to form bilayers and perform DSC analysis. Fluorescence analysis was performed by me.

## **3.3 Bilayer Formation**

### **3.3.1 Anti-Registration Project**

#### **3.3.1.1 Preparation of Lipid Vesicles**

The dry lipid film of single lipids or lipid mixtures were hydrated to 0.5 mgmL<sup>-1</sup> in Milli-Q ultrapure water, vortexed, and then tip sonicated for 30 min until the cloudy lipid solution went clear. Higher chain lipids (DSPC, 20:0PC,

22:0PC) were harder to dissolve and often took longer vortexing and sonication before they turned from cloudy to clear. The SUV sample was then centrifuged at 3000rpm for 3 min, to remove the metal sonicator tip sediment, the supernatant containing the SUVs was collected. The SUVs were then extruded to form mono-disperse SUVs. The extruder (Avanti Polar Lipids) is assembled by placing a polycarbonate membrane with 200 nm pores between filter paper supports, which is then placed between two Teflon membrane supports. This set up is then placed in a metal case and mount to secure it. The Teflon membrane supports have a single pore in each side for flowing solution in/out. A syringe was used to push the lipid solution between the two syringes and through the membrane a minimum of 11 times, so that the SUVs are not removed from the original syringe. The metal case and mount was placed on a hot plate and the procedure was performed at 5 °C above the saturated lipids chain transition temperature (DPPC  $T_m=41$ , DSPC  $T_m=55$ , 20:0PC  $T_m=66$ , 22:0PC  $T_m=75$ ).

### **3.3.1.2 Supported Lipid Bilayer Formation**

SLBs were formed using the vesicle rupture method.<sup>47</sup> 100  $\mu$ L of SUV solution was deposited onto a freshly cleaved mica disk with 50  $\mu$ L 10mM  $MgCl_2$  and incubated in a sealed humidity chamber for 1h. DPPC mixtures were incubated at 50 °C and higher chain saturated lipids were incubated at 5 °C above the saturated lipids chain transition temperature (DPPC  $T_m=41$  DSPC  $T_m=55$ , 20:0PC  $T_m=66$ , 22:0PC  $T_m=75$ ). After incubation, the bilayer was allowed to cool to room temperature and rinsed to remove any unruptured vesicles. Milli-Q water, at the same temperature as the incubated bilayer, was washed across the surface 10 times in 50  $\mu$ L bursts of a pipette.

### **3.3.2 Substrate Effects Project**

#### **3.3.2.1 Preparation of Lipid Vesicles**

The dry lipid film of DPPC/DOPC (60:40) was hydrated to 1  $mgml^{-1}$  in Milli-Q Water, vortexed for 30 min, heated in an oven at 50 °C for 30 min and then tip sonicated for 30 min at 4 °C. The SUV sample was then centrifuged at 3000rpm for 3 min, to remove SUVs from the metal sonicator tip sediment.

### 3.3.2.2 Supported Lipid Bilayers for AFM

For AFM measurements, 100  $\mu\text{L}$  of SUV solution was deposited onto a mica or glass substrate and incubated in a sealed humidity chamber for 1h at 50  $^{\circ}\text{C}$ . Halfway through incubation 100  $\mu\text{L}$  20mM  $\text{MgCl}_2$  was added. After incubation, the bilayer was cooled to room temperature and rinsed to remove any unruptured vesicles. Milli-Q water, at the same temperature as the incubated bilayer, was washed across the surface 10 times in 50  $\mu\text{L}$  bursts of a pipette.

### 3.3.2.3 Supported Lipid Bilayers for Fluorescence

For fluorescence measurements, glass or mica substrates were assembled into a home-built flow cell (Figure 3.2) consisting of a sealed incubation chamber around the substrate and an inlet and outlet for flowing the sample in and washing. The home-built flow cell was designed by Dr Matthew Cheetham and Dr Peng Bao, and built by Stuart Western in the Physics Department mechanical workshop. 1mL of 1mg/mL lipid vesicles were syringed into the cell. The vesicles were incubated on the surface for 30min (room temperature for DOPC, 50  $^{\circ}\text{C}$  for DPPC/DOPC). 1mL 20mM  $\text{MgCl}_2$  at

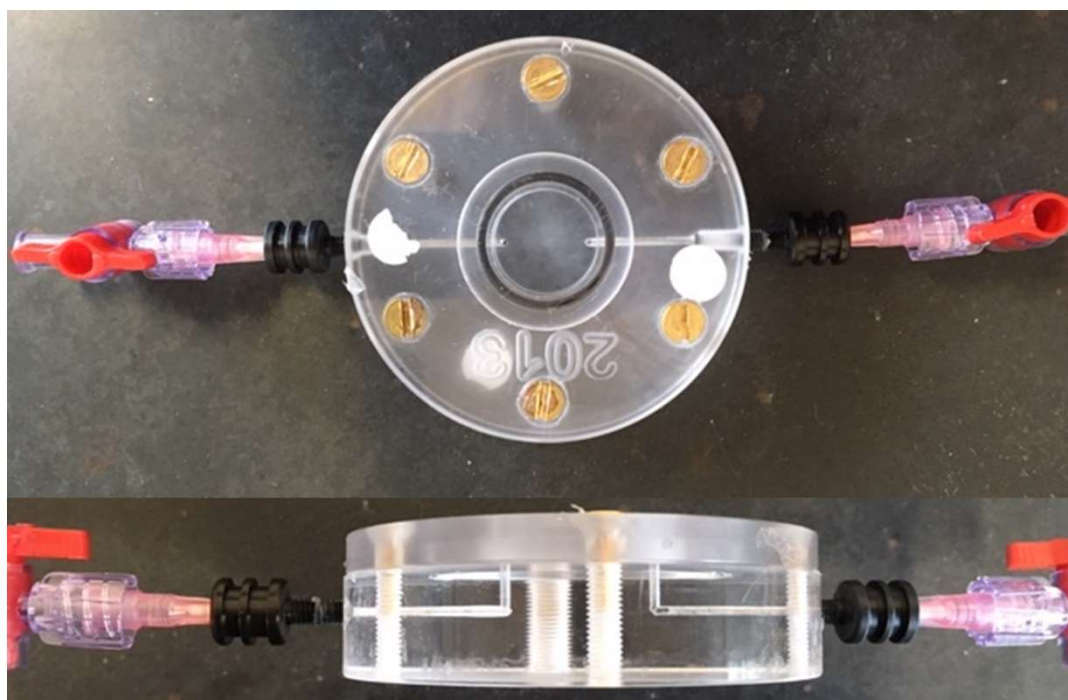


**Figure 3.2** Photos of the home-built flow cell for forming SLBs.

the same temperature was added for a further 30 min. The sample was then allowed to cool to room temperature before the surface was washed to remove any unfused vesicles. A pump was connected to flow room temperature Milli-Q water through at approx. 1 mL/min for 30 min.

#### **3.3.2.4 Temperature measurements of Supported Lipid Bilayers**

The temperature of the bilayers was measured using a K-type thermocouple positioned in the buffer, close to the substrate in both the fluorescence fluid cell and the AFM incubation dish. The cooling rates were determined by taking the gradient between 33-29 °C, this is the transition temperature range of DPPC/DOPC (60:40), determined using published DPPC/DOPC temperature phase diagrams.<sup>28,96</sup> 0.25 deg/min was the cooling rate achieved by taking the fluid cell or incubation dish out of the oven at 50 °C and allowing the bilayers to cool ambiently in the lab, where the temperature was 21 °C. 0.08 °C was the cooling rate achieved by turning off the oven and letting both the oven and bilayers cool down to room temperature. The cooling rate for pure DPPC samples was calculated between 45-35 °C to match the  $T_m$  of pure DPPC and is faster than the cooling rate between 33-29 °C to match the  $T_m$  of DPPC/DOPC (60:40).

#### **3.3.2.5 Bilayer Formation on PDMS Microspheres**

PDMS microspheres sedimented out of suspension over time. 1 mL PDMS microsphere solution, containing approximately 200  $\mu$ L sediment microspheres, was pipetted onto glass microscope slides and dried for an hour in a 50 °C oven. The dried microspheres were oxidised using oxygen plasma at 0.4 mBar for 2 min, scraped off into falcon tube and weighed. 82mg microspheres were added to 0.5mL of 1mg/mL DPPC + 0.5mol% TR-DHPE SUV solution, and this solution was made up to 4mL. The microspheres were incubated with the SUVs for 45 min at 50 °C, turning it every 10 min to account for sedimentation. The mixture was allowed to cool to room temperature. The microspheres were then washed to remove any vesicles in the solution by centrifuging at 4000rpm for 2 min, pipetting off bulk vesicle solution leaving sedimented microspheres at the bottom and re-diluting in 15mL Milli-Q water. This was repeated 5 times.

## **3.4 Atomic Force Microscopy**

### **3.4.1 Anti-Registration Project**

AFM Images were acquired using either a Bruker MultiMode 8 or a Bruker Dimension with Fastscan Head. All imaging was performed in liquid mode, as the bilayers must always remain hydrated. Tapping mode was used for acquiring images of bilayer morphologies for different lipid mixtures and compositions. Bruker NP probes (Spring Constant = 0.06 N/m, Resonant Frequency = 18 kHz) were used for the Multimode 8 and Bruker Fastscan D probes for the Dimension Fastscan (Spring Constant = 0.25 N/m, Resonant Frequency = 110 kHz in water). Peak Force Tapping mode was used for force spectroscopy to obtain bilayer mechanical properties.

### **3.4.2 Substrates Effects Project**

AFM Images were acquired using a Bruker Dimension with an ICON head. Bruker ScanAsyst Fluid probes (0.7 N/m, 150 kHz) were used. Imaging was performed using Peak Force Tapping mode in liquid using the ICON fluid tip holder. The AFM and Fluorescence images of the same bilayer sample area were acquired using a Bruker Resolve AFM integrated with an inverted confocal microscope.

### **3.4.3 Quantitative Nanomechanical Mapping AFM Tip Calibration**

AFM cantilevers were calibrated for deflection sensitivity, spring constant and tip radius prior to imaging. The linear deformation regime of a force spectroscopy ramp on clean hard flat mica was fit using Nanoscope software to obtain a deflection sensitivity in nm/V. This allows the measured cantilever deflection in V to be converted to nm. On the same flat mica surface, the parameters Sync Distance New and Sync Distance QNM were calibrated. These parameters account for the lag between maximum piezo extension and maximum force, due to the time dependent response of a substrate or sample. The cantilever was then thermally tuned to find the resonant frequency peak, which is fit to get the spring constant (N/m), all performed on Nanoscope Software. This allows cantilever deflection in nm to be converted to N. The radius of the tip was then obtained using a relative method. Specifically, a PDMS sample of known modulus (3MPa) was imaged using PeakForce



Tapping QNM AFM mode. The tip radius was altered manually in the software until the modulus channel matched 3MPa.

### **3.4.4 AFM Image Analysis**

AFM images were analysed using Nanoscope Analysis V1.9. Images were acquired at a minimum of 512 pixels, but in some cases higher resolution images up to 1536 pixels were acquired. AFM images were flattened using the appropriate order of line or plane levelling for each image, using the Flatten or Plane Fit functions on Nanoscope Analysis; 0 order (moves data to centre of image z range), 1<sup>st</sup> order (removes tilt due to tip not being perpendicular to the AFM stage), 2<sup>nd</sup> order and 3<sup>rd</sup> order (to remove bowing in the image caused by the piezo motion).

#### **3.4.4.1 Bilayer Heights and Area Fractions**

Flattened images were used to plot a histogram of bilayer heights in Nanoscope Analysis, where the two phases can be distinguished (Figure 3.3). The bearing analysis and depth/height measurements are very sensitive, so images must be flat to get two clear peaks in the histogram. Depth analysis was performed to obtain the height mismatch between the phases by measuring the distance between the two peaks. For images that were hard to flatten, height information was obtained using a single line scan over the phase boundary with repeats.

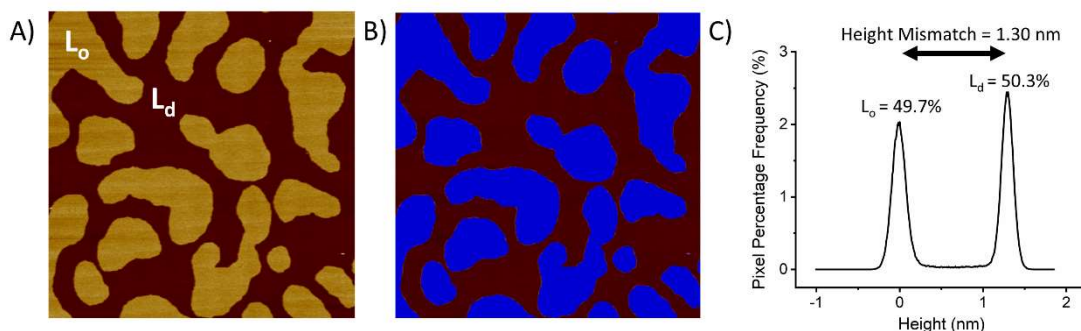


**Figure 3.3 Example Depth and Area Analysis of a Flattened Phase Separated Bilayer AFM image. DPPC/14:1PC/Chol (42.5:25:32.5) image showing phase separated  $L_o$  and  $L_d$  phases A) Flattened AFM Image B) Bearing Analysis to split two phases based on an intermediate threshold height C) Histogram showing the percentage of pixels at specific heights. The heights shown are the depths from the top of the Z piezo range of the image down to the phase, which is why the  $L_o$  phase appears lower in height than the  $L_d$  phase, despite the  $L_o$  phase being the taller of the two phases. The difference in heights between the histogram peaks gives the height mismatch between the two phases.**

A bearing analysis was also performed which involves choosing a z height threshold between the two-phase peaks to calculate the percentage of phase above and below the threshold. Bearing analysis was performed on  $10\mu\text{m}$  images with repeats, as specified in image captions (except for 1:1:1 mixtures where bearing analysis was performed on  $20\mu\text{m}^2$  images and each repeat sample is an average of 3 areas from the AFM stub).

#### 3.4.4.2 Power Spectral Density

Power Spectral Density Spectra of AFM substrate images were measured using a built in Nanoscope function. This function plots the power of height fluctuations against frequency, giving a quantitative measure of roughness at different length scales.

#### 3.4.4.3 Roughness

$R_a$  roughness is the mean deviation in height from the average height.

$$R_a = \frac{1}{n} \sum_{i=1}^n |Z_i| \quad (3.1)$$

Where  $R_a$  is the roughness,  $n$  is the number of data points and  $Z_i$  is the deviation in height from the average height. The  $R_a$  roughness of the substrates was measured using a built in Nanoscope function. The size of the image can affect the roughness calculation, so averages were taken from several images all at the same  $5\mu\text{m}$  length scale.

#### 3.4.4.4 Domain Size

Domains sizes were estimated by fitting an ellipse to the domain using Nanoscope Analysis, and then taking the average of the long and short radii of the ellipse. The analogous process for fitting domains from fluorescence images is shown in Figure 3.5.

#### 3.4.4.5 Correlation Length

The Radially Averaged Correlation Function was calculated from AFM images flattened in Nanoscope and then exported to ImageJ. The images were converted to a binary image of two phases using the threshold tool on ImageJ. The Binary image was run through a Radially Averaged Autocorrelation Function Macro (Michael Schmid, 27/9/2011 update) to produce an autocorrelation plot, giving a radially averaged quantitative measure of the length scale between black and white pixels i.e. the two different phases. This plot was fitted to an exponential decay using Origin Pro 9.1 to give a characteristic correlation length. This is shown in Figure 3.4.

$$y = Ae^{\frac{-x}{\text{Correlation Length}}} \quad (3.2)$$

This correlation length method was used for domains on glass and PDMS, which due to their complex morphologies could not be fit individually to calculate domain size. The correlation length for the larger fractal gel domains on mica underestimates the domain size compared to domain size fitting. This is due to the domain protrusions resulting in a shape where each dark domain pixel is closer to a white non-domain pixel, thus a smaller correlation length. Comparing the correlation length to domain fitting, if you start at the centre of a domain (average of all positions), the nearest opposite colour pixel is roughly half a radius away from the centre. Although the absolute number of the correlation length underestimates domain size, it provides a quantitative measure of length scale which scales with the increase in domain size.

The size and frequency of domains on glass was not homogenous. Larger 20 $\mu\text{m}$  scans enabled the heterogeneity to be seen over the micron scale, however the pixel rate in these images was too low to allow accurate thresholding for correlation length analysis. Therefore, a statistical spread of smaller 5  $\mu\text{m}$  size images with larger pixel rates were analysed.

### 3.5 Fluorescence Microscopy

Fluorescence Microscopy was performed using a Nikon Eclipse E600 microscope with an Andor Technology Zyla cCMOS camera. The microscope was equipped with a Mercury Lamp and filter cubes suitable for Texas Red (Ex. 540-580, Em. 600-660) and NBD (Ex. 465-495, Em. 515-555). Fluorescence Microscopy Images were analysed and processed using the FIJI distribution of ImageJ (NIH).

For phase separated lipid mixtures the fluorescence dye TR DHPE was used which partitions preferentially into liquid phase in a gel-liquid system. For single DPPC bilayers, both TR-DHPE and 16:0 NBD PE dyes were used. 16:0 NBD PE is a dye designed for more ordered lipid phases.

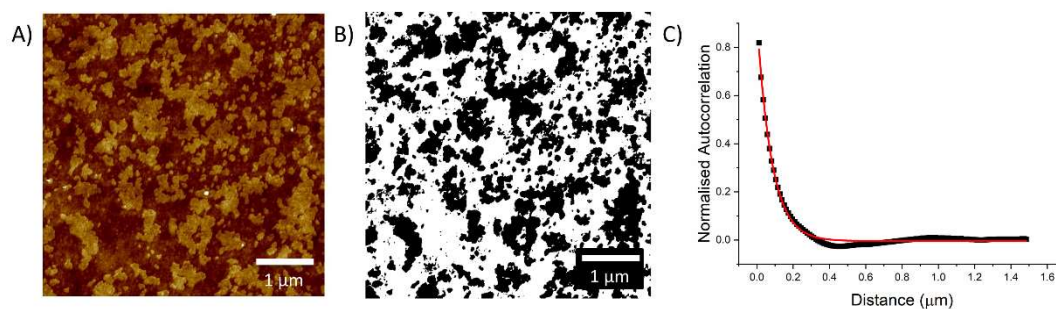


**Figure 3.4 Example Correlation Length Analysis. A) AFM image showing gel and liquid phases on glass. B) Binary Image of two phases. C) Autocorrelation curve with exponential decay fit to calculate correlation length, correlation length displayed on graph.**

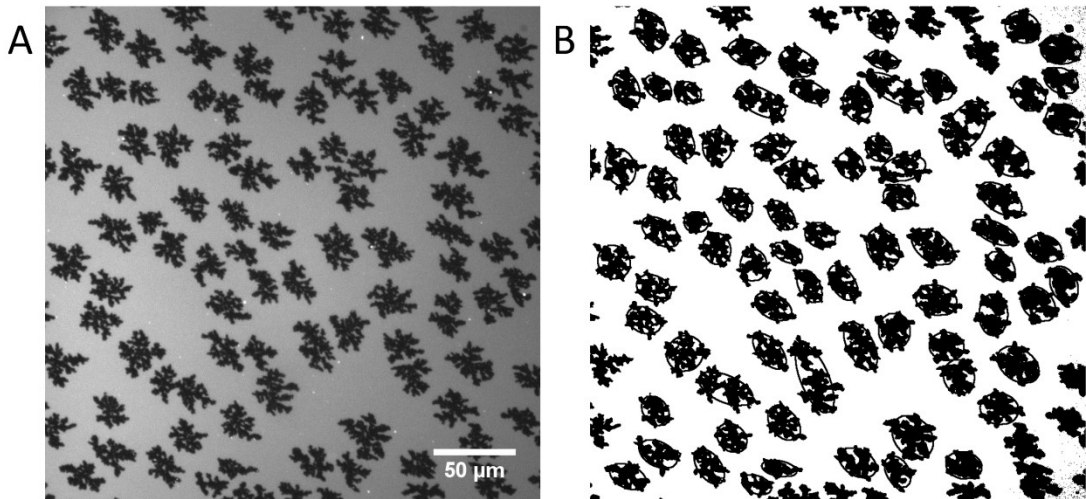


**Figure 3.5 Example Domain Fitting to Fluorescence Image. A) Fluorescence Image of DPPC/DOPC (60:40) on mica slow cooled B) Binary image of gel and liquid phase separation from image A, gel domains are black and liquid phase is white. Gel domains have been fitted to ellipses to determine domain size.**

### **3.5.1 Domain Fitting**

Domains sizes were estimated by fitting an ellipse to the domain using ImageJ for fluorescence images, and then taking the average of the long and short radii of the ellipse. This is shown in Figure 3.5.

### **3.5.2 Correlation Length**

The correlation length for fluorescence images of domains on mica were calculated by the same method used for AFM images (Section 3.4.4.5). As no clear phases were visible using fluorescence for glass and PDMS, no correlation length analysis was possible.

The correlation lengths of domains on mica measured by fluorescence and AFM are similar but not identical, explained due to the lower resolution of fluorescence compared to AFM. The domain protrusions are not always adequately resolved optically, and the correlation length measurement is more representative of a sphere of filled in shape, which has a longer distance from dark domain pixels to light non-domain pixels. There will also be a slight experimental variation in cooling rate between different runs.

### 3.5.3 FRAP (Fluorescence Recovery after Photobleaching)

An aperture was used to bleach a 30um diameter spot with white light for 30 seconds on a SLB with lipid dye (either TR-DHPE or 16:0 NBD PC). After photobleaching, images were taken at 3 seconds intervals for 2-3 minutes. Figure 3.6 shows a bilayer directly after bleaching, a bilayer after recovery and a fluorescence recovery curve. The first image was taken after 3 seconds because this gave time to switch on the fluorescence filter cube, slot the filters that are removed to increase intensity for bleaching back in, and remove the aperture. Analysis was performed using a custom macro for ImageJ (written by Dr Johannes Roth, edited by Dr Peng Bao), which compares the fluorescence intensity recovery to a reference area of non-bleached bilayer. The ratio of fluorescence intensity of the bleach spot ( $I_{Bleach}$ ) to the fluorescence intensity of a non-bleached reference area ( $I_{Ref}$ ) was calculated for each time point in the recovery series, taking account for the background intensity of the microscope. If fully recovered  $I$  is 1, and if fully bleached  $I$  is 0.

$$I = \frac{I_{Bleach} - I_{Background}}{I_{Ref} - I_{Background}} \quad (3.3)$$

Intensity was also normalised to the initial fluorescence intensity of the bleached spot ( $I_{initial}$ ) so that the recovery starts from 0.

$$I = \frac{I_{Bleach} - I_{initial}}{1 - I_{initial}} \quad (3.4)$$

The exponential recovery was fitted using Origin Pro to obtain a characteristic recovery time constant,  $b$  (Figure 3.6C).

$$I = a * (1 - e^{-bt}) \quad (3.5)$$

Where  $I$  is normalised intensity,  $t$  is time and  $a$  and  $b$  are fitting parameters.  $a$  gives the percentage intensity recovery or mobile fraction and  $b$  is the time constant of the recovery. This characteristic recovery time constant was converted to a half-life ( $t_{1/2}$ ).

$$t_{\frac{1}{2}} = \frac{\ln 0.5}{-b} \quad (3.6)$$

Half life ( $t_{1/2}$ ) was then converted to a diffusion coefficient ( $D$ ) using equation X, where  $r$  is the radius of the bleach spot and  $\gamma_D$  is a constant (0.88) related to the circular bleach shape.

$$D = \gamma_D \left( \frac{r^2}{4t_{1/2}} \right) \quad (3.7)$$

Diffusion coefficient values presented are averages of several repeat runs (Glass N=12, Mica N=6, PDMS=5), where for each repeat run the value is an average of at least 5 different areas from the substrate.

Roughly half of all the fluorescence imaging of bilayers and the FRAP of bilayers on mica, glass and PDMS was performed by Dr Danielle Walsh.

### 3.5.3.1 FRAP for Transition Temperature Determination

For transition temperature determination, DPPC SLBs were formed in the flow cell, as described earlier (Section 3.3.2.3). After the wash at room temperature, the bilayer was heated up to 60 °C and then FRAP images obtained as it cooled. As the bilayer was cooling, there was not enough time to let the bleach spot fully recover, as this would have increased the time between data points and effectively dropped the resolution. After testing, images were captured every 3 seconds for 30 seconds for each individual bleach, giving 10 images. This, along with a 20 second bleach, gave 50 seconds between time points. With an incomplete recovery curve that did not fully recover to 1 (back to reference non-bleached bilayer intensity), the exponential fits did not always converge to 1. From fully recovered DOPC SLBs e.g. Figure 3.6, we know that the bilayer recovers fully to reference non-bleached intensity. To account for the recovery curves not fully recovering, the exponential recovery was fixed to reach 1.

$$I = 1 - e^{-bt} \quad (3.8)$$

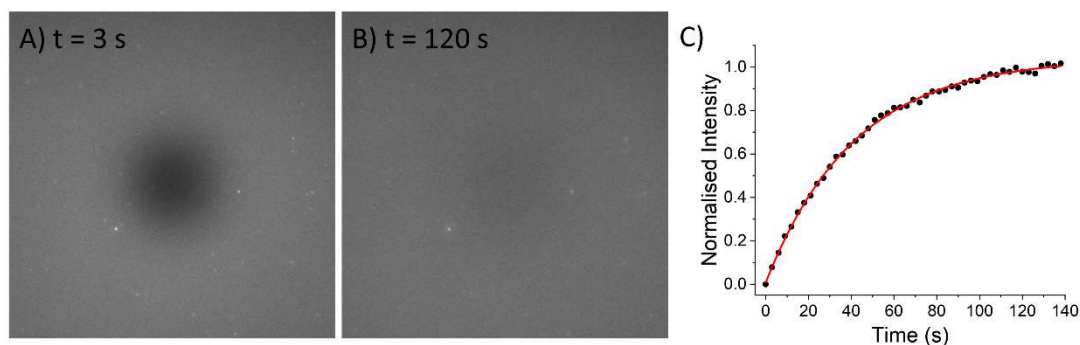


**Figure 3.6 Example FRAP Bleach and Recovery on a DOPC SLB. A) 3 seconds after photobleaching B) 120 seconds after photobleaching C) Graph showing Fluorescence Intensity Recovery with time.**

This idea can be understood by examining  $T_m$  with FRAP figures for mica, glass and PDMS in chapter 7 and 8 (Figure 7.9 and Figure 8.4).

The diffusion coefficients were plotted against temperature and these were fitted to a Boltzmann sigmoidal curve (Figure 7.8, Figure 7.9 and Figure 8.4).

$$D = A_2 + \frac{A_1 - A_2}{1 + e^{\frac{T - T_0}{dT}}} \quad (3.9)$$

Where  $A_1$  and  $A_2$  are the y values of the flat fit above and below sigmoid curve and  $T_0$  is the turning point/midpoint of the curve, which was taken as value of  $T_m$ .

## 3.6 Differential Scanning Calorimetry

### 3.6.1 Lipid Sample Preparation

Dry lipid films of DPPC, DPPC/14:1PC mixtures or DPPC/14:1PC/Chol mixtures were hydrated with Milli-Q water to  $1 \text{ mgmL}^{-1}$  and vortexed for 5 min to form large multilamellar vesicles (LMVs). Later runs of DPPC/14:1PC/Chol used a larger mass of lipid and were hydrated at a higher concentration of  $10 \text{ mgmL}^{-1}$  to increase signal in the DSC thermograms.



### 3.6.2 Filling the DSC Cells

A MicroCal VP-DSC was used. To fill the cells with water, the filling syringe, filling syringe needle and filling funnel provided with the instrument were used (Figure 3.7). The funnel was attached to the sample and then reference cells in turn, and the syringe and needle were used to fill the cell with degassed water until it visibly came up into the funnel. The syringe was pulsed in and out 5 times to ensure there were no air bubbles in the cell, as these can drastically change the heat capacity. The syringe was then used to remove the water to below the funnel level. Then a specialist collared needle was used without the funnel, which allowed a set amount of liquid volume to be removed from the top of the cell, leaving a repeatable 0.5 mL volume in the cells. Once the cells were filled, the cell cap was put on and tightened until the pressure in the cells was 28-29 PSI. If the pressure does not reach this level, it is a strong indication that there are air bubbles in one of the cells. Samples were added to the cells using the same procedure as for water, leaving the same 0.5 mL volume in the cell. To clean the cells, between samples and after use, the filling procedure above was used to rinse 3 times with Decon90 detergent and then 5 times with degassed water.

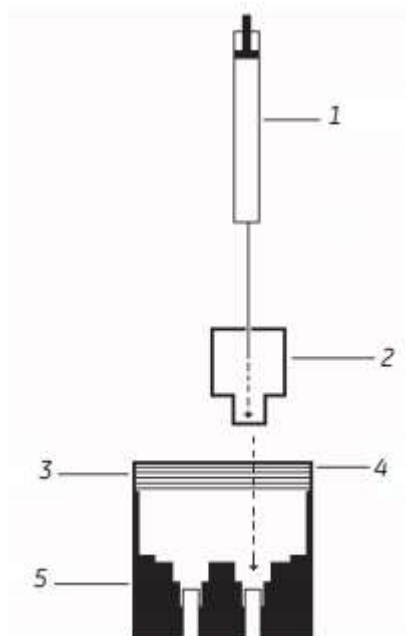


**Figure 3.7 Schematic showing the filling of DSC cells 1) Filling Syringe 2) Filling Funnel 3) Threads for pressurising cap 4) Stainless steel housing 5) Teflon reservoir insert. From reference<sup>186</sup>**

### 3.6.3 DSC Measurements

Thermograms were obtained using a MicroCal VP-DSC. The filtering period, the time over which data is averaged, was set to 10s intervals. Feedback mode was set to high, to account for the sharp transitions of lipids.

All samples and Milli-Q water for the reference cell was degassed using a ThermoVac degasser (2 x 5 min) at 10 °C, to match to the starting temperature of the DSC temperature cycles.

For single DPPC, DPPC/14:1PC mixtures and DPPC/14:1PC/Chol mixtures temperature was cycled from 10-60 °C at 90 °C/hr with a cool down from 60 °C to 10 °C and then a 15 min equilibration period at 10 °C prior to each new scan. In this case data was just collected for the heating 10-60 °C scan and not the cooling scan. For later DPPC scans and for lipid-coated PDMS microspheres, temperature was cycled continuously from 10-60 °C and then 60-10 °C at 90 °C/hr, with a 15 min equilibration period at 10 °C and 60 °C

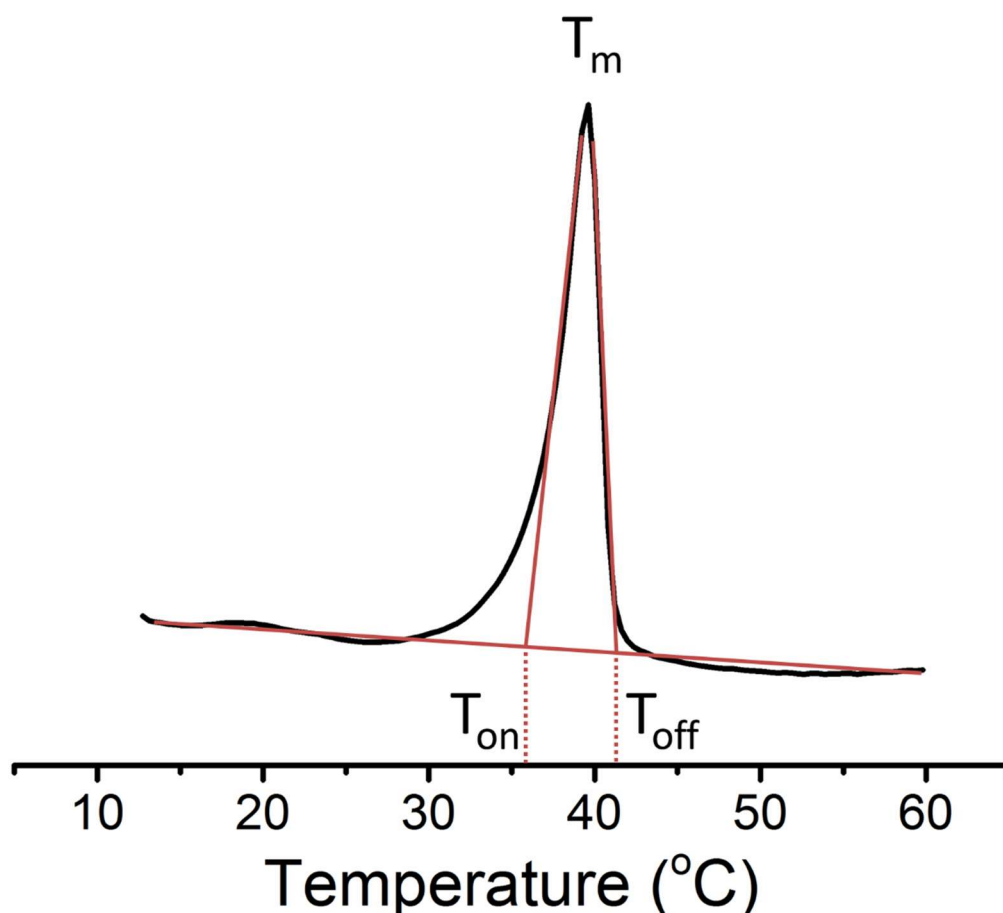


Figure 3.8 DSC Thermogram for DPPC/14:1PC (80:20) showing the calculation of  $T_m$ ,  $T_{on}$  and  $T_{off}$ .

before each new scan. In this case data was collected for both the heating 10-60 °C and cooling 60-10 °C scans. To ensure the thermal history of the sample and reference cells were similar, both cells were continuously temperature cycled overnight with degassed water prior to the first measurement.

### **3.6.4 DSC Thermogram Processing and Analysis**

On each day of obtaining DSC data, a buffer-buffer (water-water) scan was also run i.e. water in both sample and reference cells. Each sample DSC thermogram had the water-water scan subtracted from it to leave a flat baseline with the heat capacity component of the water removed to just leave heat capacity of the lipid sample.

Transition temperature values ( $T_m$ ) were measured by taking the peak value of the lipid transition (Figure 3.8). The peak onset and offset ( $T_{on}$ ,  $T_{off}$ ) were also measured, although not used for analysis, as detailed in Section 6.3.1.

For several samples the baseline shape and values for either or both of the sample-reference scan or the water-water scan were not correct, likely caused by incorrect filling of the cells to remove all air bubbles. In these cases, the baseline of the sample-reference scan was flattened using a mathematical fit on Origin Pro. This was valid as we were only quantitatively interested in the temperature value of the lipid transition (x axis). We did not need the enthalpy of the transition, which would have needed a correct heat capacity baseline (y axis).

## **3.7 Contact Angle**

Contact angle measurements were used to quantify the hydrophilicity/hydrophobicity of different bilayer substrates and were taken using a First Ten Angstroms FTA 4000 CAG instrument. A droplet of Milli-Q water was pipetted onto the surface and a side-on image captured (90° to substrate normal). The contact angle made between the water droplet and different substrates was calculated using fitting algorithms in the FTA 400 CAG software.

For mica after cleavage N=18 (3 repeats on 6 mica stubs).

For glass, contact angle measurements were taken straight out of the packet, after a water rinse, after a Decon90 detergent wash, after Piranha cleaning ( $\text{H}_2\text{SO}_4$  and  $\text{H}_2\text{O}_2$ ), and after UV ozone treatment for 30 min. The treatments were successive so included the cleaning steps mentioned before it too. For each glass contact angle measurement  $N=9$  (3 repeats on 3 glass cover slips). For untreated PDMS  $N=5$ . Contact angle measurements were taken at specific time points after plasma oxidation for PDMS stored in air and in water. Different washes of PDMS, in  $\text{CHCl}_3$ , MeOH, Acetone and IPA, were also attempted before plasma oxidation to try to slow down hydrophobic recovery. For these washes, contact angle measurements were also taken at specific time points after oxidation. For PDMS contact angle recovery experiments, each time point is an average of at least 3 different droplets deposited and imaged within +/- 1 minute of that time point.

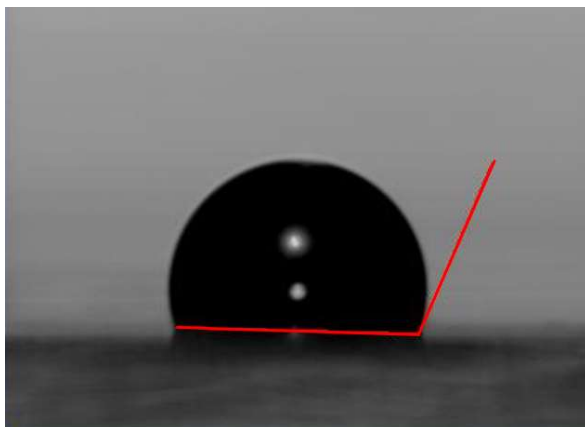


**Figure 3.9. Contact Angle Measurement Example. A water droplet on non-treated PDMS with contact angle indicated in red.**

## Chapter 4. Registration and Anti-Registration

### 4.1 Introduction

The plasma cell membrane shows asymmetry in terms of the types of lipids in each leaflet. The outer leaflet comprises mostly of PC and SM lipids and the inner leaflet PS, PE and PI lipids (Figure 1.10).<sup>16,17,51</sup> Model bilayers formed from outer leaflet lipids show phase separation between different lipid types but those formed from inner leaflet lipids form only a single homogeneous phase.<sup>10,11</sup> This means that it is possible that there are AR domains in the plasma membrane, areas where domains of one lipid phase align opposite a different phase in the opposing leaflet. Model lipid bilayers such as vesicles and SLBs, however, show complete registration between phases. This is shown by two clear fluorescence signals or two clear heights in AFM, with no intermediate.<sup>8,53</sup>

Based on the presence of a line tension at the interface between coexisting domains, caused by the exposure of hydrophobic lipid tails to water, domain AR should be the equilibrium state and not R. As this is not the case and model systems form R domains, there must be interleaflet coupling forces acting to align like domains across the leaflets. The identities of these coupling forces is not clear and there is little experimental evidence. However, based on simulations and theoretical calculations dynamic chain interdigitation and cholesterol flip-flop are considered to likely be having a strong effect.<sup>9,10</sup>

Results from a mean-field model<sup>14</sup> and coarse-grained molecular dynamics simulations<sup>13</sup> suggests that at high line tension the inter-leaflet coupling forces

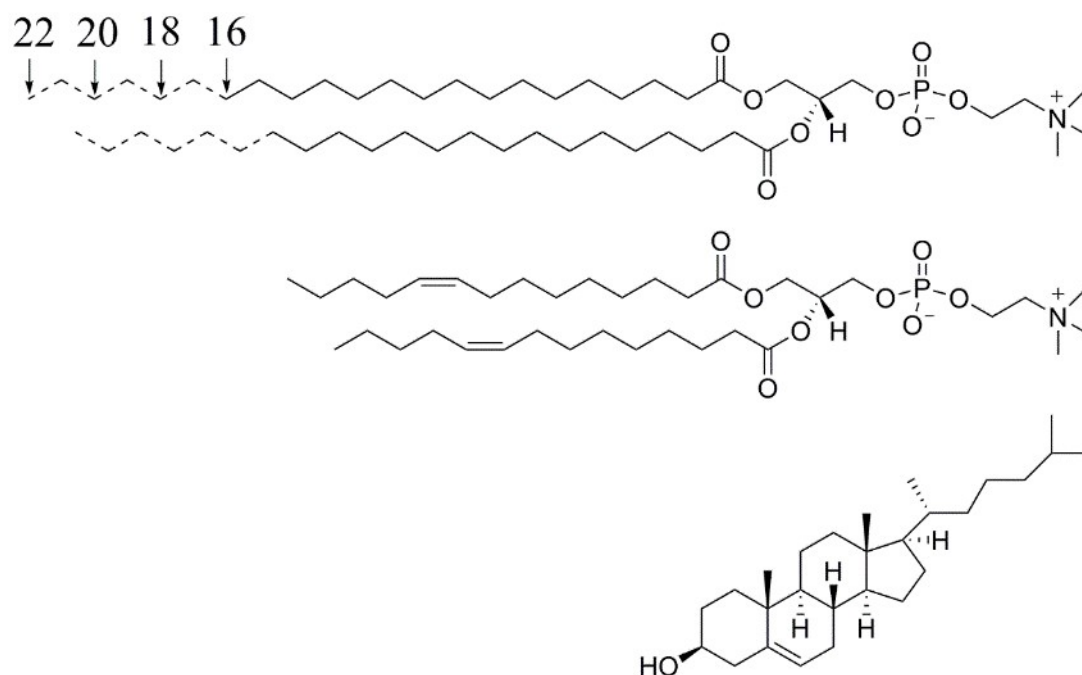


**Figure 4.1 Chemical Structures for Saturated Lipids DPPC(16:0PC), DSPC (18:0PC), 20:0PC and 22:0PC at the top, 14:1PC in the middle and Cholesterol at the bottom.**

favouring R will be overcome and AR bilayers will form. In this chapter an experiment is designed to gradually increase the hydrophobic mismatch between phase separated domains, to see if AR bilayers form. By quantifying at what hydrophobic mismatch and what line tension R domains switch to AR, it should be possible to estimate the mismatch free energy/interleaflet coupling parameter.

Lipid systems designed to increase height mismatch between coexisting  $L_o$  and  $L_d$  phases are used. This is to increase the line tension between the coexisting phases and thus the energy penalty for the interface boundary between the two phases.

Four different ternary lipid mixtures were used for this project, all consisting of a saturated lipid, an unsaturated lipid and cholesterol. As discussed in the introduction, with a knowledge of the phase behaviour of these ternary lipid systems a composition can be formed that shows phase separation into the Liquid-Ordered ( $L_o$ ) and Liquid-Disordered ( $L_d$ ) phases. For all of the mixtures cholesterol was used and the unsaturated lipid was 14:1PC. 14:1PC is not a commonly used lipid but has been used in protein reconstitution studies.<sup>97</sup> It was chosen due to its short acyl chains, which allowed a larger height

mismatch between saturated and unsaturated lipid. 14:1PC is structurally analogous to the more commonly used DOPC (18:1 PC), but with 2 less carbons in each of its two tail chains. While detailed phase diagrams of these systems have not been determined, binary and ternary phase diagrams of the various combinations of a low  $T_m$  unsaturated lipid, a high  $T_m$  saturated lipid, and cholesterol, exhibit broadly similar phase behaviour. The hydrophobic tail chain length of the saturated lipid component was increased from 16 to 22 carbons between the four mixtures (16,18,20,22) to increase the height of the  $L_o$  phase and increase the hydrophobic mismatch between the coexisting  $L_o$  and  $L_d$  phases. This will increase the line tension between the two phases and increase the free energy of the  $L_o$ - $L_d$  phase boundary. As shown by Williamson and Sachs, this should lead to a switch from symmetric R bilayers and to AR bilayers.<sup>13,14</sup>

## 4.2 Atomic Force Microscopy of DPPC/14:1PC/Chol

DPPC/14:1PC/Chol, as well as the other ternary mixtures containing the saturated lipids DSPC, 20:0PC and 22:0PC, are novel mixtures that have not been studied before. Therefore the first step was to test the simplest of the new mixtures, DPPC/14:1PC/Chol. DPPC is a commonly studied lipid and DPPC/DOPC/Chol mixtures have been well studied. As 14:1PC is structurally analogous to DOPC (18:1PC) with just 2 less carbons in each of its tail chains, it should form bilayers in ternary mixtures and show similar phase behaviour. A range of compositions from this mixture were made into SLBs, so that the phase behaviour over a range of the phase diagram could be observed. The different compositions were imaged by AFM and are shown in Figure 4.2 with their corresponding position shown on a ternary phase diagram. The choice of compositions were based on the  $L_o$ - $L_d$  coexistence region in the DPPC/DOPC/Chol phase diagram (Figure 1.5 in Introduction), where you expect to see roughly equal proportions of the two coexisting phases.

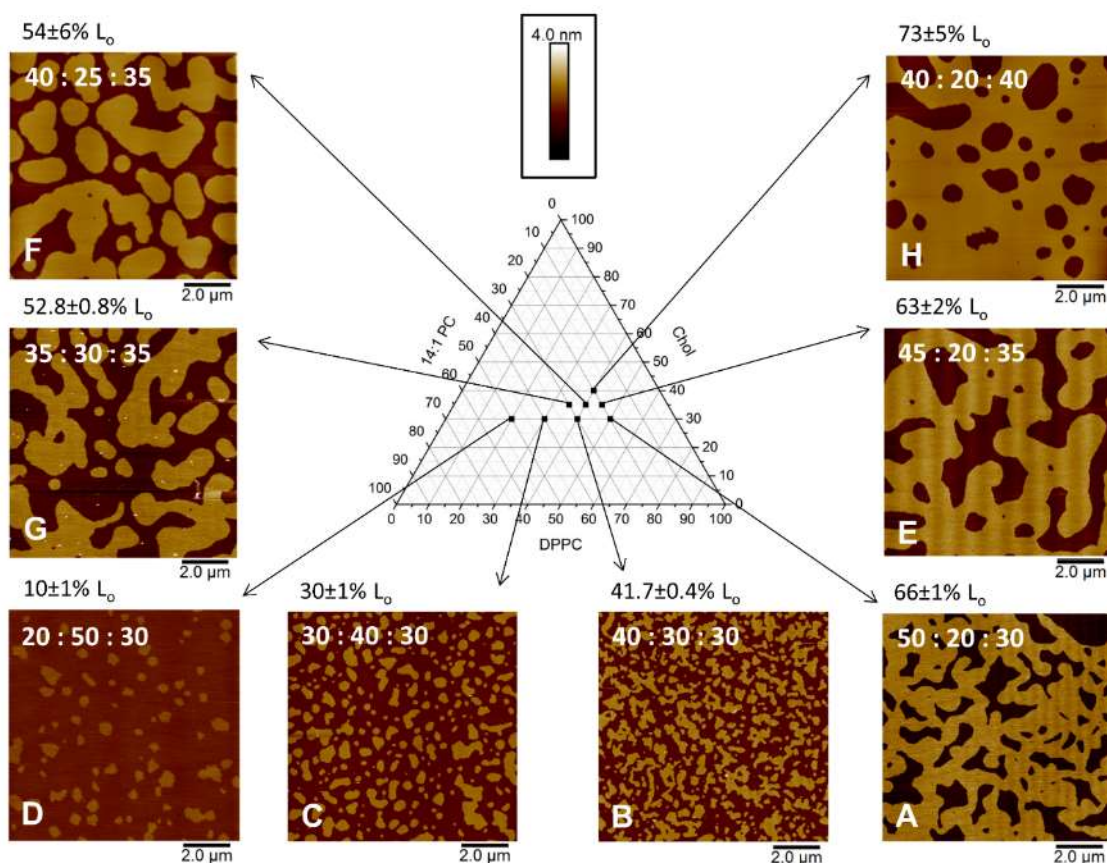


**Figure 4.2. DPPC/14:1PC/Chol Ternary Phase Diagram with AFM Images.** Images are representative examples from repeat images. The DPPC/14:1PC/Chol compositions are shown as percentage ratios at the top of each image. Percentage  $L_0$  areas are shown above each image and are averages with standard errors taken from at least three different areas of each sample. A) N=3 B) N=5 C) N=3 D) N=4 E) N=4 F) N=3 G) N=4 H) N=5.

All of the compositions formed showed  $L_0$ - $L_d$  phase separation, and the trends in area fraction and phase morphology of the two phases are as expected based on the phase behaviour in similar systems. As the percentage of saturated lipid in the mixture increases, there is an increase in the percentage of  $L_0$  phase. The percentage of  $L_0$ - $L_d$  is not just based on molecular composition but on the tie lines in the coexistence region. Figure 1.5 in the introduction shows that the tie lines, which dictate the compositions and ratios of the two coexisting phases for any point in the coexistence region, are slanted. This means that the  $L_0$  phase has a higher percentage of cholesterol, assuming a similar shape coexistence region to DPPC/DOPC/Chol and similarly angled tie lines. The area fractions in Figure 4.2 show that the coexistence region has a similar shape to DPPC/DOPC/Chol and that the tie



lines lay at similar angles. As the percentage of cholesterol is increased and the DPPC/14:1PC ratio stays similar, the ratio of phases stays similar. The phase morphologies are characteristic of nucleation and growth, many small domains, towards the left and right edges of the coexistence region. Towards the centre where the centre of the tie lines lie, the morphologies are spinodal. This indicates that the mixture formed and cooled close to a critical composition, where the free energy difference between the two phases was low and thus the energy barrier for longer domain boundaries was also low.

Domain size appears to be larger higher up in phase diagram i.e higher cholesterol content. The reason for this is not immediately obvious, but there are a few potential reasons. If both phases have higher cholesterol content, the phases will both be more fluid-like, lipids will be able to diffuse faster and domains will be able to flow faster. This should allow domains to move and coalesce into larger domains, as the mixture cools through the transition temperature from one-phase to two-phase, before the domains are trapped by substrate interactions. At lower cholesterol content the domains will be less fluid and less mobile across the substrate, resulting in smaller trapped domains that cannot coalesce. Also, a higher cholesterol content will mean that the height mismatch is lower. The  $L_o$  phase will protrude less towards the substrate, feel a weaker interaction and thus its domain's hydrodynamic motion will be less hindered.

AFM data with  $L_o$ - $L_d$  area fractions can be used to plot out phase boundaries, using the lever rule.<sup>21,43,98,99</sup> The observed area fractions are not the molar fractions however, due to the different surface area of the different lipid types and phases. Lipid surface area can be determined using X-ray Crystallography, Small Angle Neutron Scattering (SANS) and Nuclear Magnetic Resonance (NMR), for example the estimated mean surface area per molecule for DOPC is  $0.68 \text{ nm}^2$ , for DPPC is  $0.41 \text{ nm}^2$  and for Cholesterol is  $0.36 \text{ nm}^2$ .<sup>43,100</sup> There have been no literature reports on the area per molecule of 14:1PC. Cholesterol also has a concentration dependent effect on the area per molecules of lipids in both the  $L_o$  and  $L_d$  phases. Therefore it was not possible to map out phase boundaries and this was not explored any further using AFM.

### 4.3 Reproducibly Forming Supported Lipid Bilayers

Experiments were performed to ensure lipid compositions could be formed into supported bilayers reproducibly with similar phase behaviour. Figure 4.3 shows a hydrated lipid vesicle composition deposited onto five separated mica stubs and imaged using AFM. The area fractions are all similar, showing that the lipid composition in the vesicles has transferred to each of the stubs. The phase morphology on each stub is similar, showing domains characteristic of the nucleation and growth mechanism with similar shapes. There is a slight variation in domain size, likely caused by slight variations in temperature in the lab between repeats. Changes in temperature in the lab will affect the cooling rate, from incubation temperature at 50 °C to room temperature. Slower cooling rates have been shown to allow larger domains to grow.<sup>44,101</sup> Lipids have more time to diffuse and join larger domains and fluid domains

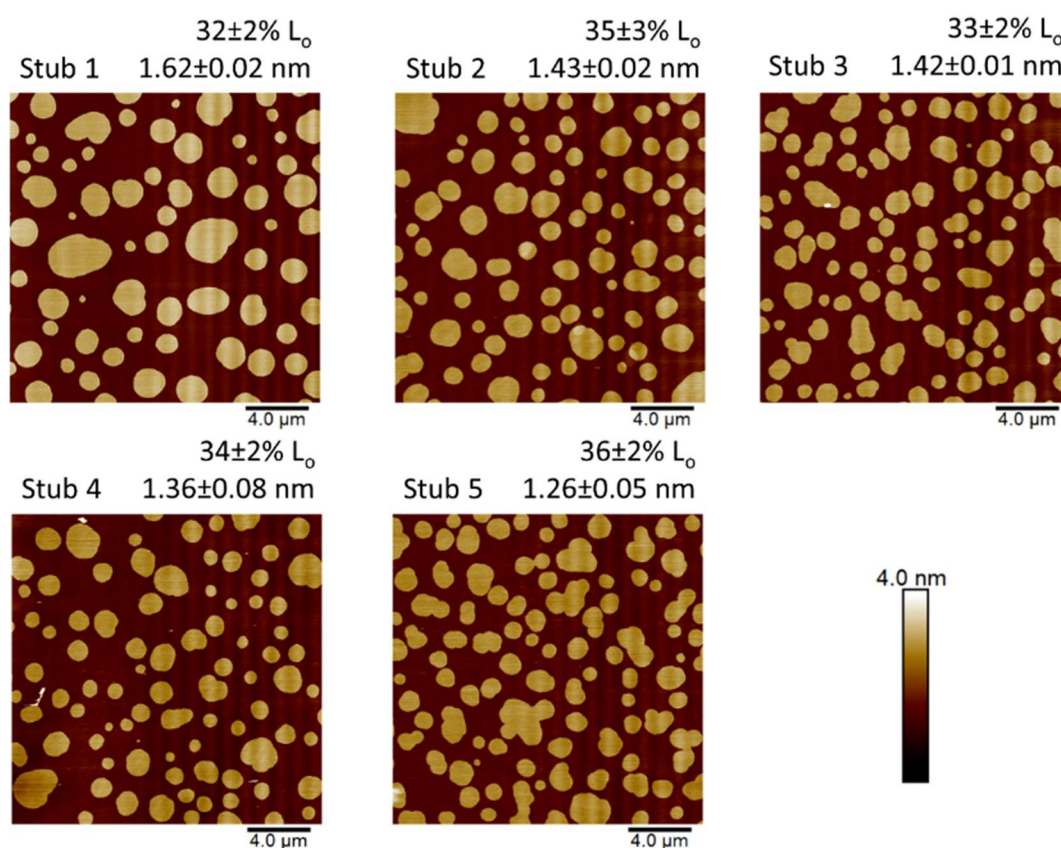


**Figure 4.3 AFM images showing five bilayers made on five different AFM stubs subsequently using the same hydrated DPPC/14:1PC/Chol (1:1:1) lipid mixture. Percentage  $L_o$  areas and height mismatches between the  $L_o$  and  $L_d$  phases are shown above each image and are averages with standard deviations taken from three different areas of the stub.**

have more time to coalesce as the mixture is slowly cooled through the miscibility transition temperature ( $T_m$ ), before the temperature is sufficiently below the  $T_m$  that phase separation is complete. This phenomenon is explored later in the chapters on Substrate Interactions (Chapters 7 and 8)

The samples from Stubs 1-5, as well as other mixtures were sent to collaborators at the University of Durham (Dr John Sanderson) for Mass Spectrometry experiments. Mass Spectrometry has been used previously to determine the composition and ratio of different lipids in vesicles.<sup>102</sup> The composition and ratio of lipids in our mixtures after imaging would show whether the composition of the SLBs matches the measured out composition i.e. is the lipid ratio maintained through hydration, sonication, extrusion and vesicle deposition. After AFM imaging, lipid films were dried under vacuum and then washed into a vial using  $\text{CHCl}_3:\text{MeOH}$ , to send to Durham on dry ice. Unfortunately, these experiments were not successful due to the small quantities of lipid from each stub (300-400 ng). No Mass Spectrometry data is presented and these experiments were not repeated.

#### **4.4 Increasing Hydrophobic Mismatch**

Coarse-grain simulations<sup>13</sup> and a mean-field free energy model<sup>14</sup> both show that as the hydrophobic mismatch between coexisting phases is increased, anti-registration becomes favoured. In this section, the hydrophobic mismatch is increased experimentally in order to verify these findings. The saturated lipid chain length in a ternary lipid mixture was increased from 16 to 22 carbons, all for the same molar ratio composition. In this section the data is presented for each hydrophobic mismatch system first and then the implication of bilayer heights on R and AR is then discussed.

Figure 4.4 and Figure 4.5 show AFM images as the hydrophobic mismatch is increased. For the lowest hydrophobic mismatch system, DPPC/14:1PC/Chol, two bilayer heights are clearly observed, the  $L_o$  and  $L_d$  phases. All of the DPPC compositions formed showed just two bilayer heights (Figure 4.2). For the DSPC and 20:0PC ternary systems at the same composition, there are also only two observable phases present. When the hydrophobic mismatch is increased in the 22:0PC system however, there are three different observable

heights, indicating that there are three different phases present (Figure 4.4 and Figure 4.5).

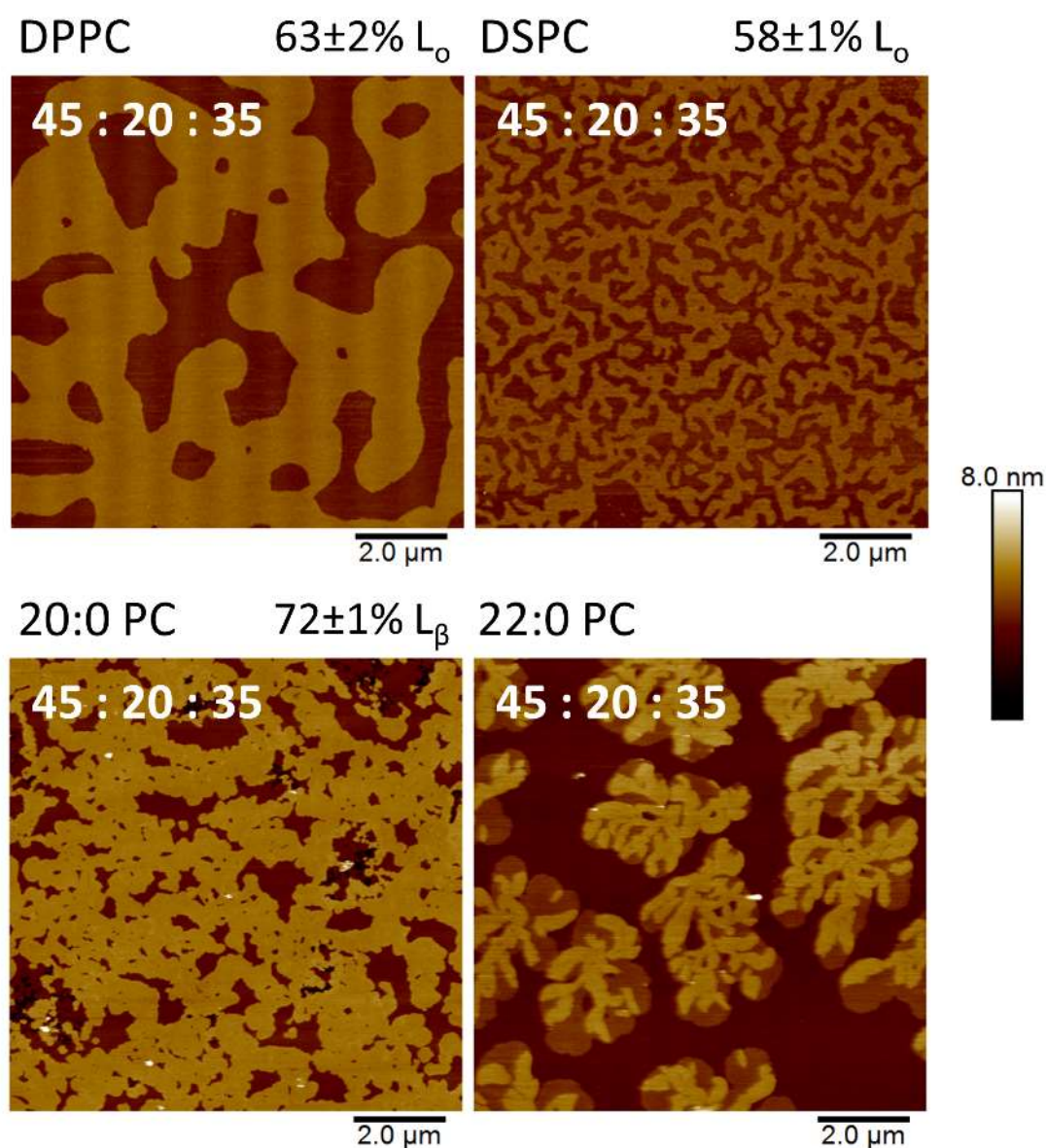


**Figure 4.4 Increasing hydrophobic mismatch in ternary lipid mixtures. AFM images of DPPC/14:1PC/Chol, DSPC/14:1PC/Chol, 20:0PC/14:1PC/Chol, 22:0PC/14:1PC/Chol at the same 45:20:35 composition, showing the morphologies of domains as the length of the saturated lipid hydrocarbon tail in the mixture is increased from 16 to 22 carbons. The  $L_o$  area percentage is shown above each image, except for 22:0PC where assigning phases and calculating areas is more challenging and is addressed in a later section. The  $L_o$  area is an average of repeat readings with standard error. DPPC) N=4 DSPC) N=4 20:0PC) N=3.**



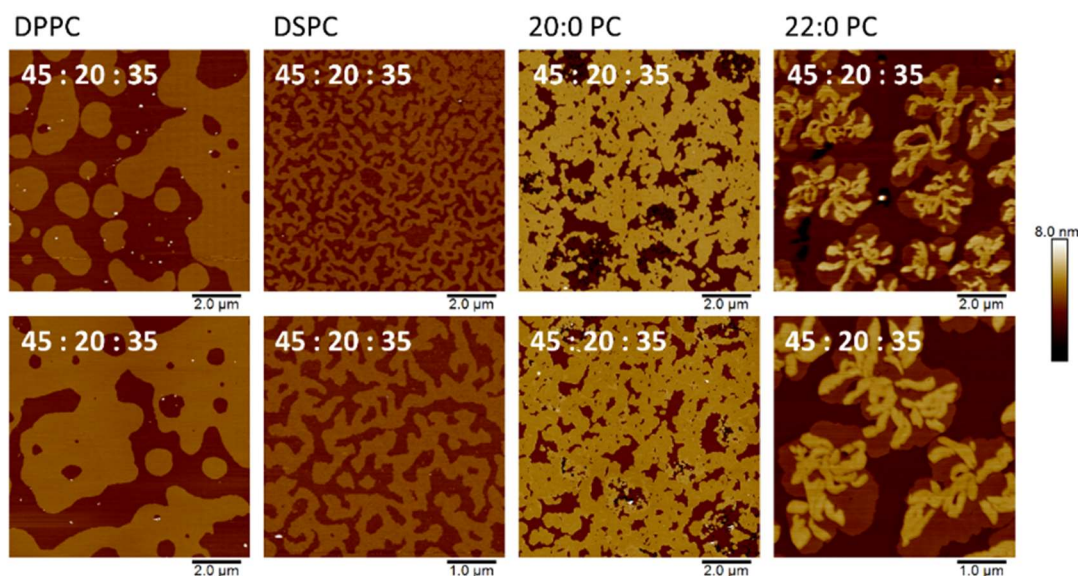


**Figure 4.5** More example AFM images of increasing hydrophobic mismatch. The images shown in this figure are from the same sample stubs as Figure 4.4 and show the mixtures DPPC/14:1PC/Chol, DSPC/14:1PC/Chol, 20:0PC/14:1PC/Chol, 22:0PC/14:1PC/Chol, all 45:20:35. The morphologies are similar to the images in Figure 4.4 and show the same number of phases.

#### 4.4.1 Further DSPC and 20:0 PC Registered Examples

As with the DPPC system, several different compositions within the ternary phase diagram were formed for DPSC and 20:0PC. Example images for a range of DPSC compositions are shown in Figure 4.6. Again at each composition there are just two phases present. The compositions have not been presented on a phase diagram. This is because the trends in composition were not all as expected, unlike the DPPC phase diagram (Figure 4.2). The data is instead presented in increasing  $L_o$  area fraction (Figure 4.6). Generally as the percentage of DSPC is increased the fraction of  $L_o$  increases. This makes sense as the mixture will be closer towards the phase boundary on the right hand side of the coexistence region, and thus the position on the tie line will dictate that there is a larger fraction of the  $L_o$  phase. The DPPC/14:1PC/Chol (50:15:35) mixture however does not match this trend. This mixture should be closer to the right hand side of the coexistence region than any of the other mixtures. Therefore the mixture should not only show a higher  $L_o$  area fraction but should also be predominantly  $L_o$  with domains of  $L_d$ , and not the opposite as shown in the data (Figure 4.6). There is also a remarkably large change in composition between the 40:25:35 and 41:21:38

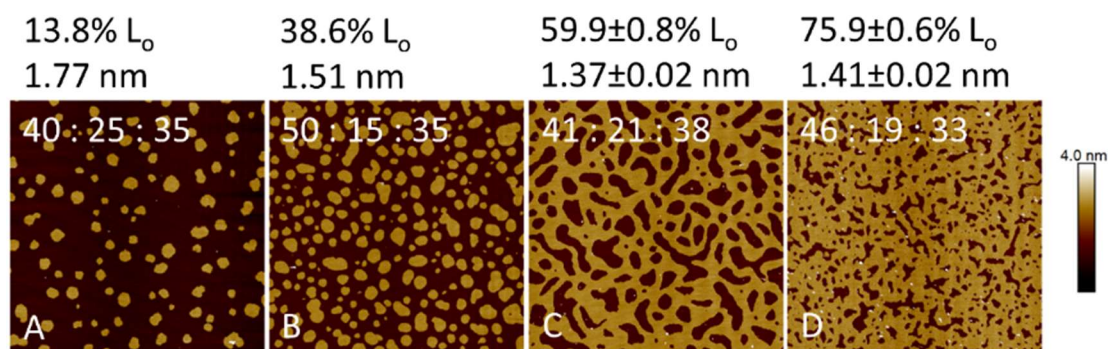


**Figure 4.6 Examples of different DSPC/14:1PC/Chol compositions, all showing two heights and registered phases. The compositions are shown at the top of each image. The percentage L<sub>o</sub> area is shown above the image, with standard error for C and D and an average with no standard error for A and B. A) N=2 B) N=2 C) N=6 D) N=6.**

samples, despite a relatively small movement in the phase diagram. This all suggests that the compositions that are imaged in the SLBs are not necessarily the same compositions mixed together. At some stage in the process of mixing lipid CHCl<sub>3</sub> stocks to form ternary mixtures, drying to form lipid films, rehydrating in water, vortexing, sonicating and extrusion to form vesicles, and incubation on the mica surface, the lipid ratios are potentially altered. The reasons for this are not clear but there are several possibilities. Lipid may be lost during the formation of vesicles because aggregates of the longer chain lipids are not broken down sufficiently by the sonication and extrusion process. Vesicles may not have a monodisperse composition of lipids and sediment and fuse to the surface at different rates.

Example images for a range of 20:0PC/14:1PC/Chol compositions are shown in Figure 4.7. Like DPPC and DSPC, all the mixtures show just two phases. Like DSPC, there appear to be potential issues with compositions potentially not matching the measured out compositions. For example the change in area fraction between 45:25:30 and 50:20:30 is significantly larger than the small change between 50:20:30 and 55:15:30, despite the same change in 20:0PC composition and change in phase diagram position.

The issue with composition was only present in the systems of higher saturated chain length and not DPPC. It may be that the methods refined for DPPC systems were not adequately adapted for the higher hydrophobic

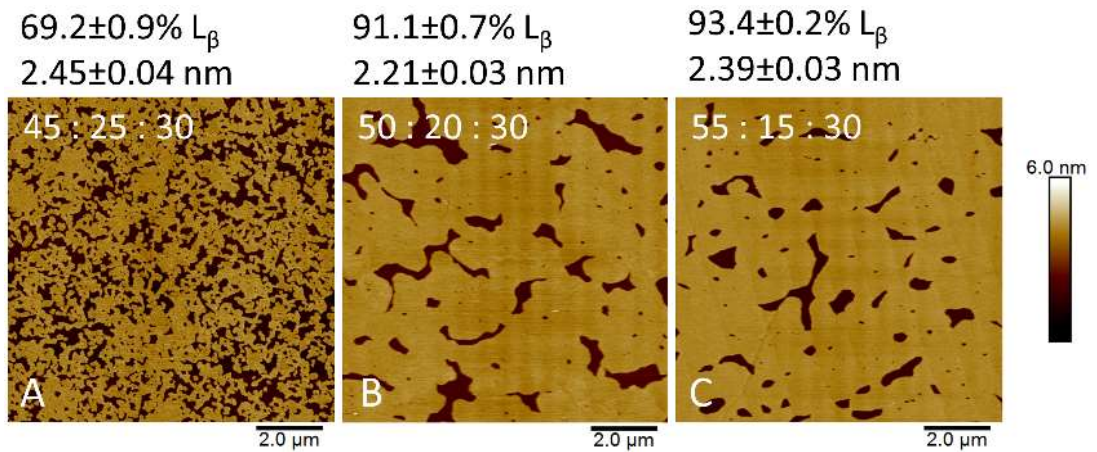


**Figure 4.7** Examples of different 20:0PC/14:1PC/Chol compositions, all showing two heights and registered phases. The compositions are shown at the top of each image. The percentage  $L_{\beta}$  area and height mismatch is shown above each image with standard error. A) N=4 B) N=5 C) N=5

mismatch systems. Despite this issue, the data collected show just two heights and enabled height mismatch to be measured.

#### 4.4.2 22:0 PC Heights and Morphologies

As was shown in Figure 4.4, when the hydrophobic mismatch was increased to 8 carbons in the 22:0PC/14:1PC/Chol system, there were three different bilayer heights present. A range of different morphologies were seen for different 22:0PC compositions, as well as for the same composition and within the same sample stub. This is shown in Figure 4.8. Images A-D all have the composition 22:0PC/14:1PC/Chol (55:15:30), and all show the presence of three heights. The morphology of domains and the relative areas of the three phases varies greatly between the samples however. A, B/C and D are from 3 separate mixtures of the same composition, and B and C are from the same



sample stub. These differences could be a manifestation of the issues discussed for DSPC and 20:0PC, where the composition mixed may not be reproducibly forming into a SLB of the same composition. For example longer chain lipid aggregates may be resulting in lost lipid, or polydispersity in vesicle compositions may result in different sedimentation and rupture. However this cannot explain why the morphologies and area fraction are so drastically

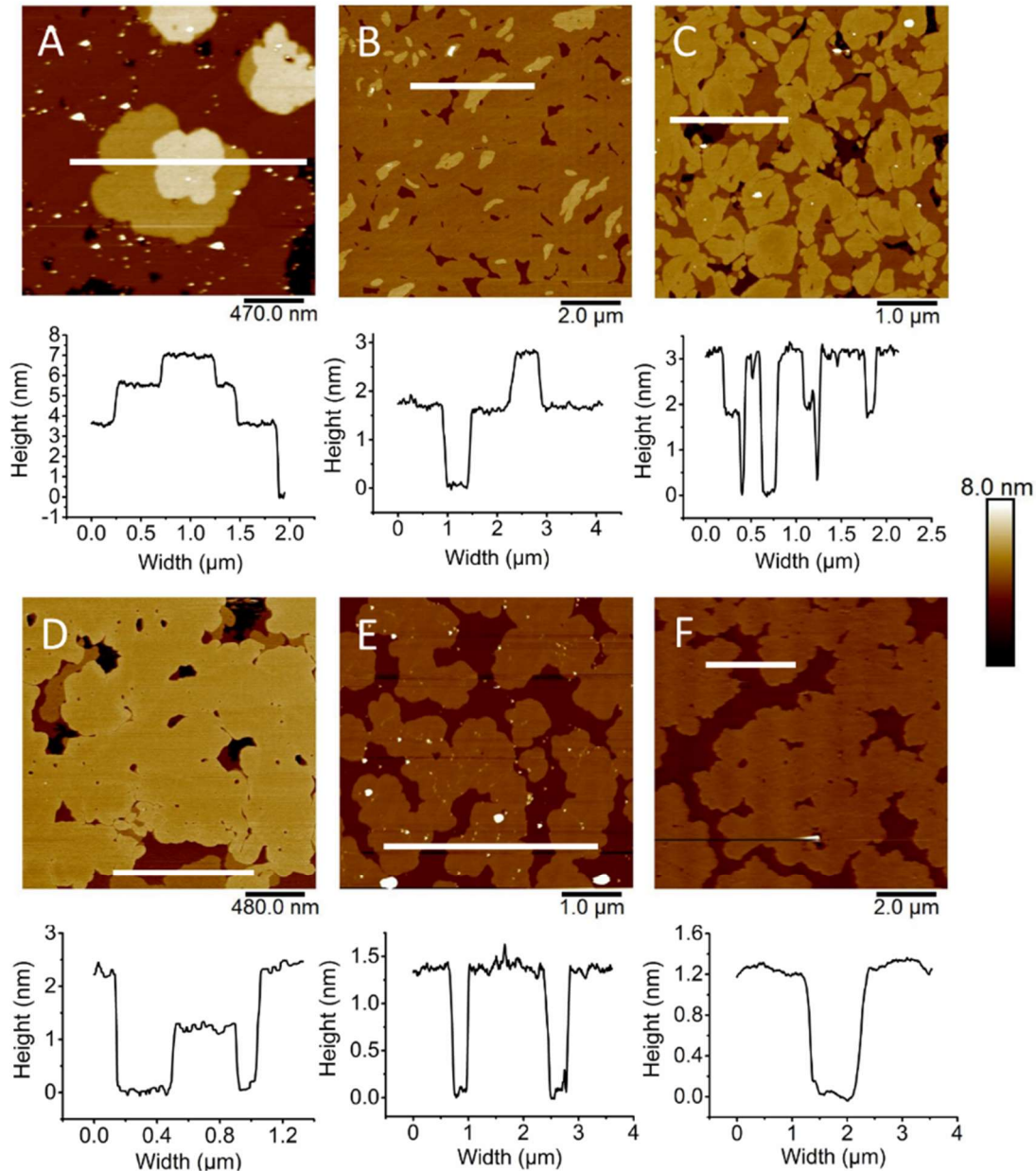


**Figure 4.8 Example Images of 22:0PC/14:1PC/Chol Bilayers, showing a range of morphologies. A-D show three bilayer heights, E and F show only two. Below each image is a line height profile corresponding to the white line in the image above. A-D = DPPC/14:1PC/Chol (50:20:30). E = 45:25:30, F = 45:20:35.**



different for B and C which are from the same sample stub. This could be due to variations in cooling rate across the stub or variations in local lipid density.

Although three heights were observed for the 22:0PC/14:1PC/Chol composition in A-D, only two heights were observed for the compositions in E and F. As will be shown in the next section, the height of the top phase matches closely to the middle height in the systems with 3 heights.

Figure 4.9 shows examples of the more unusual morphologies observed for 22:0PC/14:1PC/Chol mixtures. Figure 4.9A shows three bilayer heights but there are periodic corrugations in the top phase. This phase was identified as the ripple phase and structure matches to AFM images of known ripple phases.<sup>103</sup> The ripple phase forms as a pre-transition before the gel phase melts to the fluid phase (the transition can be observed in the DPPC DSC in Figure 6.3). It is not fully understood but is thought to form as a result of local spontaneous curvature, likely to accommodate packing constraints caused by coexistence of gel and fluid phases at a local level.<sup>103,104</sup> The only explanation for its presence in this 22:0PC ternary lipid system is that this specific composition formed at room temperature lies between the ripple pre-transition and the main transition for the mixture. Figure 4.9B has the same composition as A, but shows thin filament morphologies which could be small extensions of the ripple phase. Figure 4.9C shows three heights but in two drastically different coexisting states. There are areas with 100-300 nm domains of the top height within the middle height, as well as areas of small nanoscale middle height domains within the lower height.

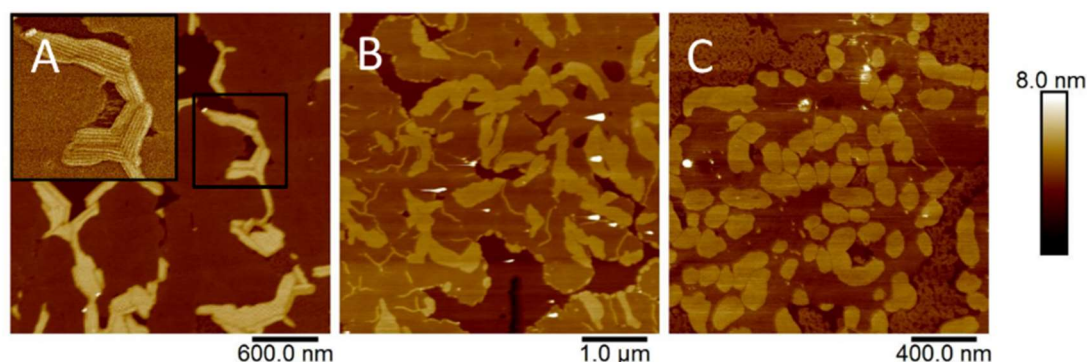


**Figure 4.9 Examples of other morphologies observed in 22:0PC/14:1PC/Chol ternary mixtures. A = 22:0PC/14:1PC/Chol (50:15:35), B = 55:15:30, C = 50:15:35.**

Overall three heights were observed for at least one area of a sample stub for four out of the five different compositions formed, with the exception 22:0PC/14:1PC/Chol (45:25:30). This can be seen by examining Figure 4.4, Figure 4.5, Figure 4.8 and Figure 4.9.

### 4.4.3 Hydrophobic Mismatch

The height mismatch between coexisting phases was measured and the results summarised in Figure 4.10. There is quite a large range of height mismatch values for the DPPC and DSPC systems. One of the reasons for this is that the data is averaged from across different compositions within the phase diagram. When the height mismatch values for the DPPC system are plotted on a phase diagram the variation in heights can be partially rationalised (Figure 4.11). Different compositions will lie along a different tie line in the 2-phase coexistence region in the phase diagram, and thus will have different

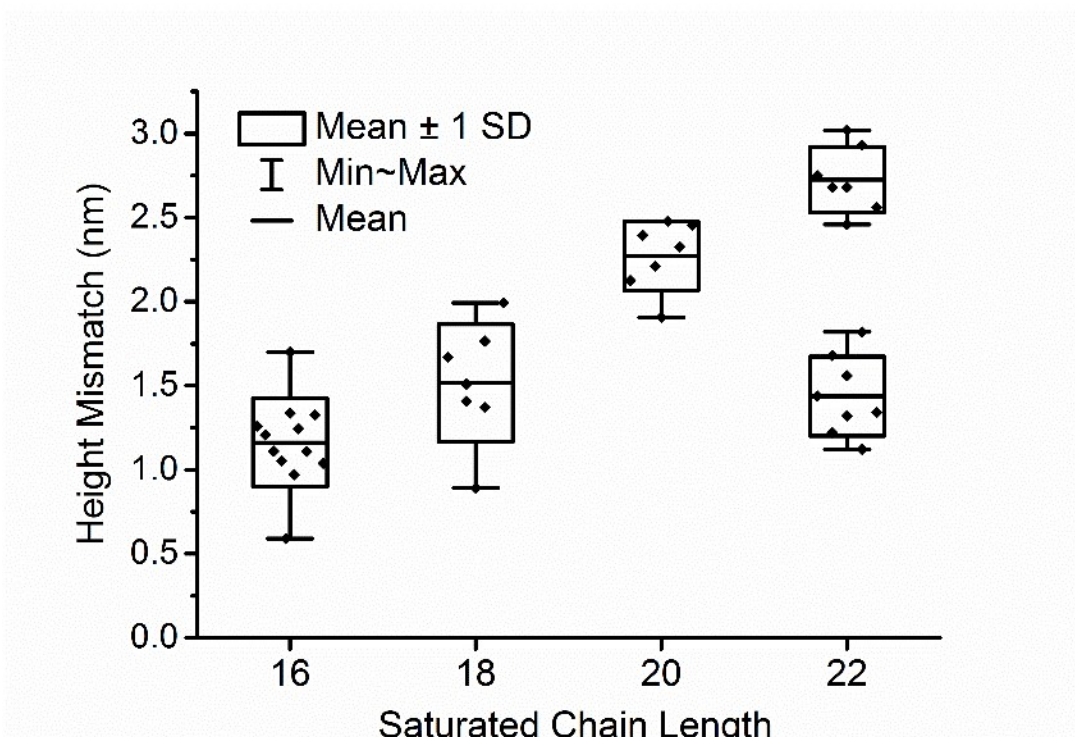


**Figure 4.10 Change in height mismatch between bilayer phases with increase in saturated chain length. Each data point is a separate experiment on a separate day with a different composition of DPPC (16)/14:1PC/Chol, DSPC (18)/14:1PC/Chol, 20:0PC/14:1PC/Chol or 22:0PC/14:1PC/Chol. Data points for 16, 18 and 20 are averages of at least three images with depth measurements over the whole image. Some of the data for 22 is the average of at least three images with 5-10 individual line profile measurements at domain boundaries, for images where the levelling was not sufficient to take accurate depth measurements. The data points are arranged laterally to avoid overlap.**

$L_o$  and  $L_d$  compositions. Towards the critical point (star in Figure 4.11B), the two phase will have similar heights, and the height mismatch will be smaller. The tie lines shown in Figure 4.11B are for DPPC/DOPC/Chol. The tie lines for DPPC/14:1PC/Chol are unknown. The trend in heights in Figure 4.11A show an overall decrease as the composition of DPPC drops and 14:1PC increases. There are a few anomalous values, but the values only vary from the trend by a few Ångstroms. Based on these heights, the tie lines would need to be tilted at a larger angle compared to DPPC/14:1PC/Chol, which is entirely possible.

Ideally with fully mapped phase diagrams and boundaries for each of the ternary systems, it would be easier to directly compare the increase in height mismatch. It is likely that the position of phase boundaries move as the saturated lipid length is increased. For a direct comparison in Figure 4.4 the four hydrophobic mismatch systems are compared at the same molar ratios, however due to the moving phase boundaries the heights could be affected by their position along a tie line and proximity to a boundary instead of just the increase in saturated lipid length. With a full knowledge of the phase diagrams, a composition could be picked for comparison that was a set distance from the critical composition for example. Without the phase diagrams, the average across a range of compositions is used to compare height mismatch between the different hydrophobic mismatch systems.

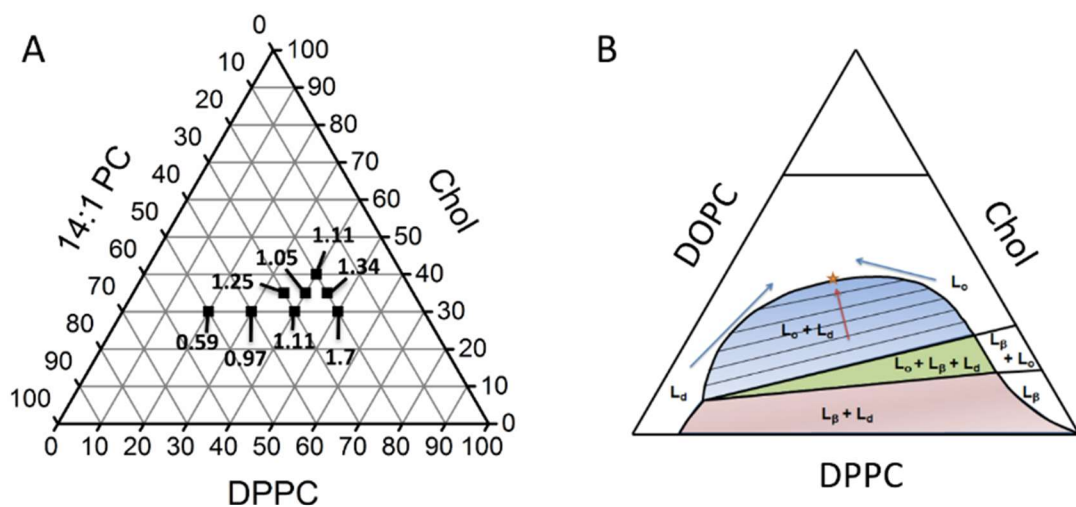


**Figure 4.11 Change in height mismatch with composition across a phase diagram. A) Ternary Phase Diagram for DPPC/14:1PC/Chol with height mismatch values. B) Example Literature Phase diagram for DPPC/DOPC/Chol<sup>20</sup>**

A SM bilayer, which is a mixture of chain lengths but predominantly 16:0, has a  $L_o$  tail thickness of 1.64 nm, based on published data.<sup>26,44,105</sup> Assuming that the thickness of the bilayer increases linearly with increasing carbon chain length and that the bilayer is still in the  $L_o$  phase, an increase in bilayer thickness of 0.41 nm can be estimated when 2 carbons are added. The measured height mismatch values for the DPPC and DSPC systems are  $1.16 \pm 0.08$  nm and  $1.51 \pm 0.13$  nm (mean  $\pm$  standard error). This is an increase of 0.35 nm between the mean values for DPPC and DSPC, matching closely to the estimated increase of 0.41 nm inferred from literature values.<sup>26,44,105</sup> However the increase to the 20:0PC system (2.27 nm) is 0.76 nm, significantly larger than the estimated height increase. This estimate assumed a  $L_o$  chain length, but as the saturated chain length increases it is likely that the bilayer will form a gel ( $L_\beta$ ) phase. The  $L_\beta$  phase has fully extended tail chains, which for DPPC gives a tail thickness of 1.9 nm.<sup>26,44</sup> Using this value to calculate the bilayer thickness gives an expected increase of 1.06 nm between the DPSC and 20:0PC systems. This is larger than 0.76 nm, but the observed jump in height mismatch can be explained by a straightening of the acyl tail lipid chains. This is strong evidence that the coexistence observed in the 20:0PC system is  $L_\beta$ - $L_d$  and not  $L_o$ - $L_d$ . The phase boundary between the  $L_\beta$ - $L_d$  and  $L_o$ - $L_d$  regions must have risen above the compositions imaged when height mismatch was increased between DSPC and 20:0PC.

As there are three phases present in the 22:0PC system, there are two height mismatches shown in Figure 4.10, from the bottom to intermediate height and from the bottom to the top height. The jump in height mismatch from the 20:0PC to the top 22:0PC height was 0.45 nm. This matches closely to the expected increase in  $L_\beta$  chain length, 0.48 nm, assuming a linear increase in chain length with carbon chain length. This is evidence that the 22:0PC system, like the 20:0PC system, is showing  $L_\beta$ - $L_\beta$  phase coexistence. Considering the symmetry and two leaflets of the bilayer now, the heights imply that the top height is the R  $L_\beta$ - $L_\beta$  state.

The observed increases in height mismatch match closely to those inferred from bilayer thickness in the literature.<sup>26,44,105</sup> This provides circumstantial evidence that the bilayer headgroups of both phases are the same distance from the substrate, and that the height mismatch between the bilayers is fully

accommodated on the top of the bilayer. For a free-floating bilayer the two coexisting phases would align at the midplane between the two bilayer leaflets, and the height mismatch would be equally distributed on each side. If this was true for the SLBs in this study the increases in height mismatch would be half. The midplanes are likely aligned at the interface between phases but curve down to the substrate over nm length scales not observable by AFM. This suggests a strong substrate-lipid interaction.

#### 4.4.4 Absolute Bilayer Heights

The preparation of SLBs was optimised to achieve full surface coverage of the substrate. This includes optimisation of vesicle formation, incubation time and  $\text{MgCl}_2$  concentration. Defects are still sometimes observed in bilayers. They can be due to degraded lipid which is unstable and collapses upon AFM force, not washing with  $\text{MgCl}_2$  to make vesicles burst and form onto the substrate, washing with buffer at a different temperature to the bilayer, and exposure to air. Defects often mean that the images are hard to process, level and analyse. Despite all of this however, defects can be incredibly useful for measuring the absolute heights of bilayers and phases, not the just the height mismatch between phases. Assuming that the defect reaches down to the substrate, shown by a clean flattened bottom as the probe images the substrate, the

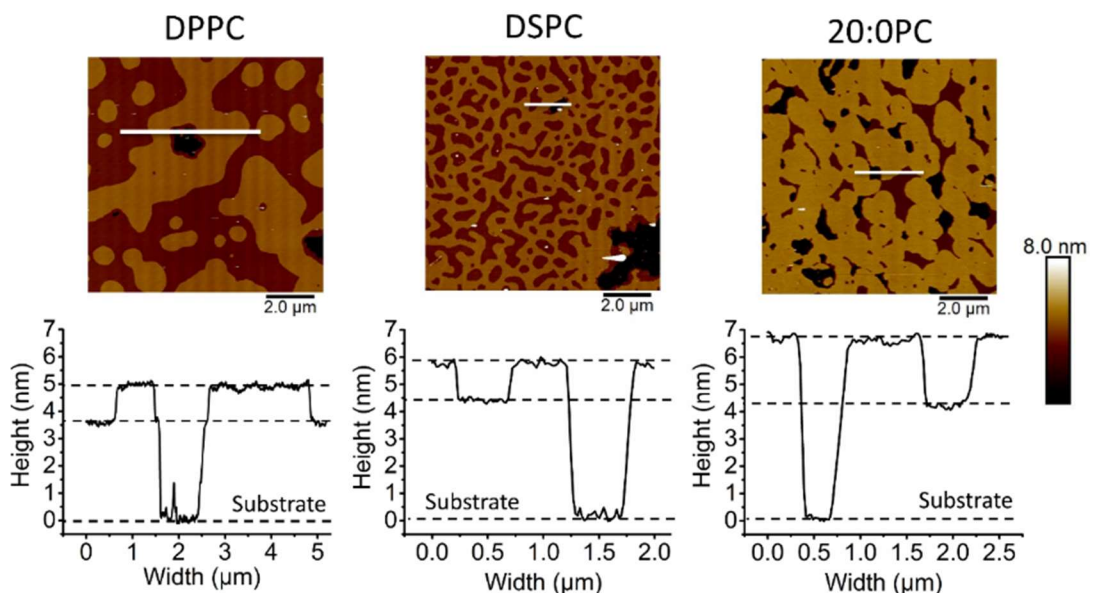


**Figure 4.12 Line profiles of Defect Bilayers.** Line profiles across defects in DPPC, DSPC and 20:0PC images highlighting the height mismatch and also the absolute phase heights. Line scans correspond to the white line on the AFM image above.

height of the bilayer can be measured (Figure 4.12). From the limited data with defects across the four hydrophobic mismatch systems, the absolute height of the lowest phase stays constant at  $3.9 \pm 0.1$  nm. There is not the same volume of data as obtained on height mismatch. If there had been, many repeat measurements could have been taken to obtain statistically relevant absolute bilayer heights and the height mismatch values in Figure 4.10 could be normalised. Due to limited data however, this was not done. This analysis shows that all of the height mismatch values are relative to this base 14:1PC height of  $3.9 \pm 0.1$  nm. It should be noted that SLBs sit upon an interstitial water layer 0.3-2 nm thick.<sup>106</sup> It is not immediately clear whether the absolute height measured included this water layer and whether the hydration shell of the substrate in the defect is a similar size.

#### 4.5 Anti-Registration

As has been discussed, the height mismatch of the DPPC, DSPC and 20:0PC systems show the expected increase as saturated chain length is increased, assuming complete symmetry between the two leaflets. The height mismatch between the bottom and top phases in the 22:0PC also matches to the expected increase assuming symmetry between the two leaflets. The bottom height is the 14:1PC  $L_d$  phase in both leaflets, a symmetric registered phase. The intermediate height in the 22:0PC system however does not match to any

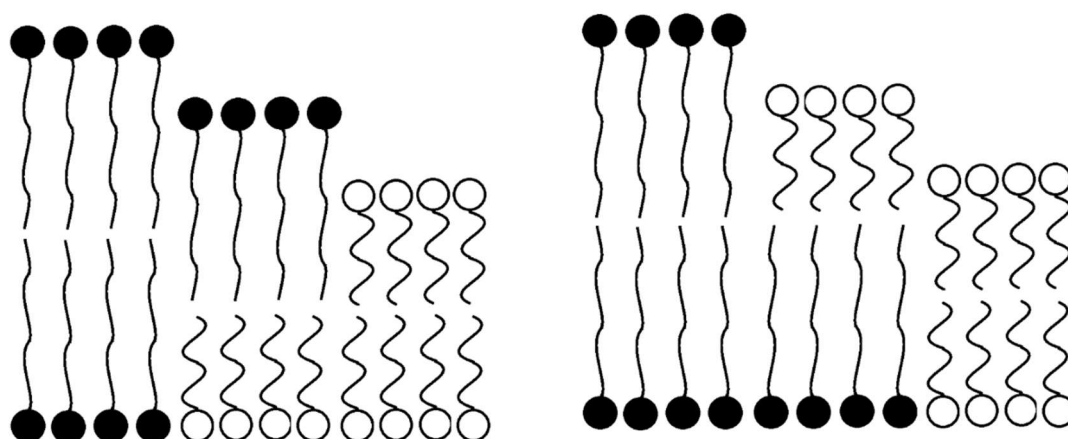


**Figure 4.13 Schematic showing the two possible orientations of an AR Bilayer. Black headgroups are gel phase, white headgroups are fluid phase.**



expected symmetric heights. For an AR bilayer, with  $L_d$  phase in one leaflet opposite  $L_\beta$  in the other leaflet, the expected height would be exactly halfway between the  $R L_d$  and  $L_\beta$  phases. This can be understood by examining the schematics in Figure 4.13. The average height of the intermediate phase above the bottom phase (1.44 nm) is almost exactly halfway (53%) between the average height of the top phase above the bottom phase (2.73 nm), matching the expected height of the AR state.

Figure 4.8 E and F show that not all 22:0PC systems have three heights, some compositions and areas only show two. The height mismatch between the bottom and top heights in the two phase system matches with the height mismatch between the bottom and intermediate height of the three phase system. Both the two phase and three phase 22:0PC height data are included in Figure 4.10. This suggests that the two phase 22:0PC system is a coexistence of  $R L_d$ - $L_d$  and AR  $L_d$ - $L_\beta$ . The thorough measurements of height mismatch values and comparison with expected literature values was vital to understand the heights seen here, otherwise the two phase 22:0PC system could easily have been mis-assigned as a completely symmetric  $L_\beta$ - $L_d$  coexistence.

It should be noted that three bilayer heights can also be observed for compositions within the three phase region of the ternary phase diagram. The three phase region is a thin region in the phase diagram with coexisting  $L_\beta$ ,  $L_o$  and  $L_d$  phases. The three phase region can be observed in the DPPC/DOPC/Chol phase diagram in Figure 4.11. It is plausible that the three phase region boundaries move up higher (compositions closer to the top cholesterol vertex of the ternary phase diagram) in the 22:0PC phase diagram compared to lower hydrophobic mismatch systems and that the compositions formed in this work are within this region. Based on the observation that 20:0PC shows  $L_\beta$ - $L_o$ , and that this region is below the three phase region it is extremely unlikely that the 22:0PC mixtures are in this region. Imaging and obtaining the heights of this region have been challenging, but published work from our lab has shown that at low imaging force the  $L_\beta$  and  $L_o$  phases are so similar in height they are almost indistinguishable.<sup>44</sup> The three phase region heights do not match up at all with the AR heights shown by bilayers in this work.

## 4.6 Summary

In this chapter the hydrophobic mismatch in ternary lipid bilayers was sequentially increased, resulting in three phase bilayers for 22:0PC. Thorough analysis of the height mismatches in all the ternary lipid mixtures, provides strong evidence that the intermediate phase in the 3 phase system is an asymmetric AR state. This validates the simulations and the mean-free model that predicted that if line tension was increased high enough it would overcome the interleaflet coupling forces favouring R, and that amount is a mismatch of 8 carbons.

Although the ternary lipid compositions used in this project are a vast simplification of the plasma membrane, which has many lipid types as well as proteins and other bio-molecules incorporated, the results here have implications biologically. The physical mechanisms and interactions between the two leaflets of the bilayer that cause model bilayers to register must also be acting in biological membranes. This study shows that there is a finite coupling that can be overcome to force domains in opposite leaflets to anti-register. The dynamic plasma membrane must be overcoming this coupling force to enable asymmetry. Linked in to this idea is the plasma membrane's ability to hold the lipid compositions of the two leaflets away from symmetry. Identical lipid compositions in both leaflets would be the equilibrium state, and lipid flip-flop enables translocation of lipids between the two leaflets, which would allow the system to move towards equilibrium. The mechanisms by which the plasma membrane holds the lipid compositions out of symmetry, including spontaneous flip-flop and translocase proteins, and the identity of the interleaflet coupling mechanisms which favour domain registration, are still to be fully understood. With a further understanding of these specific areas, a deeper understanding of the dynamic and asymmetric plasma membrane will be gained.

In the next chapter (Chapter 5), methods are explored to distinguish between the two leaflets of the bilayer, in order to figure out whether the AR state is orientated with the  $L_{\beta}$  on the top or on the bottom. In Chapter 6, experiments are designed to attempt to force out anti-registration in lower hydrophobic



mismatch systems. At the end of Chapter 6, the value of the interleaflet coupling is estimated using existing theory.

## Chapter 5. Determining Anti-Registration Orientation

### 5.1 Introduction

The previous chapter showed how increasing the hydrophobic mismatch in two-phase bilayers, by increasing the length of the saturated lipid chain in ternary mixtures, resulted in the formation of AR bilayers. The AR state appeared in the 22:0PC/14:1PC/Chol system, when the lipid chain lengths mismatch between the two phases was 8 carbons, and height mismatch above  $2.27 \pm 0.07$  nm. The AR state was inferred from the bilayer heights. For the 22:0PC bilayers, there were either two or three phases present, with the middle height in 3 phase bilayers and the top height in the two-phase bilayers being too short to be the R  $L_{\beta}$ - $L_{\beta}$  state. The AR height was also close to the predicted height halfway between the R  $L_d$ - $L_d$  and  $L_{\beta}$ - $L_{\beta}$  states.

The next question to ask concerns the orientation of the AR state. Is the  $L_{\beta}$  or  $L_d$  phase on top of the asymmetric state? Based on the mean-field free energy model of Williamson et al., both possible AR orientation states have the same energy.<sup>14</sup> However, the model does not currently take into account the substrate interactions in SLBs. It is possible that the substrate is breaking the symmetry of the AR states and favouring a certain orientation. By determining the orientation of the AR state in our experimental model, it will be possible to answer many outstanding questions from the research of Williamson et al. Is the orientation of AR the same across a single sample stub, is the same AR orientation repeatably observed for the same mixture and is the same AR orientation observed for all mixtures?

There are several possible methods which could distinguish between the two different possible AR states. This chapter will focus on AFM methods to do this and in particular how mechanical properties can be used to distinguish between different phases.

## 5.2 Tapping Mode Phase Imaging

Initially tapping mode phase (TM Phase) imaging was tested to try to isolate the lipid phase identity of the top leaflet. TM phase is the phase lag between the sinusoid of the driving piezo for tapping mode and the oscillating cantilever which is damped when in contact or close proximity with the surface. At the resonant frequency the lag between the driving piezo and the cantilever is  $90^\circ$  in free air. The TM phase signal represents the lag away from this value. As the cantilever is damped by the surface, this implies a transfer of energy to the sample. The lag can be a value that is positive or negative in relation to  $90^\circ$ , depending on whether the interaction of the probe is attractive due to Van der Waals forces, or repulsive when in hard contact due to coulombic forces. The phase image therefore contains information on the mechanism by which tapping energy is lost to surface, which in turn is sensitive to the material properties of the surface. Tapping mode was first developed in 1996, and until 2012/13 was the only means of obtaining high resolution material discrimination via AFM.

Using TM phase to look at three height AR bilayers, reveals just two different contrasts in the phase, despite there being three phases (Figure 5.1). Therefore, it seems reasonable to infer that the tip is detecting the same surface physical properties for the AR top phase as one of the other R phases. In Figure 5.1, the two examples show the intermediate AR phase matching to the opposite R state, one to the R gel and one to the R fluid. This is shown schematically below the images. Based on this interpretation, the AR state can be orientated either  $L_\beta$  up or  $L_o$  up and has formed both in different systems.

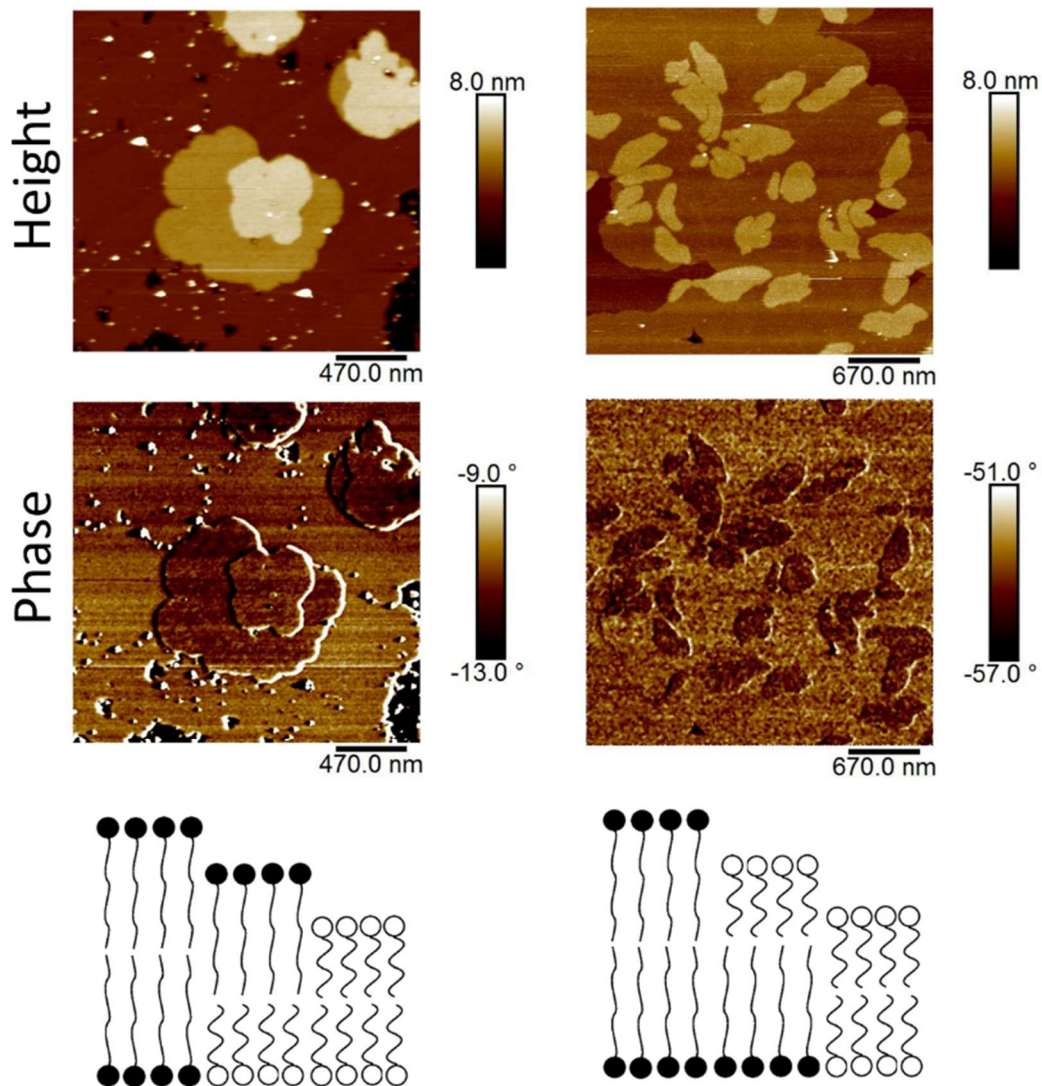


**Figure 5.1 Tapping Mode Phase Imaging of three height AR bilayers. Two different three height AR bilayers are shown, with height images, tapping mode phase images and a schematic bilayer showing the orientation of the intermediate AR state as implied by the phase signals.**

### 5.3 Quantitative Nanomechanical Mapping

This section details the development of QNM. Whilst TM-AFM can produce phase images which give good mechanical contrast, the images can be difficult, if not impossible, to interpret due to the many and varied ways in which energy can be damped. Much research effort was expended in disentangling these complex responses and met with some success when imaging in air.<sup>81</sup> Unfortunately, the difficulty is exacerbated when imaging in liquid which further damps the response.<sup>81</sup> Hence around 10 years after TM-AFM was introduced, new modes were developed to enhance the quantitative aspect of mechanical imaging, with the development of QNM by Bruker. QNM uses Peak Force Tapping (PFT) imaging mode to obtain force curves for every pixel of an AFM image and then fits the curves in real time to give AFM image maps of modulus, dissipation, adhesion and deformation (Figure 5.2). QNM was only introduced commercially in 2012. When this project was started there

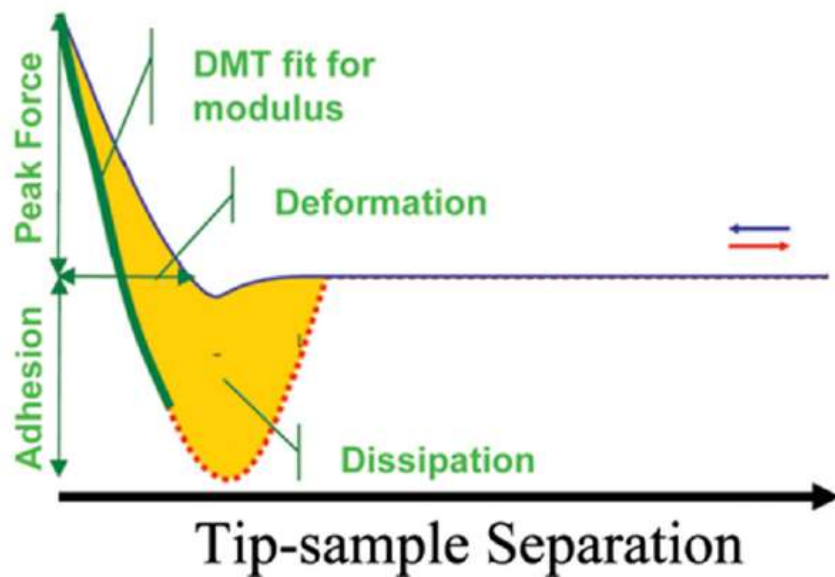


**Figure 5.2 Example QNM Force Curve showing how physical properties can be obtained. The blue arrow and line represent the approach curve and the red arrow and dotted line represent the retract curve. The y axis is force. Peak Force is the maximum force exerted on the sample and this is set by the user for AFM feedback. The green line on the retract portion of the curve is fit for the DMT model to obtain modulus. The dissipation is the area under the curve. Deformation is the distance from initial contact of the tip with the sample to the tip-sample separation at the Peak Force. Adhesion is the negative force on the y axis as the tip retracts and sticks to the sample. From reference<sup>87</sup>**

was only one paper, from the group of Simon Scheuring, using QNM to look at SLBs.<sup>84</sup> They successfully distinguished between liquid and gel phases by differences in modulus using QNM. This is a new technique which was still in the development phase in the authors laboratory. This section details the development of this technique towards using it to study the mechanical properties of lipid bilayers, focussing first on the important calibration steps.

### **5.3.1 Calibrating Peak Force Quantitative Nanomechanical**

#### **Mapping**

First of all the AFM cantilever must be calibrated for deflection sensitivity, spring constant and tip radius. These are the calibration steps that would be required to get quantitative information from a standard linear ramp force spectroscopy curve (detailed in sections 2.8.1 and 3.4.3). Then there are a few important extra calibration steps unique to QNM, and some of these were introduced by the manufacturers in the period 2015-17.<sup>107</sup>

The first of these parameters, and most important, is 'sync distance'. This is actually a time constant between the start of a force curve and the maximum force/lowest point reached by tip i.e. peak force. It is the turning point between the approach and retract parts of the force curve. When sync distance is not calibrated properly, the peak force registered by the QNM software does not match the actual maximum force i.e. the maximum piezo extension. When this is the case there is hysteresis in the force curves that are being analysed in real time to give live physical property maps, and this results in incorrect and sometimes meaningless property values.

To calibrate sync distance, a force curve must be performed on a hard surface prior to imaging any sample. There is now an auto-configuration option which will match up the peak force registered by the QNM software and the actual maximum force, but in the period when most of the data in the thesis was taken this was a manual operation. Once this has been performed on a hard sample, this value must be used for all subsequent imaging with that cantilever. It is vital that the sync distance is calibrated on a hard sample as when viscoelastic samples are imaged, such as bilayers, there can be time-dependent deformation. This means that when the tip reaches its lowest position, the force might not yet be at its highest because of the time-

dependent response of the viscoelastic surface. By calibrating on a hard surface initially to get a correct sync distance, i.e. maximum force is at cantilevers lowest position, the time dependent response of the viscoelastic material is known to be correct and should give correct physical property values.

Another property that needs to be calibrated for QNM is the Drive3 Amplitude Sensitivity. This is the signal from the Z offset Digital to Analogue Convertor (DAC) to drive the oscillation and force curves in PFT. The deflection sensitivity calculation for regular Z ramp force curves and QNM force curves use different Digital to Analogue Convertors to drive the force curve. Therefore, the Drive3 sensitivity needs to be calibrated to match to the regular deflection sensitivity. There is also a frequency dependence of Drive3 sensitivity, so different PF frequencies can amplify the oscillation of the lever. In simple terms, the oscillatory motion of the z-piezo (which has mass) has its own frequency dependant inherent lag due to inertia. Drive3 amplitude sensitivity can be calibrated, as long as regular z ramp sensitivity has been calibrated. A force curve must be captured against a hard surface using the PFT DAC and not the linear Z ramp DAC. The gradient of the linear deflection regime of this force curve must be taken. As the regular deflection set point has been calibrated, the gradient of a force curve should be 1 if the deflection axis is set in nm. If it is not, then the Drive3 amplitude sensitivity is out. To calibrate the actual gradient of the graph can be used to scale the Drive3 sensitivity to make the gradient 1. In the later version of the Nasoscope software (v9.2, circa Oct 2017), Drive3 amplitude sensitivity can be automatically calibrated without the need for the force curves and taking gradients.

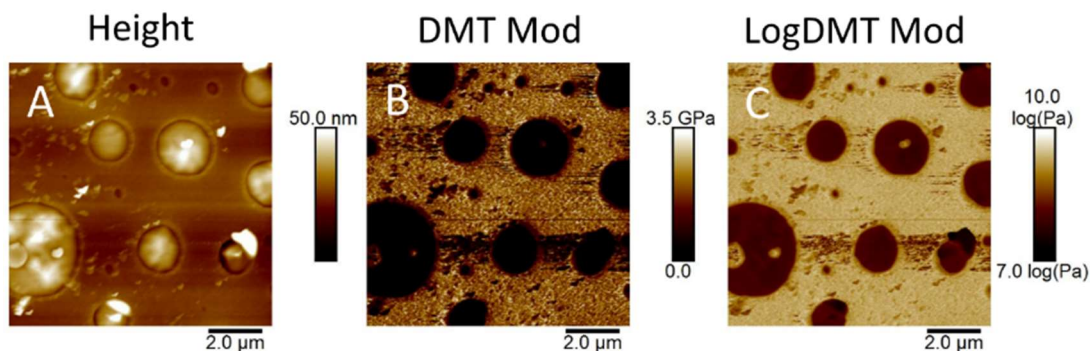


**Figure 5.3 QNM AFM images on a test sample with a mix of Polystyrene (PS) and Low Density Polyethylene (LDPE). The LDPE is the bulk surface and the PS is the circle within it. The modulus of the PS was 2.04GPa and the LDPE 87MPa.**

### 5.3.2 Test samples

First of all, QNM was tested against test samples of known modulus, once all of the calibration steps had been achieved (deflection sensitivity, spring constant, sync distance and Drive3 amplitude sensitivity). Figure 5.3 shows a PFT tapping height image with a QNM DMT modulus image and a logDMT modulus image (log modulus is used because the values can vary over up to 4 decades with a single probe, 1 MPa to 10 GPa) . This is for a calibration test sample of polystyrene blended with low density polyethylene (PS-LDPE). This sample of known modulus values enables checking and refining of the calibration (calibrated modulus values for PS-LDPE provided by Bruker). Due to the potential damage to the tip from imaging the sharp sample needed to measure tip radius, it was decided that this step would be skipped. A sharp sample can break tips and change all the calibration. Instead the test sample of known modulus is used for a relative calibration. The tip radius can now be altered manually on the software while imaging the sample of known modulus values, until the measured modulus values are correct.

### 5.3.3 Symmetric two phase bilayers

Next QNM was used to look at DPPC/14:1PC/Chol  $L_o$ - $L_d$  bilayers. Figure 5.4 shows how the  $L_o$  and  $L_d$  phases can be distinguished based on physical properties as well as height. The trends in the channels are as expected. The modulus is higher on the stiffer and more tightly packed  $L_o$  phase (101 MPa) and less on the softer  $L_d$  phase (75.1 MPa). These modulus values are within



the expected 10s of MPa regime.<sup>84</sup> The deformation is much higher on the softer  $L_d$  phase than the stiffer  $L_o$  phase.

PeakForce Tapping also allows fine control of the force exerted on the bilayer by the AFM tip, a parameter that cannot be controlled directly in TM-AFM. By systematically increasing the force on the bilayer, the bilayer phases can be compressed. The less dense and less rigid  $L_d$  phase compresses more than the  $L_o$  phase and thus an increase in force (0.25-1.5nN) manifests itself as an increase in height mismatch between the two phases (1.24-1.66 nm, 33.9% increase). This increase in height mismatch is shown in Figure 5.5.

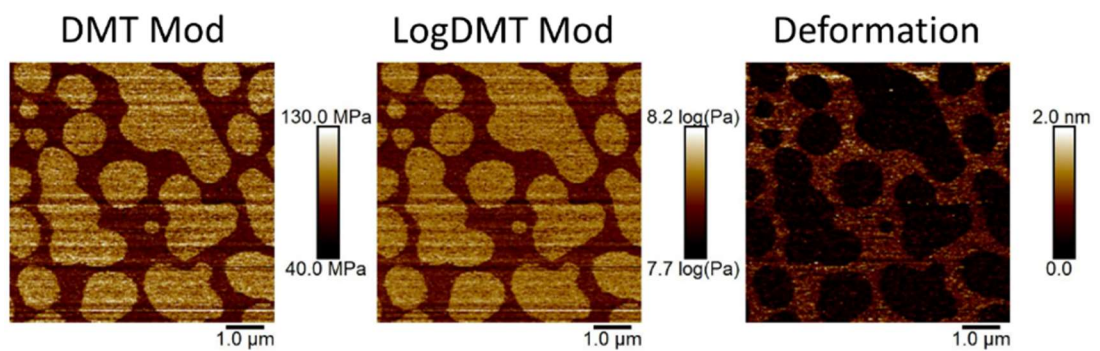


**Figure 5.4 QNM images of two-phase DPPC/14:1PC/Chol bilayers**

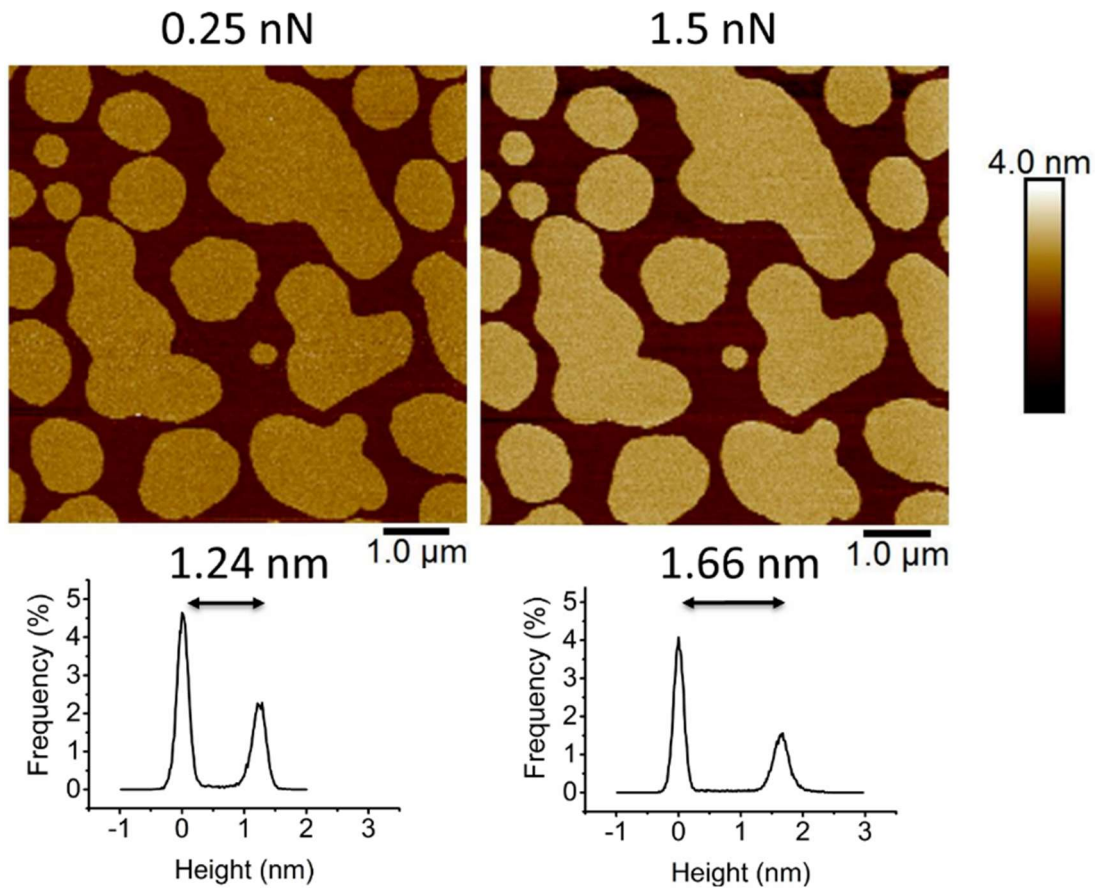


**Figure 5.5 Increasing imaging force increases Hydrophobic Mismatch. Peak Force Tapping Imaging of a DPPC/14:1PC/Chol bilayer at two forces, with histograms of heights in the images. An increased imaging force increases the height mismatch between the  $L_o$  and the  $L_d$  phases.**

### 5.3.4 Anti-Registered 3 phase bilayers

Next QNM was used to image three phase AR bilayers. This was in an attempt to isolate the different leaflets, and try to distinguish whether the intermediate

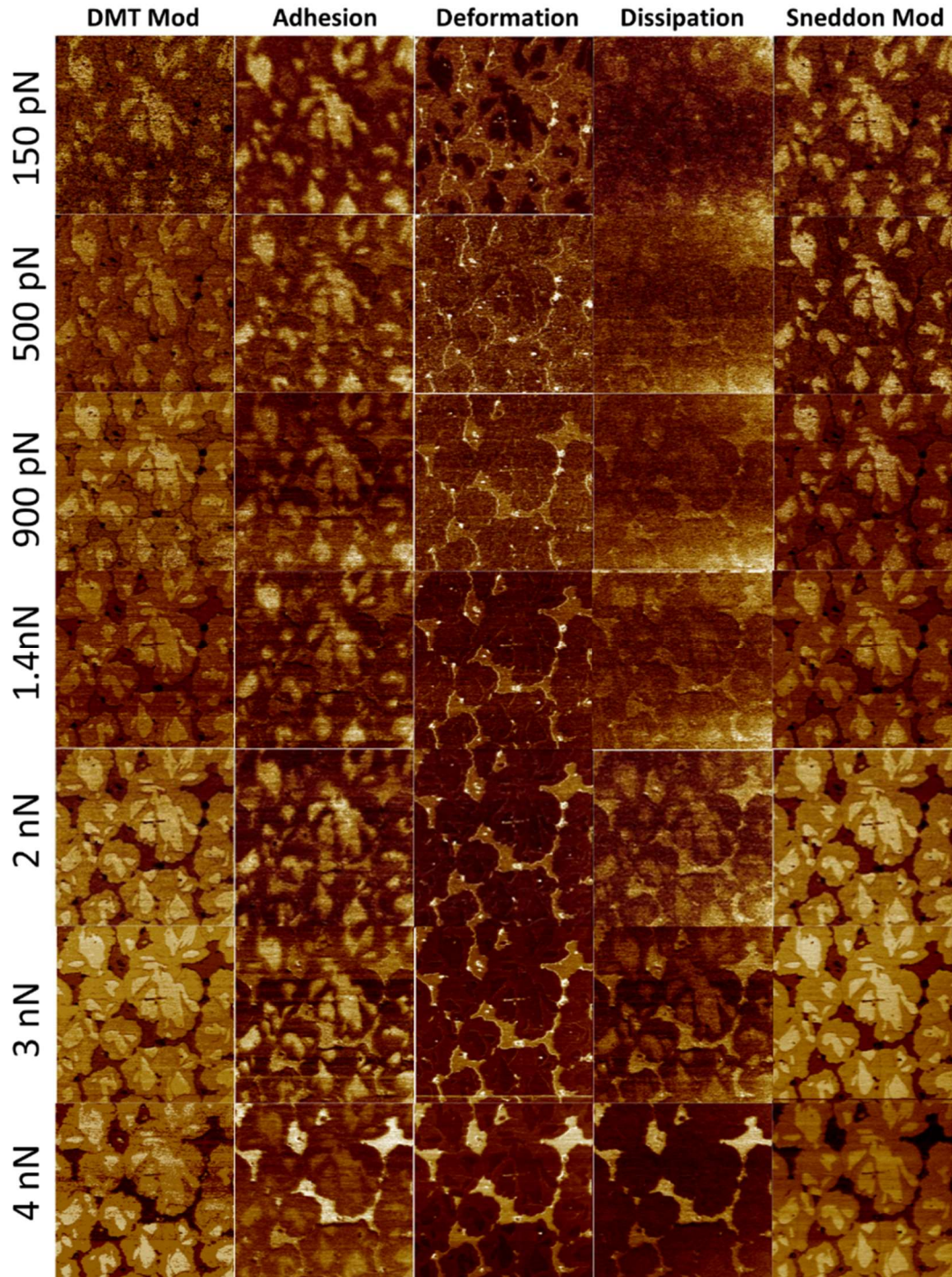
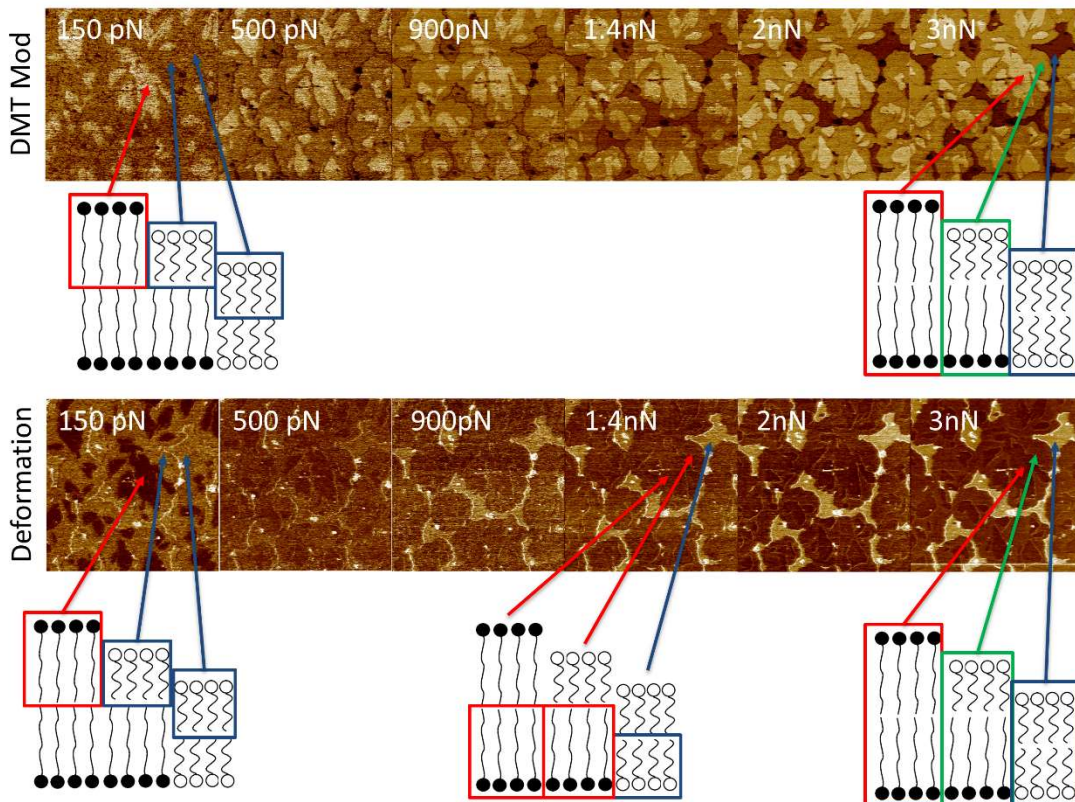


Figure 5.6 QNM channels with increasing force on a three Phase 22:0PC/14:1PC/Chol bilayer. DMT modulus, Adhesion, Deformation, Dissipation and Sneddon Modulus images are shown as force is increased from 150-pn-4nN. Details on the fits to obtain physical porperties are included in Figure 5.2.



AR height is  $L_{\beta}$  up or  $L_d$  up. Figure 5.6 shows a scheme of QNM modulus channels as the imaging force is increased. It should be noted that although every effort was made to calibrate and obtain quantitative values, some of the interpretations in this section rely on relative values between different phases, as can be observed from the images. Absolute values are given when it is helpful for clarity.

At low force the DMT modulus channel shows only two modulus values (for example 13.4 MPa and 16.0 MPa at 150 pN), even though there are three bilayer heights (Figure 5.6). Then as force is increased, three clear modulus values are seen for the 3 different heights (for example 14.5 MPa, 15.5 MPa and 16 MPa at 3 nN). This is shown again in Figure 5.7, but with the Z scales corrected so the relative values (colours) between images match. The Sneddon model should not provide a good model for bilayers as the deformation on bilayers should not be high enough for the contact area to become conical.<sup>87</sup> Despite this however, the trends in Sneddon modulus



**Figure 5.7 QNM DMT modulus and deformation with increasing force on a three phase 22:0PC/14:1PC/Chol bilayer. These are the same images as in Figure 5.6 with the Z scales corrected. Bilayer schematics are shown to indicate the interpreted bilayer phases and symmetries from DMT and deformation channels.**

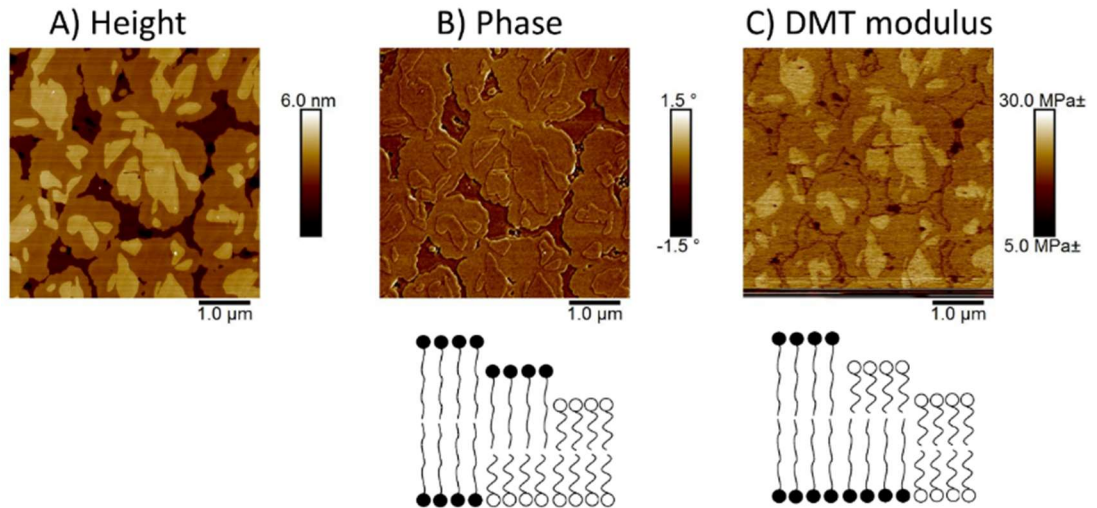


**Figure 5.8 Tapping Mode Height, Tapping Mode Phase and QNM of the same three phase AR 22:0PC/14:1PC/Chol bilayer area.**

match up with the DMT modulus trends as force is increased. The absolute values do not match to the DMT modulus (for example at 3 nN the Sneddon modulus values are 32.1 MPa, 36.1 MPa and 38.4 MPa), but in relative terms Sneddon modulus shows the same trends as DMT modulus with increased force. The fact that the intermediate AR height matches with the bottom R fluid-fluid height, in terms of modulus at low force, gives an insight to the top leaflet of the AR phase. At a low force, the tip is likely only lightly deforming the top leaflet of the bilayer. The force from the tip is dissipated within the upper leaflet of the viscoelastic bilayer, instead of being coupled through to the bottom leaflet. If this was not the case and the force was coupled through to the bottom leaflet, it would be expected that there would be three different modulus values from the beginning. As the force is increased, the force begins to be translated to the bottom leaflet too and the modulus value then starts to reflect the whole bilayer, resulting in three modulus values.

Initially at low force, deformation is much lower in the top phase, the R gel phase. This makes sense as this would be the stiffest phase. The intermediate AR state and the bottom R fluid state show the same deformation, matching to the modulus channel which also showed these two states matched at low force. At low force, if the tip is only lightly deforming the top leaflet it makes sense that the deformations would match, based on both the heights having the fluid phase in their top leaflet. Then as force increases, unusually the

deformation in the AR intermediate state begins to match to the lower height R fluid instead of upper height R gel. This could be explained if the fluid phases in the top leaflet have been significantly deformed that they stop deforming anymore and instead the bottom leaflet start to deform. The AR state has the opposite lipid phase in the bottom leaflet, so this would explain the switch in deformation. At even higher force, there are three different deformations observed indicating that both of the leaflets are being observed. The R gel phase now shows the lowest deformation, then the AR state and then the R fluid state shows the largest deformation. This is reiterated in Figure 5.9, which shows that the bottom height, the R fluid compresses the most (0.5 nm deformation between 200 and 4000 pN).

The modulus and deformation channels are consistent with the AR state being  $L_d$  fluid phase up. This is shown schematically in Figure 5.8 below the DMT modulus channel. The trends in the adhesion and dissipation channels are slightly more complicated to interpret with the R gel phase confusingly showing the highest adhesion at low force. Usually the fluid phase, in which the tip can penetrate more deeply and the contact area between the tip and the bilayers is larger, shows higher adhesion. The effect might have something to do with the contact between tip-water-bilayer at high frequency used (1 or 2 kHz), but the adhesion and dissipation channels are not analysed further here.

When tapping mode phase imaging was applied to the same bilayer area, the results were unexpected (Figure 5.8). Based on how the AR state was assigned orientation in Figure 5.1, the AR state would have the opposite orientation for the data shown in Figure 5.8 when examined by tapping mode phase imaging and by QNM. This throws into doubt the orientation AR state assignments made via phase lag imaging in Figure 5.1. Based on observations over multiple controlled force regimes consistent with the AR state being orientated  $L_d$  up, this is likely to be the correct orientation. As explained earlier, it is not possible to directly control imaging force in tapping mode, and it is even difficult to measure what the force is in controlled experiments designed for the purpose. Therefore, we do not know the force regime in which the tapping mode is interacting with the bilayer. As the TM phase image matches the QNM deformation and dissipation channel at quite

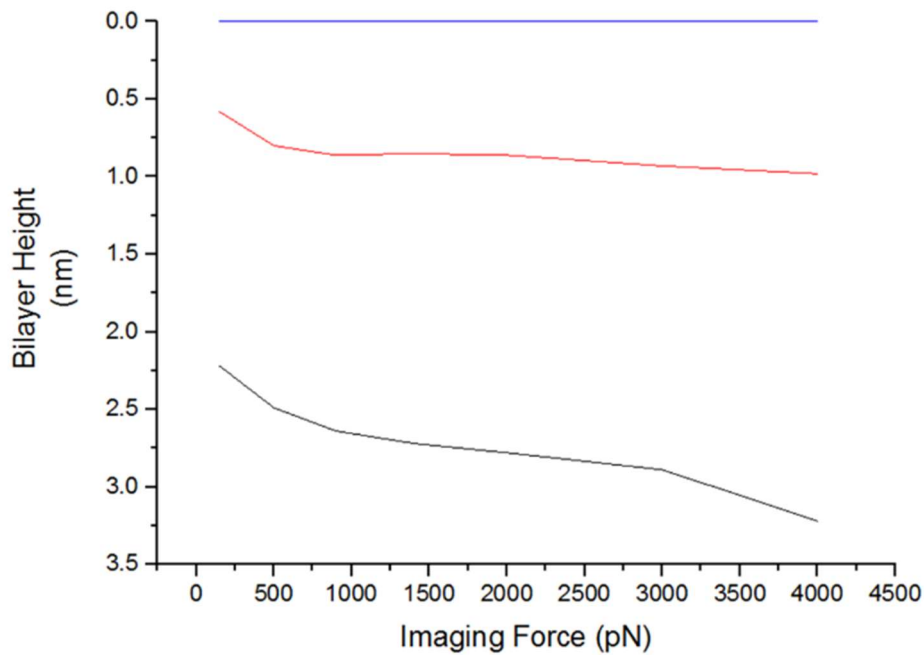


**Figure 5.9 Graph showing the change in height mismatch between the three phase AR heights for a 22:0PC/14:1PC/Chol bilayer with increasing force. Blue is top phase identified as registered Gel-Gel, Red is the intermediate phase identified as AR Gel-Fluid, and black is the bottom phase identified as registered Fluid-Fluid. The absolute heights were not known, so the top height was fixed to zero.**

high forces  $> 1$  nN, an explanation is that the tapping mode phase image is operating in the same imaging regime where the bottom leaflet is being shown more clearly. This shows that apparently clear phase contrast images can be highly misleading, despite their high resolution and ability to resolve fine differences in material property. It is still useful to see difference, but what that difference is must be measured by other means.

### 5.3.5 Summary

QNM was successfully used to image phase separated bilayers with physical property values. A significant amount of time was spent ensuring that the calibration procedures were correct. Applied to two phase symmetric  $L_o$ - $L_d$  bilayers, the phases can clearly be distinguished based on modulus, and also the height mismatch can be increased by increasing the force and compressing the  $L_d$  phase more than the  $L_o$ . When applied to asymmetric AR states, the QNM modulus and deformation channels provide evidence that

the AR state is orientated with the  $L_d$  phase up in the example shown. This is based on the modulus and deformation matching to the R fluid-fluid phase at low force. The tapping mode phase imaging suggests the opposite orientation for the AR state. It is suspected that the tapping mode image, where force cannot be as precisely controlled or known, is compressing the bilayer more than at low force with PFT, and thus bringing in contributions from the bottom leaflet.

In relation to the mean-field free energy model of Williamson et al. we can begin to consider key outstanding questions from their work.<sup>14</sup> One of these questions relates to whether the substrate for SLBs will break symmetry and favour one AR orientation, or whether both orientations will be equally likely. From the QNM data shown, the orientation of the AR state is  $L_d$  in the top leaflet (Figure 5.7). However, based on tapping mode phase imaging, the data suggests that the orientation could be either way around (Figure 5.8). As already discussed, the phase contrasts in tapping mode can be misleading as it is not possible to directly control imaging force. Based on the TM phase images matching to the QNM deformation and dissipation channels at higher forces ( $> 1$  nN), it is likely that the TM phase imaging is operating in the same regime where the bottom leaflet is more clearly observed. QNM with controlled force over multiple force regimes gives data consistent with the AR state being orientated  $L_d$  up, and this is likely the correct orientation. The TM phase data does however suggest that both orientations of AR are possible. The limited data indicate that the substrate prefers the  $L_\beta$  phase in the lower leaflet and  $L_d$  in the top leaflet, however more repeat QNM data is needed. This would show whether the same AR orientation is observed across a whole sample stub, across repeated samples, and across different compositions.

One important question which arises, is how the orientation of AR bilayers may link to possible AR in vivo. The paragraph preceding this one discussed the potential symmetry breaking of the bilayer by a substrate and the potential preference for one AR orientation over the other. Is this biologically relevant, as the bilayer does not sit on a mica substrate? What would be the orientation of AR domains in free-floating systems? Would AR states be stable long enough to even observe in free-floating systems? These are all



questions which need answering if the findings of this thesis can be linked to the plasma membrane. Interestingly, the plasma membrane is not like a free-floating vesicle but sit between the cytoskeleton and extracellular matrix polymer networks. Therefore the properties of lipid bilayers on substrates may be a more accurate model of the plasma membrane than free-floating systems. This idea is discussed further in Chapter 7 and Chapter 8, where the effects of different substrates on domains formation is investigated.

## **Chapter 6. Attempting to form Anti-Registered Bilayers in Shorter Chain Mixtures**

### **6.1 Introduction**

Since it has been established that bilayer anti-registration will spontaneously occur once the hydrophobic mismatch reaches between 6 and 8 carbons in adjacent phases in each leaflet (so an energy cost arising from approximately 12-16 carbons in the two leaflets of a R bilayer), experiments were attempted to establish a more refined basis for the limit of AR in terms of kinetics and possible regions of metastability. The strategy developed was to increase the probability of an AR state forming in lower height mismatch systems.

AR should be most favoured when the energy cost of the hydrophobic mismatch between phases is maximised. As this cost is proportional to the length of domain boundaries, the solution is to design a phase structure with the largest domain perimeter length. This can be achieved in two ways. Firstly, a phase structure containing 50% of each phase by area will maximise the domain perimeter, all else being equal. This can easily be justified by reference to a typical ternary phase diagram (Figure 1.5) where composition close to a phase boundary will have very small isolated domains of one phase in a majority of the other. Hence the optimal composition will be equidistant between the end-points of the tie-lines in the two phase coexistence region.

A perfectly 50:50 mixture favouring AR should mean that it is possible for the whole of a bilayer to be AR. If however the majority of the bilayer and thus the two leaflets is one of the two phases, the majority of the bilayer is forced into registration. This is better explained by observing Figure 6.2, which shows that if 20% of the bilayer is phase 1 and 80% is phase 2, then only 40% of the bilayer can possibly anti-register. The interleaflet coupling forces favouring R occur across the bilayer midplane and are therefore proportional to domain area. The energy penalty for hydrophobic mismatch between domains increases with the perimeter of the domains.

Secondly the phase structure is governed by the route taken through the phase diagram as it develops. If, upon cooling from the single phase melt it passes through the demixing transition close to a critical point, the hydrophobic mismatch at that point is at a minimum (by definition), hence the energy penalty for domain boundary is also minimised, resulting directly in a low line tension. This results in the entire phase structure emerging instantaneously from the melt with a very long and convoluted boundary, with interdigitating fingers of phase. This process is termed spinodal decomposition (Figure 1.6), large in extent but small in energy terms, and is the type of structure required to maximise the energy penalty driving AR. Cooling away from the critical region into a region termed the bimodal results in nucleation and growth mechanisms of phase separation where the large extent of phase mismatch leads to an immediately high energy cost for phase nucleation, and subsequent minimisation of phase boundary by subsequent growth of isolated circular domains.

One caveat to the above design rules is that if the composition remains too close to the critical point at the final temperature, the hydrophobic mismatch will remain small. The composition must be sufficiently below the critical point (i.e. 10 °C) to make sure the ordered and disordered phases are eventually sufficiently different and have a large hydrophobic mismatch, whilst still retaining the spinodal structure locked in during cooling.

The same mean-field free energy model that predicted increased hydrophobic mismatch would cause AR, also predicts that these AR states may be formed preferentially by temperature quenching the bilayers. This results in the formation of smaller domains, with larger perimeter to area ratios. This results in a larger energy penalty for R, and AR is favoured.

This section details attempts to form close to critical 50:50 compositions and use temperature controlled AFM to heat them above  $T_m$  into a single phase, and then quench down through a critical point.

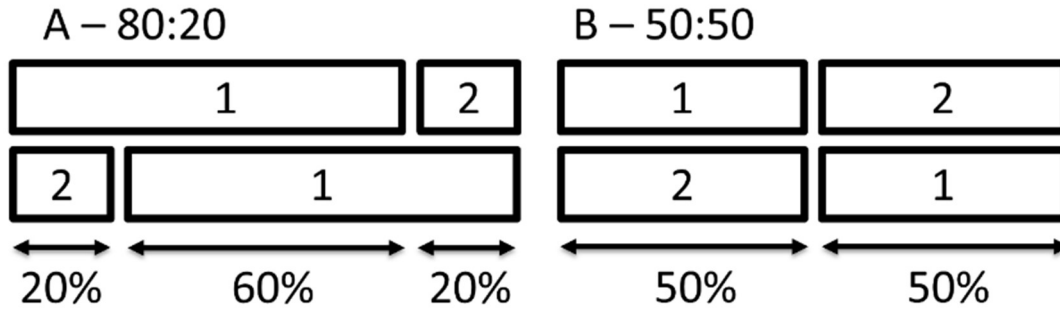


Figure 6.2 Schematic showing the maximum possible anti-registration (AR) bilayer area for two different bilayers of different compositions of Phase 1 and Phase 2. Bilayer A has a 80:20 ratio of Phase 1:2 and has a maximum possible AR area of 40%, 60% is forced into registration (R). Bilayer B has a 50:50 ratio of Phase 1:2 and has a possible AR area of 100%, none of the bilayer area is forced into registration.

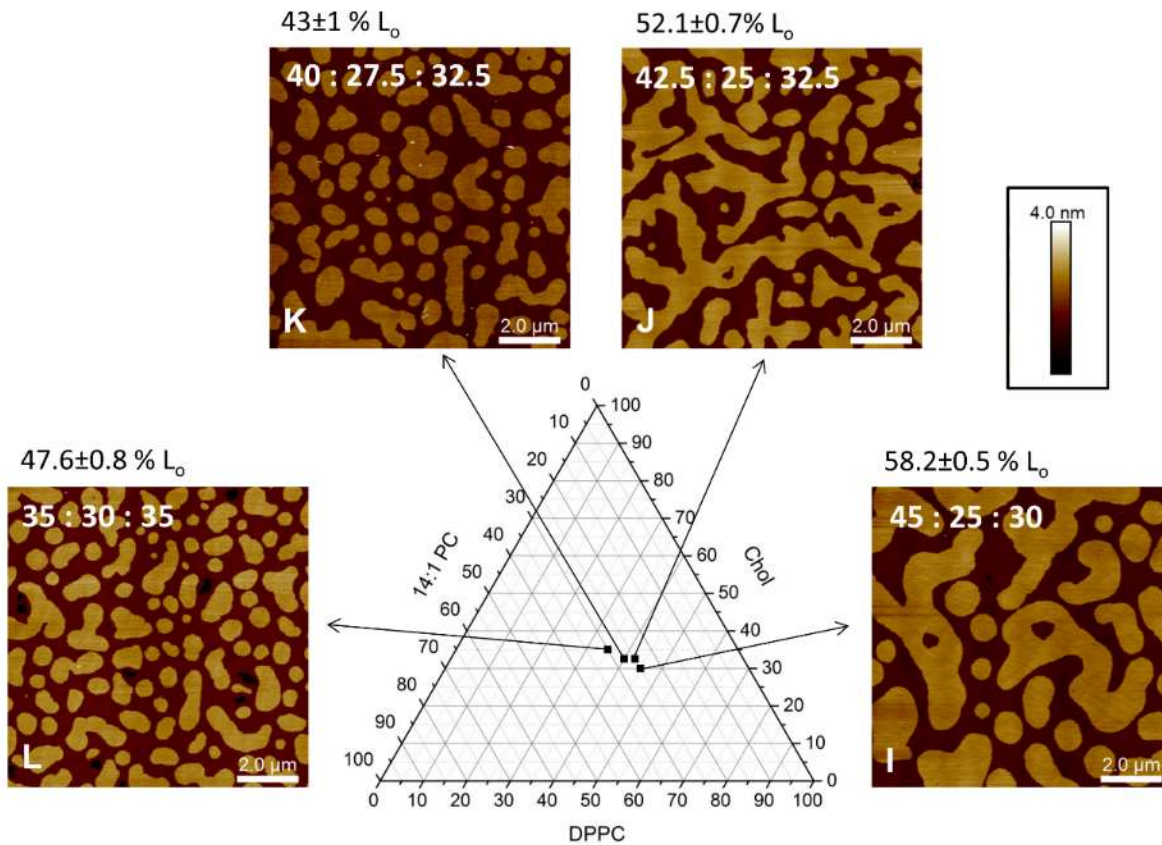


Figure 6.1. DPPC/14:1PC/Chol Ternary Phase Diagram with AFM Images.

Images are representative examples from repeat images. The DPPC/14:1PC/Chol compositions are shown as percentage ratios at the top of each image. Percentage  $L_o$  areas are shown above each image and are averages with standard errors taken from at least three different areas across two different repeat stubs from the same hydrated mixture. L) N=3 I) N=4 J) N=5, K) N=15. Sample L is the same composition as sample G in Figure 4.2.

## 6.2 Critical Compositions in DPPC/14:1PC/Chol

Using the percentage  $L_o$  area fractions and morphologies from Figure 4.2, a second set of compositions were formed deep in the two phase coexistence region that will pass as close as possible to the critical point during cooling, and hence spinodally decompose. All of the compositions show two heights consistent with R, and are close to 50:50  $L_o:L_d$  area fraction. Compositions J and I show convoluted domain boundaries formed via spinodal decomposition, whereas the domains in K and L are a little more characteristic of nucleated domains. This suggests that the critical line in the ternary phase diagram that maps out the critical composition at each temperature follows a line that intercepts close to composition I and J. Compositions K and L lie to the left of the critical line closer to the  $L_d$  phase boundary and thus have  $L_o$  domains nucleated in a majority  $L_d$  phase.

## 6.3 Differential Scanning Calorimetry of DPPC/14:1PC/Chol

DSC was used as a complimentary method to AFM to attempt to map out the phase boundaries of the ternary lipid systems used. DSC of MLVs is in theory faster than forming and imaging SLBs, but more importantly gives the  $T_m$  of mixtures. This is complimentary to the information gained from AFM images on phase behaviour. AFM can be used with temperature to obtain  $T_m$  values,<sup>19</sup> although it is non-trivial as detailed in Section 6.4 of this thesis. Also, AFM temperature measurements are complicated by water evaporation at higher temperatures. DPPC has a  $T_m$  of 41 °C so evaporation is not a big issue, but for higher hydrophobic mismatch systems with longer saturated lipid chains, the  $T_m$  values are higher (DSPC = 55 °C, 20:0PC = 66 °C, 22:0PC = 75 °C)<sup>108</sup> and evaporation is a bigger problem. Engaging AFM cantilevers on surfaces also becomes increasingly more difficult as temperature is increased due to the increased disturbance due to convection in the liquid surrounding the cantilever (detailed further in section 6.4). Therefore for the higher hydrophobic mismatch systems, DSC is a faster way to map out the phase boundaries with temperature. The DSC sample cells are pressurised so there is no evaporation. The phase behaviour of the higher hydrophobic mismatch systems is unknown, and more specifically it is not known how the phase

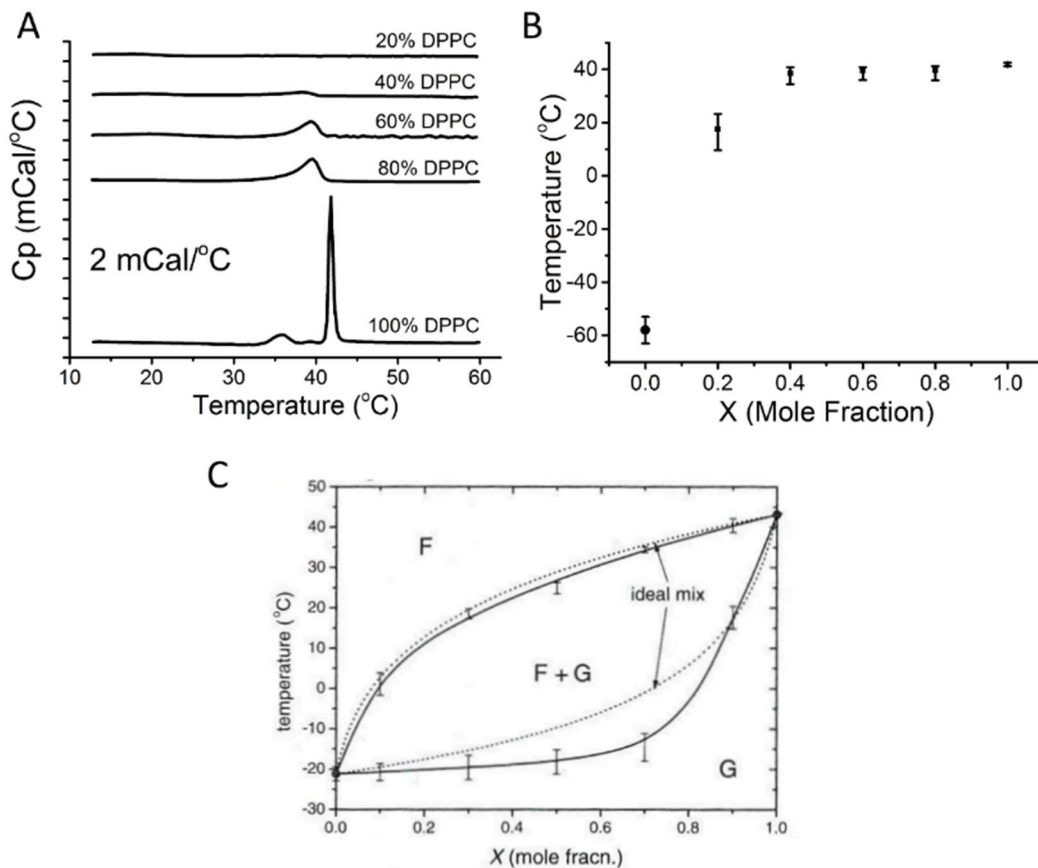


**Figure 6.3 DSC of DPPC/14:1PC Mixtures. A) DSC Thermograms, which are heat capacity (mcal/°C) plotted against temperature (°C), for Binary DPPC/14:1PC mixtures ranging from 100% DPPC to 20% DPPC, with the remaining percentage made up of 14:1PC. The thermograms for 40% and 20% are shown on expanded y axes in Figure 6.5 D and E. B) Calculated transition temperature ( $T_m$ ) from the peaks of the DPPC/14:1PC thermograms plotted against the mole fraction of DPPC,  $X = X_{DPPC} / (X_{DPPC} + X_{14:1PC})$ . The  $T_m$  of 14:1PC was estimated from known lipid values as detailed in Figure 6.4. Plotting temperature against mole fraction forms a binary temperature phase diagram for the DPPC/14:1PC mixture. C) Reference binary temperature phase diagram for DPPC/DOPC determined by X-ray diffraction, from reference<sup>110,111</sup>**

boundary between the two phase coexistence region and the single fluid phase region moves as the saturated lipid chain length is increased. Before attempting DSC on longer saturated lipid systems, DPPC/14:1PC/Chol was studied to test the technique and assess if it was capable of adequately mapping out phase boundaries.

### 6.3.1 DPPC/14:1PC Binary Mixtures

Before investigating mixtures in the ternary phase diagram, simpler binary DPPC/14:1PC mixtures were first measured. Figure 6.3A shows DSC thermograms for a set of binary DPPC/14:1PC bilayers, ranging from 100% to 20% DPPC. The pure DPPC thermogram shows a sharp endothermic peak at  $41.7 \pm 0.05$  °C, in agreement with its known  $T_m$  value, and the thermogram matches published DPPC DSC data.<sup>108,109</sup> The small peak at 35 °C corresponds to the pre-transition from the  $L_\beta$  phase to the ripple phase. The ripple phase is an intermediate state between the gel and liquid phases, containing parts of both phase to form periodic undulations.<sup>104</sup> As the percentage of 14:1PC in the mixtures is increased the  $T_m$  values drop in temperature, and the peaks become broader and weaker.

To obtain the most accurate transition temperature value and ranges, we extracted the peak ( $T_m$ ) and also the peak onset ( $T_{on}$ ) and offset ( $T_{off}$ ). This is shown in Figure 3.8. In this situation however  $T_{on}$  and  $T_{off}$  provide no real additional information for plotting phase diagrams (besides giving a range). In reality  $T_{on}$  and  $T_{off}$  are affected by the scanning rate. A faster scanning rate would give a broader peak and a slower scan a sharper peak, thus they are not directly related to the pure transition temperature (this is discussed further in section 7.6). The  $T_m$  values were plotted against mole fraction (1 = pure DPPC, 0 = pure 14:1PC) in Figure 6.3B. For 20% and 40% DPPC the peaks are not clear in Figure 6.3A, but they are shown on expanded Y axes in Figure 6.5 D and E.

There is no published value for the melting transition temperature of 14:1PC. DOPC (18:1PC) melts at between -17 °C and -20 °C, below the experimental range of the DSC used for this study.<sup>28,108,110,111</sup>  $T_m$  drops with decreasing lipid acyl chain length for saturated PC, PE and PS headgroup lipids, as shown in Figure 6.4B.<sup>108</sup> In Figure 6.4A the known values for PC lipids with single unsaturated bonds in each tail are plotted.<sup>108</sup> The trend in  $T_m$  is similar to the trends for the saturated lipids, but at lower temperatures. By extrapolating an estimated  $T_m$  for 14:1PC can be obtained. An exponential fit showed a similar trend, giving a  $T_m$  value of -58 °C. This value could not be measured using DSC, as the limit of the instrument used was 10 °C.

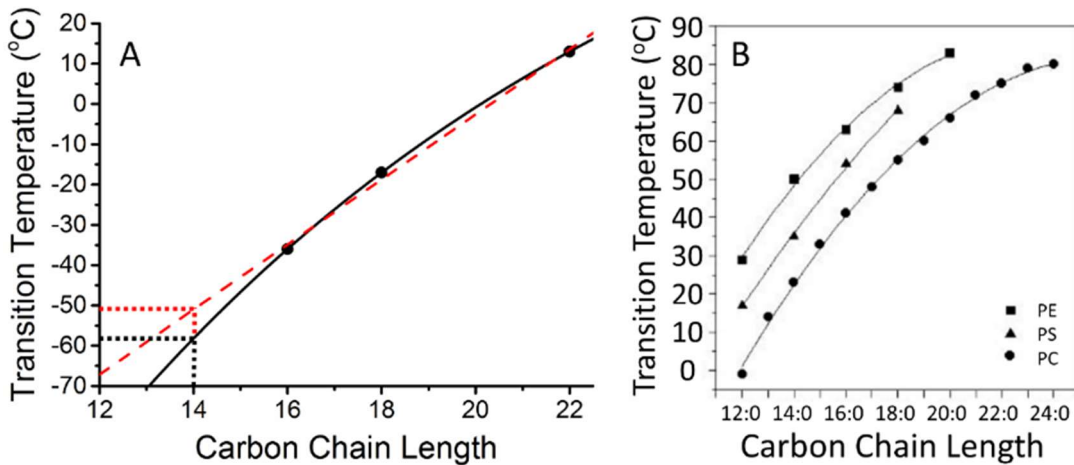


**Figure 6.4 Estimating the transition temperature ( $T_m$ ) of 14:1PC. A) Known  $T_m$  values for other PC lipids with single double bonds in both hydrocarbon tails, 16:1PC, 18:1PC (DOPC) and 22:1PC, were plotted against carbon chain length. Both an exponential fit and linear fit were used to estimate the  $T_m$  for 14:1PC, -58.2  $^{\circ}\text{C}$  and -51.0  $^{\circ}\text{C}$  respectively. Values were all for cis not trans double bonds and the double bond approximately half way down the hydrocarbon tail. B) Known  $T_m$  values for saturated PC, PS and PE lipids from reference<sup>108</sup>**

By fitting a line through the  $T_m$  values the phase boundary between the two-phase coexistence region and the single fluid phase region can be mapped, making Figure 6.3B a phase diagram. There are no DPPC/14:1PC systems in the literature but there are phase diagrams for DPPC/DOPC systems.<sup>28,110</sup> An example DPPC/DOPC phase diagram is shown in Figure 6.3C. The shape of the phase boundary for the DPPC/14:1PC system is similar to the DPPC/DOPC system, but the 14:1PC system drops down to a lower temperature. The top of the phase diagram is flatter, suggesting that 14:1PC does not reduce the miscibility transition of the mixture until it has a high concentration.

### 6.3.2 DPPC/14:1PC/Chol Ternary Mixtures

In the previous section, DSC was used to plot a binary phase diagram with temperature for DPPC/14:1PC, and found it to replicate the features of the published DPPC/DOPC binary phase diagram, but with lower  $T_m$  at high unsaturated lipid content. Next a wide range of mixtures including cholesterol were investigated from across the ternary phase diagram (DPPC/14:1PC/Chol). The obtained thermograms and position in the ternary phase diagram are shown in Figure 6.5. From the thermograms across the



ternary phase diagram, it is clear that as more 14:1PC and/or Cholesterol is added the signals become broader and weaker. For example at constant

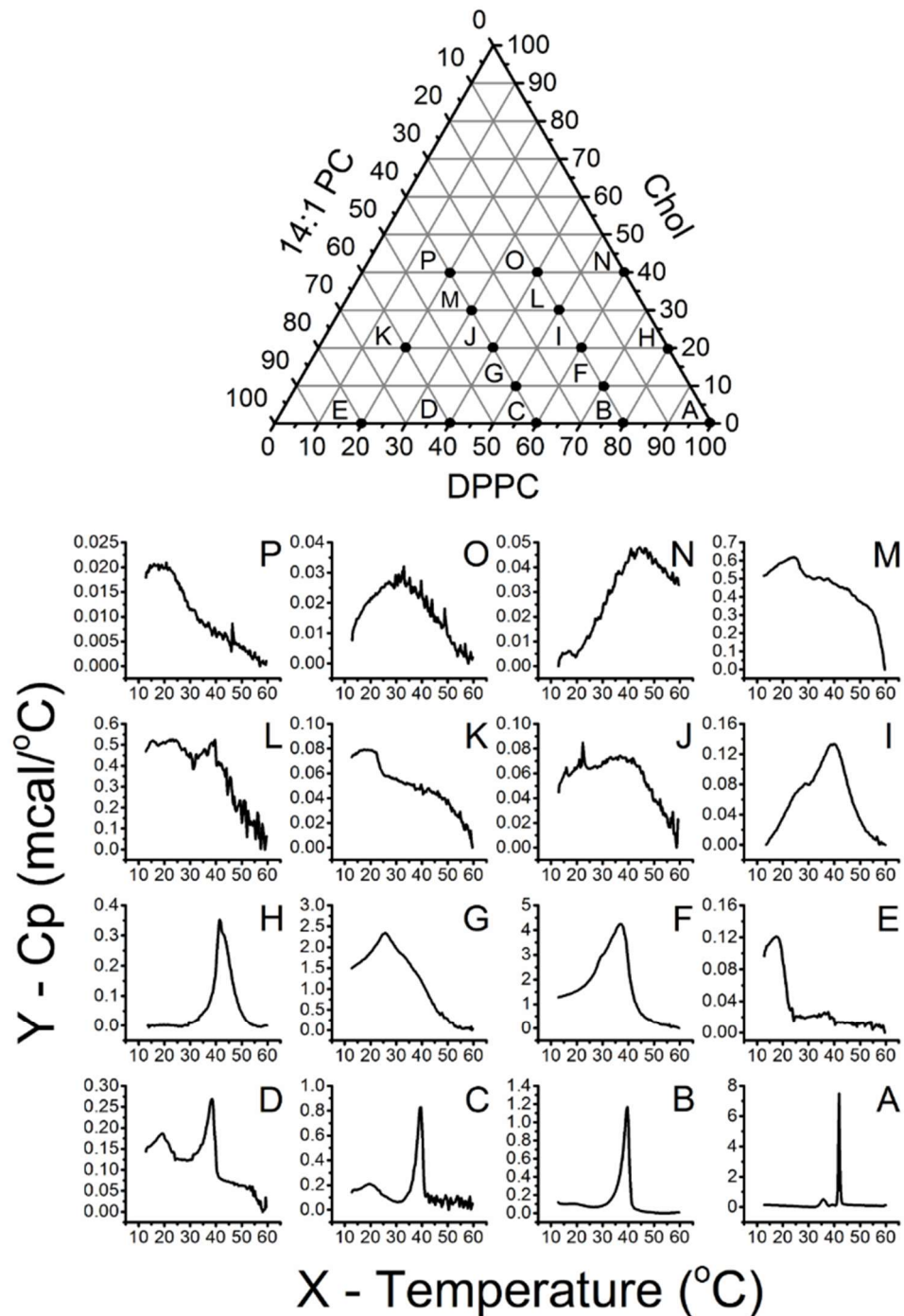


**Figure 6.5 DSC of DPPC/14:1PC/Chol mixtures. At the top is a ternary phase diagram for DPPC/14:1PC/Chol with the compositions of mixtures A-P plotted. Below the phase diagram are the thermograms, heat capacity (mcal/°C) plotted against temperature (°C), of mixtures A-P. The extracted  $T_m$  values from the thermogram peaks are as follows: A = 41.8 °C, B = 39.6 °C, C = 39.5 °C, D = 38.6 °C, E = 17.58 °C, F = 37.2 °C, G = 25.9 °C, H = 41.5 °C, I = 39.7 °C, J = 38 °C, K = 18 °C, L = 39 °C, M = 24 °C, N = 45 °C, O = 32 °C, P = 19 °C**

20mol% Chol as the percentage of 14:1PC is increased there is decrease in signal (Data points H-I-J-K). For the binary DPPC-Chol axis with no 14:1PC (right side of phase diagram) there is a decrease in signal as cholesterol is increased. This is shown in Figure 6.6A, where signals have had to be scaled up so that the signal can be seen. Once 14:1PC is taken out, the DSC on this axis can be compared directly with published data as DPPC-Chol systems are well studied.<sup>109,112</sup> At 20mol% and 40mol% Chol the peak shapes match strongly with both the literature phase diagrams in Figure 6.6B+C.<sup>109,112</sup> There appears to be a similar drop in signal as Chol is increased in the published phase diagrams, although a direct comparison is difficult as the exact heat capacity units and concentrations are not made clear in the publications.<sup>109,112</sup>

The signal of the transitions in the thermograms is proportional to the amount of ordered lipid phase present. For pure DPPC, which melts cooperatively over a narrow temperature range, the signal is high and sharp. As 14:1 PC is added, there is coexistence of gel and fluid so a smaller percentage of the membrane is ordered and thus there is a smaller signal. In addition, the

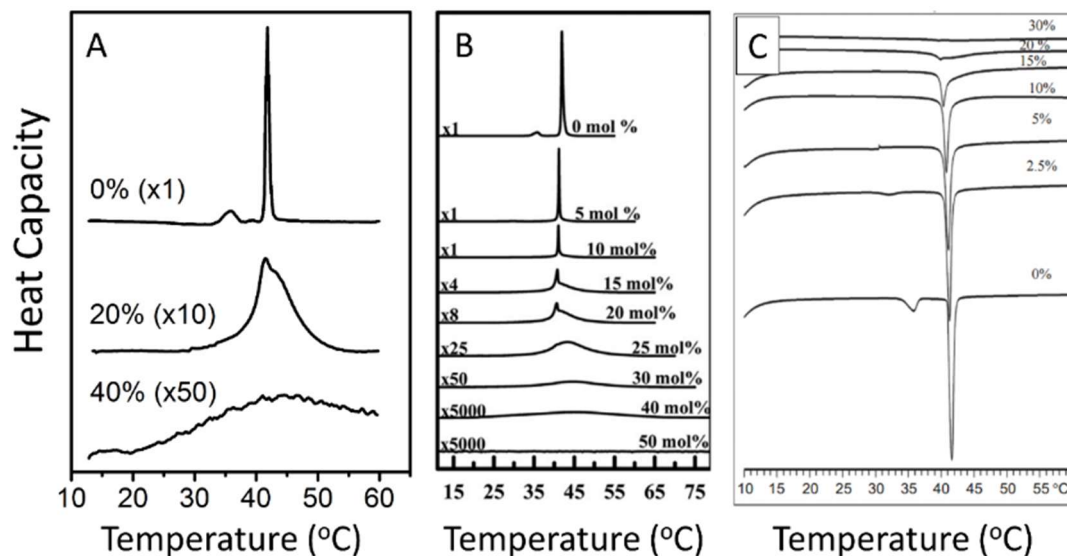


**Figure 6.6 DSC of the binary DPPC/Chol axes. A) Thermograms A, H and N from Figure 6.5 shown with the percentage of cholesterol in the mixture, the remaining percentage being DPPC. The plots have been magnified by a set factor to make the shape visible. B<sup>112</sup> and C<sup>109</sup> are published DSC data examples of the DPPC/Chol axes. All 3 graphs have the separate thermograms offset on the y axis so they can all be seen, B) and C) has also magnified lower signal data to make it visible. The y axis on all graphs is heat capacity, for A it is in mcal/°C, but for B and C the exact units are not made clear in the respective publications.**

change in quantity of the ordered phase is a function of the movement of the phase boundaries with temperature, hence the ordered phase will only gradually separate upon cooling. Cholesterol also has the effect of fluidising solid phases (hence removing co-operative melting) and of decreasing order in saturated lipids. Furthermore, within the region where two liquid phases co-exist, increasing cholesterol leads to an  $L_d$  and  $L_o$  phase that are more similar in character, with a less ordered  $L_o$  phase and more ordered  $L_d$  phase, together meaning there is a much smaller enthalpic change to be measured. The outcome of all the effects of cholesterol is an  $L_o$ - $L_d$  coexistence region with extremely small enthalpy changes, and low signals in DSC. Samples F,G,L and M were made up at a concentration of 10mg/mL instead of the 1mg/mL of every other sample in order to increase signal (the letter ordering is based on composition and position on the phase diagram, but these four samples were measured after the rest of the samples). The signal increased by roughly a factor of 10 but the peaks are still broad and indistinct.

Assigning  $T_m$  values is now more difficult, due to the broad weak peaks and also the unusual shapes. A literature search revealed no papers on ternary lipid systems using DSC, despite there being many on single and binary lipid systems, and the results obtained here likely explain why there has been nothing published.

Thermograms F and I both show a hump on the transition peak. One possible explanation for this hump on the peak is the presence of the ripple phase, as observed in pure DPPC.<sup>103</sup> The broadening of the two peaks results in the ripple phase appearing as a hump in the larger peak. Another unlikely explanation is that these compositions are within the three-phase region of the phase diagram.<sup>44</sup> Figure 1.5 (Introduction) shows an example DPPC/DOPC/Chol ternary phase diagram, with a small triangular three-phase region where the  $L_o$ ,  $L_d$  and  $L_\beta$  phases all coexist. A similar region may exist in the DPPC/14:1PC/Chol phase diagram and the two peaks represent the melting of both the  $L_\beta$  and the  $L_o$  phases. Both explanations are possible but for the assignment of  $T_m$  the main peak will be used.

When these experiments were planned, it was thought that absence of a transition would indicate compositions where there was no phase separation

at room temperature i.e. the  $T_m$  was below room temperature. In reality, with such weak signals, it is not easy to distinguish whether mixtures might be an uneven baseline or a transition. That being said, each thermogram does show a peak, but some with ranges seemingly over the whole temperature range studied (10-60 °C). A longer temperature range may elucidate this and show a whole transition.

Despite the broad weak signals and the difficulties in assigning peaks, the assigned  $T_m$  values allowed a temperature contour map on a ternary phase diagram to be plotted (Figure 6.7A). The trends in  $T_m$  match remarkably well with similar DPPC/DOPC/Chol systems mapped using fluorescence microscopy of GUVs (Figure 6.7B).<sup>21</sup> The  $T_m$  values recede across the phase diagram towards the top left, dropping to slightly lower values than the DOPC phase diagram due to 14:1PC's lower individual  $T_m$ .

### 6.3.3 DSC Conclusions

The trends in  $T_m$  across the ternary phase diagram of DPPC/14:1PC/Chol were successfully plotted from DSC data, despite the individual thermograms showing weak and broad signals and not being simple to interpret. The plotted  $T_m$  values matched well with a similar published system mapped using

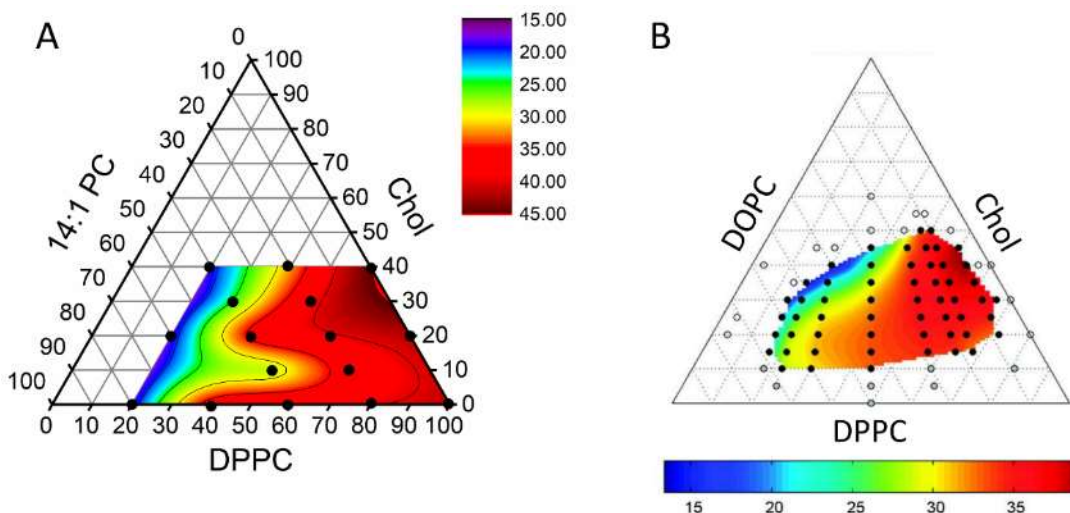


**Figure 6.7 Ternary phase Diagrams with transition temperature colour contour plots. A) DPPC/14:1PC/Chol phase diagram with  $T_m$  values from the thermograms in Figure 6.5, plotted on a false colour plot with the scale shown to the top right of the phase diagram. B) Literature<sup>6</sup> DPPC/DOPC/Chol phase diagram with transition temperatures plotted on a false colour scale (shown below phase diagram). This data was obtained using fluorescence microscopy experiments of GUVs**

fluorescence.<sup>6</sup> It is clear that the lack of reports of ternary phase diagrams mapped by DSC can be explained by the weak signal and difficulty in interpreting the data.

The obtained data is for the DPPC system, where the phase diagram has already been partially revealed using AFM, and the system is not too dissimilar from the well-studied DPPC/DOPC/Chol system. The intention of this work was to use DSC to map out the phase diagrams of the higher hydrophobic mismatch systems with longer saturated lipids. This information would be interesting in itself as it is not known how phase boundaries move as the length of the saturated lipid of a ternary mixture is increased.

Overall it was decided that this DSC project would not be continued. Initially it was thought that the DSC would be a quicker method to map out phase diagrams compared to AFM, but it actually took a similar amount of time. Despite the  $T_m$  ternary phase diagram matching closely with literature, this relied on several ambiguous interpretations of  $T_m$  from thermograms. To accurately map the phase boundaries, an even larger range of compositions would need to be mapped, and areas of the two phase coexistence region containing a low quantity of ordered phase, and regions of high cholesterol around the critical point, would all have vanishingly small signals. Initially it was thought the critical point could be potentially important for forcing AR in bilayers, but experiments that were being run simultaneously to this DSC work provided AR without the need for near critical mixtures as detailed in Chapter 4. This meant that it was not so vital to map out the phase diagrams of the higher hydrophobic mismatch systems, and time was put into other aspects of the project.



## 6.4 AFM with Temperature

To be able to perform temperature quenches on critical bilayers, bilayers must first be heated then cooled controllably, all whilst AFM imaging. Different equipment and methods that were tested for this are detailed in this section. By increasing the temperature of bilayers while AFM imaging, the transition temperature ( $T_m$ ) can be determined by observing the phases mixing to a single phase.<sup>19</sup> As was shown earlier with DSC, ternary mixtures give weak and broad signals and so it is hard to determine  $T_m$ . AFM with controlled temperature may provide more accurate  $T_m$  values for ternary mixtures and provide quantitative data for tie-line determination and hence boundary

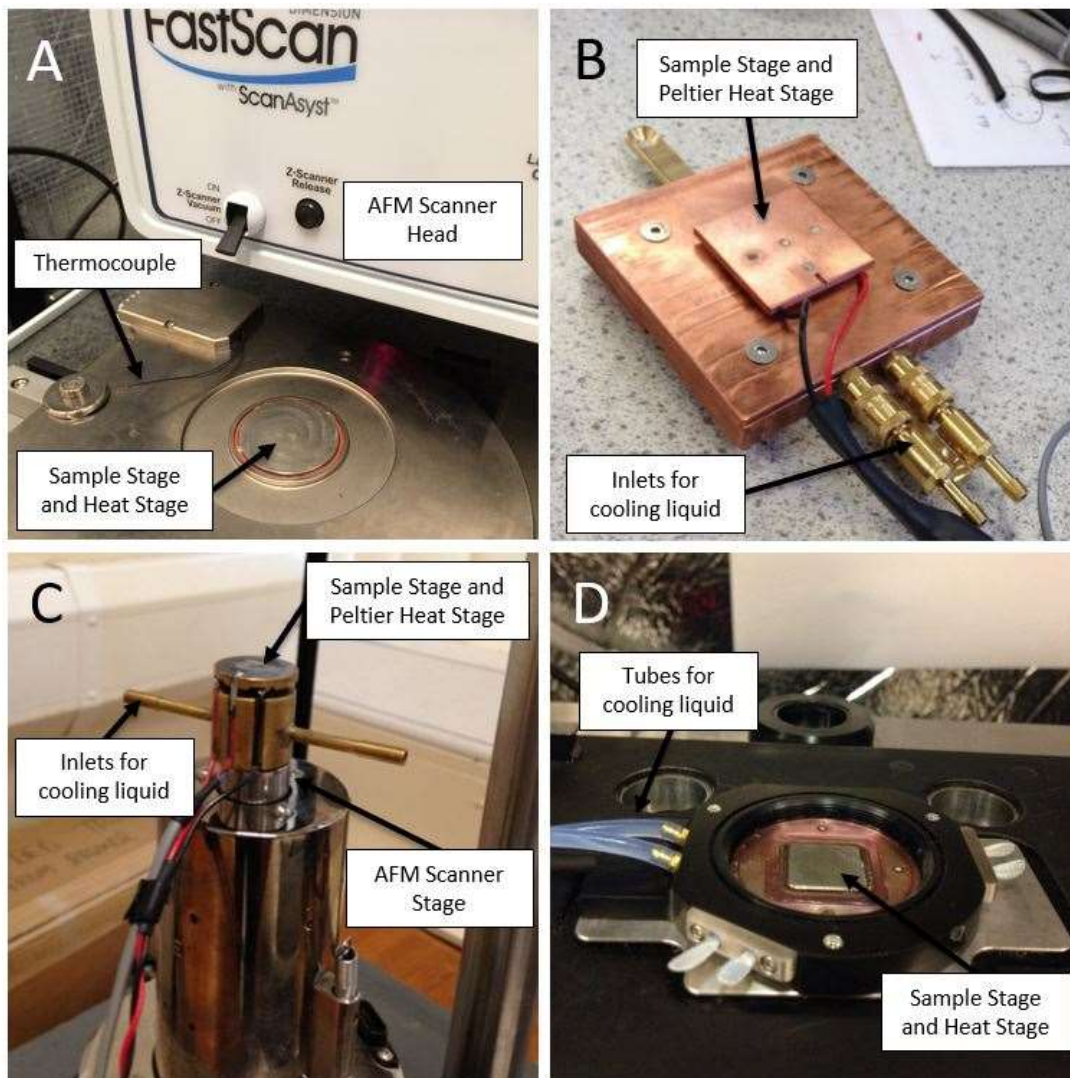


**Figure 6.8 Images of AFM temperature stages. A) Bruker Fastscan Built-in Temperature Stage B) Home built Peltier Heater/Cooler for Bruker Fastscan C) Home built Peltier Heater/Cooler for Bruker Multimode D) Asylum MFP3D heat stage.**

compositions. There were many experimental issues which meant that it was difficult to image bilayers at increased temperatures and not possible to perform controlled quenches on critical bilayers and image using AFM. This section demonstrates the different methods and equipment that were used to attempt controlled temperature ramps and quenches, along with experimental issues and demonstrations of how far each method was progressed.

#### **6.4.1 Bruker Fastscan Built-in Temperature Stage**

The first AFM temperature stage used was a built-in stage for the Bruker Fastscan AFM (Figure 6.8A). It consisted of a heating stage which sits below the sample and a temperature controller that can feedback on either the temperature of the stage or of a thermocouple temperature probe which can be placed in/on the sample. The temperature probe was large and bulky which made it difficult to use in fluid as it often made the small volume of water used in bilayer experiments spill from the mica stub, destroying the bilayer sample. Therefore temperature was controlled by feeding back on the temperature below the stage, and the temperature of the bilayer was measured using a separate thin thermocouple which was not part of the heating system and did not cause the water to spill. There is a difference in temperature between the stage and the bilayer sample, due to the loss of heat through the steel stub and mica and the setting up of a thermal gradient. Hence the need for a separate temperature probe to accurately measure the bilayer sample temperature.

The Fastscan AFM has very sensitive crash protection software, designed to stop the tip crashing into the sample surface. When the cantilever deflection is too high or fluctuating too much, the AFM will not engage the tip on the sample and instead return a 'Crash protection' error message. Temperature fluctuations from the heater in liquid cause cantilever noise, leading to a false detection of imminent tip crash and a Crash Protection Error message. This made it hard to use the temperature controller as the AFM would rarely engage. Also when the temperature stage was on, the laser would often drift and become misaligned on the cantilever. On the advice of AFM Application Specialists at Bruker, the parameters 'Tapping Mode Engage Gain' and 'Sample Clearance' were altered to reduce the sensitivity of the crash

protection. Sample Clearance is the distance the AFM retracts the tip from the surface after engaging, and lowering this means that the tip is closer to the surface and has less distance to move in which it can be made to fluctuate due to a thermal current. Tapping Mode Engage Gain is the feedback gain on the cantilever deflection before the tip engages, and lowering this means that the system responds more slowly to changes in cantilever deflection due to thermal currents. Altering these parameters enabled slightly easier engaging without crash protection but it still often took numerous attempts and failed engages before the tip would engage on the bilayer surface, or did not engage at all. The crash protection is more sensitive in fluid than in air, in air the AFM will engage more easily with the heater on. This is likely due to thermal currents in the volume of liquid between the heater and the cantilever, with the system not reaching equilibrium.

Despite the experimental issues with imaging while heating, it was possible to image if parameters were optimised and engaging was repeated several times until the tip engaged. Figure 6.9 shows an example of a phase separated DPPC/14:1PC/Chol bilayer heated up using the Fastscan built-in temperature stage. As Area 1 is heated up there is a gradual and small change in domain

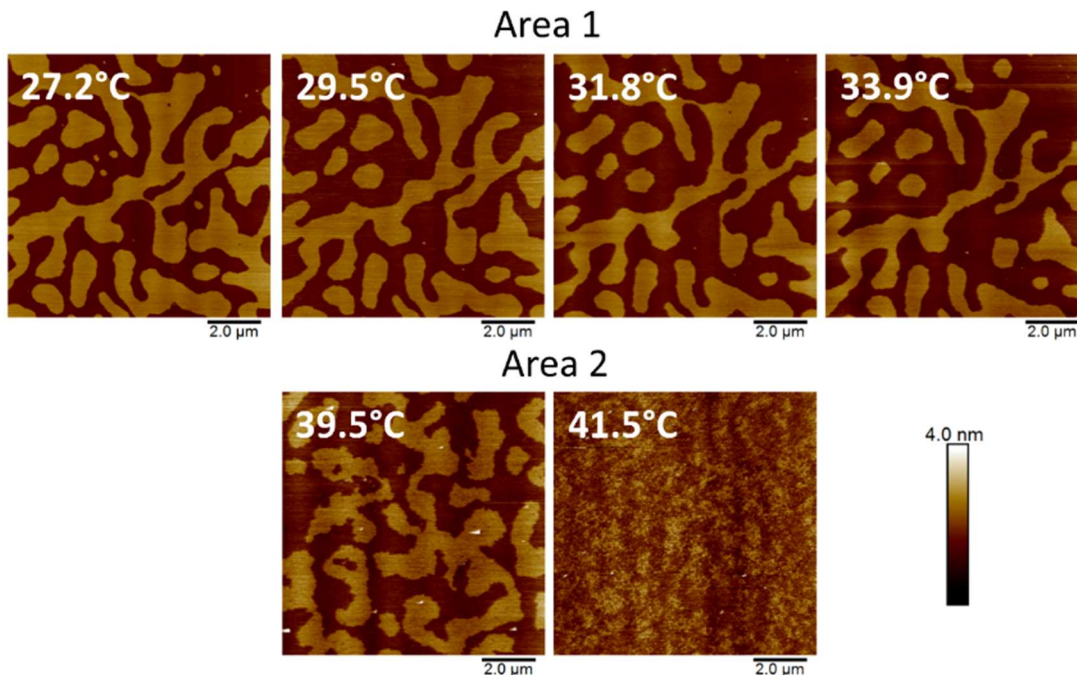


**Figure 6.9 AFM with Controlled temperature on a DPPC/14:1PC/Chol (42.5:25:32.5) bilayer using the built in heat stage on the Bruker Dimension Fastscan AFM.**



size, but the morphology stays very similar. As Area 2 is heated the bilayer passes through its  $T_m$  and is transitioning from a 2-phase to 1-phase region. In this particular example, the bilayer crosses the  $T_m$  close to the critical point where the difference between the  $L_o$  and  $L_d$  phase is very small, leading to the domains breaking down into critical fluctuations. This provides proof that the mixtures being investigated would pass close to a critical temperature as they transition from single phase to two phase in the phase diagram. This is important as this is the point needed to be quenched through to best favour AR.

As shown it is possible to observe bilayers as they were heated up using this system, but the heater had no active cooling mechanism so bilayers could only be cooled at ambient cooling rate or slower. This made it impossible to perform fast temperature quenches, which are required to attempt to observe the early stage kinetics of domain formation and possible AR.

#### **6.4.2 Peltier Heater and Cooler**

As the built-in temperature control system had no active cooling mechanism a temperature stage was designed using a peltier chip as shown in Figure 6.8B. The device was designed by Dr Anders Aufderhorst-Roberts and Dr Simon Connell alongside members of the Physics electronic and mechanical workshops. A peltier device uses the thermoelectric effect to convert voltage to temperature changes at a junction of two dissimilar conductors, p- and n-doped semi-conductors. It enables both heating and cooling of a sample, by changing the voltage polarity across the semiconductors. The peltier chip was attached to a copper stage which can be attached to the AFM stage. The copper stage acts as a heat sink and has inner channels built in to enable water to be circulated to help dissipate excess heat quickly from the underside of the chip when in cooling mode, thereby extending the cooling range of the peltier device.

The main issue with this temperature stage was that the PID feedback controller was difficult to adjust to achieve a stable setpoint temperature. The temperature often fluctuated up to  $\pm 2$  °C, which triggered the Fastscan crash protection software and the system would not engage. When the fluctuations were small enough to allow the system to engage, there was periodic noise in

the images (Figure 6.10A and B). Whilst the device had a proportional feedback controller, it could only maintain a constant setpoint temperature by switching repeatedly between heating and cooling mode, involving a constant switching of the voltage polarity. This switching in polarity of the voltage, changed the electric field felt by the AFM piezo which lies only 1 mm away. As an AFM piezo relies on the direct conversion of voltage to displacement, this electric field causes a tiny extra movement in the piezo, manifested as noise in the image at the frequency of the voltage polarity switching in the peltier. The amplitude of this noise was only on the order of several nanometres in a total z-travel of 4 micrometres (hence a noise of 0.05%) but with bilayer domain steps of the order of 1 nm this periodic noise made it difficult to analyse images to obtain area and height information, and in some cases is not easy to observe domains at all. Figure 6.10 C and D show a bilayer imaged before and after attempting to controllably increase the temperature. The temperature spikes caused by the feedback control caused the bilayer to be heated and cooled quickly. The bilayer can be seen breaking down into critical fluctuations, showing that as it was heated up it was close to a critical point and the fast cool caused the small critical domains to be trapped.

Another issue with this system was that the temperature probe (platinum resistor) was affected by the AFM piezo voltage, meaning that the temperature displayed was often incorrect and erratically changing (as high as 5000 °C). The platinum resistor probe was replaced by a thermocouple for the controller

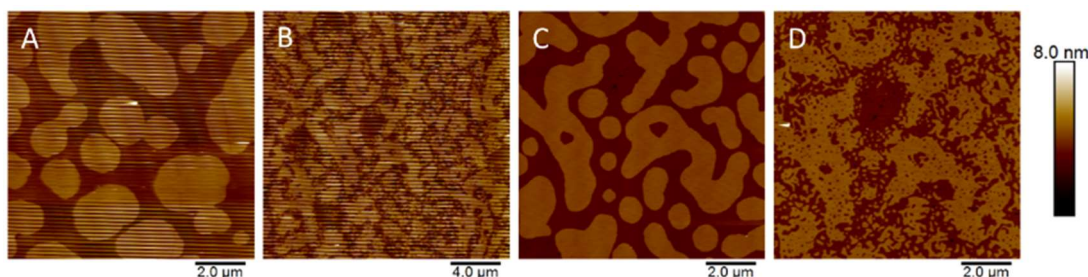


**Figure 6.10 AFM with controlled temperature on a DPPC/14:1PC/Chol bilayer (45:25:30) using a peltier stage built for the Dimension Fastscan AFM. A and B show two different bilayer areas with noise from the temperature controller. C and D show a bilayer area subjected to an uncontrolled temperature spike causing the domains to break down towards critical fluctuations, imaged after the temperature controlled was turned off.**

to feedback on. This was not affected by the piezo voltage but still had temperature fluctuation issues. The reason that the platinum resistor was effected by the piezo voltage and not the thermocouple is unclear. Both the metal in the platinum resistor and the two metals in a thermocouple could possibly be effected by the electric field from the peltier voltage, or through stray leakage currents passing through the liquid cell.

A peltier system was also designed to fit on another AFM system, a Bruker Multimode (Figure 6.8C). The peltier had the same feedback and temperature fluctuation issues but the crash protection was less sensitive on the multimode, so it was easier to engage. However there was still periodic noise in the images when the heater was turned on and the same issue with the piezo affecting the platinum resistor probe was seen.

The peltier systems should be able to perform fast quenches but when tested the measured cooling rates did not match and lagged behind the set cool rates. This was likely due to build-up of heat in the copper stage that could not be dissipated fast enough.

### **6.4.3 Asylum MFP3D Heater Stage**

As the heaters used so far have had issues with stably controlling temperature, an Asylum MFP3D AFM with a much more stable temperature stage was used (Figure 6.8D). The feedback control for the stage is tuned by the AFM software and the stage has channels for coolant liquid to be pumped through for cooling. This coolant enables fast cooling by dissipating heat and also aids the control of stable temperature as there is a controlled cooling mechanism to equal out the heating. There is no periodic noise from the heating stage when imaging, and low fluctuations in heat do not cause large cantilever fluctuations.

Bilayers were successfully imaged with controlled temperature but a new issue arose with the water on the bilayer stub evaporating when the temperature was raised for prolonged periods. Figure 6.11 shows how once water had evaporated, the bilayer was ripped apart due to the hydrophilic lipid heads being exposed to air, and this caused holes to form in the bilayer. Evaporation also occurred on the Bruker system, but water kept at a similar temperature in a hot plate or an oven could be added to the bilayer to keep it

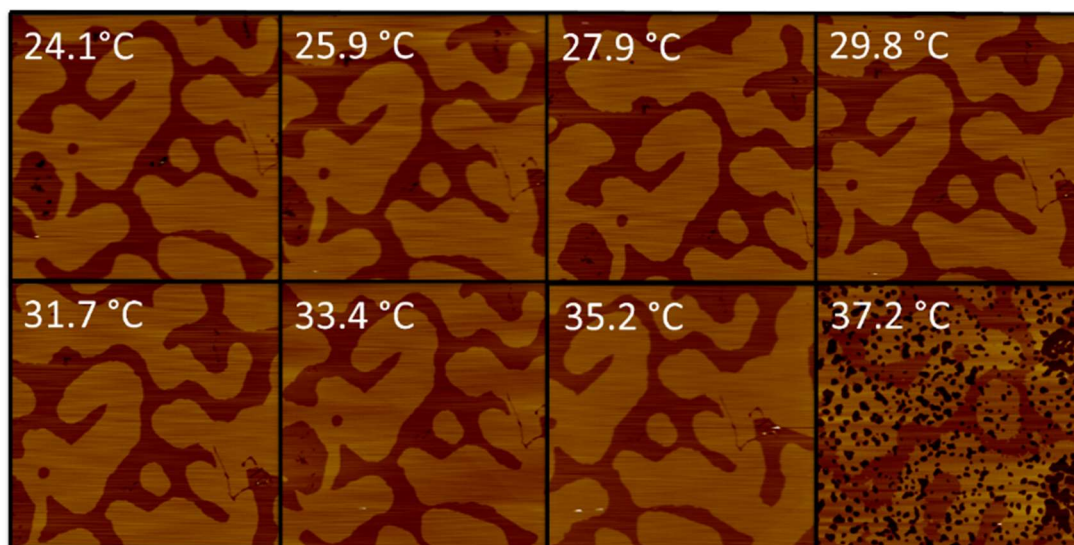


**Figure 6.11 AFM with controlled temperature on a DPPC/14:1PC/Chol bilayer (42.5:25:32.5) using a temperature stage on an Asylum MFP3D AFM.**

hydrated. With the Asylum MFP3D this is not possible when the scanner head is attached, as a pipette cannot reach the sample. One of the reasons for evaporation being such an issue is the small approx. 200  $\mu\text{L}$  water volume on the bilayer AFM stubs. To solve this issue, the whole heating cell was filled with water (approx. 2/3 mL) to cover the bilayer stub instead of just placing the water stub on the heater. This larger volume of water takes longer to evaporate and can be filled up more easily. Filling the whole heater cell with water introduced a new problem, how to put the stub into bulk liquid without the stub de-wetting and destroying the bilayer. When adding the stub into the bulk water or when filling the temperature stage once the stub is in there, the result was the water de-wetting from the sample stub. This results in the bilayer being destroyed and holes appearing.

This was as far as the project was taken with the Asylum Heating stage. By moving the AFM head down so that the water on the stub forms a meniscus around the tip on the tip holder, and then filling the whole heat cell with water, there was no de-wetting when this was tested briefly. At this stage however other parts of the project took precedence and the aim was for this to be revisited at a later date. The Asylum temperature stage is theoretically capable of performing fast quenches (120  $^{\circ}\text{C}/\text{min}$ ), which would enable critical mixtures to be quenched in an attempt to force out AR. However the larger

volume of water needed to stop evaporation will likely cause issues when quenching temperature, as the larger thermal mass will take longer to cool.

#### **6.4.4 Temperature Work Summary**

This section has shown the difficulties in performing AFM imaging while increasing and controlling temperature, it can be achieved but the process is often temperamental. This made it difficult to be able to obtain information such as melting transition temperatures. The ultimate goal was to be able to perform fast temperature quenches on critical mixtures to try to force out AR. The Asylum MF3PD system is capable of performing quenches but the experiments did not reach a stage where this was possible. The Asylum MFP3D would enable quenching and imaging at room temperature afterwards and possibly even imaging while quenching a few degrees through the  $T_m$ . Imaging at room temperature would enable the imaging of metastable kinetically trapped domains like those in 22:0PC mixtures, if these were also present in lower height mismatch lipid systems. However only the Bruker Fastscan AFM has the imaging speed to be able to image early stage kinetics, which theory has suggested is when AR domains may form.<sup>14,75,77,78</sup> Although these domains in the theory are only in the AR state for microseconds, it is likely that the frictional drag effect of the substrate on domain movement would cause them to be stable for longer, as shown in 22:0PC examples. The fast scan imaging may not be needed at all. Imaging just above  $T_m$  and then cooling a few degrees to just below  $T_m$  to see in real time how domains were forming and evolving was a future goal, but the Asylum AFM could not image fast enough and the Bruker AFMs would not engage with controlled temperature.

#### **6.5 Mismatch Free Energy**

It has been shown that it is possible to reliably and repeatedly form AR bilayers by increasing the hydrophobic mismatch. Up to 6 carbons per leaflet difference always resulted in R bilayers despite attempts to force out AR. A mismatch of 8 carbons per leaflet led to AR, either as a mix of AR and R states leading to three visible heights, or as fully AR as the proportion of the  $L_d$  and  $L_o$  phases would allow, leading to two visible domain heights. One of the main

goals of this study was to quantify the force, or energy, that results in domain registration. Whilst several simulation studies had derived a value,<sup>9,10,57–59</sup> no experimental data existed at the start of this project. During the project a single study emerged from one of the world leading groups in membrane biophysics using a completely different method to the one employed here, using the frictional force due to fluid flow to decouple the upper R leaflet.<sup>73</sup> The method used in this thesis was to calculate the mismatch free energy (also known as the interleaflet coupling parameter), in relation to the hydrophobic mismatch between phases. By calculating the free energy for bilayer systems at the different hydrophobic mismatches, the mismatch free energy i.e. the energy that must be overcome to form AR bilayers can be estimated.

By using the equation below, free energy of the bilayer was calculated based on hydrophobic mismatch.<sup>113</sup>

$$G = G^o + k \left( \frac{\rho_P}{\pi \xi_L} + 1 \right) |d_P - d_L|^2 \quad (6.1)$$

Where  $G^o$  is the free energy of the unperturbed membrane,  $k$  is a phenomenological constant related to the bilayer area compressibility modulus,  $\xi_L$  is the persistence length of lipid-bilayer fluctuations or phases and  $\rho_P$  is the circumference of the domains. The physics in this equation was developed to calculate the free energy of a membrane in terms of hydrophobic mismatch with inserted proteins. However, the terms can just as readily be applied to phase separated domains, and simply take account of the hydrophobic mismatch, the length of the boundary and the density/spacing of domains, and hence the energy density in a given area. Hence, the theory should apply similarly to hydrophobic mismatch between lipid phases.

As the free energy being considered here is only the relative difference between the unperturbed bilayer with no hydrophobic mismatch, and the different cases with hydrophobic mismatch, the free energy of the unperturbed bilayer is not needed. The area compressibility modulus,  $k$ , was estimated as  $0.193 \text{ Nm}^{-1}$ .<sup>114</sup> This is the value for a fluid SOPC (1-stearoyl-2-oleoyl-sn-glycero-3-phosphcholine) bilayer measured using micropipette aspiration of GUVs, and matches closely to measurements made using AFM.<sup>84,115</sup> The persistence length was estimated by the measuring the average distance

between domains manually, although this parameter could also be determined using a correlation function. The distance between phase separated domains in the registered DPPC, DSPC and 20:0PC systems was simple to measure, but in the anti-registered systems it was more complicated, due to the three different heights. Ideally, the phase structure before AR is the value that should be measured, but as the domain sizes and spacing are likely to be similar, it was decided that the distance between fully R domains would be taken.

Lipid Chain Length	Hydrophobic Mismatch (nm)	Free Energy ( $K_B T/nm^2$ )
16	1.16	0.000194
18	1.52	0.00136
20	2.27	0.00848
22	2.73	0.0490

**Table 6.1 Table showing free energy values calculated for lipid bilayer systems of different hydrophobic mismatch**

The output of this equation was free energy values in Joules, which were converted to  $K_B T/nm^2$ , the unit used for published values of mismatch free energy, simply obtained by dividing through by the average area of the domains.<sup>9,10,57-59</sup> Figure 6.12 shows the free energy of the bilayer plotted as a function of the hydrophobic mismatch between the coexisting phases (data is shown in Table 6.1). The free energy increases as the square of the hydrophobic mismatch, hence the large jump between 20:0PC and 22:0PC. This is the area of interest as this is where the bilayers change from being R

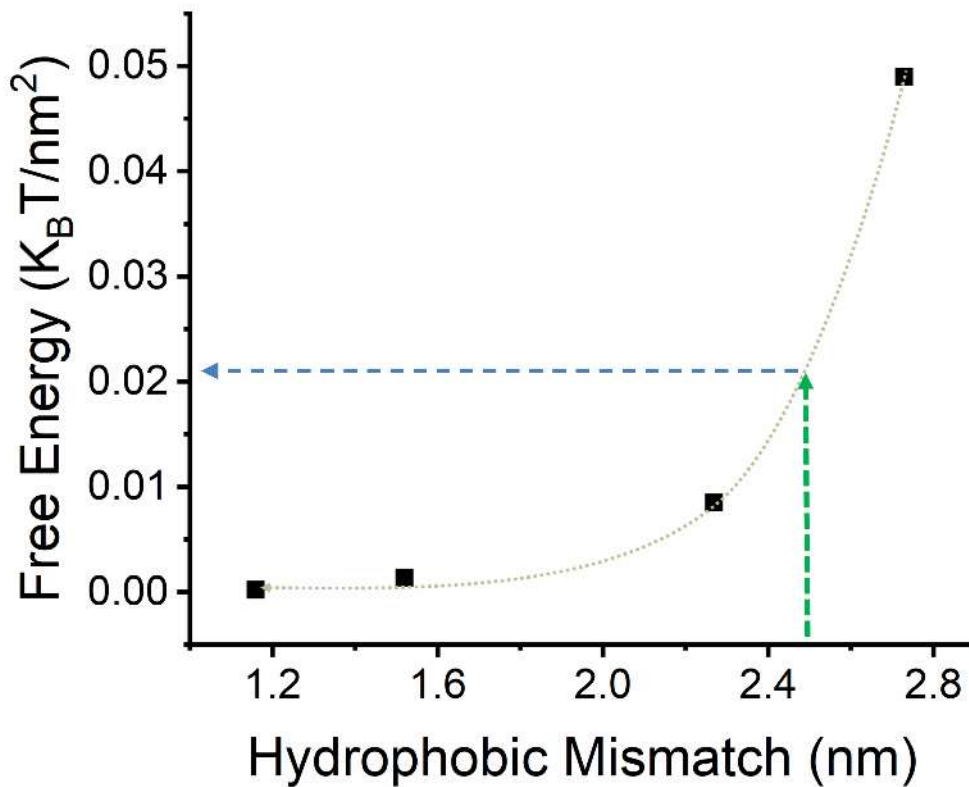


**Figure 6.12 Mismatch Free Energy of a bilayer plotted against hydrophobic mismatch. The fit is a smooth line used in the absence of a physical model, to interpolate the free energy at the hydrophobic mismatch of the 21:0PC ternary lipid system. 21:0PC was not investigated but is the boundary for AR. The hydrophobic mismatch for 21:0PC is taken as the halfway point between 20:0PC and 22:0PC**

to being AR, and where the mismatch free energy, or the interleaflet coupling parameter, is overcome by the increased line tension due to the hydrophobic mismatch. This means that the interleaflet coupling parameter is somewhere between 0.0085-0.049  $K_B T/nm^2$ . Furthermore, if C20 is R, and C22 is AR, and we say the boundary is at C21, then the value for interleaflet coupling is 0.021  $K_B T/nm^2$ . This estimate is remarkably close to the published estimates. Estimates based on simulations and theoretical calculations are as follows; 0.01-0.03  $k_B T/nm^2$  <sup>(57)</sup>, 0.1-0.2  $k_B T/nm^2$  <sup>(9)</sup>, 0.146  $k_B T/nm^2$  <sup>(58)</sup>, 0.15±0.05  $k_B T/nm^2$  <sup>(59)</sup> and 0.5  $k_B T/nm^2$  <sup>(10)</sup>. The only estimate based on experimental work was recently determined by using flow to force the domains in the top leaflet of a bilayer out of registration, giving a value of 0.016±0.004  $k_B T/nm^2$ .<sup>73</sup> This value sits within the range calculated based on the AR observed in this thesis, and is remarkably similar to our estimate considering the entirely



different method utilised. It should be noted that type and compositions of lipid will affect the coupling, and this must also be taken into account.

## 6.6 Chapter Summary

Several methods were explored that might help to force out AR in lower height mismatch ternary lipid systems. DPPC/14:1PC/Chol mixtures, formed close to critical points with 50:50  $L_o:L_d$  compositions, still show two bilayer heights and complete bilayer registration (Figure 6.1). DSPC mixtures also form two height R mixtures at close to critical compositions (Figure 4.5). More is needed to force out AR in these low height mismatch systems. Models from the literature suggest that temperature quenching through critical points may favour metastable AR states.<sup>14,75,77,78</sup> A range of temperature stages were tested to control bilayer temperature while AFM imaging, but this proved challenging. Once a system was developed for controlling temperature and quenching while imaging, critical bilayers can be quenched to attempt to further favour AR.

DSC was used in an attempt to more accurately map out the phase diagrams for the ternary lipid systems used in this thesis, some of which have not been studied before and thus there are no phase diagrams. This would help to locate critical points for performing quenches and attempting to force AR. The simplest system, DPPC/14:1PC/Chol, was mapped first which is a similar system to the well-studied DPPC/DOPC/Chol. It was found that as the proportion of cholesterol and 14:1PC was increased the DSC signals become broader and weaker. Although it was possible to plot a ternary phase diagram with temperature that matched well with literature, this relied on several ambiguous interpretations of peaks and the data collection took longer than expected. It was decided that this would not be continued as the time to get the extra data for all the ternary systems would be huge, and the broad and weak peaks made the data slightly unreliable.

Using the hydrophobic mismatch values measured for the different lipid systems, the free energy of the bilayers as a function of this mismatch could be calculated. The mismatch free-energy calculated matches remarkably well

with published estimates from simulation and theoretical calculations as well as one experimentally determined value.

Now we have an estimate for the energy that the plasma membrane must overcome to force bilayers out of the equilibrium registered state seen in model membranes. The same physical mechanisms and interactions in model membranes must also be present in the plasma membrane, so these energies must be overcome to maintain the dynamic and asymmetric membrane. If AR could have been forced out in lower height mismatch systems, this value could be refined further. The 20:0PC/14:1PC/Chol system is the key in this regard as it is the height mismatch system before AR is observed for 22:0PC. There was not enough time, but this chapter was logically leading to the formation of spinodal 20:0PC mixtures and quenching these to try to force AR. Forming mixtures using 21:0PC could enable further refinement of the interleaflet coupling value and the absolute height mismatch in terms of carbons and in terms of nm. This could also be achieved by using multiple different phase separated systems with different lipids e.g. SM or PE, and observing if the height mismatch where AR occurs is the same.

## **Chapter 7. Substrate Coupling in Supported Lipid Bilayers - Glass**

### **7.1 Introduction**

This chapter and the next concern substrate coupling to SLBs, and how this affects domain formation. There are two main justifications for this work;

1. The simulations of Williamson et al. show that AR states are metastable kinetically trapped states on the way to R equilibrium, and they are only stable for microseconds.<sup>14</sup> This would be hard to observe experimentally. However, the AR systems observed in this thesis remain stable at least for hours/days, perhaps due to the presence of a substrate.
2. Now that AR systems have been formed, fluorescence can be used to investigate them. AR states should show three different intensities, and this could be easily tested. Langmuir Blodgett bilayers would also be useful for experiments looking into interleaflet coupling forces and mismatch free energy. Although mica is used for AFM, glass is usually used for optical microscopy, due to its transparency. Do different substrates effect phase behaviour?

Before results are presented, the relevant literature regarding substrate effects will be summarised briefly. A larger bulk of the literature is then discussed in relation to the results presented, at the end of the next chapter.

### **7.2 Brief Overview of Substrate Coupling in Bilayers**

Substrates can affect bilayer properties compared to free-floating systems. Although there is a thin interstitial water layer between the bilayer and the substrate which allows the bilayer to remain fluid, the diffusion has been shown to drop for both mica and glass SLBs compared to free standing GUVs and Black Lipid Membranes (BLMs).<sup>29,46</sup> Phase separation can also change significantly in SLBs. Phase domains on solid supports can vary in shape and size compared to GUVs, and in particular domains appear to be static in SLBs

due to an interaction with the surface.<sup>40,116</sup> Domains in GUVs however can collide and coalesce to form larger domains,<sup>40,116</sup> driven by the reduction in free energy due to the hydrophobic mismatch at the boundary between phases.

Issues arise when comparing results between different surface sensitive techniques due to the different substrates used. As an experimental group using different techniques and different substrates, it is vital to understand the effects the different substrates are having. This will enable comparison of SLBs between different surface-sensitive instruments and with free-floating vesicles.

Phase behaviour has been well characterised on mica, to give information on domains such as size, height and dynamics.<sup>19,43,54</sup> This is demonstrated in literature but also in the first three results chapters of this thesis (Chapter 4, Chapter 5 and Chapter 6). However, reports of phase separation on glass are scarce. Domains have been observed on glass from Langmuir-Blodgett Deposition,<sup>40,53,117</sup> where the domains are already present at the liquid-air interface before deposition, and in phase separated GUVs ruptured onto glass.<sup>40,45,118</sup> However, these domains do not re-form upon temperature cycling.<sup>40,45</sup> In the literature there are only a few studies showing domains forming on glass via vesicle fusion, where the domains would have to nucleate and grow from a single homogenous phase on the substrate.<sup>35,38,119</sup> This is remarkable considering the ubiquitous use of glass in optical microscopy,<sup>39,106,120</sup> and the hundreds if not thousands of papers showing phase separation in free-floating GUVs,<sup>28,45,121</sup> and in SLBs on mica.<sup>43,44,54,116</sup>

Strategies to decouple the bilayer from the substrate include the use of multi-bilayer stacks, as used in scattering experiments,<sup>122</sup> tethering of a free floating bilayer to a surface,<sup>123,124</sup> or supporting the bilayer on a hydrated polymer cushion.<sup>125</sup> Whilst these methods can be effective, they increase the complexity of the sample preparation, and are only suitable for certain techniques, for example AFM and fluorescence microscopy require a single bilayer.

In this chapter and the next, phase separated bilayers are formed on different substrates (mica, glass and PDMS), to characterise how phase separation is affected by substrate interactions.

### 7.3 Phase Separation is Different on Mica and Glass

DPPC/DOPC (60:40)+TR-DHPE SLBs were prepared on both freshly cleaved mica, and on a Piranha and UV Ozone cleaned glass substrate. This mixture was chosen, by examining the phase diagram of DPPC/DOPC and trying to form mixtures with a high percentage of nucleated domains. The Fluorescence Microscopy images on mica show clear gel-liquid phase separation, with the fractal domain morphology matching closely to DPPC/DOPC domains in literature.<sup>54</sup> The TR-DHPE dye associates preferentially with the fluid phase lipids (bright areas) and is excluded from the tightly packed gel domains (dark areas) (Figure 7.1A). AFM images show the

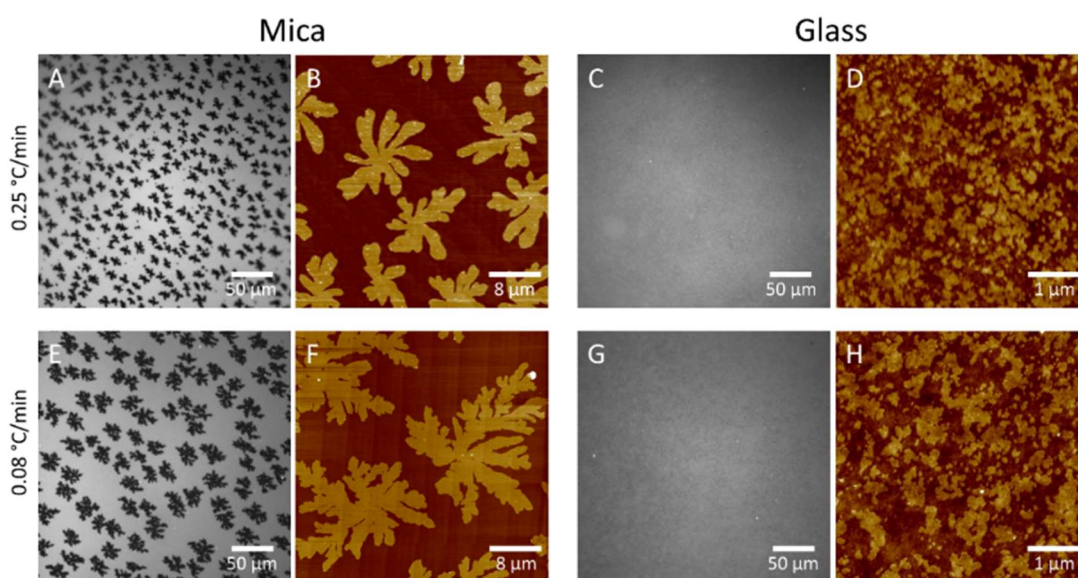


**Figure 7.1 DPPC/DOPC (60:40) SLBs imaged with AFM (B,D,F,H) and DPPC/DOPC (60:40) + 0.5%TR SLBs imaged with fluorescence (A,C,E,G). A,B,E,F are on mica and C,D,G,H are on glass. The AFM images on glass are representative examples from a heterogeneous surface, heterogeneity highlighted in Figure 7.7. The XY scales are indicated on all images with a scale bar. The Z range of all the AFM images is 4 nm. The cooling rates from incubation temperature to room temperature are shown on the left-hand side and apply to the whole row. Standard Errors for cooling rates =  $0.080 \pm 0.008$  °C/Min (N=4),  $0.25 \pm 0.02$  °C/min (N=3). A-H are 8 separate experiments i.e. A and B are not the same sample, but the same lipid mixture incubated similarly for two different techniques.**

same gel phase domain morphology (Figure 7.1B). The two sets of domains, formed separately for different techniques but with the same incubation conditions, have a similar average radius (Table 7.1). Details on radius calculation are shown in Figure 3.5 (Methods Chapter). Figure 7.2 shows AFM and Fluorescence images of the same bilayer area, proving that the domains observed by the two techniques are the same.

When the same DPPC/DOPC (60:40) lipid mixture was identically incubated on a glass substrate, fluorescence images showed no clear phase separation (Figure 7.1C). FRAP bleaching and recovery confirmed that freely diffusing bilayers had formed. Imaging with AFM enabled a much higher resolution and confirmed that domains had formed on the glass substrate but were below the diffraction limit of the fluorescence microscope. The domains formed on glass (Figure 7.1D) have a significantly smaller length scale and show rough domain boundaries, compared to the larger domains with smoother boundaries and fractal morphologies on mica.

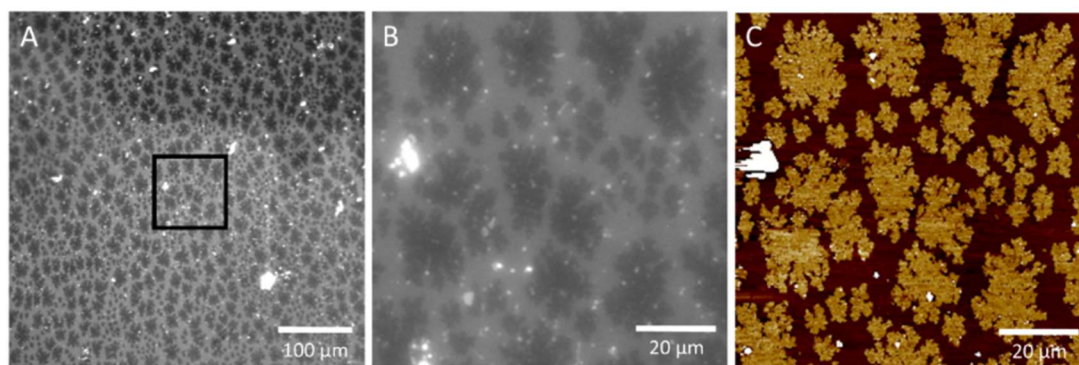


**Figure 7.2 DPPC/DOPC (60:40) SLBs on mica, imaged using both fluorescence (A and B) and AFM (C) on the same area using a combined AFM/Fluorescence microscope. B is a separate image from A taken at a higher magnification. B and C are the same area as the black box in A. Z Scale of C is 3.5 nm. The white specks in the images correspond to lipid vesicles and aggregates stuck to the bilayer surface. The two different populations of domain size present in these images (large 20um domains and small 5um domains) demonstrates the effects of a non-controlled faster cool on domain formation. Domains nucleate and grow large but as the solution becomes super-saturated smaller domains crash out.**

Substrate	Cooling Rate (°C/min)	Domain Radius (AFM)	Domain Radius (Fluorescence)	Correlation Length (AFM)	Correlation Length (Fluorescence)
Mica	0.25±0.02	5.3±0.2 μm	4.57±0.04 μm	2.26±0.4 μm	3.2±0.2 μm
Mica	0.080±0.008	8±1 μm	8.9±0.2 μm	3.31±0.09 μm	7.3±0.1 μm
Glass	0.25±0.02	Domains connected so analysis fails	Resolution too low	74±5 nm	Resolution too low
Glass	0.080±0.008	Domains connected so analysis fails	Resolution too low	65±7 nm	Resolution too low

**Table 7.1 Domain Sizes and Correlation Lengths for Mica and Glass bilayers at different cooling rates. Domain fitting and correlation length methods can be found in Methods Section**

It should be highlighted how extreme the contrast in length scales between the domains formed on glass and mica are. This is shown both by AFM images with the same X,Y and Z scales in Figure 7.3, but also using correlation length analysis. The partially interconnected morphology of the domains on glass meant that fitting the domains to ellipses, as was done for the micron size domains on mica, was impossible. Correlation length analysis has been used previously to measure the length scales of critically fluctuating bilayer mixtures.<sup>43,126</sup> When a two phase bilayer image is converted to a binary black and white image, the correlation length is a radially averaged quantitative measure of the length scale between black and white pixels i.e. the two different phases. The average AFM image correlation length of domains on glass was 74±5 nm, but almost 2 orders of magnitude larger for domains on mica at 2.26±0.4 μm. (Table 7.1).

Visualising the nanoscale domains on glass optically is challenging due to the diffraction limited optics. At high magnification the fluorescence images of bilayers on glass show a fine speckled structure (Figure 7.4C). Even though the correlation length of the domains is only  $74\pm 5$  nm, there is a heterogeneity in domain sizes and also aggregation of domains. This results in features that are just on the resolution threshold. An AFM image (Figure 7.4A) of the same size as the optical image was converted to greyscale so the domains have the same intensity as gel domains depleted of dye in the fluorescence, and the background fluid phase appears light grey like the domains enriched in dye in the fluorescence. The AFM image was then processed using a Gaussian filter of 500 nm, recreating the diffraction limiting effects of the optical microscope, governed by the of the wavelength of light used to image, and the numerical aperture of the lens, and the imaging medium. The result of this AFM image processing is shown in Figure 7.4B, and as can be seen the observable pattern made by domains is similar to the optical image (bearing in mind they are not the exact same area and the domains on the surface are heterogeneous). This shows that although the fluorescence images appear to show no domains but just a speckled pattern, the nanoscale domain images by AFM run through an optical resolution mimicking process show a similar pattern.

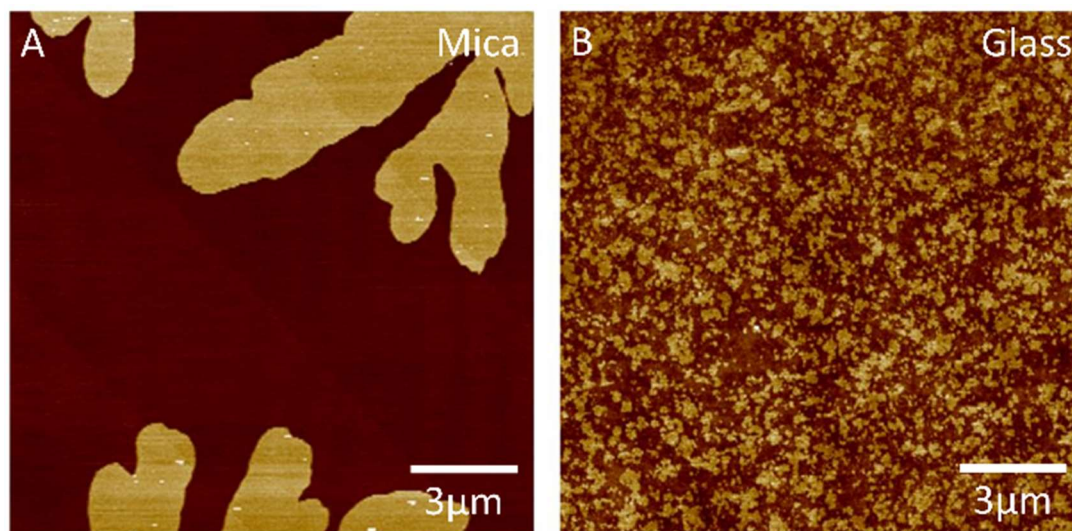


**Figure 7.3 DPPC/DOPC (60:40) SLBs on mica (A) and glass (B), highlighting the discrepancy in size and morphology of domains. X,Y and Z scales of the two images are the same. Z scale is 4 nm. Both A and B were cooled at  $0.25\pm 0.02$  °C/min.**



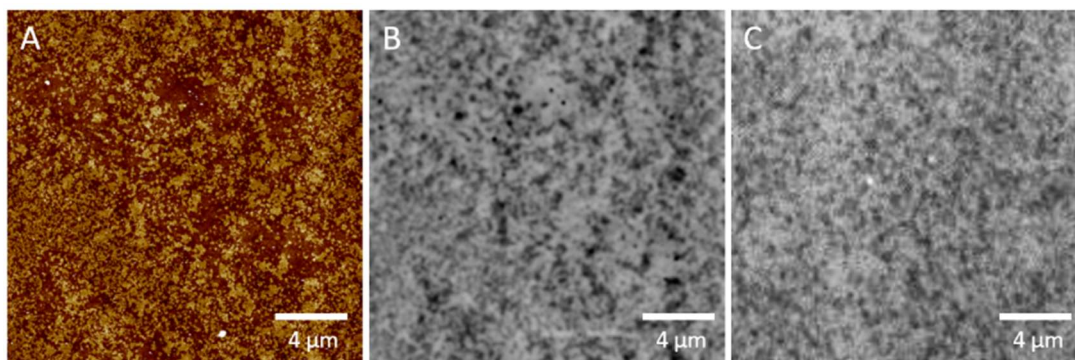


**Figure 7.4 Using a gaussian blur on an AFM image of nanoscale domains on glass, to mimic the diffraction limit of an optical microscope. A) AFM image of DPPC/DOPC (60:40) bilayer on glass. Cool rate is 0.08 °C/min. Z scale is 4 nm B) The AFM image A changed to greyscale and processed using a 500 nm Gaussian blur, mimicking the diffraction limit of a microscope. C) Fluorescence microscope image of DPPC/DOPC (60:40) on glass, zoomed in to the same size as AFM image A. Cool rate is 0.08±0.008 °C/min. Scale bars are shown on all images.**

#### **7.4 Single Lipid Gel Phase Structure is also different on Mica and Glass**

In the next section (7.5), experiments are described that look at lipid dynamics to investigate how diffusion might affect domain formation. Interestingly, during these experiments it was noticed that in pure DPPC +16:0 NBD PC bilayers the dye was preferentially segregated during domain growth. This left behind a signature of domains with the same shape as the DPPC domains in the mixed DPPC/DOPC system (Figure 7.5). We attribute the structure to exclusion of the sterically bulky head-group fluorophore, as the DPPC crystallises. Pure DPPC bilayers with a different dye, TR-DHPE, show similar behaviour (Figure 7.5). The much bulkier Texas Red group however is excluded from the crystallising DPPC even more vigorously, leading to a much more concentrated and thin boundary around the nucleated domains and not a gradient, and the final liquid phase to freeze contains all of the TR-DHPE.

Above the  $T_m$ , DPPC is in the fluid phase and mixes with the dye molecules, shown by a homogenous phase (Figure 7.6). As the bilayer cools through DPPC's  $T_m$  (40-41 °C), pure DPPC crystallises excluding the DPPC molecules containing the fluorophore. Sufficiently below the  $T_m$  and at room temperature

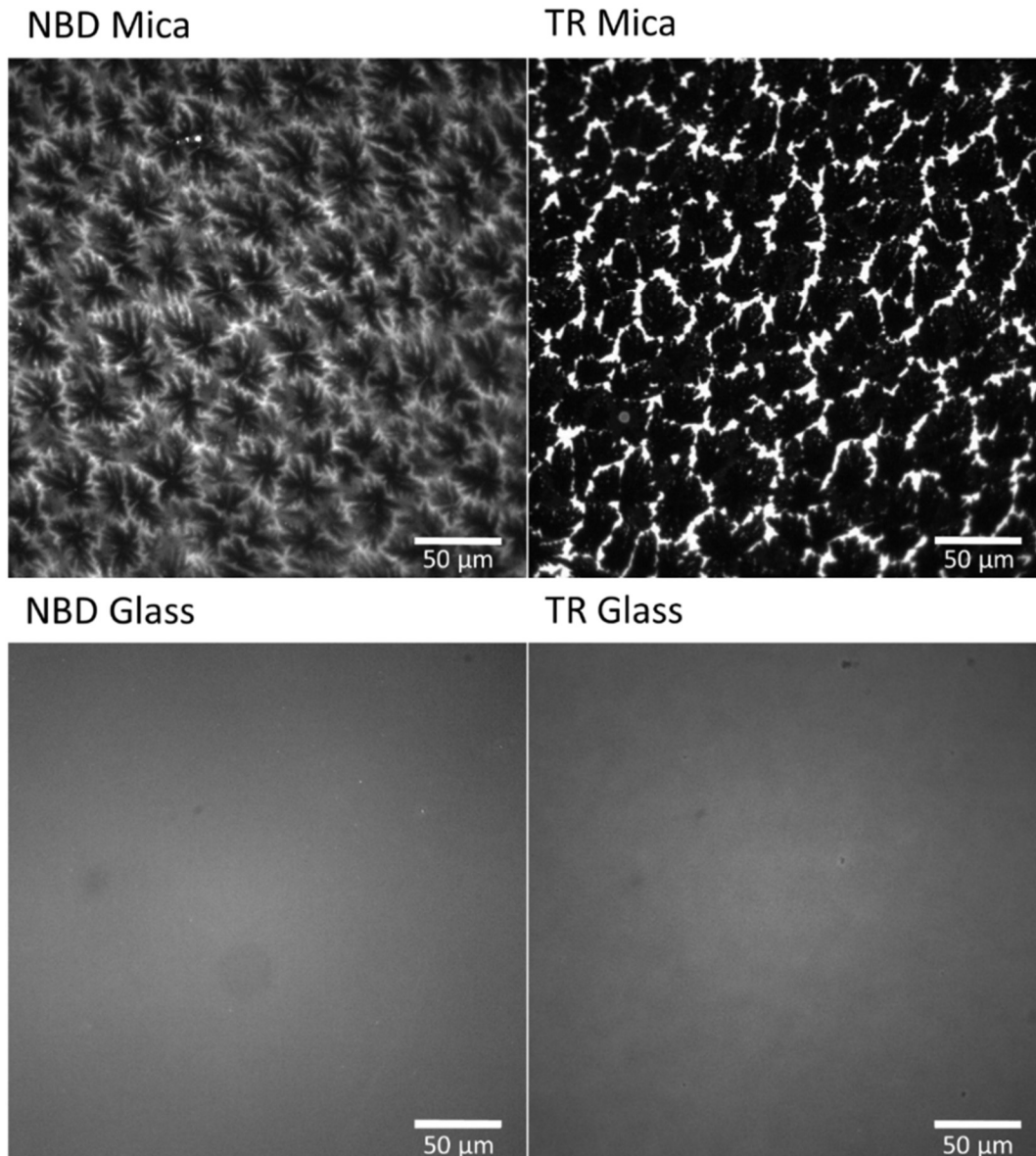


**Figure 7.5 Room Temperature Images of DPPC with 0.5mol% NBD or 0.5mol% TR on mica and glass. On mica DPPC domains are observed, as they have nucleated the dye molecules have been excluded. The bulky TR dye is more excluded than the smaller NBD dye. On glass no exclusion is observed, likely because it is below the diffraction limit.**

all the molecules are crystallised, as the dyes have the same PC chains. This leaves the original nucleated domains of pure DPPC surrounded by an increasing gradient of dye, with the final remnants to freeze containing the highest concentration of dye.

When DPPC +16:0 NBD PC and DPPC +TR-DHPE were formed on glass, no structure was observed optically (Figure 7.5). Even the fluid phase TR-DHPE

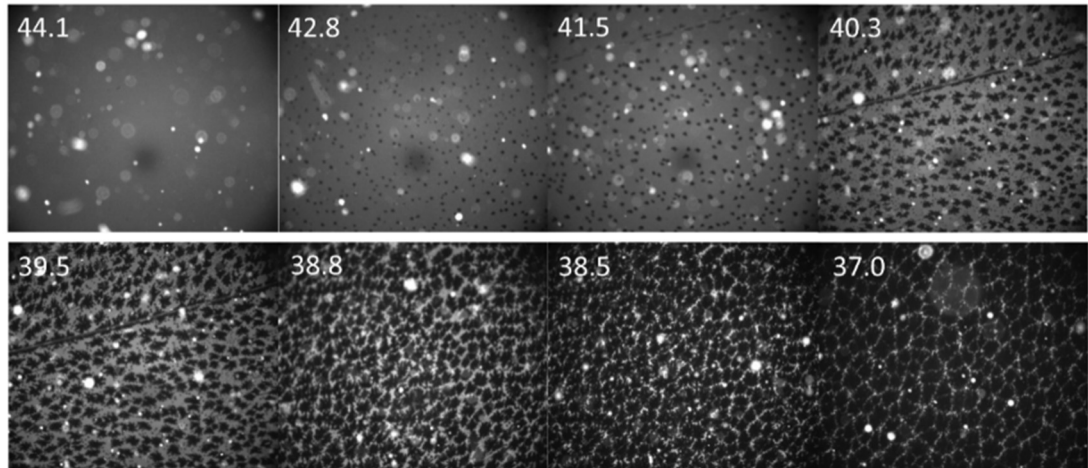


**Figure 7.6 DPPC + 0.5mol% TR DHPE cooling from through DPPC's transition temperature. The bilayer is initially homogenous in the fluid phase. As the bilayer cools nucleation of pure DPPC domains excludes TR-DHPE dye.**

dye that was significantly excluded from pure DPPC on mica, does not show any separation on glass optically. Just like for the phase separated systems, the glass substrate is hindering the growth of lipid structures compared to mica. There have not been many studies showing a pure lipid bilayer excluding a lipid dye, perhaps due to the ubiquitous use of glass, where the exclusion might not be noticed due to the sub diffraction limited structures. However similar gel-like structures of cationic lipids excluding dyes were observed by McKienan et al. which they attribute to a coexisting tilted lipid phase,<sup>127</sup> and Crane et al. note the exclusion of dyes from the gel phase during compression in a Langmuir Trough.<sup>55,117</sup>

## **7.5 Difference in Phase Separation between Mica and Glass is not due to Molecular Diffusion Rate**

To understand the factors affecting domain sizes on the different substrates, we investigated lipid dynamics on glass and mica. Fluorescence Recovery after Photobleaching (FRAP) was performed on DOPC + 0.5mol% TR-DHPE bilayers. The diffusion coefficients on mica ( $0.96 \pm 0.04 \mu\text{m}^2/\text{s}$ ) and glass ( $1.02 \pm 0.04 \mu\text{m}^2/\text{s}$ ) were remarkably similar. The diffusion coefficients of DPPC + 0.5mol% 16:0 NBD PE above its  $T_m$  on mica ( $2.1 \pm 0.1 \mu\text{m}^2/\text{s}$ ) and glass ( $2.1 \pm 0.3 \mu\text{m}^2/\text{s}$ ) were also the same.

The diffusion values match with literature values from different techniques, which vary between 0.5-5.0  $\mu\text{m}^2/\text{s}$  for fluid lipid systems.<sup>29,36,120,128</sup> Fluorescence Correlation Spectroscopy (FCS) experiments have also found that DOPC diffusion is the same on glass and mica, all other experimental parameters being identical.<sup>36</sup> Harb et al. find DPPC FRAP diffusion on glass and mica to be the same when high ionic strength buffers are used, but it is faster on glass when ionic strength is low.<sup>129</sup> These two studies vary in bilayer deposition technique, the first using Vesicle Fusion (such as in this study), the second using Langmuir Blodgett Deposition, and this can potentially affect bilayer properties. Langmuir-Blodgett Bilayers are formed by pulling a substrate through a monolayer at the air-water interface to deposit a monolayer, and then a second time to create a bilayer. Also, the different ionic strengths of buffers used clearly affect bilayer-substrate interactions. Diffusion values can vary significantly for different lipid types and on other surfaces than mica or glass. Studies often use different dyes, different buffers, different techniques, different substrate manufacturers and different bilayer deposition methods, so these must be considered when comparing results. Seu et al. also show how the preparation procedure and etch time of glass can have a big effect on the diffusion of DOPC by FRAP.<sup>38</sup> As long as the methods used within an experimental group's own experiments are consistent, this allows comparison between those experiments. For the experiments presented in this thesis, where the same lipid, dye, buffer, deposition technique, equipment and analysis methods are used, the molecular diffusion is not affected by the different substrates, so cannot be affecting the growth of different size domains.

As the FRAP data shows that overall lipid diffusion is not hindered on glass, we attempted to produce larger domains by using slower cooling rates, giving more time for phase growth following nucleation. This would give information on whether domain motion is being hindered by the surface, despite lipid diffusion being similar. Decreasing the cooling rate through the miscibility transition temperature ( $T_m$ ) has been shown to increase the size of domains formed on mica.<sup>44,101</sup> Moving through  $T_m$  more slowly, allows more time for lipids to diffuse towards and attach to an expanding nucleating domain, creating larger domains with larger area to perimeter ratios and thus lowering

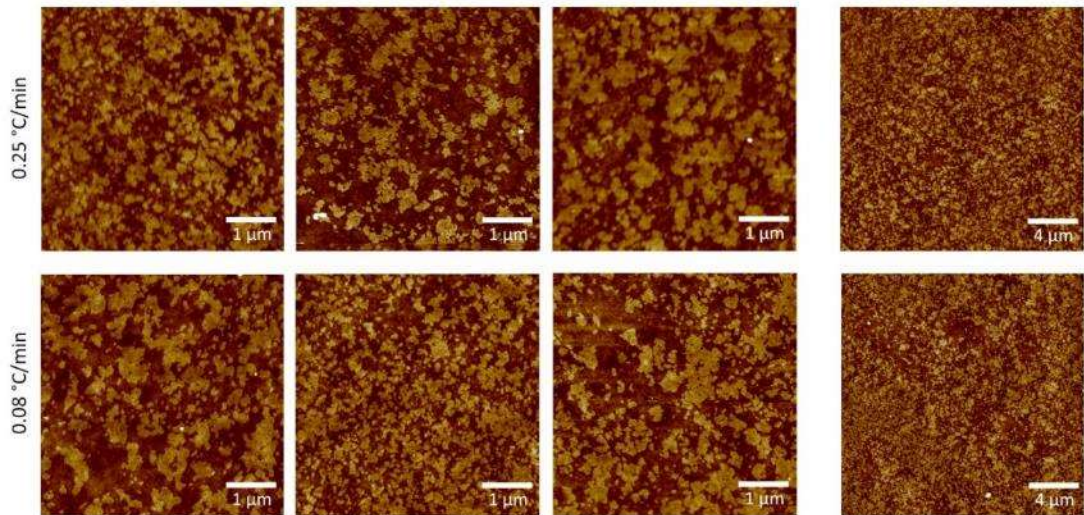


**Figure 7.7 Example AFM images of DPPC/DOPC (60:40) on glass at different cooling rates. Image sizes are 5µm and 20µm. Images show heterogeneity in different areas of the substrates, and how a similar range of sizes, morphologies and clustering are seen with both the ambient (0.25 °C/min) and slow (0.08 °C/min) cool.**

the free energy due to hydrophobic mismatch between phases. A faster quench through the  $T_m$  however, means there is less time for lipids to diffuse and they are kinetically trapped into many smaller nucleated domains. As expected, when the cooling rate from incubation temperature (50 °C) down to room temperature was slowed from  $0.25 \pm 0.02$  °C/min to  $0.080 \pm 0.008$  °C/min, the size of the gel domains on mica increased both in AFM and Fluorescence experiments (Figure 7.1A to E and B to F, and Table 7.1). The correlation length of domains on mica was shown to increase by 46% as cooling rate was slowed, matching closely to the increase of 51% in domain size fitting, showing that correlation length is a good quantitative indicator of length scale. Importantly, the average correlation length on glass does not increase as the cooling rate is increased. The images in Figure 7.1 are example images, Figure 7.7 highlights the heterogeneity of different substrate areas. The correlation length averaged across repeat images produces similar values for both cooling rates. Even though there is more time for molecular lipid diffusion, larger domains do not form. The glass substrate is the limiting factor hindering the formation of larger domains.



## 7.6 Molecular Ordering is affected by Different Substrates

Next, it was investigated if the substrates were having an effect on the molecular ordering of the lipids. An experiment was designed to determine the transition temperature ( $T_m$ ) of a DPPC bilayer on both glass and mica (similar to methods used in literature<sup>37,130</sup>), as  $T_m$  gives a quantitative measure of molecular ordering in a bilayer. DPPC was chosen instead of DPPC/DOPC (60:40) due to the sharper co-operative melting transition of pure lipids. The  $T_m$  value is just above room temperature, making it easy to observe.

The  $T_m$  of free-floating DPPC MLVs was characterised first using DSC (Figure 7.8A). DPPC shows a sharp melting point at  $41.72 \pm 0.05$  °C and sharp freezing point at  $39.73 \pm 0.02$  °C, with a 1.5 °C/min ramp rate. These values match to DPPC values from literature for MLVs and LUVs, where the dependence of heating and cooling rates on  $T_m$  offset is also observed.<sup>30,131,132</sup> DSC instruments have a finite capacity to transfer heat from heat source to the sample or vice versa, and if the heat required for a thermotropic transition

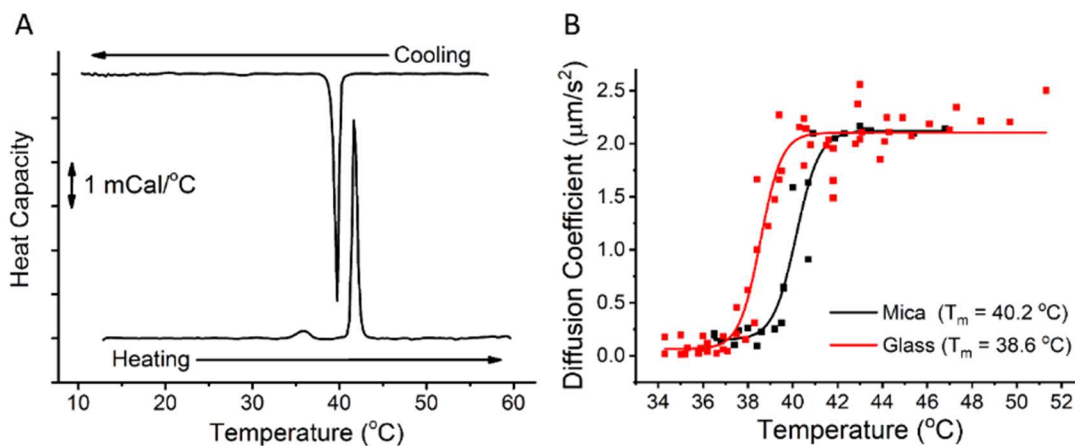


**Figure 7.8 Transition Temperature Determination for DPPC with DSC and temperature FRAP studies. A) DSC of DPPC MLVs showing the change in Differential Power/Heat Capacity with heating and Cooling. The peaks correspond to the gel-liquid transition temperature of the lipid (Heating cycle shows a pre-transition (?)) and a sharp peak at 41.65 (this image) and  $41.72 \pm 0.05$  (Average, N =5). Cooling cycle shows a transition at 39.75 (this image) and  $39.73 \pm 0.02$  (Average, N=3) B) Calculated Diffusion coefficients (D) at each temperature for mica and glass, plotted against temperature. For Mica 4 repeat runs are plotted, for glass 5 repeat runs. Data fitted to a Boltzmann sigmoid,  $T_m$  value taken as midpoint of sigmoid.  $T_m$  values are averages of all repeats**

exceeds this, the measured temperature will lag behind.<sup>133</sup> On the heating scan the  $T_m$  is offset to a higher temperature and on the cooling scan the  $T_m$  is offset to a lower temperature. Slower cooling rates would reduce these offsets.

A DPPC SLB was formed on mica and cooled from 50 °C down to room temperature through  $T_m$ , performing FRAP at regular intervals (Figure 7.9A-C). Above  $T_m$  the bleached FRAP area recovered as it was in a fluid phase and could freely diffuse. Below  $T_m$  the bleached spot did not recover or recovered very slowly, indicative of a gel phase. Fitting the exponential recoveries allowed diffusion coefficients ( $D$ ) to be calculated, which could then be plotted against temperature. A sigmoidal fit of this data revealed where the transition occurred (taken as the midpoint of the curve). The transition temperature determined by this method for mica was  $40.2 \pm 0.3$  °C ( $N=4$ ). This value is close to the cooling scan DSC value for MLVs,  $39.73 \pm 0.02$  °C. The cooling rate for the FRAP Fluid Cell (0.6 °C/min) was slower than the DSC (1.5 °C/min), thus the measured  $T_m$  from the FRAP is less offset towards lower temperatures. Other FRAP with temperature studies also show DPPC's  $T_m$  on mica to be similar to free-floating MLVs.<sup>37,129,130</sup> Some AFM studies report a similar  $T_m$ , but others report an increase of a few degrees.<sup>134</sup>

The  $T_m$  determined by FRAP on glass was  $38.6 \pm 0.2$  ( $N=5$ ). This is shown in Figure 7.9D-F. There is a small but significant drop in  $T_m$  of 1.6 °C from mica,  $40.2 \pm 0.3$  °C ( $N=4$ ), to glass. This implies a slight disordering of the lipid molecules within the bilayer on glass compared to mica. The second bilayer in DPPC double supported bilayers has been shown to have a 1.4 °C higher  $T_m$  than single bilayer SLBs on glass, more evidence that  $T_m$  is reduced slightly by proximity to the glass surface.<sup>37</sup> A reduction of 2 °C in the  $T_m$  of DPPC supported on glass-like Silica beads compared to MLVs has also been observed.<sup>132</sup>

The method used could be improved by controlling the temperature of the bilayer instead of allowing it to cool ambiently. This could be achieved by flowing water through the bilayer flow cell using a pump and a water bath at controlled temperatures. This would enable smaller temperature increments

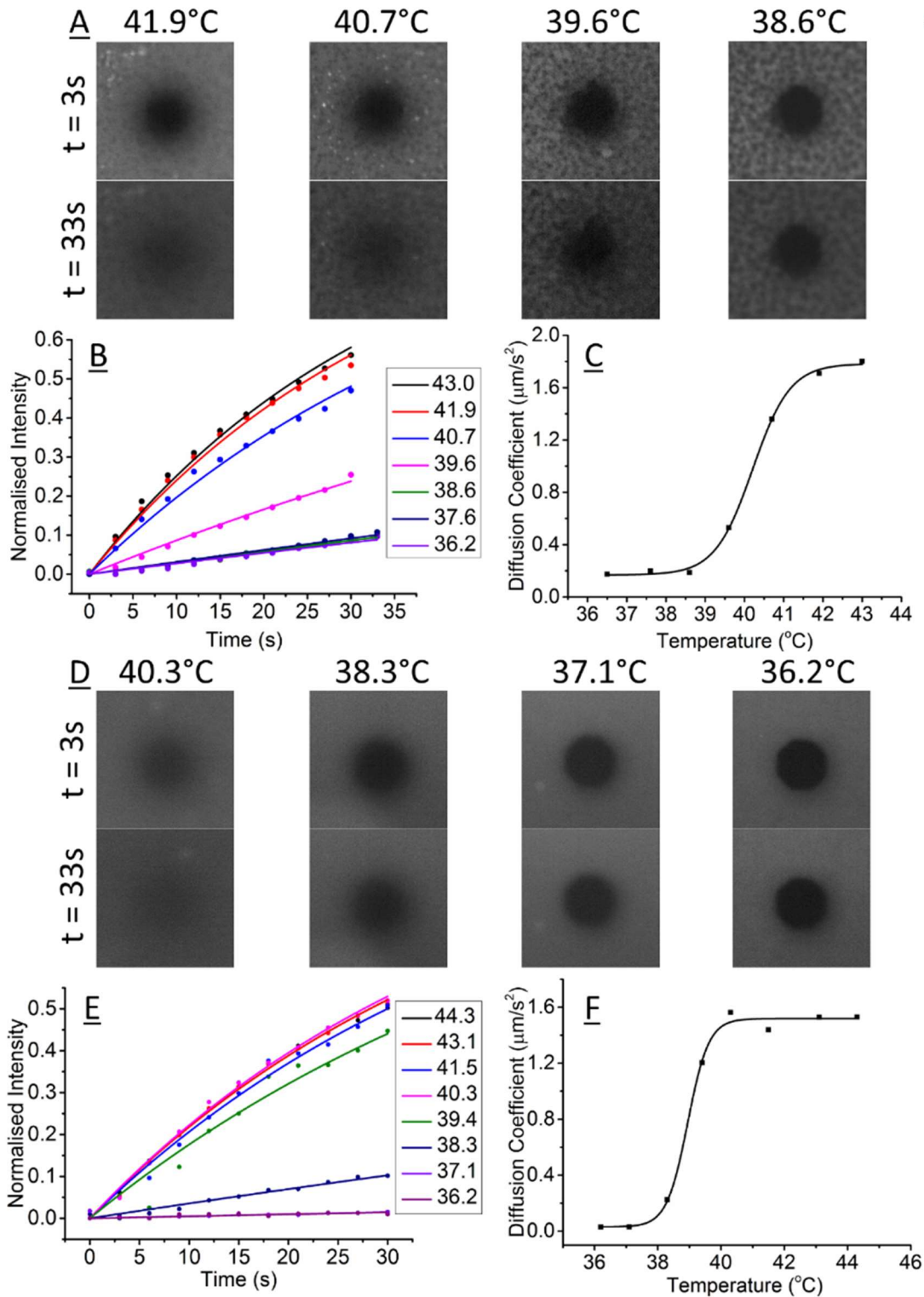


**Figure 7.9** FRAP on DPPC+ 0.5mol% NBD bilayer on mica (A,B,C) and glass (D,E,F) as the bilayer cools. A+D are fluorescence Images at 3s and 33s after photobleach as the bilayer cools. Temperature is indicated above images. B and E are Fluorescence recovery over time at each temperature with exponential recovery fit. C and F are calculated Diffusion coefficients (D) plotted against temperature. Data fitted to a Boltzmann sigmoid. Averages across data shown in this figure and repeat experiments gave  $T_m$  on glass  $38.6 \pm 0.2$  (N=5) and  $T_m$  on mica  $40.2 \pm 0.3$  °C (N=4).



meant the temperature was not decreasing during the FRAP measurements. The chemical nature of the surfaces may be influencing domain formation and bilayer order. The contact angle is a measure of the hydrophilicity of the surface and the density of hydrophilic functional groups i.e. hydroxyl groups. Hydrophilic surfaces have contact angles close to 0°, hydrophobic surfaces approaching 90-110°. The contact angle of mica was measured to be 3.0±0.2° after cleavage and glass to be 4.8±0.4° after Piranha and UV ozone cleaning. There is little difference, both surfaces are hydrophilic before the vesicles are deposited and the bilayer is formed. This is unlikely to be having any effect on ordering or dynamics. We also show using contact angle how successive cleaning treatments are needed to form the most hydrophilic glass possible for bilayer formation. (Table 7.2).

Washing Steps	No wash	Water Rinse	Decon Rinse	Decon +Piranha	Decon +Piranha +UV Ozone
Average Contact Angle	83±2	56±2	36±1	17±2	4.8±0.4

**Table 7.2 Contact Angle Measurements of glass cover slips after successive cleaning steps. *N=9 for all (3 repeats on 3 different glass cover slips)***

## 7.7 Substrate Roughness is linked to Domain Size

AFM images were used to measure the physical roughness of mica and glass, to see if roughness could be affecting domain formation and bilayer ordering. The  $R_a$  roughness of glass (0.148±0.004 nm) after piranha cleaning and UV ozone cleaning is over 4 times rougher than the mica (0.029±0.002 nm) after cleavage (Figure 7.10A+B). These values match closely to previous AFM roughness measurements of mica,<sup>39,128</sup> and piranha cleaned glass.<sup>38</sup> Power

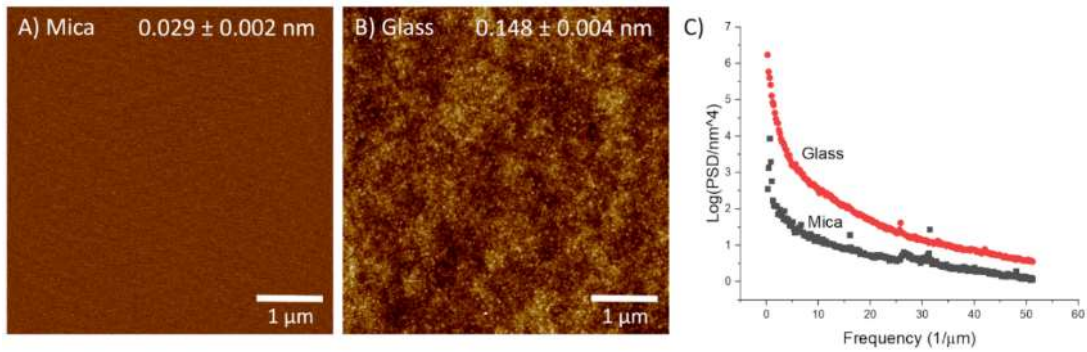


**Figure 7.10 AFM images and roughness of mica after cleavage (A) and Glass after Piranha and UV ozone clean (B). The  $R_a$  roughness measurements averaged over repeat images are included in top right of images. Scale bars are included on images, Z scale for A and B is 2 nm. C is A power Spectral Density Plot with Frequency, highlighting that the roughness is higher for glass over mica for all length scales.**

density spectra, which show the power of different length scale fluctuations, are shown for the 3D surface topography AFM images of glass and mica. The spectra show that the roughness is larger on glass than mica across all length scales (Figure 7.10C).

As such a significant difference in domain size and morphology is seen on the rougher glass compared to the smoother mica, we developed a method for investigating the effect of roughness by introducing a defined and controllable degree of roughness to the mica substrate. Mica was treated using Hydrofluoric Acid (HF) to form 1 nm deep etch pits (Figure 7.11A).<sup>90</sup> The etched mica used has an order of magnitude larger  $R_a$  roughness than freshly cleaved mica, from  $0.029 \pm 0.002$  nm to  $0.26 \pm 0.01$  nm. Forming DPPC/DOPC (60:40) bilayers on etched mica produced much smaller domains than on flat mica (Figure 7.11B), with morphologies and correlation lengths (57 nm) much

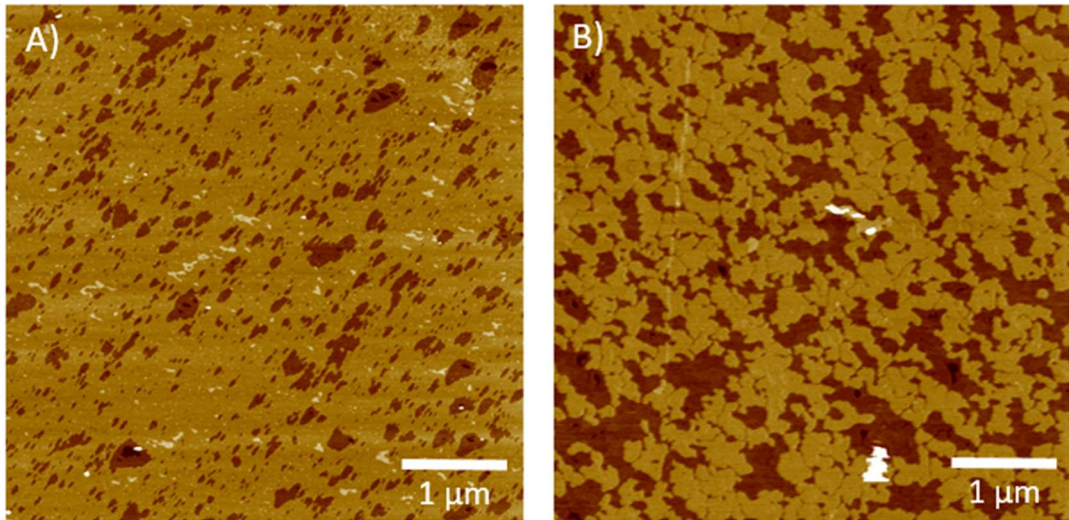


**Figure 7.11** AFM images of A) Mica etched in 40% HF for 30 min, and B) DPPC/DOPC(60:40) bilayer on HF etched mica. Note - A and B are not the same area, but are on the same sample stub. Scale bars are shown on images and z scale is 5 nm. RMS roughness of A is  $0.26 \pm 0.01$  nm. Correlation length of Domains in B is  $0.057 \mu\text{m}$  /57 nm.

closer to the domains on glass. The roughness is higher than glass, but proves that as the surface is roughened, large scale domain formation is hindered.

## 7.8 Glass as a substrate for bilayer formation

Although glass is used ubiquitously for optical imaging purposes, in many ways it is not ideally suited for reproducibly forming bilayers. Glass requires extensive cleaning in harsh chemicals to render it clean enough and hydrophilic enough to support lipid bilayers, and after this treatment the surface is still molecularly rough and heterogeneous. Mica in comparison, can be cleaved in a matter of seconds using tape/tweezers/scalpel, leaving a

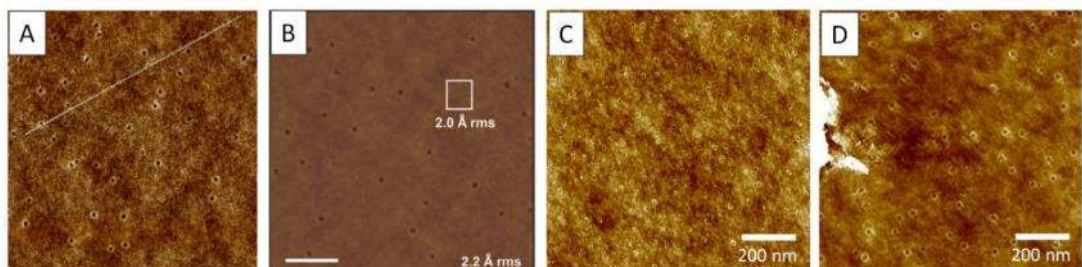


**Figure 7.12** Variability and Nanoholes on glass substrates A) From reference<sup>187</sup> B) From reference<sup>39</sup> C) and D) Different glass slides showing different distributions of nanoholes. Z Scale of a is 4nm, Z scale of b is 12 nm, Z scales for c and D are 3 nm. All images are  $1 \mu\text{m}^2$ .

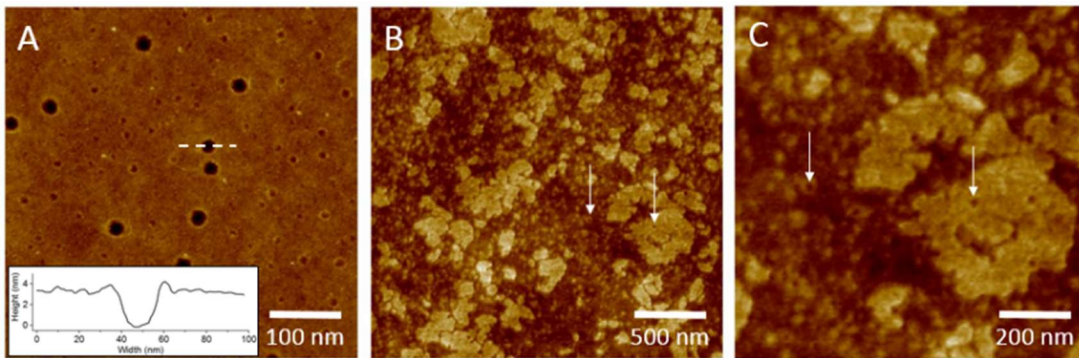


**Figure 7.13 AFM images of A) Glass substrate before Piranha/UV Ozone with nanoholes B) and C) DPPC/DOPC (60:40) bilayer on glass, where nanoholes are visible in the bilayer at the same size as holes in the substrate. (Note – different glass stubs in A and B) C) Zoom in of B, showing the nanoholes more clearly. Z scales of A is 8 nm, B and C are 4 nm.**

clean, hydrophilic and atomically flat surface. Mica is commonly used as an AFM substrate but can be used optically, if the mica is cleaved thinly and a suitable working distance objective is chosen. This is shown by the results presented here and also in literature,<sup>37,128</sup> but mica is still less common than glass for microscopy.

Glass samples from different manufacturers can vary significantly in terms of surface structure (Figure 7.12), one of the reasons why a harsh chemical etch is so necessary. The glass used in this study shows nanoscale hole defects (Figure 7.13), observed but not thoroughly discussed in other literature reports (Figure 7.12).<sup>39,135,136</sup> The frequency and size of the holes is not consistent. No further analysis of these holes was performed, but the images are included to highlight the variability and defects in glass surfaces. The nanoholes can also be observed through a SLB (Figure 7.13 B+C), although further work is needed to investigate how the nanoholes affect phase separation.

## **7.9 Formation of Optically Visible Domains on Glass**

As shown in Figure 7.1, domains on glass that are beyond the resolution of traditional microscopy are clearly visible using AFM. This is likely why there is a disproportionate number of publications researching phase separating systems on glass, compared for example to the ubiquitous phase separation in GUVs and SLBs on mica. It has likely been tried by many researchers who

have assumed that no domains have formed and thus not published, when in fact the domains were likely forming but were not observed by lower resolution techniques. Only one paper shows similar nanoscale domains on glass as in this study.<sup>35</sup> Using DPPC/DPhPC/Chol SLBs they observed distinct micron scale liquid-liquid ( $L_o$ - $L_d$ ) domains on mica using fluorescence. DPhPC (1,2-diphytanoyl-sn-glycero-2-phosphocholine, 4ME 16:0PC) is used as an equivalent to an unsaturated lipid to avoid photo degradation of the susceptible double bonds. Despite having saturated chain, the four methyl groups on each tail chain, disrupt the chain packing and form a fluid phase. The same lipid system on glass however only showed unclear phase separation, not fully resolvable due to the diffraction limit. Experiments using STED and STED-FCS, enabling super resolution, showed the presence of nanoscale domains ranging from 40-300 nm with an average of 90 nm. The study complements the finding in this thesis, by showing that the nanoscale domains formed on glass occur for liquid-liquid phase separating systems as well as gel-liquid systems. It should be noted that highlighting the difference in phase separation on different substrates was not the focus of their research. They had developed and were testing a new far-red emitting fluorescent dye that preferentially partitions into the  $L_o$  phase. They used this dye to observe phase separation in  $L_o$ - $L_d$  bilayers and measure diffusion using FCS.

Seu et al. and Burns et al. show domains on glass with DPPC/DOPC and DPPC/DOPC/Chol systems respectively that do not match with any domains we have observed in similar systems, or with domains observed by Honigmann et al.<sup>35,38,119</sup> The reason for this discrepancy is unknown, however it is telling that these are the only two papers showing phase separated domains on glass (with the exception of Honigmann et al.) and that they have never been reproduced in the literature in over ten years since their publications.

Based on examples in the literature, silicon substrates with roughness values matching those of glass, seem to also hinder the formation of phase separating systems of phospholipid/glycolipid<sup>137</sup> and phospholipid/protein,<sup>138</sup> compared to the same systems on mica. Reports of domains on silicon substrates in the literature are also rare, like on glass.

Visible domains have been observed in GUVs deposited onto glass substrates, if domains were already present in the GUVs before deposition.<sup>40,45,118</sup> These domains do not reform when the temperature is increased above  $T_m$  and then cooled down again,<sup>40,45</sup> but a 'speckle' pattern is observed.<sup>40</sup> From the AFM studies of bilayers on glass in this thesis, these results can be explained. Pre-formed micron size domains in GUVs are not hindered in growth by the substrate as they have already formed. Once raised sufficiently above the miscibility transition temperature the lipids are mixed homogeneously. When the lipids are cooled and become immiscible again, the presence of the glass surface hinders the growth of domains and results in a 'speckle' pattern of domains just below the optical resolution, like observed optically in Figure 7.4. Similarly to GUVs, Langmuir-Blodgett/Langmuir Schaefer bilayers formed on glass show phase separation, provided there was phase separation in the initial monolayers before deposition.<sup>40,53</sup> Again when the temperature is cycled these domains do not re-form but a 'speckle' pattern is observed.<sup>40</sup>

## **7.10 Summary**

Nanoscale domains have been shown to form on glass, in lipid mixtures that form micron scale domains on mica and in GUVs. These domains have likely only been observed once before, despite the 100s if not 1000s of studies on phase separated lipid systems and of lipid bilayers on glass, due to the domains being below the resolution of diffraction limited optics. Molecular diffusion is not affected by the different surfaces, but instead it is likely hydrodynamic flow of groups of lipids and domains that is hindered on glass, preventing formation of micron scale domains. This is discussed in much more detail at the end of the next chapter, after reporting the effects of PDMS substrates on domain formation. There is a link between the micron scale domains formed on molecular smooth mica and the hindered domain formation on rough glass, as well as the hindered domain formation on mica roughened on the nanoscale. The effect of roughness on domain formation is further discussed at the end of the next chapter. There is a more thorough discussion of the results in this and the next chapter, and how they are related

to literature. There is also discussion regarding the potential mechanisms by which domain formation is hindered.

Although the effects of substrates on bilayer properties may only seem relevant in terms of understanding the limitations of a surface sensitive technique, which needs a substrate, there is a more important biological relevance too. The plasma membrane is not free floating but sits between the cytoskeleton and extracellular matrix polymer networks. With this in mind, supported bilayer systems may be more biologically relevant than free floating systems, with properties that better model the plasma membrane. In fact, substrates formed from polymers could be used to replicate the cytoskeleton and extracellular matrix, and design artificial membranes that more closely mimic *in vivo* membranes.



## **Chapter 8. Substrate Coupling in Supported Lipid Bilayers - PDMS**

### **8.1 Introduction**

A longer term aim of this project was to investigate how asymmetry and curvature are linked in lipid bilayers. Curvature is responsible for many in vivo processes such as controlling cell and organelle shape, vesicle and protein tethering, protein sorting and enzyme activation.<sup>139</sup> Curvature can be induced by changes in lipid composition, lipid asymmetry, conical shaped transmembrane proteins, insertion of hydrophobic protein motifs, peripheral protein scaffolding and cytoskeleton scaffolding.<sup>139,140</sup> It has been shown in model systems how  $L_d$  domains in  $L_o$ - $L_d$  systems align with areas of high curvature in supported double bilayers systems<sup>141,142</sup> and in GUVs<sup>121</sup>. The bending modulus of the  $L_d$  phase is much lower than the  $L_o$  phase, resulting in a lower free energy when the  $L_d$  domains align with high curvature.

It is not fully understood, however, how asymmetric bilayers would behave on curved surfaces. Would the high curvature areas remain symmetric in terms of domains, or would an AR state reduce the free energy? Could lipids be used with different positive and negative intrinsic curvatures, to design asymmetric systems where the localisation of AR is controllable? Over time, would the flip-flop of lipids between leaflets alter the asymmetry to reduce the free energy on the curved surface? These questions could be investigated by forming the AR bilayers formed on mica in this thesis, but on curved substrates. Langmuir-Blodgett Deposition could also potentially be used to make bilayers with forced asymmetry on curved substrates.

In order to investigate asymmetry and curvature, a topographically patterned substrate with controllable curvature is required upon which to form curved SLBs. PDMS (polydimethylsiloxane) is an optically clear polymer that is easy and fast to fabricate into a wide array of microscale and nanoscale patterns. PDMS has emerged as a versatile substrate for investigating bilayers because the surface can be easily patterned, mechanically deformed, and



curved.<sup>141,143–145</sup> PDMS was chosen to form curved substrates to investigate how asymmetry and curvature are linked. It will also be interesting, in light of the hindered domain formation on glass findings in the previous chapter, to observe how other substrates affect domain growth.

Before results are presented, the literature regarding the use of PDMS as a bilayer substrate will be summarised briefly.

## **8.2 Overview of PDMS as a Substrate for Supported Lipids Bilayers**

Hovis and Boxer first demonstrated lipid self-assembly on PDMS, with hydrophobic PDMS surfaces supporting monolayers and plasma oxidised hydrophilic PDMS surfaces supporting bilayers.<sup>143,144</sup> Oxidising the surface of PDMS using oxygen plasma, UV Ozone or chemical treatment, results in chemical and structural changes at the surface of PDMS. PDMS has a silicone backbone with methyl sidechains,  $[\text{Si-O}(\text{CH}_3)_2]_n$ . X-ray Photoelectron Spectroscopy (XPS) shows that after oxidation there is a decrease in carbon content, an increase in oxygen content, and silicon content remains similar.<sup>146–148</sup> There is also an increase in the number of Si-O bonds, with Silicon bonded to 3 or 4 oxygens instead of 2 as in unoxidised PDMS.<sup>146,148,149</sup> Volatile low molecular weight carbon compounds are lost to the atmosphere, while oxidative cross-links result in the  $\text{SiO}(\text{CH}_3)_2$  surface structure being replaced by a crosslinked silica network ( $\text{SiO}_x$ ). Silanol groups, Si-OH, at the surface result in a hydrophilic surface suitable for bilayer formation.

PDMS can be used for patterning bilayer arrays in chosen geometries. Oxidised PDMS stamps brought into contact with lipid bilayers results in the transfer of the bilayer to the stamp, that can then be printed onto a fresh surface.<sup>143,144</sup> PDMS is also being utilised to enable the mechanical stresses in cells to be mimicked.<sup>150</sup> The cell membrane is not isolated but sits between the actin cytoskeleton and the extracellular matrix, both elastic and dynamic polymer networks. This can be far more accurately modelled using PDMS compared to mica, glass or silicon substrates. Using flexible PDMS to controllably stretch and compress lipid bilayers, they have been shown to accommodate the strain by sliding, fusing with adhered vesicles and reversibly

opening pores.<sup>145,150</sup> Bilayers can also accommodate compression by forming membrane tubules/protrusions.<sup>145,150</sup>

### 8.3 Curved PDMS

A novel device (Figure 3.1) was developed to stretch PDMS, oxidise the surface and then controllably release the strain to form a curved wrinkled surface.<sup>91–94</sup> When the PDMS surface is oxidised, a brittle silica  $\text{SiO}_x$  layer is formed between 8-150 nm thick, dependent on oxidation method and conditions.<sup>147–149</sup> There is a modulus difference between the silica layer and the bulk PDMS below. If the PDMS is pre-strained before oxygen plasma exposure, when released post-oxidation the difference in moduli between the glassy surface and the elastic bulk causes nanoscale periodic sinusoidal wrinkles to spontaneously form on the surface, so long as a critical strain is overcome. This strain must also be below 200% as this is the breaking point of the PDMS. The inelastic surface layer cannot contract in conjunction with the underlying elastic bulk and so the excess surface area is compensated by the introduction of the surface waves. The wavelength and height of the

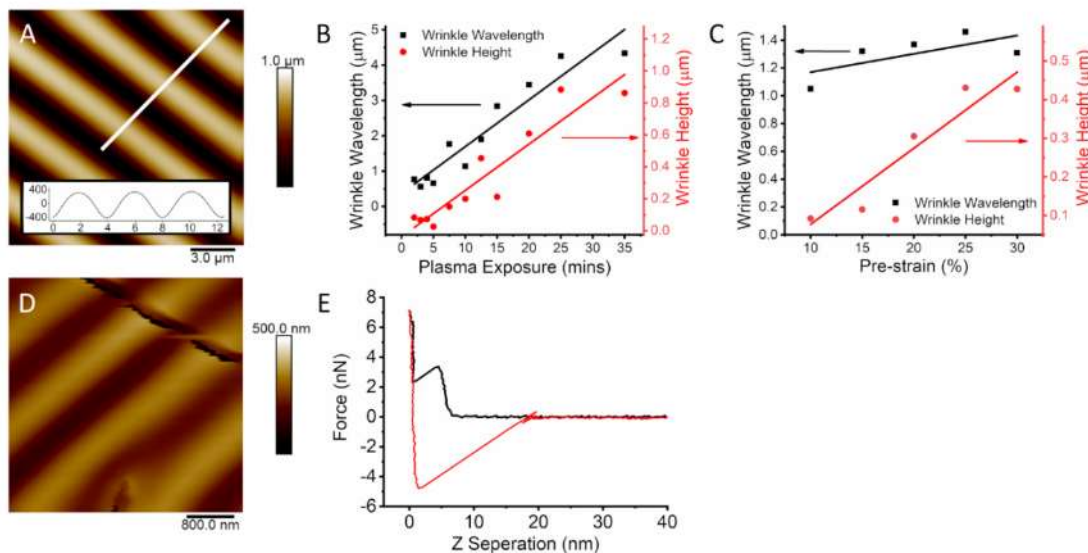


**Figure 8.1 AFM images showing curved PDMS A) An example AFM image of wrinkled PDMS formed with 15% pre-Strain and Oxygen Plasma for 25 min, inset is height line profile of the white line on the image B) Wrinkle wavelength and height as a function of oxygen plasma exposure time C) Wrinkle wavelength and height as a function of pre-strain (%) – For B and C a linear fit is provided as a guide to the eye. D) An example AFM image of a Sphingomyelin/DOPC (60:40) bilayer on wrinkled PDMS. E) Force curve on D showing the characteristic rupture of a lipid bilayer.**

wrinkles can be controlled by changing the amount of excess surface via two methods: i) the pre-strain (%) applied to the PDMS before plasma exposure, and ii) the depth of the inelastic layer by varying the oxygen plasma exposure time.<sup>91–94</sup> Strain release rate can also influence the surface waves, but in this study it was not possible to dial in a rate, and so this was controlled slowly by hand, in turning a micrometer screw.

The relationships between the experimental conditions and PDMS surface structure is described in the graphs in Figure 8.1. Wavelength and height followed a linear relationship with plasma exposure, i.e. both increasing relative to the surface layer thickness, up to a maximum wavelength of 5  $\mu\text{m}$  and height of 1  $\mu\text{m}$ . The ratio between wavelength and peak height was more controlled by the amount of pre-strain applied and using both factors the dimension of the surface waves could easily be controlled. Whilst this was undoubtedly a success, the smallest wavelengths achieved were on the order of 500 nm, with heights of around 50 nm which might not have had sufficient curvature to observe bilayer curvature effects. However, bilayers were successfully formed on the curved PDMS shown by the characteristic bilayer break-through using AFM force spectroscopy (Figure 8.1E).<sup>85,115</sup>

#### **8.4 Phase Separation on PDMS**

Despite literature reports of phase separation being observed in double bilayers on curved PDMS,<sup>141</sup> and GUVs ruptured on curved PDMS,<sup>151</sup> large scale phase separation was not observed in SLBs directly on PDMS, for mixtures that are well known to phase separate in GUVs and in SLBs on mica. Figure 8.2G shows a fluorescence microscopy image of a DPPC/DOPC (60:40) SLB incubated on flat PDMS and there is no observable phase separation, much like on glass. The only examples of phase separation directly on PDMS are from ruptured GUVs with phases already present before rupturing,<sup>151</sup> and potentially on curved PDMS after dynamic buckling once the bilayer has formed.<sup>152,153</sup> In this last case, there are no observable phases before this dynamic buckling and there are no publications showing phases from vesicle rupture on PDMS, despite this being common on mica. This is a curiosity considering how many published studies have looked at phase

separating systems in other model systems, and how common it has become to use PDMS as a bilayer substrate. PDMS is well studied in the literature and is being used and tested for many bilayer applications. It is therefore vital to understand the way it is affecting bilayer properties, specifically phase separation.

## 8.5 Phase Separation on PDMS shown by AFM

DPPC/DOPC (60:40) bilayers were prepared on plasma oxidised PDMS and nanoscale gel domains were observed using AFM (Figure 8.2). These domains however are not observable when imaged using fluorescent microscopy, as they are below the diffraction limit. The nanoscale domains on PDMS are in stark contrast to the micron scale domains on mica, but are similar to the domains observed on glass (as detailed in the previous chapter),

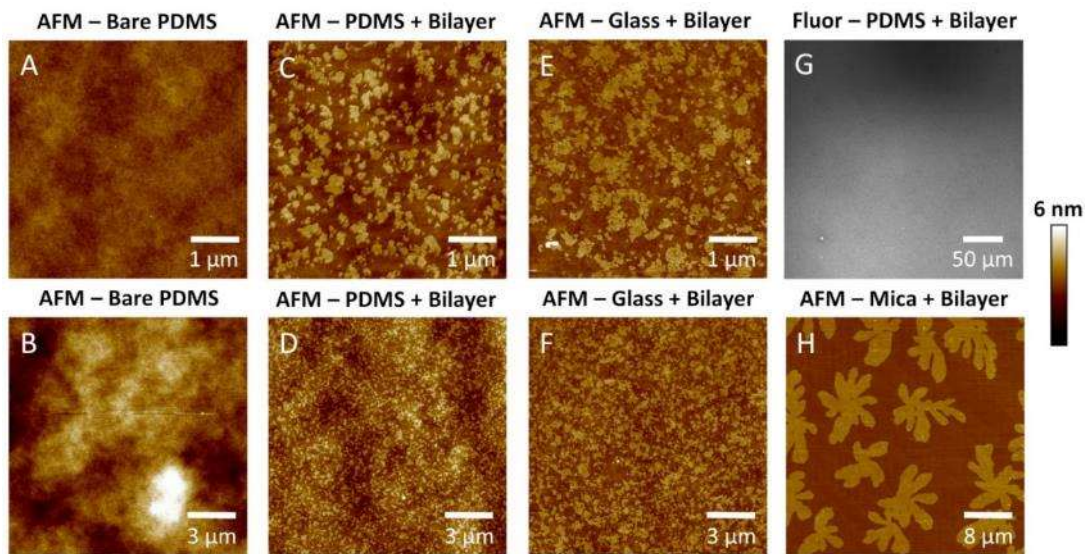


**Figure 8.2 AFM images of plasma oxidised PDMS with and without DPPC/DOPC (60:40) bilayers, and comparison to bilayers on Glass and mica. AFM images of plasma oxidised PDMS with no bilayer, A-5μm, B-15μm. AFM images of plasma oxidised PDMS with a DPPC/DOPC (60:40) bilayer showing nanoscale domains, C-5μm, D-15μm. C and D are not the same substrate areas as A and B, but relative examples.**

**AFM images of piranha and UV ozone cleaned glass with a DPPC/DOPC (60:40) bilayer showing nanoscale domains, comparable to those on PDMS, E-5μm, F-15μm. Fluorescence Microscopy image of plasma oxidised PDMS with a DPPC/DOPC (60:40) bilayer, showing an apparently homogenous bilayer, domains are below the diffraction limit, G-300μm. AFM image of mica with a DPPC/DOPC (60:40) bilayer showing micron scale domains, in contrast to the domains on PDMS and glass, H-40μm.**

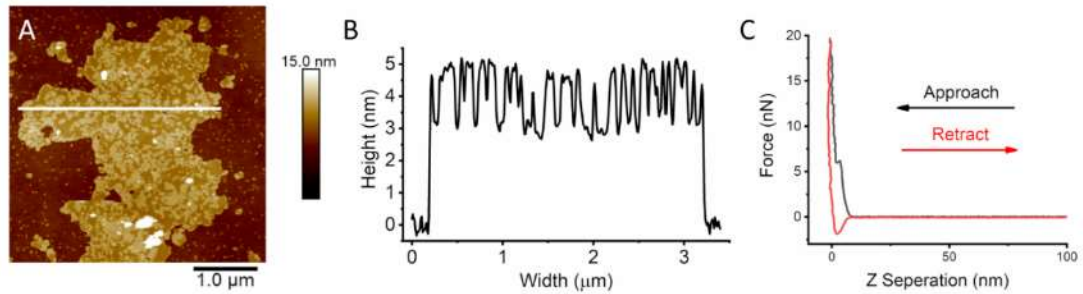


**Figure 8.3 AFM images of a patch of DPPC/DOPC (60:40) bilayer on PDMS. A) A patch of DPPC/DOPC (60:40) bilayer on PDMS showing phase separation B) Height line profile of white line in A showing the height of bilayer from the PDMS substrate and the height of the gel and fluid phases. C) An example of a force curve on a DPPC/DOPC (60:40) bilayer on PDMS showing the characteristic bilayer rupture.**

all using the same lipid mixture and incubation conditions. Patches of bilayer on PDMS confirmed the presence of bilayers, showing an overall bilayer height of 5 nm and a 1.5-2 nm height difference between the gel and fluid phases (Figure 8.3). Force Spectroscopy also confirmed the presence of a bilayer, due to the characteristic bilayer rupture at around 5 nN. Due to the small and partially attached and connected domains on PDMS, it was hard to fit individual domains to obtain a characteristic size. Correlation length was used, as for the nanoscale domains on glass in the previous chapter. The domains on PDMS are around 2 orders of magnitude smaller than the domains on mica (Table 8.1), and show rough corrugated edges compared to the fractal domains on mica. AFM shows clear phase separation on plasma oxidised PDMS surfaces, but the surface is clearly having an effect on the size and morphology of domains, much like on glass.

## 8.6 Lipid Mobility

To investigate the origins of the change in size and morphology of domains on PDMS, lipid diffusion was investigated. The diffusion of DOPC+ 0.5mol% TR-DHPE measured by FRAP on PDMS ( $1.04 \pm 0.03 \mu\text{m}^2/\text{s}$ ) was shown to be similar to both mica ( $0.96 \pm 0.04 \mu\text{m}^2/\text{s}$ ) and glass ( $1.02 \pm 0.04 \mu\text{m}^2/\text{s}$ ). This shows that molecular diffusion is not hindered on PDMS and so this cannot be affecting the size and morphology of domains. Blachon et al. have shown that increased nanoroughness can effect lipid mobility but this is for etched surfaces with higher roughness values than our substrates, over much larger

wavelengths.<sup>154</sup> Slowing the cooling rate from incubation temperature (50 °C) to room temperature, has been shown to increase the size of domains on mica<sup>44</sup> but not on glass as shown in the previous chapter. The correlation length of domains on mica increases by 46% as the cooling rate is slowed from  $0.25 \pm 0.02$  °C/min to  $0.080 \pm 0.008$  °C/min, (Table 8.1). The correlation length on PDMS does not increase as the cooling rate is reduced,  $49 \pm 7$  nm to  $37 \pm 8$  nm (Table 8.1). In fact it slightly decreases, although the two values are within error. This shows that even though the lipids have more time to diffuse and flow to form larger domains at slower cooling rates, the surface is acting to hinder the formation of large scale domains.

Substrate	Cooling Rate (°C/min)	Domain Radius (AFM)	Correlation Length (AFM)
Mica	$0.25 \pm 0.02$	$5.3 \pm 0.2 \mu\text{m}$	$2.26 \pm 0.4 \mu\text{m}$
Mica	$0.080 \pm 0.008$	$8 \pm 1 \mu\text{m}$	$3.31 \pm 0.09 \mu\text{m}$
PDMS	$0.25 \pm 0.02$	Domains connected so analysis fails	$49 \pm 7$ nm
PDMS	$0.080 \pm 0.008$	Domains connected so analysis fails	$37 \pm 8$ nm

**Table 8.1 Domain Sizes and Correlation Lengths for DPPC/DOPC(60:40) domains on Mica and PDMS, at different cooling rates from incubation temperature down to room temperature.**

## 8.7 Molecular Ordering of Bilayers on PDMS

To further investigate how the surface is affecting bilayer properties, the lipid transition temperature ( $T_m$ ) on PDMS was measured. As for glass, a DPPC SLB was formed on PDMS and FRAP was performed as the bilayer cooled (Figure 8.4). The FRAP recoveries were fit to exponentials to calculate Diffusion Coefficient ( $D$ ), plotted against temperature and then fit to a sigmoid to calculate  $T_m$ . The  $T_m$  is lower on PDMS,  $38.2 \pm 0.2$  °C, than for free MLVs measured by DSC,  $39.73 \pm 0.02$  °C. It is also lower than on mica,  $40.2 \pm 0.3$  °C, but similar to glass,  $38.6 \pm 0.2$  °C. The  $T_m$  is linked to the intermolecular attractions between lipid molecules and will be lower for a more disordered



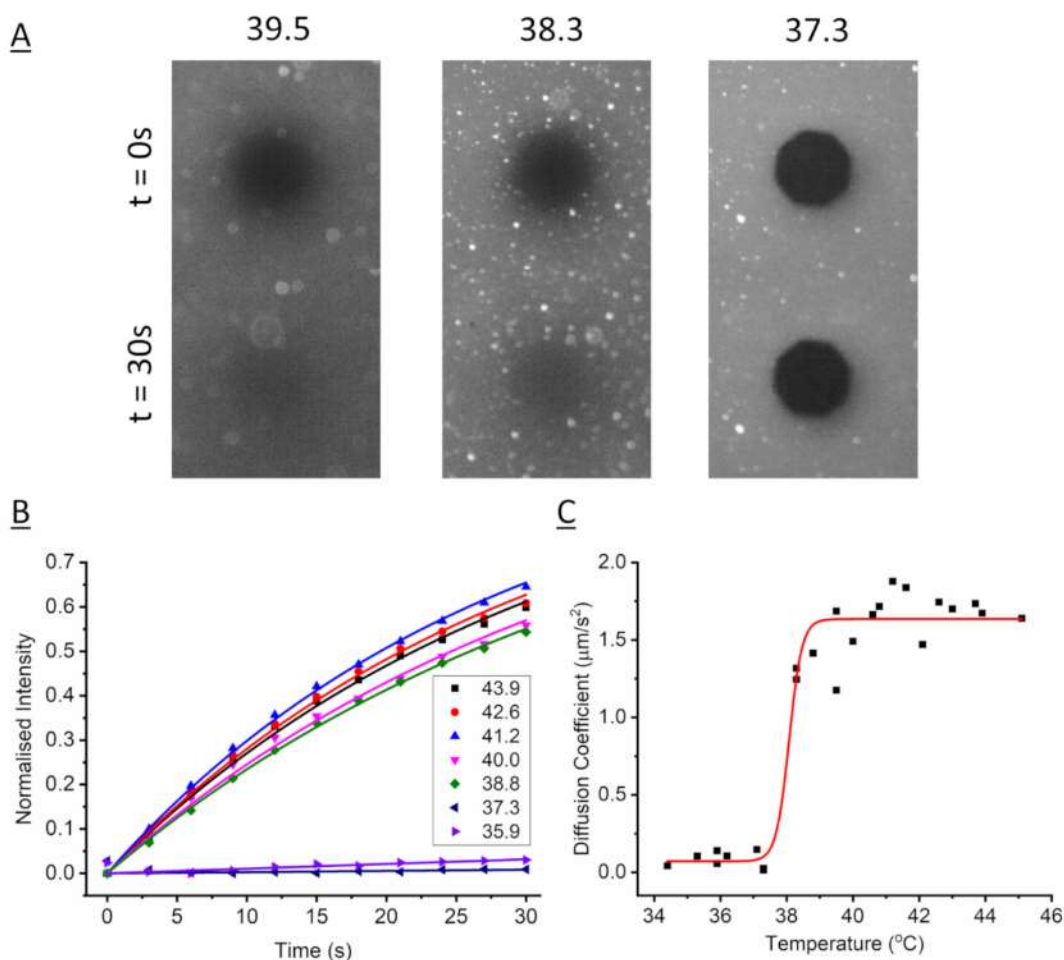


**Figure 8.4 FRAP on a DPPC+ 0.5mol% NBD bilayer on PDMS as the bilayer cools. A) An Example of Fluorescence Images at 0s and 30s after photobleach as the bilayer cools. Temperature is indicated above images B) An Example of fluorescence recovery curves over time at each temperature with exponential recovery fits C) Calculated Diffusion coefficient (D) at different temperatures, 3 repeat experiments (normalised) plotted on same axes. Data fitted to a Boltzmann sigmoid.**

system. Based on observations that rough glass surfaces are reflected in more disordered SLBs,<sup>39,128</sup> it is likely that the surface roughness of PDMS is being reflected in the bilayers thermal transition. Roughness is causing disorder in the bilayer and thus slightly reducing the transition temperature.

### 8.7.1 Lipid-Coated PDMS microspheres

Another method was attempted to measure the  $T_m$  of DPPC on PDMS, this time using DSC, a more traditional and established method for measuring the temperature and enthalpy of thermal transitions. However, the criteria for this

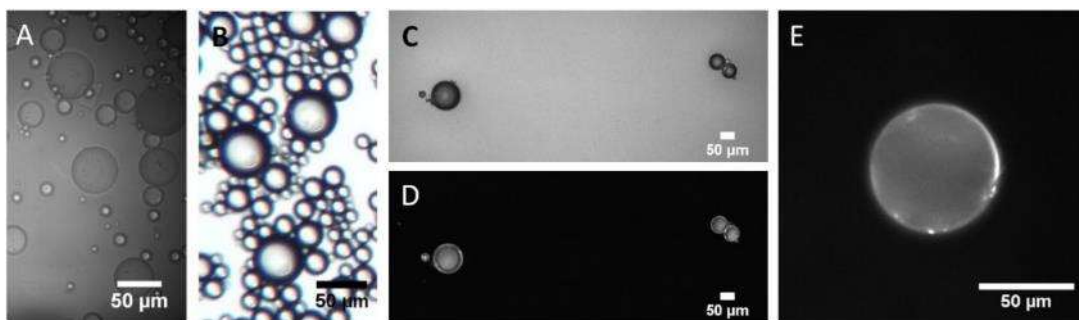


**Figure 8.5 Images of PDMS Microspheres with and without DPPC+ 0.5 mol% TR-DHPE bilayer coating. A) In water B) In air C)-E) Coated with DPPC + 0.5 mol% TR-DHPE bilayer. A and B are imaged using white light and C and D using TR fluorescence. All scale bars are 50µm.**

study was that the bilayers must be supported single layers on the PDMS which will inevitably cause sensitivity problems due to the nanogram mass of bilayer on a 1 cm<sup>2</sup> surface area. A solution developed was to coat small micro-particles or micro-spheres of the substrate under study to magnify the surface area. For this purpose we created microspheres of PDMS and deposited a bilayer on them using the standard vesicle fusion method. The PDMS microspheres (Figure 8.5A+B) were formed using emulsion polymerisation and were random in size, ranging from the optical limit < 1 µm up to 80 µm. These microspheres were then successfully coated with DPPC+0.5mol% TR-DHPE bilayers, with excess solution vesicles subsequently removed by gentle centrifugation and replacing the supernatant (Figure 8.5C-D). As far as the author is aware this is the first time single bilayers have been supported on PDMS microspheres, which could find uses in many areas, such as surface force or colloidal probe measurement on biomimetic systems, for molecular recognition measurements involving membrane proteins, and in tribology of biological systems, such as joints and in the mouth.

The lipid-coated microspheres were analysed using DSC to measure the  $T_m$ . This experiment was run twice, the first time a small peak at 41.8 °C was observed and the second time there was no peak at all. The data was inconclusive and this is probably because the amount of PDMS microspheres was insufficient to register a clear signal in the micro-calorimeter. Based on the observation that the  $T_m$  dropped on PDMS compared to free vesicles, it is likely that in the first experiment there were leftover vesicles in the solution that had not been washed away, resulting in the peak at 41.8 °C which



matches the peak in MLVs perfectly. For both sets of experiments it is likely that the concentration of the lipid on the particles was too low to be observed in the DSC. Based on the volume of microspheres by eye in the microscopy images and their packing, there was a maximum lipid concentration of 40ug/mL based on full coverage of each sphere. This is 25x more dilute than the 1mg/mL used for measuring pure DPPC, explaining why there was likely no signal. Based on the absence of any peaks in the second run, it is likely that the washing procedure was successful at getting rid of vesicles.

Lipid-coated PDMS microspheres could also have potential uses for high throughput screening against protein targets, similar to lipid bilayers supported on silicon nanoparticles.<sup>155</sup> Bilayers supported on PDMS microspheres may have additional benefits due to the ability to pattern the PDMS microsphere surface,<sup>95</sup> and also to mechanically deform the microspheres.

## **8.8 Hydrophobic Recovery**

The SLBs on PDMS showed disruption over time (Figure 8.6), with bilayer height defects appearing. This was not observed when the same mixture was incubated and imaged on glass or mica. Hovis et al. report seeing patches of bilayers coming off of PDMS SLBs on the hour/day timescale, which were not observed on glass.<sup>144</sup> Faysal et al. also observe large bilayer defects appearing by around 60 hours on PDMS using fluorescence, but not on glass.<sup>156</sup> We see holes appearing after around 6/7 hours, the resolution of AFM enabling us to observe the bilayer patches forming sooner than in the published optical microscopy observations.

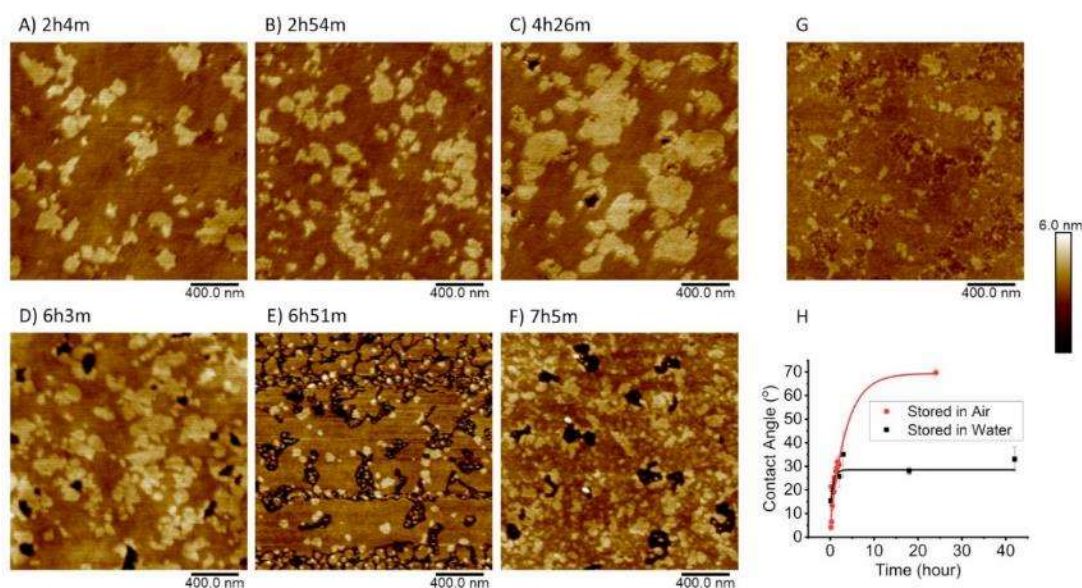


**Figure 8.6 The effect of PDMS hydrophobic recovery on DPPC/DOPC (60:40) bilayers. A)-F) AFM images of DPPC/DOPC (60:40) bilayers on plasma oxidised PDMS, showing nanoscale domains. The time after the PDMS was oxidised with oxygen plasma is shown above each image. The images show defects appearing over time as the bilayer becomes less mechanically stable. G) shows another example of how PDMS can destabilise the bilayer. H) Graph showing the contact angle recovery of oxidised PDMS over time when stored in water and in air. Exponential fits are included as a guide to the eye. Each experimental point is a separate piece of PDMS stored in water for the specified time, hence explaining the slight variability in contact angle and why it appears to drop at around 20 hours.**

It is well-documented that PDMS undergoes hydrophobic recovery over time.<sup>148,157–159</sup> When oxidised, the  $\text{SiO}(\text{CH}_3)_2$  structure is replaced by a cross-linked  $\text{SiO}_x$  silica structure with silanol groups at the surface, resulting in a hydrophilic substrate. The recovery is due to free unreacted monomers or low molecular weight oligomers in the bulk PDMS diffusing to the PDMS-air interface either through the microporous silica PDMS surface or through cracks in the PDMS surface.<sup>147,148</sup> This results in hydrophobic  $\text{SiO}(\text{CH}_3)_2$  and hydrophilic Si-OH groups being mixed on the nanoscale, as shown by XPS and Chemical Force Microscopy.<sup>148,160</sup> This is reflected in the gradual hydrophobic recovery as the ratio of hydrophilic silanol to hydrophobic methyl increases, and this recovery can be monitored using contact angle measurements (Figure 8.6H).

Untreated PDMS is hydrophobic with a contact angle of  $105\pm 1^\circ$ , but after oxygen plasma treatment the contact angle drops to around  $15^\circ$ , reflecting the higher proportion of silanol groups at the surface. This is hydrophilic but not as hydrophilic as mica ( $3.0\pm 0.2^\circ$ ) or glass ( $4.8\pm 0.4^\circ$ ). Fluid Bilayers have been reported to form up to approximately  $30^\circ$ .<sup>160</sup> Interestingly when the contact angle of PDMS stored in water over time recovers to above  $30^\circ$  at around 3/4 hours (Figure 8.6H). This is close to when the holes start to appear in the bilayers, 4/5hours. There is a clear link between the bilayer structure and the PDMS surface structure. Lenz et al. have also shown how contact angle of PDMS can be linked to bilayer structure and self-assembly.<sup>160</sup> By varying the extent of oxygen plasma to a PDMS surface they find that contact angles of  $109-110^\circ$  support lipid monolayers,  $98-100^\circ$  show no vesicle adsorption,  $60-62^\circ$  supports unruptured adsorbed vesicles and  $<20/30^\circ$  supports bilayers. The fact that they see no lipid self-assembly on intermediate PDMS hydrophilicities matches with our observations that a hydrophobically recovering surface becomes unstable to bilayers with defects appearing.

The hydrophobic recovery of PDMS in water is significantly slower compared to in air (Figure 8.6H), which matches literature observations<sup>158</sup>. The water PDMS recovery in water is closer to the situation where a bilayer is present at the interface than the recovery in air. The reason that hydrophobic residues such as unreacted PDMS monomer or short chain oligomers diffuse to the PDMS-air interface is to reduce the surface tension between the hydrophilic silanol groups and air. The thermodynamic drive for this diffusion and recovery is significantly reduced when the hydrophilic silanol groups are in contact with water. It is also likely that the hydrophobic recovery of PDMS with a bilayer film at the interface with water is slowed further, due to the hydrophobic lipid heads at the oxidised PDMS surface. This could not be tested due to bilayers being ripped from the surface when exposed to air, when taking contact angle measurements.

### **8.8.1 Attempting to slow down hydrophobic recovery**

Next, methods were investigated to try to slow the hydrophobic recovery of PDMS so that bilayers are longer-lived or permanent. For PDMS to be used to look at curvature and how this affects asymmetry, there may be effects that

take place on hour/day timescales, such as lipid flip-flop. Therefore longer lived bilayers on PDMS are essential, if this is to be studied without defects forming in the bilayers. As discussed in the last section, hydrophobic recovery of PDMS is due to unreacted monomers and short chain oligomers diffusing from the bulk PDMS to the surface. Therefore if these monomers are removed then, the hydrophobic recovery should not proceed.

First of all PDMS was soaked in  $\text{CHCl}_3$  or MeOH for 2 hours, in an attempt to wash out the free monomers. Neither of these washes slowed down the recovery compared to unwashed in air (Figure 8.7). Next a washing method suggested in the literature was attempted.<sup>156</sup> PDMS was sonicated in acetone, then IPA, then ultrapure water. However, the same procedure did not bring about a significant change in recovery. The published data was based on observation of bilayers on PDMS over time using fluorescence. When PDMS was washed using the stated method, the onset of defects (like those seen in Figure 8.6) is slowed compared to unwashed PDMS. However, this does not

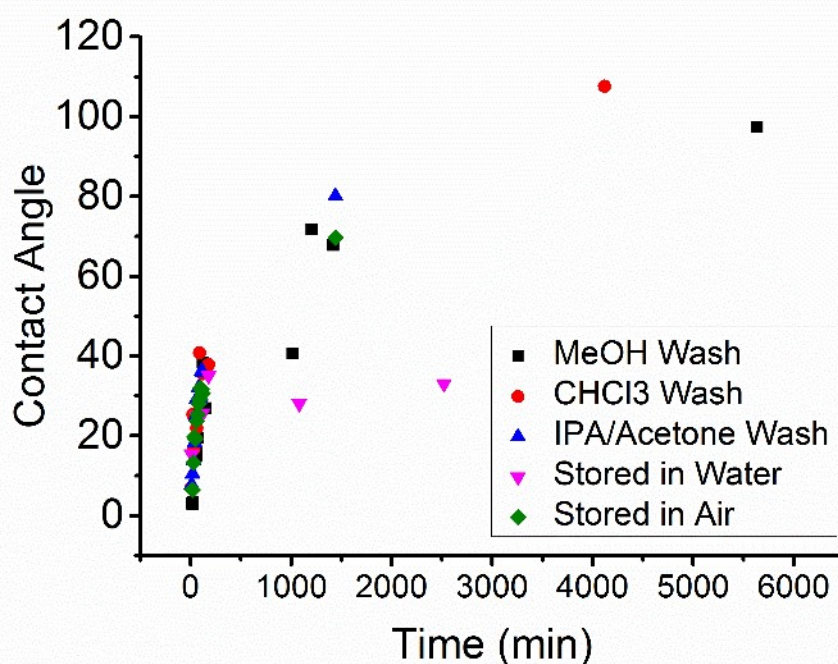


**Figure 8.7 Attempting to slow down hydrophobic recovery of PDMS using solvent washes, shown by contact angle measurements with time. Contact angle measurements over time for PDMS 1)washed in Methanol (MeOH) for 2 hours, 2) Washed in Chloroform ( $\text{CHCl}_3$ ) for 2 hours and 3) Washed in Acetone/IPA/Water for 30 min each in a sonicator bath. After the washes the samples were stored in air between measurements. The hydrophobic recoveries of PDMS stored in water and air are shown for reference.**

necessarily link straight to contact angle recovery, as measured here. The washed PDMS in Figure 8.7 was stored in air not water after oxidation and between measurements. Hydrophobic recovery in water is slower than in air, so perhaps in air the thermodynamic drive to recover is so large that the solvent washes have little effect. Stored in water, the recovery might have in fact been more hindered after the solvent wash compared to in air, however there was not time to perform these experiments.

Overall none of the washes of PDMS slowed down recovery. This may be due to the thickness of PDMS used. When the surface is oxidised with plasma, only a finite layer is oxidised and cross-linked, but it is dependent on power and oxidation time. Therefore the rest is bulk with unreacted monomer that can diffuse to the surface and cause PDMS to recover. The PDMS used for contact angle measurements and washes was approximately 5 mm thick, so there was lots of volume for monomer, and this was likely hard to completely wash out. Lawton et al. show that a thin spin-coated 30 nm piece of PDMS oxidised for 1 min shows drastically reduced recovery.<sup>161</sup> This is rationalised by considering the fact that a higher percentage of the thickness will be oxidised in a thin film, so there will be less bulk monomer to cause recovery.

Practical difficulties were encountered when trying to measure the contact angle of PDMS stored in water, to mimic bilayer formation conditions. Water drop contact angle measurements require a dry surface, so PDMS had to be dried before measurement. Therefore, during the time to take 3 repeat measurements (form droplet, deposit droplet and take picture), the surface with air will be recovering at a different rate. A better suited method would have been to measure the contact angle of an air droplet in a chamber of water. This would remove the practical constraints on this experiment and ensure that all hydrophobic recovery occurs while PDMS is in contact with water. There was not access to equipment for air-in-water contact angle measurements, and not time in this project for developing this new technique.

## **8.9 PDMS Surface Structure and Roughness**

The surface structure and roughness of PDMS were measured from AFM images, to assess the potential impact on bilayer structure and phase

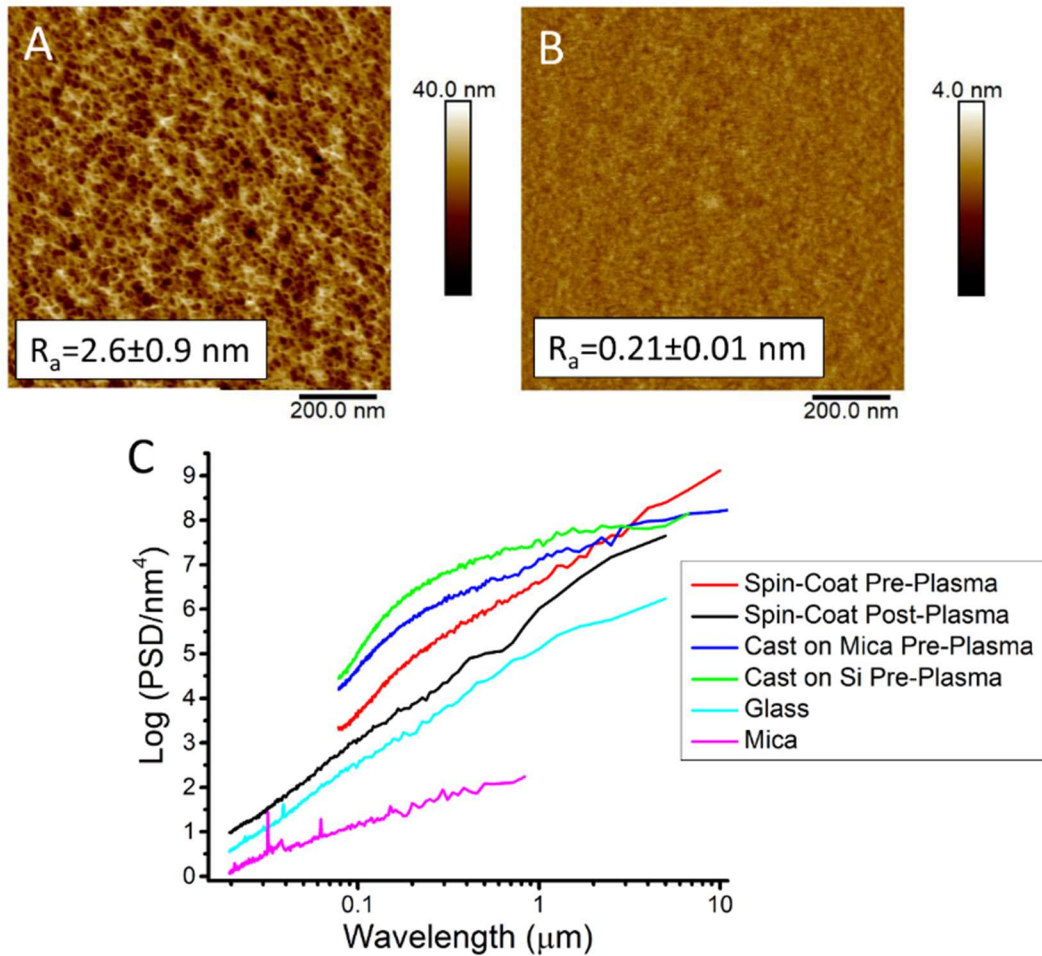


**Figure 8.8 AFM images of PDMS structure and roughness measurements pre and post oxygen plasma treatment. A) AFM image of spin-coated PDMS pre oxygen plasma B) AFM image of spin-coated PDMS post oxygen plasma C) Power Spectral Density plotted against wavelength to quantify the relative roughness values over different length scales. PDMS samples are spin-coated pre and post oxygen plasma, and cast against mica and silicon pre oxygen plasma. Mica is after cleaving. Glass is after Piranha and UV ozone Clean. Note the roughness is plotted on a log scale.**

behaviour. Figure 8.2A-D show that the waves and corrugations in the PDMS can also be seen in the bilayer images, showing that the bilayer is mapping to the micron scale surface features of PDMS.<sup>153,154</sup> when imaging cured PDMS before plasma treatment, there is a honeycomb-like polymer structure with 10-20 nm pores (Figure 8.8). This reflects the porous nature of PDMS, and the origin of its low modulus, being reminiscent of gel or hydrogel structures, such as Agar and Poly-acrylamide used in gel electrophoresis. This surface morphology can also be considered to be extremely high aspect ratio features, with deep holes and sharp protruding side-walls, and it is highly likely that this



surface structure contributes to the hydrophobicity of PDMS, much in the same way as nano-structured surfaces can be designed to be super-hydrophobic.

After oxygen plasma treatment this structure disappears, and the surface roughness drops by around an order of magnitude, shown by  $R_a$  roughness measurements ( $2.6 \pm 0.9$  nm to  $0.21 \pm 0.01$  nm, both over  $1 \mu\text{m}^2$  images).

A more powerful method for comparing roughness is using power spectra, which show the power of different length scale fluctuations in the 3D topography of a surface, or in other words, the roughness as a function of feature size. This is important because the average  $R_a$  value is usually dominated by large wavelength undulations, and might not report on the smaller and potentially more important scales that affect bilayers. The power spectra in Figure 8.8C clearly show that post oxygen plasma, roughness is lower across all length scales measured, 100 nm - 5  $\mu\text{m}$ , compared to pre-oxygen plasma. This matches the  $R_a$  roughness measurements but allows characterisation and comparisons of all measured length scales and not the average over the whole image size.

When the PDMS surface is exposed to oxygen plasma,  $\text{SiO}(\text{CH}_3)_2$  groups are replaced by a silica structure with increased cross-linking Si-O bonds. The disappearance of the honeycomb polymer structure and the drop in roughness is the topographical result of this chemical change in the polymer structure. Hillborg et al. report diffusion of PDMS oligomers through non-cracked PDMS

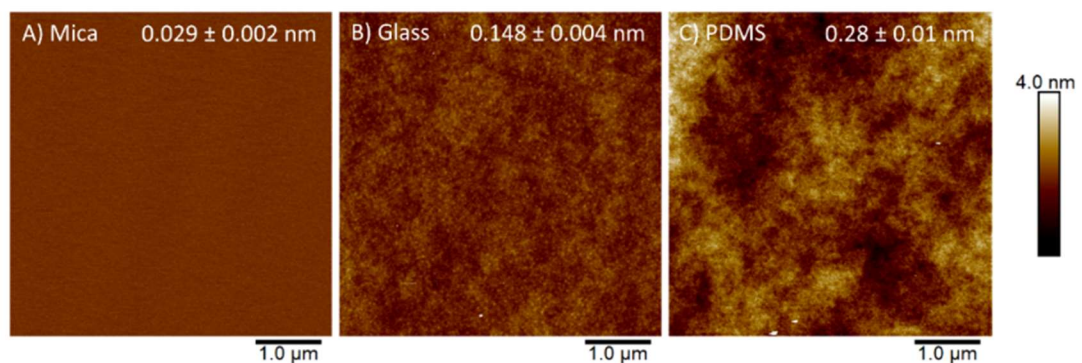


**Figure 8.9 AFM images of mica, glass and PDMS substrates with no bilayers. A) Mica after cleavage B) Glass after Piranha and UV Ozone clean C) PDMS after oxygen plasma.  $R_a$  roughness values are quoted in the top corner of each image and are averages with standard errors across multiple  $5 \mu\text{m}$  images.**

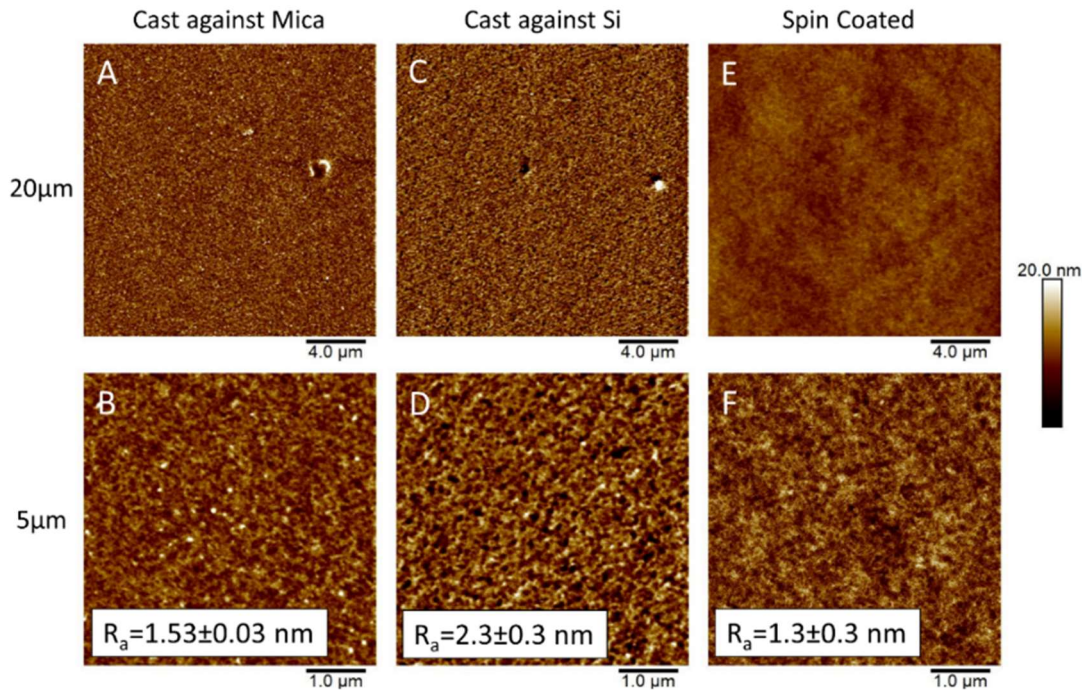


**Figure 8.10 AFM images of PDMS structure cast against mica, silicon and spin coated. A)+B) PDMS Cast against Mica C)+D) PDMS cast against Silicon wafer E)+F) Spin-coated PDMS. A),C) and E) are 20  $\mu\text{m}$  images. B), D) and F) are 5  $\mu\text{m}$  images. The roughness values quoted on the 5  $\mu\text{m}$  images are average values from multiple 5  $\mu\text{m}$  images.**

to cause hydrophobic recovery. It is likely that there is still a microporous structure in the PDMS surface silica layer, otherwise the molecules would not get to the surface and cause the surface to recover. However, the structure is likely at a length scale that is hard to observe.

Despite this reduction in roughness with oxygen plasma treatment ( $0.21 \pm 0.01$  nm), the roughness of PDMS is still an order of magnitude higher than mica after cleavage ( $0.029 \pm 0.002$  nm), and the same order of magnitude but slightly rougher than glass after Piranha and UV Ozone ( $0.148 \pm 0.004$  nm). This can be seen in Figure 8.8C, showing the power spectra of the three surfaces, with PDMS clearly rougher than mica and glass across all length scales. The side by side raw images are shown in Figure 8.9 on the same Z scale, and the differences in roughness are clear to see. The roughness values and power spectra reflect the surface immediately before bilayers are incubated on the substrates.

Relating roughness back to phase behaviour, there is a clear correlation between the micron scale fractal bilayer domains that grow on atomically



smooth mica, and the rough nanoscale domains that form on the molecularly rough PDMS surface. This matches the findings on glass. Mica roughened on the nanoscale, using HF to form 1nm steps, hinders the formation of micron scale phase separation (as shown in the previous chapter). We attempted to render PDMS smoother by casting and curing against mica and silicon, which would then allow us to observe if larger phase separation could occur. The PDMS was actually rougher over the 100 nm - 3  $\mu$ m scale than the spin-coated PDMS, although it was flatter over  $>3\mu$ m (Figure 8.8C). This can be seen in representative images in Figure 8.10, with the surface structure appearing similar for PDMS cast against silicon and mica as for spin-coated, except the micron scale corrugations in spin-coated PDMS. This shows that the limiting factor is the polymer structure of the PDMS formed during the crosslinking/curing process, and despite being able to mould PDMS to different shapes, this is usually on the micron scale and not at the molecular scale. Therefore, it was not possible to investigate phase separation on smoother PDMS, and it is unlikely that it will ever be possible to study phase behaviour directly on PDMS. More permanent solutions to the hydrophobic recovery of PDMS have recently been proposed, for example by coating with hydrophilic PVA and it is possible that this surface could be made smooth enough to allow bilayer deposition and maintain bilayer fluidity.<sup>162</sup>

## **8.10 Implications for Phase Separation on PDMS Substrates in Published Literature**

Domains have clearly been visualised with AFM on PDMS (Figure 8.2). Despite there being thousands of papers on phase separation in SLBs and many groups working on bilayers on PDMS, it is telling that we can only find a single group, that of Parikh claiming to show phase separation of SLBs on PDMS.<sup>152,153</sup> They form bilayers with known phase separating mixtures on pre-strained PDMS, which they then release to form wrinkles. This is in a similar fashion to the surface shown in Figure 8.1, but the bilayer is formed prior to the wrinkling. Before wrinkling there are no domains observed optically, matching to our findings. They say that the wrinkling causes a dynamic domain reorganisation, leading to domain formation. The domains

are characterised by an absence of fluorophore, but the domain size and morphologies observed do not match any previously observed (on which the authors comment), or of the domains we have observed on PDMS in this study. Whilst they go to great lengths to prove these domains are  $L_0$  phase with complex labelling and binding experiments, we believe what is actually happening is local compression and rarefaction of the lipid bilayer. It is unable to flow on the PDMS surface and therefore holes open up in the low bilayer density areas, which also explains the correspondence with their pattern direction. With this one exception, we have found no other literature showing domain formation on PDMS. It is likely that the nanoscale domains that form on PDMS have not been observed because they are below the diffraction limit of the optical fluorescence techniques used so commonly in bilayer studies. Many researchers have likely attempted to form phase separating bilayers on PDMS but have been unable to observe them without specifically looking for them with high resolution techniques such as AFM.

There is one study that uses PDMS to investigate how phase separated domains align on curved substrates, but for this they used a double bilayer.<sup>141</sup> The decoupling from the substrate cited as the reason for double bilayers, was perhaps in part due to initial experiments where no phase separation was observed in a single SLB of a known phase separating composition. Reproducible production of double bilayers is extremely difficult to achieve, and seemingly limited to particular lipid systems, so is not universally applicable as a method of studying lipids on PDMS.

Finally, a recent paper from the group of Staykova investigates the effect of PDMS expansion and contraction upon a supported bilayer.<sup>145</sup> They do so on both PDMS which is only mildly treated with plasma and somewhat hydrophobic (water contact angle 35-60°), and on hydrophilic PDMS that fully wets. Lipid was clearly bound tightly to the more hydrophobic surface (their “sticky membrane” surface), probably due to the minimal lubricating interstitial water layer and hence close proximity of the bilayer to the surface. This leads to the behaviour of membrane patches rupturing upon PDMS expansion, but then rather than reforming upon compression would induce out-of-surface bilayer tubes to form. Sliding is prohibited. Conversely, the bilayer on hydrophilic PDMS (“sliding membranes”) exhibited complex decoupled

behaviour that could not be fully explained. Whilst the sliding membrane could cope with 10% PDMS expansion, after this pores began to open up, but they would reform once the PDMS returned to its original size. However, the motion of the domain boundaries is anomalous, with some areas constant, other regions seeming to flow, on a fine length scale (according to optical microscopy). Upon cycling of expansion and compression the same patch boundary would be recreated, and this could not be explained. From the work in this thesis, it is clear that the PDMS surface has a particular structure which hinders bilayer hydrodynamic flow (but not diffusion) via pinning. This controls how and where the bilayer will flow, and where it becomes fixed. In this fully hydrophilic surface the bilayer can flow to small degree but the flow pattern will be controlled by the underlying nanoscale topography of the PDMS. They also observe that membrane patch-substrate friction is area dependent, as would be expected in any friction scenario. Our interpretation is similar, but is more due to the density of local pinning sites in the PDMS.

### **8.11 Summary of PDMS Substrate Coupling**

Phase separated domains form on PDMS, but they are nanoscale and below the diffraction limit of optical microscopy. This is likely why these domains have not been observed in the literature before. The rough-edged, nanoscale domains observed on PDMS are in stark contrast to the micron scale fractal domains observed on mica with the same lipid mixture, but match closely with domains observed on glass. Molecular diffusion is not significantly affected by the different substrates, but it is the hydrodynamic flow of lipid domains that is hindered. The roughness of PDMS is similar to glass, and this is likely a cause for the hindered domain formation. A decrease in transition temperature ( $T_m$ ) on PDMS compared to free vesicles and mica was also observed, attributed to induced disorder in the bilayer from the rougher surface. Again, this matches observations on glass. There is also a link between the surface properties of PDMS and its hydrophobic recovery after oxidation, to the formation of defects in the bilayer with time.

The PDMS findings in this chapter may have implications beyond membrane biophysics. The high-resolution images of the rough and porous surface

structure of cured PDMS changing to a smoother less rough and porous structure after plasma treatment, and the link to the surface chemistry, will be of interest to any researcher using PDMS. The finding that the polymer structure of PDMS has a limiting intrinsic structure despite being cast against atomically flat mica, will have ramifications for anyone trying to use PDMS for any patterning on the nanoscale.

## **8.12 Overall Substrate Discussion Points**

### **8.12.1 Roughness affects Bilayer Structure**

Blachon et al. show how increasing the roughness of glass and silicon substrates from 0.1-3 nm using etching methods, decreases fluid phase bilayer diffusion 5 fold.<sup>154</sup> Goksu et al. also show reduction in diffusion on 0.71 nm roughness silicon xerogels compared to mica.<sup>163</sup> The proposed mechanisms for this decrease in diffusion on rough surfaces are based on the observation that bilayers have been shown to map to the surface topography, as shown using AFM and Neutron Reflectometry.<sup>153,154,164,165</sup> These mechanisms are;

- 1) Curvature induced areas of ordered bilayer with slower diffusion coexisting with the bulk fluid phase to reduce average diffusion<sup>154</sup>. The coexistence is below optical resolution, hence an average diffusion value.
- 2) Curvature induced holes if the curvature is too high (radius of curvature is <40 nm) and the bilayer cannot curve over the features.<sup>154</sup> This reduces diffusion.
- 3) Hidden area effects due to the vertical component of diffusion up and down the side of rough features.<sup>154,165</sup> Vertical diffusion does not appear in the lateral diffusion measurements.

The roughness values of mica (0.029 nm) and glass (0.148 nm) in this thesis follow on from the lower range investigated by Blachon et al. (0.1-3 nm), and there is no reduction in diffusion between mica and glass. This suggests at these small roughness values, there are no sufficiently high curvature areas to introduce the mechanisms discussed above.

AFM observations show that bilayers are rougher on rougher glass and silicon compared to mica,<sup>39,128,163</sup> CG simulations show that molecular scale corrugations 0.3 nm in height and width decrease the degree of periodic bilayer ordering,<sup>166</sup> and the FRAP experiments in this thesis showed that  $T_m$  and thus lipid ordering was reduced on rougher glass compared to mica. These results suggest that relatively low underlying substrate roughness values are being transferred through the interstitial water layer and being observed through the bilayer.

The lateral dimensions of surface roughness are also important. For 1-10 nm surface features, the bilayer does not simply follow the surface curvature,<sup>163</sup> and bilayers can span across pores that are less than twice the bilayer width (around 8-10 nm).<sup>167</sup> This all suggests if the roughness is a small percentage of the lipid bilayer height and the lateral separation between roughness peaks is small compared to bilayer dimensions, instead of curving to follow the surface corrugations of the surface, the roughness induces disorder in the bilayer.

### **8.12.2 Substrate Roughness affects Hydrodynamic Lipid Flow and Domain Formation**

There is a clear correlation between the micron scale fractal domains that form on atomically smooth mica and the rougher nanoscale domains that form on PDMS and glass. Molecular diffusion of lipids is not significantly affected by the different substrates. Slower cooling rates, allowing more time for the lipids to diffuse, results in larger domains on mica but not on glass or PDMS. This suggests that the rough surfaces are limiting the hydrodynamic motion of domains and pinning them to a limiting length scale. Radler et al. show that lipid spreading velocity is 1-2 orders of magnitude slower on glass than on mica and this is attributed to the increased roughness on glass.<sup>168</sup> The surface of PDMS is rougher than glass but a similar order of magnitude. As both the rough PDMS and glass surfaces result in hindered domain formation while smooth mica does not, this is strong evidence that the roughness is the cause of the hindered domain formation. Mica deliberately roughened on the nanoscale also hinders domain growth to a similar length scale.

There are several mechanisms by which roughness can affect domain formation and lipid flow;

- 1) The rough surface provides local pinning sites, where the substrate to bilayer distance is smaller and the interaction is larger.<sup>168</sup> These sites increase the friction on the bilayer, and reduce the hydrodynamic flow of groups of lipids and domains.
- 2) Rougher surfaces mean more highly curved areas. For a bilayer to maintain the same positive Van der Waals attraction to the surface it must curve over the surface, which involves an energy penalty for bending.<sup>106</sup> If this energy penalty is too high then domains will not be able to flow over this area. Gel domains have a higher bending modulus than fluid phases due to their tightly packed solid structure, and so gel domains will have a larger energy penalty to flow over molecularly rough and curved areas. For large scale surface corrugations with low curvature (large radius of curvature), the bilayer follows the surface corrugations due to the low bending penalty. This is seen in bilayers on PDMS (Figure 8.2) and also in literature.<sup>153,154</sup> For smaller scale molecular roughness where the curvature is higher (lower radius of curvature), the hydrodynamic flow of gel domains can be significantly hindered due to the energy penalty for flowing over a curved area. This may be having an affect here but the molecular scale roughness is likely having more of an effect on the overall bilayer order than the hydrodynamic flow, as shown by the decreased  $T_m$  on rough surfaces.
- 3) There is a thin lubricating water layer between the SLB and the substrate. Changes in the structure of this water layer due to pH have been shown to affect the spreading of groups of lipid, due to the change in flow and lubrication.<sup>106</sup> It is likely that the structure of this water layer is different on substrates of different roughness values i.e. mica, PDMS, glass. The rough surfaces could disrupt the flow of water and in turn disrupt the hydrodynamic flow of groups of lipids and domains. The local pinning points discussed earlier could also disrupt the water flow. An important consideration is this thickness of the lubricating water layer, which for SLBs is around 0.3-2 nm.<sup>106,154</sup> Blachon et al. show that the thickness of the interstitial water layer does not change on silicon surfaces as roughness is

increased.<sup>154</sup> It is not known however, how the thickness of this layer changes between different substrates. The thickness and structure of the water layer on different substrates could be affecting the flow of lipid domains.

It is likely a combination of the effects discussed and further experiments are needed to isolate the specifics of the physical mechanisms by which roughness effects lipid flow and domain formation. It is clear however that the hydrodynamic motion of lipid domains is hindered on the rougher PDMS, and the rougher glass. After incubation, the single phase bilayer is cooled to room temperature. As the temperature reaches  $T_m$  gel phases begin to nucleate out. On the atomically flat mica, once a gel domain has nucleated, it is able to grow to micron size via lipid diffusion and by hydrodynamic lipid flow. Small gel domains can flow and join together to form larger domains via coarsening (flow) or Ostwald Ripening (diffusive). On rougher substrates such as PDMS and glass however, there are lots more sites for nucleation due to the roughness surface. This results in a larger number of domains. As these domains grow, they reach a critical size where they become pinned to the local surface roughness, to the higher pinning point. This friction, due to the pinning sites, curvature and interstitial water, scales with domain area. As the domains become immobile, they are not able to flow and join together to form larger domains. The simulations of Ngamsaad et al. show that the asymmetric bilayer leaflet dynamics induced by proximity to a surface, result in a limited characteristic domain size in phase separating mixtures.<sup>169</sup> Two 2D fluids capable of phase separation are made dynamically asymmetric, where phases can grow diffusively in one leaflet and by hydrodynamic flow in the other leaflet. This matches the situation in an SLB we have been describing where the lipids in contact with the substrate cannot grow by hydrodynamic flow. Due to a coupling of domains across the two leaflets, i.e. an energy penalty for misaligned AR domains, domains become pinned across the two leaflets and the size of the domains in both leaflets is limited to a characteristic size,  $L_{pin}$ .<sup>169</sup> Although this model does not account for the roughness of different substrates, it is consistent with our findings that domain length scales are limited due to the frictional effects of substrates. The length scale just varies on different substrates.

### 8.12.3 Leaflet Decoupling due to Substrate

SLB substrates can potentially affect the proximal (bottom) leaflet more than the distal (top) leaflet, resulting in decoupling of physical properties. Recent Single-Particle Tracking (SPT) experiments have shown two separate diffusion coefficients for a DOPC bilayer on glass, the slower attributed to the proximal bilayer leaflet.<sup>120</sup> FCS experiments of DOPC however show no clear decoupling of the two leaflets on mica or glass<sup>29,36</sup> Several studies have also shown that decoupling of leaflet dynamics may be substrate dependent, with decoupling on mica but not glass or silica.<sup>37,128</sup>

Lipid dyes may be excluded from the proximal leaflet of a SLB, due to steric constraints with the surface or the more tightly packed proximal leaflet. Based on Fluorescence Interference Contrast Microscopy (FLIC) and Fluorescence Quenching experiments, the TR-DHPE dye is likely partitioning 70-78% into the distal bilayer leaflet in the DOPC fluid lipid system used in this thesis, and the NBD 16:0 PE 50:50 between the two leaflets.<sup>55,56</sup> Therefore an average of the two leaflets is observed when measuring diffusion, and it is not possible discern if there is dynamic asymmetry. Diffusion decoupling is possible and further studies may link asymmetric lipid dynamics to domain formation.

Decoupling of the leaflet melting transitions ( $T_m$ ) have also been reported multiple times for DPPC and DMPC SLBs on mica by AFM, the results summed up nicely by Giocondi et al.<sup>19,134,170-173</sup> The  $T_m$  transitions are broad with the lower of the two decoupled transitions between 41-52 °C and the higher between 46.5-60 °C. The values from the different studies vary significantly within these ranges, with the lower range just above the  $T_m$  of MLVs. DSC of DPPC supported on mica chips also shows two transitions but closer together at 42.4 °C and 44.8 °C.<sup>174</sup> There is a possibility that if the decoupled transitions are close in temperature then this might be hard to observe with the temperature resolution of the FRAP cooling experiments (around 1°C).

The FRAP with temperature results in this thesis show only one transition on mica, glass and PDMS up to a temperature of 55 °C, which is above the onset of all upper temperature decoupled transitions reported. The dyes are present in both leaflets, so decoupling of  $T_m$  should be observed if it is occurring. For



mica, glass and PDMS the fluorescence did not show partial recovery during the transition, which would be indicative of one leaflet crystallising and its diffusion dropping earlier than the other. Instead they showed close to total recovery above  $T_m$  and close to no recovery below, meaning both leaflets have gone through the transition. Literature FRAP studies with temperature show similar results with no decoupling of  $T_m$ .<sup>37,129,130</sup> Also, on mica DPPC crystallises from liquid to gel excluding the dye in a single event, not two (Figure 7.6). Both the crystallisation and the growth are coupled across the leaflets.

#### 8.12.4 Cytoskeleton

The limitation in domain sizes in SLBs compared to GUVs is due to asymmetry introduced by the surface. In vivo the cytoskeleton, a dense layer of actin filaments which is pinned to the membrane by protein interactions, can potentially provide this asymmetry. Macroscopic optically resolvable phase separation is not observable in the plasma membrane of cultured mammalian cells, but is observable in induced Giant Plasma Membrane Vesicle (GPMVs) from these same cells.<sup>175</sup> GPMVs have lipid compositions similar to the mammalian cell but are free from the cytoskeleton. This provides evidence that the presence of the cytoskeleton is a factor in restricting macroscopic

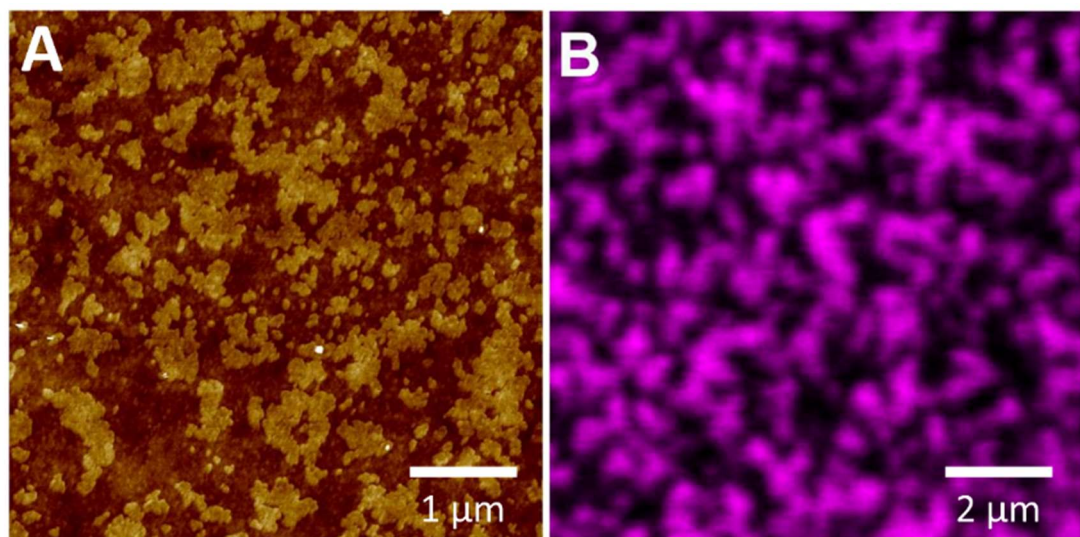


**Figure 8.11 Comparison of Hindered Domain Formation to Domains formed by pinning of a cytoskeleton to the bilayer. A) DPPC/DOPC (60:40) bilayer on glass B) From reference<sup>42</sup> showing DPPC/DOPC/Chol bilayer domains when biotinylated lipid streptavidin complexes are used to pin an actin meshwork to the  $L_o$  and  $L_d$  phases.**

phase separation. Simulations have linked how the phase separation of membranes, some of them critically fluctuating, is affected by the presence of cytoskeleton-like pinning sites.<sup>176–179</sup> Honigmaan et al. show experimentally the effect that pinning a minimal cytoskeleton to a DPPC/DOPC/chol mixture has on phase separation.<sup>42</sup> They show nanoscale domains restricted from growing to the micron scale by pinning of the cytoskeleton, like in the simulations. When they add pinning sites to both the  $L_o$  and the  $L_d$  phase via biotin-streptavidin links, the nanoscale phase structure is strikingly similar to the phase separation we see in our study on glass (Figure 8.11). Although curvature has been proposed as a possible mechanism for this nanostructure, we show that roughness on a smaller scale can provide the same nanoscale structure as the cytoskeleton, suggesting that the rough glass acts to pin domains much like the cytoskeleton. It should also be noted that there are several other proposed mechanisms for why macroscopic phase separation is limited in vivo, and like most biological cases it is likely a combination of several factors.<sup>175</sup>

As the membrane biophysics community search for more accurate and controllable models for the cell membrane it is important to try to replicate the effects of the polymeric networks of extracellular matrix and actin cortex supporting the outer and inner surfaces of the lipid bilayer. The nucleation of domains could be effected by the properties of the cytoskeleton and extracellular matrix. This implies strongly that the cytoskeleton could be hindering the formation of large scale domains, much like the roughness of glass in this study. The next stages would be to look at bilayers on a range of polymeric substrates that could have properties controlled to match those of the surfaces in contact with cell membranes.

### **8.12.5 Summary of Substrate Coupling Chapters**

Blachon et al. have shown how increasing substrate roughness of silicon and glass using etching between 0.1-3 nm reduces bilayer diffusion 5-fold.<sup>154</sup> For commonly used bilayer substrates with common preparation procedures, such as piranha cleaned glass and cleaved mica, the roughness values are 0.148 nm and 0.029 nm. At this scale, molecular diffusion is not affect by the substrate, likely due to the absence of high curvature features on the smoother

surfaces to induce ordering or holes in the bilayer. Instead hydrodynamic flow of groups of lipids and domains is hindered on rough surfaces, preventing the formation of micron scale domains. The mechanism by which the roughness reduces hydrodynamic flow is not fully understood but it is likely a combination of increased interactions through pinning points, bending energy penalties for flow over high curvature surface features, and disrupted flow in the interstitial water layer. Electrostatics may also effect domain formation. Salt concentration has been shown to have an effect on diffusion,<sup>129</sup> and changes in pH can affect water structure and flow, which can affect hydrodynamic flow of domains.<sup>106</sup> Further study is needed to investigate how varying salt concentration affects domain formation.

Decoupling of diffusion or  $T_m$  between the two bilayer leaflets was not observed in our study, but both have been observed in the literature.<sup>120,128,134</sup> There is still much to understand regarding asymmetry in physical bilayer properties, coupling between the two leaflets, how asymmetry and coupling link to domain formation and how all of this is affected by different substrates.

The hindered domain formation presented in this thesis for gel-liquid systems is also observed when a minimal cytoskeleton network is pinned to a fluid-fluid phase separating SLB.<sup>42</sup> Rough surfaces like glass and PDMS can act to pin domains and restrict their growth similarly to the cytoskeleton in vivo. Despite SLBs being altered from their equilibrium state and from the simpler biophysical models of GUVs, the supported systems may actually be more accurate models for in vivo membranes. As the membrane biophysics community search for more accurate and controllable models for the cell membrane, it is important to try to replicate the effects of the extracellular matrix and the actin cortex polymer networks.

## Chapter 9. Conclusions and Future Work

### 9.1 Conclusions

There is a puzzling disparity between the asymmetry of the plasma membrane and the symmetry observed in model lipid membranes. For phase separation in self-assembled model systems the domains are observed to perfectly align in the opposing leaflets of the bilayer (LB/LS bilayers are an exception, raising questions about the validity of coupling between two self-assembled monolayers that are artificially formed into a bilayer). Some force exists that somehow transmits information about the position of phase separated domains across the bilayer midplane. For the plasma membrane of live cells, however, there is an ever-present asymmetry maintained by synthesis in the leaflet, or by ATP-driven flippases or translocases, proteins that transport lipids across the bilayer. An important example is the selective transport by aminophospholipid translocase of PS and PE lipids from the exoplasmic (external) leaflet to the cytosolic (internal) leaflet of mammalian plasma membranes.<sup>51</sup> Lipid compositions in the outer leaflet that phase separate and lipid compositions in the inner leaflet that do not, implies that it is possible for bilayer leaflets to anti-register, when domains mis-align, or even align with the domains of the other phase. Without the active bilayer remodelling taking place in cell then the leaflets are expected to equalise and register, for instance that occurs in cancer cells when the PE and PS lipids leak to the exoplasmic side of the cell becoming more symmetric.<sup>51</sup> Based on the line tension between the coexisting phases, arising from hydrophobic mismatch, anti-registration *should* be more energetically favourable than registration in membranes with compositions equal in both leaflets. As this is not what is observed in model membranes, this implies the existence of interleaflet coupling forces that favour domain registration, and that these forces must be overcome in the plasma membrane to force asymmetry. The identity and magnitudes of these interleaflet coupling forces are not agreed upon and experimental evidence is severely lacking. Results from a mean-field model<sup>14</sup> and coarse-grained molecular dynamics simulations<sup>13</sup> suggest

that at high line tension the inter-leaflet coupling forces favouring R will be overcome and AR bilayers will form.

In Chapter 4, ternary lipid mixtures of saturated lipid, unsaturated lipid and cholesterol were used to sequentially increase the hydrophobic mismatch between coexisting phases. This was achieved by increasing the length of the saturated lipid chain length. For lower height mismatch systems, registration of domains was observed shown by two bilayer heights with the expected height mismatch values. When the saturated lipid chain length was increased from 20 to 22, resulting in an 8 carbon difference with the unsaturated lipid 14:1PC, AR was observed. AR was identified by three different heights in the bilayers, R gel, R fluid, and an intermediate AR gel-fluid state. The mismatch between the R gel and R fluid was always minimised by positioning the AR domains in between the two R phases, leading to a more gradual step-up and step-down. When the proportion of each phase was almost 50:50 by area, an almost entirely AR bilayer was observed, where some of the bilayer was R fluid, with the majority being AR gel-fluid, with no R gel-gel.

In chapter 5, AFM methods were used to try to isolate the different leaflets of SLBs and determine the orientation of asymmetric AR bilayers. QNM was used to show that at low force the signal is isolated to the top leaflet and this can be used to match the phase in the top leaflet of the AR state with one of the R phases. This enables the orientation of the AR state,  $L_d$  up or  $L_\beta$ , to be calculated.

In Chapter 6, different methods were explored to attempt to force out AR in the lower height mismatch systems. This involved using both AFM and DSC to try to locate 50:50 area fractions close to critical mixtures. This idea was fully explored using the lower height mismatch system, DPPC/14:1PC/Chol as a proof of principle but there was insufficient time to fully optimise the same principle in the 20:0PC system. This was the hydrophobic mismatch system before interleaflet coupling forces were overcome to form AR states. However, in all of the images gathered of various 20:0PC/14:1PC composition bilayers, some of which possessed phase boundaries that were some way between spinodal and nucleated, no AR states were observed. This system would have been the most likely to form AR states with conditions optimised to make it more energetically favourable. Using temperature quenches can also potentially increase the chance of AR state formation by reducing the time available for registration to occur if the registration force had been weakened by the hydrophobic mismatch. A

variety of AFM systems and temperature control systems were tested to control the temperature of bilayers. There were issues with each system as detailed in the chapter, but AFM imaging at increased temperature was achieved. Unfortunately, no temperature quenches were successfully performed. One of the next stages of the project going forward, would be to locate the critical composition for the 20:0PC system and then perform temperature quenches on the 20:0PC, DSPC and DPPC systems to observe whether AR can be forced.

At the end of chapter 6, the magnitude of the interleaflet coupling force parameter favouring registration was estimated. Using the measured hydrophobic mismatch, along with domain perimeter and length scale between domains measured from the images, together with a literature value for the bilayer area compressibility modulus, the free energy density of the bilayers with increasing hydrophobic mismatch was calculated. Based on the experimentally determined point where the interleaflet coupling parameter is overcome by increased hydrophobic mismatch and line tension, a range can be obtained for the mismatch free energy. The estimated free energy range for the 20:0PC to the 22:0PC systems was 0.0085-0.048  $k_B T/nm^2$ . Furthermore, as the 20:0PC system is R, and the 22:0PC system is AR, if we choose 21:0PC as the boundary the value for interleaflet coupling is 0.021  $k_B T/nm^2$ . The only other estimate of the mismatch free energy based on experiments that have taken place in the last couple of years gave a value of  $0.016 \pm 0.004 k_B T/nm^2$ , within the range and remarkably close to the calculated value here, but with an entirely different method.<sup>73</sup> Estimates based on simulations and theoretical calculations also cover the range calculated here, but have values up to an order of magnitude higher, and vary more widely, with a range in published values; 0.01-0.03  $k_B T/nm^2$  <sup>(57)</sup>, 0.1-0.2  $k_B T/nm^2$  <sup>(9)</sup>, 0.146  $k_B T/nm^2$  <sup>(58)</sup>,  $0.15 \pm 0.05 k_B T/nm^2$  <sup>(59)</sup> and 0.5  $k_B T/nm^2$  <sup>(10)</sup>. Overall, the value calculated here directly from the hydrophobic mismatch value for which interleaflet coupling forces are overcome, matches well with the other experimental measurement, lending weight to the experimental determinations, and thereby confining the theoretical predictions to a narrower and lower range.

In Chapters 7 and 8, the effect of substrates on phase separation in SLBs was investigated. This project was initiated to provide a secondary source of experimental data to back-up observations of AR using optical microscopy fluorescence experiments. This would theoretically provide further evidence that the three heights

observed were AR from areas where intensity was half way between the two fully R domains, or even by being able to discriminate by absolute intensity if the fluorescence was carefully calibrated. This also tied directly into the need for temperature control (described above) as slow controlled cooling was essential to be able to crystallise domains large enough to be observable by optical microscopy. Fluorescence microscopy of SLBs is predominantly performed on glass, so standard symmetric two-phase bilayers were formed on both mica and glass to test with fluorescence. It was observed that the optically observable micron scale domains on mica were not formed on glass and there appeared to be no phase separation. There are also only a handful of published studies showing phase separation on glass,<sup>35,38,119</sup> despite the 100s or 1000s of studies on phase separation in GUVs and in mica SLBs. Using AFM, the presence of nanoscale domains, below the diffraction limit were detected. Using FRAP, controlled cooling rates and roughness measurements, it was inferred that rougher substrates such as glass result in the hindering of hydrodynamic domain motion of groups of lipid molecules. This is despite the individual diffusion of lipid molecules remaining identical at around  $1 \mu\text{m}^2 \text{s}^{-1}$  (which is also the approximate diffusion rate of lipids in cells, and around 10x lower than in free floating vesicles). This hindering of hydrodynamic motion results in domains not being able to coalesce to form large micron scale domains.

The effect of PDMS, which has a similar roughness to glass, was also shown to have the same hindering effect on domain motion and growth, but with some other effects unique to PDMS. The implications of this understanding of lipid-substrate interaction is widespread, and can explain many puzzling and unusual results in the scientific literature, which often have convoluted technical arguments to explain a result that arises from an unforeseen substrate effect.

Importantly, it provides a solid base for understanding the validity of experiments on SLBs. There is always dispute between groups in the highly contentious field of lipid membrane biophysics, between experimentalists using different techniques (and hence substrates), between experimentalists, simulators and theoreticians, and between physical scientists and biologists. The research presented in these two chapters can be used to counter objections invoked on the use of SLBs which usually cite the unknown nature of the bilayer substrate interaction, which would invalidate the research using SLBs in the eyes of the membrane community.

In this thesis, interleaflet coupling has been investigated, which is the interaction between lipid tail to lipid tails. The interaction between headgroups and substrates has also been investigated. Another unconsidered aspect is the lipid headgroup-headgroup interactions, although these are generally not found in mammalian cells. One example in nature might be in the chloroplasts of plant cells, where the antenna complex of the chlorosome exists in a highly convoluted stacked membrane system composed of thylakoid lipids. Tayebi et al. have shown how  $L_0$  domains between stacks of bilayers co-align, in an inter-bilayer registration analogous to the interleaflet registration researched in this thesis.<sup>122</sup>



## 9.2 Future Work

### 9.2.1 Anti-Registration

The experiments performed in this project were based in part on the predictions of mean-field free energy calculations by Williamson et al.<sup>14,77,78</sup> The experiments have proved their predictions that increasing hydrophobic mismatch, and thus line tension, results in the formation of AR bilayers. The mean-field theory also predicts that these phases might only be metastable and will equilibrate to become R with time. It was originally intended to look at early stage kinetics of the high hydrophobic mismatch ternary lipid systems. Fastscan AFM imaging was going to be used to attempt to image early stage kinetics and the evolution of domains. This ended up being not needed, as AR states in 22:0PC/14:1PC/Chol were stable over hours/days. Based on the work on substrates in this thesis, it is likely that this is due to domains being kinetically trapped by the substrate once they reach a certain length scale, and they are unable to move and reach equilibrium. Therefore, these experiments were not required as AR had already been observed. Also, the problems highlighted in Chapter 5, where AFM imaging was incredibly unstable while trying to increase and change temperature, suggest that it would not have been possible to image stably, immediately after a temperature quench.

Now that there is an experimental system, in which AR bilayers can be controllably formed through a change in hydrophobic mismatch, there are many more theoretical questions based on the work of Williamson et al. that can potentially be answered.<sup>14,77,78</sup> Figure 9.1 shows an example leaflet-leaflet free energy diagram from the work of Williamson et al. The  $x=y$  plane represents a symmetric bilayer and would be equivalent to a single tie line on a standard symmetric ternary phase diagram. Any deviation from this line represents asymmetry between the two bilayer leaflets. Analogous to how a tie line must be drawn between two compositions on a symmetric ternary phase diagram for those two compositions to coexist, a line or a plane must be drawn between the different asymmetric compositions in Figure 9.1 for them to coexist. In this project the coexistence of one AR and one R (two heights) state has been observed as well as the coexistence of both R states

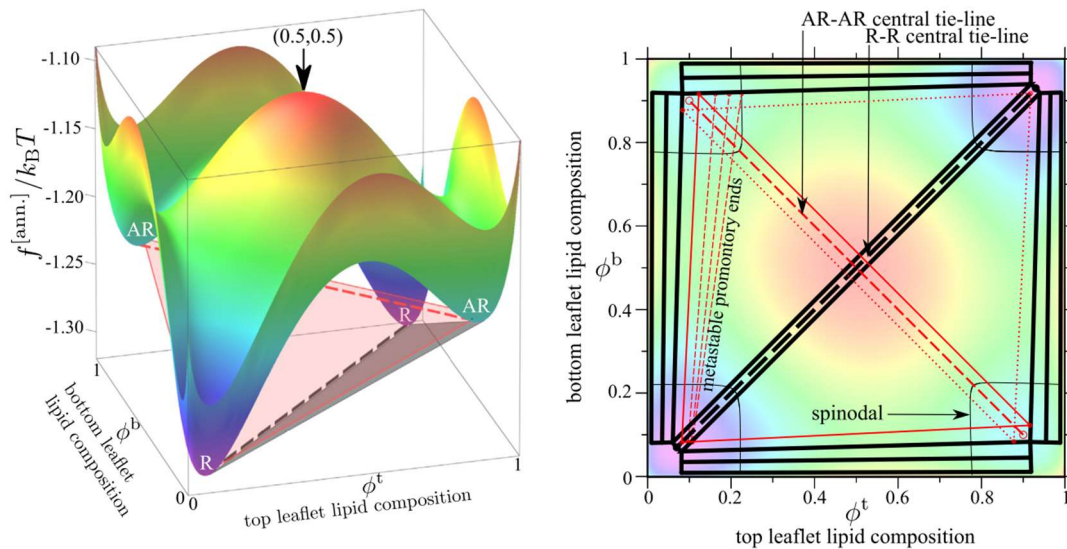


**Figure 9.1 Local 3D free energy landscape and leaflet-leaflet phase diagram showing asymmetry within phase separated bilayers. In both, the x and y axes are the individual compositions of the two leaflets and the x=y line corresponds to a symmetric bilayer. Left) Local 3D free energy landscape shown for set values of  $J$ , which represents line tension and promotes anti-registration, and  $B$ , which represents the mismatch free energy or interleaflet coupling parameter and promotes registration. Right) Phase Diagram calculated from free energy landscape. Black lines or triangles represent equilibrium two or three phase coexistence. Red lines and triangles show metastable two or three phase coexistence. Two phase coexistence can be R-R or AR-AR. Three phase coexistence can be R-R-AR or AR-AR-R. From reference<sup>14</sup>**

and one AR state (three heights). These coexistence states can have lines or planes drawn between them on the phase diagram. However, there can be no plane drawn to join all four minima, two R and two AR states. The experimental results presented here match this prediction from the theory, however it should be noted that the nanoscale coexistence of both AR states together is possible.

The next question to ask is which orientation AR state forms,  $L_\alpha$  up or  $L_\beta$  up? Based on the leaflet-leaflet free energy diagram both AR states are at the same energy, suggesting an equal chance of each forming. However, there is possibly a symmetry breaking due to the substrate where one state will be favoured. Preliminary results from QNM indicate that the  $L_\beta$  phase aligns in the bottom leaflet close to the substrate. Tapping mode phase imaging however suggests that both AR orientations are potentially possible, but this data is less reliable and more difficult to interpret. The number of experiments

was too low to give a definitive answer at this stage but repeat QNM imaging on AR bilayers should enable the preference for AR orientations to be observed. With QNM to determine AR orientation, we should be able to observe whether the same AR state is observed across a whole bilayer sample, whether the same AR state is repeatably observed for the same mixture and whether the same AR state is seen for all mixtures. If the substrate does prefer the  $L_{\beta}$  in the lower leaflet, this could be explained by the proximity of the substrate lending slightly more order to the lower leaflet, although this would tend to be contradicted by our results on the transition temperature of DPPC on various substrates. Certainly, mica has no effect on the transition temperature, whereas glass and PDMS have a small disordering effect equivalent to 1.5 °C. Many questions remain and further QNM imaging should help to provide answers.

Another question is how AR domains evolve over time. The theory suggest that AR domains will evolve back to R states with time, via nucleation of R domains or via lipid flip-flop.<sup>78</sup> Monitoring AR domains over hour and day timescales would show whether this does happen.

As mentioned above the substrate is potentially key to enabling the observation of AR states. Therefore, one of the next questions is whether AR states can be observed in free-floating unsupported systems. In unsupported systems the AR states may only be stable over short periods of time. There are several ways in which it could be tested if AR states form in free-floating systems. One of these would be to use 22:0PC/14:1PC/Chol to form multilamellar stacks and investigate using X-ray Diffraction (XRD). X-ray diffraction can be used to distinguish between different lipid phases based on their height, which will give a different d-spacing.<sup>180</sup> For AR systems, XRD should show three different d spacings, for the three different bilayer heights. Another potential way to test this would be to form 22:0PC/14:1PC/Chol GUVs and use fluorescence to image them.

As soon as AR bilayers had been observed in SLBs using AFM, the plan was to image these same bilayers using fluorescence. If there are AR bilayers and a single dye which preferentially partitions into the fluid phase is used, there should be three observable fluorescent intensities, one for R fluid, half

intensity for the AR state and close to zero background intensity for R gel. As bilayer fluorescence experiments predominantly use glass as a substrate, these experiments were planned on glass. The first mixtures to be looked at were symmetric two phase SLBs, to test that the experiments worked in these known systems, before looking at the more complicated AR systems. This is when it was observed that the large micron scale domains formed on mica do not form on glass and that the domains are below the diffraction limit. This meant that these fluorescence experiments to look at AR could not be achieved in the way intended but did lead to incredibly revealing experiments regarding the effect of substrates on phase separation.

However, what was discovered from this work is that fluorescence could be observed for SLBs on mica, if the mica was thin. Although this has been achieved before, it is not common, had not been achieved in our lab, and problems with birefringence of mica were anticipated. With this knowledge, the next experiments would be to image three phase AR bilayers on mica using fluorescence. Another factor that needs to be considered is the size of domains. To be able to observe three clear fluorescent signals the domains would have to be well above the diffraction limit. With the knowledge of cooling rates to make domains larger, gained from the work on different substrates in this thesis, AR domains could potentially be grown larger. Also, by using a fluorescent quencher such as iodide or cobalt, the fluorescence effects of the two bilayer leaflets could be isolated. Langmuir-Blodgett (LB) bilayers could also have been used to only have fluorescent dye in one leaflet and isolate the two leaflets of an SLB, although there is considerable dispute around the correspondence of LB bilayers formed from two pre-formed monolayers. They do not display the phase behaviour of a self-assembled bilayer, so it is unclear whether they are a useful model. A better method might be the enzymatic modification of one leaflet, perhaps after deposition to a substrate.

### **9.2.2 Substrates**

It has been shown that roughness causes the hindering of domains on substrates, and it is likely the combination of local pinning sites where the friction on the bilayer is increased, bending energy penalties for flow over high curvature surface features, and disrupted flow in the interstitial water layer.

An interesting experiment now would be to observe how and where domains nucleate, and how they grow before they are completely hindered. Imaging using AFM while the temperature is cooling has proven to be challenging. However, AFM could be used to image an area of the glass substrate, and then observe the same area after bilayer formation. The areas where domains have nucleated and grown could be correlated to the rougher areas of the substrate. It would also be interesting to then increase the temperature to above  $T_m$  and then cool back down again. Repeated temperature cycling and observation of the same area, would reveal if the domains always form in the same places and also if they always nucleate on areas of roughness.

One important aspect that could be affecting the formation and flow of domains are electrostatic interactions. Electrostatics have been shown to affect diffusion, with experiments that alter salt buffer concentrations.<sup>129</sup> Also, changes in pH can affect water structure and flow, which can affect hydrodynamic flow of domains.<sup>106</sup> These effects could be investigated using variations in buffer concentrations to change the charge screening and observe whether the structure of domains changes. Another important consideration is the chemical roughness of the substrates. In sections 7.6 and 8.8, the contact angle was used to investigate the chemical nature of substrates in terms of the hydrophilicity and the density of hydrophilic functional groups. A further consideration is how salt concentrations affect the roughness of the substrates. Ions on the surface can alter the chemical interactions on a local level between the substrates and a bilayer, but can also potentially affect the physical roughness of the substrate. By using variations in salt concentration, for example a range from across the Hofmeister series, we could observe how the chemical and physical roughness of the substrates changes and how the water structure at the surface changes. Then these changes in water structure and surface roughness could be linked to changes in lipid bilayer phase behaviour and domain flow. The chemical and physical roughness could be measured using AFM, the structure of the water layer potentially using scattering techniques, and the effect on phase behaviour using AFM, fluorescence microscopy and FRAP.

Nanoscale hindered domains were observed in gel-liquid bilayers, but Honigmann et al. have also observed what appear to be similar domains in

liquid-liquid systems using fluorescence. AFM imaging could be used to confirm the formation of hindered nanoscale domains in fluid-fluid systems also.

Another important aspect of substrate interactions with bilayers, that is also potentially relevant to the AR work too, is the decoupling of bilayer properties of the two leaflets due to proximity to the substrate. In chapter 8, the conflicting literature reports regarding the decoupling of diffusion and  $T_m$  between the two leaflets of SLBs were discussed. One way to isolate the effects of the two leaflets in relation to the experiments in this thesis, would be to use fluorescent quenchers that selectively quench just the top leaflet of a SLB. Then FRAP could be performed to observe if there is a difference in diffusion between the two leaflets. With Single Particle Tracking, decoupling of  $D$  and of  $T_m$  could be observed simultaneously. If there was decoupling of both  $D$  and  $T_m$ , then the two discrete  $D$  values for each leaflet would then be observed changing through a phase transition to the gel phase at different temperatures as a bilayer was cooled down.

## References

- (1) Simons, K.; Ikonen, E. Functional Rafts in Cell Membranes. *Nature* **1997**, *387* (6633), 569–572.
- (2) Hancock, J. F. Lipid Rafts: Contentious Only from Simplistic Standpoints. *Nat. Rev. Mol. Cell Biol.* **2006**, *7* (6), 456–462.
- (3) Owen, D. M.; Magenau, A.; Williamson, D.; Gaus, K. The Lipid Raft Hypothesis Revisited-New Insights on Raft Composition and Function from Super-Resolution Fluorescence Microscopy. *Bioessays* **2012**, *34* (9), 739–747.
- (4) Lingwood, D.; Simons, K. Lipid Rafts As a Membrane- Organizing Principle. *Science* **2010**, *327* (5961), 46–50.
- (5) Sezgin, E.; Levental, I.; Mayor, S.; Eggeling, C. The Mystery of Membrane Organization: Composition, Regulation and Roles of Lipid Rafts. *Nat. Rev. Mol. Cell Biol.* **2017**, *18* (6), 361–374.
- (6) Veatch, S. L.; Keller, S. L. Separation of Liquid Phases in Giant Vesicles of Ternary Mixtures of Phospholipids and Cholesterol. *Biophys. J.* **2003**, *85* (5), 3074–3083.
- (7) Bagatolli, L. A.; Gratton, E. Direct Observation of Lipid Domains in Free-Standing Bilayers Using Two-Photon Excitation Fluorescence Microscopy. *J. Fluoresc.* **2001**, *11* (3), 141–160.
- (8) Korlach, J.; Schwille, P.; Webb, W. W.; Feigenson, G. W. Characterization of Lipid Bilayer Phases by Confocal Microscopy. *Proc. Natl. Acad. Sci. USA* **1999**, *96* (15), 8461–8466.
- (9) May, S. Trans-Monolayer Coupling of Fluid Domains in Lipid Bilayers. *Soft Matter* **2009**, *5* (17), 3148.
- (10) Collins, M. D. Interleaflet Coupling Mechanisms in Bilayers of Lipids and Cholesterol. *Biophys. J.* **2008**, *94* (5), L32-4.
- (11) Kiessling, V.; Wan, C.; Tamm, L. K. Domain Coupling in Asymmetric Lipid Bilayers. *Biochim. Biophys. Acta* **2009**, *1788* (1), 64–71.
- (12) Collins, M. D.; Keller, S. L. Tuning Lipid Mixtures to Induce or Suppress

- Domain Formation across Leaflets of Unsupported Asymmetric Bilayers. *Proc. Natl. Acad. Sci. U. S. A.* **2008**, *105* (1), 124–128.
- (13) Perlmutter, J. D.; Sachs, J. N. Interleaflet Interaction and Asymmetry in Phase Separated Lipid Bilayers: Molecular Dynamics Simulations. *J. Am. Chem. Soc.* **2011**, *133* (17), 6563–6577.
- (14) Williamson, J. J.; Olmsted, P. D. Registered and Antiregistered Phase Separation of Mixed Amphiphilic Bilayers. *Biophys. J.* **2015**, *108* (8), 1963–1976.
- (15) García-Sáez, A. J.; Chiantia, S.; Schwille, P. Effect of Line Tension on the Lateral Organization of Lipid Membranes. *J. Biol. Chem.* **2007**, *282* (46), 33537–33544.
- (16) Fujimoto, T.; Parmryd, I. Interleaflet Coupling, Pinning, and Leaflet Asymmetry—Major Players in Plasma Membrane Nanodomain Formation. *Front. Cell Dev. Biol.* **2017**, *4* (155), 1–12.
- (17) Kobayashi, T.; Menon, A. K. Transbilayer Lipid Asymmetry. *Curr. Biol.* **2018**, *28* (8), R386–R391.
- (18) Israelachvili, J. N. *Intermolecular and Surface Force*, Third Edit.; Academic Press, 1985.
- (19) Alessandrini, A.; Facci, P. Phase Transitions in Supported Lipid Bilayers Studied by AFM. *Soft Matter* **2014**, *10* (37), 7145–7164.
- (20) Heberle, F. A.; Feigenson, G. W. Phase Separation in Lipid Membranes. *Cold Spring Harb. Perspect. Biol.* **2011**, *3*, 1–13.
- (21) Veatch, S. L.; Gawrisch, K.; Keller, S. L. Closed-Loop Miscibility Gap and Quantitative Tie-Lines in Ternary Membranes Containing Diphytanoyl PC. *Biophys. J.* **2006**, *90* (12), 4428–4436.
- (22) Krapf, D. Compartmentalization of the Plasma Membrane. *Curr. Opin. Cell Biol.* **2018**, *53*, 15–21.
- (23) Singer, S. J.; Nicolson, G. L. The Fluid Mosaic Model of the Structure of Cell Membranes. *Science* **1972**, *175* (4023), 720–731.
- (24) Connell, S. D.; Smith, D. A. The Atomic Force Microscope as a Tool for Studying Phase Separation in Lipid Membranes. *Mol. Membr. Biol.*



**2006**, 23 (1), 17–28.

- (25) Heberle, F. A.; Petruzielo, R. S.; Pan, J.; Drazba, P.; Kučerka, N.; Standaert, R. F.; Feigenson, G. W.; Katsaras, J. Bilayer Thickness Mismatch Controls Domain Size in Model Membranes. *J. Am. Chem. Soc.* **2013**, 135 (18), 6853–6859.
- (26) Clarke, J. A.; Seddon, J. M.; Law, R. V. Cholesterol Containing Model Membranes Studied by Multinuclear Solid State NMR Spectroscopy. *Soft Matter* **2009**, 5, 369.
- (27) Levental, I.; Veatch, S. L. The Continuing Mystery of Lipid Rafts. *J. Mol. Biol.* **2016**, 428 (24), 4749–4764.
- (28) Schmidt, M. L.; Ziani, L.; Boudreau, M.; Davis, J. H. Phase Equilibria in DOPC/DPPC: Conversion from Gel to Subgel in Two Component Mixtures. *J. Chem. Phys.* **2009**, 131 (175103).
- (29) Przybylo, M.; Sýkora, J.; Humpolíčová, J.; Benda, A.; Zan, A.; Hof, M. Lipid Diffusion in Giant Unilamellar Vesicles Is More than 2 Times Faster than in Supported Phospholipid Bilayers under Identical Conditions. *Langmuir* **2006**, 22, 9096–9099.
- (30) Biltonen, R. L.; Lichtenberg, D. The Use of Differential Scanning Calorimetry as a Tool to Characterize Liposome Preparations. *Chem. Phys. Lipids* **1993**, 64 (1–3), 129–142.
- (31) Mazur, F.; Bally, M.; Städler, B.; Chandrawati, R. Liposomes and Lipid Bilayers in Biosensors. *Adv. Colloid Interface Sci.* **2017**, 249, 88–99.
- (32) Pattni, B. S.; Chupin, V. V.; Torchilin, V. P. New Developments in Liposomal Drug Delivery. *Chem. Rev.* **2015**, 115 (19), 10938–10966.
- (33) Angelova, M. I.; Dimitrov, D. S. Liposome Electro Formation. **1986**, 81, 303–311.
- (34) Richter, R. P.; Brisson, A. R. Following the Formation of Supported Lipid Bilayers on Mica: A Study Combining AFM, QCM-D, and Ellipsometry. *Biophys. J.* **2005**, 88 (5), 3422–3433.
- (35) Honigmann, A.; Mueller, V.; Hell, S. W.; Eggeling, C. STED Microscopy Detects and Quantifies Liquid Phase Separation in Lipid Membranes

- Using a New Far-Red Emitting Fluorescent Phosphoglycerolipid Analogue. *Faraday Discuss.* **2013**, *161*, 77–89.
- (36) Benda, A.; Beneš, M.; Mareček, V.; Lhotský, A.; Hermens, W. T.; Hof, M. How to Determine Diffusion Coefficients in Planar Phospholipid Systems by Confocal Fluorescence Correlation Spectroscopy. *Langmuir* **2003**, *19* (10), 4120–4126.
- (37) Scomparin, C.; Lecuyer, S.; Ferreira, M.; Charitat, T.; Tinland, B. Diffusion in Supported Lipid Bilayers: Influence of Substrate and Preparation Technique on the Internal Dynamics. *Eur. Phys. J. E* **2009**, *28* (2), 211–220.
- (38) Seu, K. J.; Pandey, A. P.; Haque, F.; Proctor, E. A.; Ribbe, A. E.; Hovis, J. S. Effect of Surface Treatment on Diffusion and Domain Formation in Supported Lipid Bilayers. *Biophys. J.* **2007**, *92* (7), 2445–2450.
- (39) Chada, N.; Sigdel, K. P.; Sanganna Gari, R. R.; Matin, T. R.; Randall, L. L.; King, G. M. Glass Is a Viable Substrate for Precision Force Microscopy of Membrane Proteins. *Sci. Rep.* **2015**, *5*, 1–8.
- (40) Stottrup, B. L.; Veatch, S. L.; Keller, S. L. Nonequilibrium Behavior in Supported Lipid Membranes Containing Cholesterol. *Biophys. J.* **2004**, *86* (5), 2942–2950.
- (41) Heath, G. R.; Johnson, B. R. G.; Olmsted, P. D.; Connell, S. D.; Evans, S. D. Actin Assembly at Model-Supported Lipid Bilayers. *Biophys. J.* **2013**, *105* (10), 2355–2365.
- (42) Honigmann, A.; Sadeghi, S.; Keller, J.; Hell, S. W.; Eggeling, C.; Vink, R. A Lipid Bound Actin Meshwork Organizes Liquid Phase Separation in Model Membranes. *Elife* **2014**, *2014* (3), 1–16.
- (43) Connell, S. D.; Heath, G.; Olmsted, P. D.; Kisil, A. Critical Point Fluctuations in Supported Lipid Membranes. *Faraday Discuss.* **2013**, *161*, 91.
- (44) Aufderhorst-Roberts, A.; Chandra, U.; Connell, S. D. Three-Phase Coexistence in Lipid Membranes. *Biophys. J.* **2017**, *112* (2), 313–324.
- (45) Gunderson, R. S.; Honerkamp-Smith, A. R. Liquid-Liquid Phase

Transition Temperatures Increase When Lipid Bilayers Are Supported on Glass. *Biochim. Biophys. Acta - Biomembr.* **2018**, *1860* (10), 1965–1971.

- (46) Sonnleitner, A.; Schütz, G. J.; Schmidt, T. Free Brownian Motion of Individual Lipid Molecules in Biomembranes. *Biophys. J.* **1999**, *77* (5), 2638–2642.
- (47) Mingeot-Leclercq, M.-P.; Deleu, M.; Brasseur, R.; Dufrêne, Y. F. Atomic Force Microscopy of Supported Lipid Bilayers. *Nat. Protoc.* **2008**, *3* (10), 1654–1659.
- (48) Mapar, M.; Jõemetsa, S.; Pace, H. P.; Zhdanov, V. P.; Agnarsson, B.; Höök, F. Spatio-Temporal Kinetics of Supported Lipid Bilayer Formation on Glass via Vesicle Adsorption and Rupture. *J. Phys. Chem. Lett.* **2018**, *9* (17), 5143–5149.
- (49) Lind, T. K.; Cárdenas, M.; Wacklin, H. P. Formation of Supported Lipid Bilayers by Vesicle Fusion: Effect of Deposition Temperature. *Langmuir* **2014**, *30* (25), 7259–7263.
- (50) Harayama, T.; Riezman, H. Understanding the Diversity of Membrane Lipid Composition. *Nat. Rev. Mol. Cell Biol.* **2018**, *19*, 281–296.
- (51) Leite, N. B.; Aufderhorst-Roberts, A.; Palma, M. S.; Connell, S. D.; Neto, J. R.; Beales, P. A. PE and PS Lipids Synergistically Enhance Membrane Poration by a Peptide with Anticancer Properties. *Biophys. J.* **2015**, *109* (5), 936–947.
- (52) Zwaal, R. F. A.; Comfurius, P.; Bevers, E. M. Surface Exposure of Phosphatidylserine in Pathological Cells. *Cell. Mol. Life Sci.* **2005**, *62* (9), 971–988.
- (53) Dietrich, C.; Bagatolli, L. A.; Volovyk, Z. N.; Thompson, N. L.; Levi, M.; Jacobson, K.; Gratton, E. Lipid Rafts Reconstituted in Model Membranes. *Biophys. J.* **2001**, *80* (3), 1417–1428.
- (54) Bernchou, U.; Ipsen, J. H.; Simonsen, A. C. Growth of Solid Domains in Model Membranes: Quantitative Image Analysis Reveals a Strong Correlation between Domain Shape and Spatial Position. *J. Phys. Chem.* **2009**, *113*, 7170–7177.

- (55) Crane, J. M.; Kiessling, V.; Tamm, L. K. Measuring Lipid Asymmetry in Planar Supported Bilayers by Fluorescence Interference Contrast Microscopy. *Langmuir* **2005**, *21* (4), 1377–1388.
- (56) Ajo-Franklin, C. M.; Yoshina-Ishii, C.; Boxer, S. G. Probing the Structure of Supported Membranes and Tethered Oligonucleotides by Fluorescence Interference Contrast Microscopy. *Langmuir* **2005**, *21* (11), 4976–4983.
- (57) Putzel, G. G.; Uline, M. J.; Szleifer, I.; Schick, M. Interleaflet Coupling and Domain Registry in Phase-Separated Lipid Bilayers. *Biophys. J.* **2011**, *100* (4), 996–1004.
- (58) Polley, A.; Mayor, S.; Rao, M. Bilayer Registry in a Multicomponent Asymmetric Membrane : Dependence on Lipid Composition and Chain Length. *J. Chem. Phys.* **2014**, *141* (064903).
- (59) Risselada, H. J.; Marrink, S. J. The Molecular Face of Lipid Rafts in Model Membranes. *Proc. Natl. Acad. Sci. U. S. A.* **2008**, *105* (45), 17367–17372.
- (60) Blanchette, C. D.; Lin, W.-C.; Orme, C. a; Ratto, T. V; Longo, M. L. Domain Nucleation Rates and Interfacial Line Tensions in Supported Bilayers of Ternary Mixtures Containing Galactosylceramide. *Biophys. J.* **2008**, *94* (7), 2691–2697.
- (61) Tian, A.; Johnson, C.; Wang, W.; Baumgart, T. Line Tension at Fluid Membrane Domain Boundaries Measured by Micropipette Aspiration. *Phys. Rev. Lett.* **2007**, *98* (20), 208102.
- (62) Jefferys, E.; Sansom, M. S. P.; Fowler, P. W. NRas Slows the Rate at Which a Model Lipid Bilayer Phase Separates. *Faraday Discuss.* **2014**, *169*, 209–223.
- (63) Wan, C.; Kiessling, V.; Tamm, L. K.; Charlottes, V. Coupling of Cholesterol-Rich Lipid Phases in Asymmetric Bilayers. *Biochemistry* **2008**, *47*, 2190–2198.
- (64) Pantano, D. A.; Moore, P. B.; Klein, M. L.; Discher, D. E. Raft Registration across Bilayers in a Molecularly Detailed Model. *Soft Matter* **2011**, *7* (18), 8182.

- (65) Thallmair, S.; Ingólfsson, H. I.; Marrink, S. J. Cholesterol Flip-Flop Impacts Domain Registration in Plasma Membrane Models. *J. Phys. Chem. Lett.* **2018**, *9*, 5527–5533.
- (66) Galimzyanov, T. R.; Molotkovsky, R. J.; Bozdaganyan, M. E.; Cohen, F. S.; Pohl, P.; Akimov, S. a. Elastic Membrane Deformations Govern Interleaflet Coupling of Lipid-Ordered Domains. *Phys. Rev. Lett.* **2015**, *115* (088101), 1–5.
- (67) Williamson, J. J.; Olmsted, P. D. Comment on “Elastic Membrane Deformations Govern Interleaflet Coupling of Lipid-Ordered Domains.” *Phys. Rev. Lett.* **2016**, *116*, 079801.
- (68) Doktorova, M.; Heberle, F. A.; Eicher, B.; Standaert, R. F.; Katsaras, J.; London, E.; Pabst, G.; Marquardt, D. Preparation of Asymmetric Phospholipid Vesicles for Use as Cell Membrane Models. *Nat. Protoc.* **2018**, *13* (9), 2086–2101.
- (69) Middleton Boon, J.; Smith, B. D. Chemical Control of Phospholipid Distribution across Bilayer Membranes. *Med. Res. Rev.* **2002**, *22* (3), 251–281.
- (70) Cheng, H. T.; London, E. Preparation and Properties of Asymmetric Large Unilamellar Vesicles: Interleaflet Coupling in Asymmetric Vesicles Is Dependent on Temperature but Not Curvature. *Biophys. J.* **2011**, *100* (11), 2671–2678.
- (71) Pautot, S.; Frisken, B. J.; Weitz, D. A. Engineering Asymmetric Vesicles. *Proc. Natl. Acad. Sci.* **2003**, *100* (19), 10718–10721.
- (72) Karamdad, K.; Ces, O.; Brooks, N. J.; Law, R. V.; Seddon, J. Studying the Effects of Asymmetry on the Bending Rigidity of Lipid Membranes Formed by Microfluidics. *Chem. Commun.* **2016**, *52*, 5277–5280.
- (73) Blosser, M. C.; Honerkamp-Smith, A. R.; Han, T.; Haataja, M.; Keller, S. L. Transbilayer Colocalization of Lipid Domains Explained via Measurement of Strong Coupling Parameters. *Biophys. J.* **2015**, *109* (11), 2317–2327.
- (74) Lin, W.-C.; Blanchette, C. D.; Ratto, T. V; Longo, M. L. Lipid Asymmetry in DLPC/DSPC-Supported Lipid Bilayers: A Combined AFM and

- Fluorescence Microscopy Study. *Biophys. J.* **2006**, *90* (1), 228–237.
- (75) Fowler, P. W.; Williamson, J. J.; Sansom, M. S. P.; Olmsted, P. D. Roles of Inter-Leaflet Coupling and Hydrophobic Mismatch in Lipid Membrane Phase-Separation Kinetics. *J. Am. Chem. Soc.* **2016**, *138* (36), 11633–11642.
- (76) Weiner, M. D.; Feigenson, G. W. Presence and Role of Midplane Cholesterol in Lipid Bilayers Containing Registered or Antiregistered Phase Domains. *J. Phys. Chem. B* **2018**, *122*, 8193–8200.
- (77) Williamson, J. J.; Olmsted, P. D. Nucleation of Symmetric Domains in the Coupled Leaflets of a Bilayer. *Soft Matter* **2015**, *11*, 8948–8959.
- (78) Williamson, J. J.; Olmsted, P. D. Kinetics of Symmetry and Asymmetry in a Phase-Separating Bilayer Membrane. *Phys. Rev. E - Stat. Nonlinear, Soft Matter Phys.* **2015**, *92* (052721), 1–15.
- (79) Binnig, G.; Rohrer, H.; Gerber, C.; Weibel, E. Surface Studies by Scanning Tunneling Microscopy. *Physical Review Letters*. 1982, pp 57–61.
- (80) Binnig, G.; Quate, C. F. Atomic Force Microscope. *Phys. Rev. Lett.* **1986**, *56* (9), 930–933.
- (81) Eaton, P.; West, P. *Atomic Force Microscopy*; Oxford University Press: Oxford, 2010.
- (82) Gross, L.; Wang, Z. L.; Ugarte, D.; Mohn, F.; Moll, N.; Heer, W. a; Vincent, P.; Liljeroth, P.; Journet, C.; Meyer, G.; et al. The Chemical Structure of a Molecule Resolved by Atomic Force Microscopy. *Science* (80-. ). **2009**, *325*, 1110–1114.
- (83) Hansma, P. K.; Cleveland, J. P.; Radmacher, M.; Walters, D. a.; Hillner, P. E.; Bezanilla, M.; Fritz, M.; Vie, D.; Hansma, H. G.; Prater, C. B.; et al. Tapping Mode Atomic Force Microscopy in Liquids. *Appl. Phys. Lett.* **1994**, *64* (1994), 1738–1740.
- (84) Picas, L.; Rico, F.; Scheuring, S. Direct Measurement of the Mechanical Properties of Lipid Phases in Supported Bilayers. *Biophys. J.* **2012**, *102* (1), L01–L03.

- (85) Garcia-Manyes, S.; Sanz, F. Nanomechanics of Lipid Bilayers by Force Spectroscopy with AFM: A Perspective. *Biochim. Biophys. Acta - Biomembr.* **2010**, *1798* (4), 741–749.
- (86) Introduction to Bruker's ScanAsyst and PeakForce Tapping AFM Technology [https://www.bruker.com/fileadmin/user\\_upload/8-PDF-Docs/SurfaceAnalysis/AFM/ApplicationNotes/Introduction\\_to\\_Brukers\\_ScanAsyst\\_and\\_PeakForce\\_Tapping\\_Atomic\\_Force\\_Microscopy\\_Technology\\_AFM\\_AN133.pdf](https://www.bruker.com/fileadmin/user_upload/8-PDF-Docs/SurfaceAnalysis/AFM/ApplicationNotes/Introduction_to_Brukers_ScanAsyst_and_PeakForce_Tapping_Atomic_Force_Microscopy_Technology_AFM_AN133.pdf) (accessed Nov 27, 2018).
- (87) Hua, Y. PeakForce-QNM Advanced Applications Training 2014 [http://mmrc.caltech.edu/AFM\\_Dimension\\_Icon/Bruker\\_Training/Peak\\_Force\\_QNM\\_Adv\\_Apps\\_Training\\_2014.pdf](http://mmrc.caltech.edu/AFM_Dimension_Icon/Bruker_Training/Peak_Force_QNM_Adv_Apps_Training_2014.pdf) (accessed Nov 27, 2018).
- (88) Spring, K. R.; Davidson, M. W. Introduction to Fluorescence Microscopy <https://www.microscopyu.com/techniques/fluorescence/introduction-to-fluorescence-microscopy> (accessed Dec 18, 2018).
- (89) Axelrod, D.; Koppel, D. E.; Schlessinger, J.; Elson, E.; Webb, W. W. Mobility Measurement by Analysis of Fluorescence Photobleaching Recovery Kinetics. *Biophys. J.* **1976**, *16* (9), 1055–1069.
- (90) Nagahara, L. A.; Hashimoto, K.; Fujishima, A.; Snowden-Ifft, D.; Price, P. B. Mica Etch Pits as a Height Calibration Source for Atomic Force Microscopy. *J. Vac. Sci. Technol. B Microelectron. Nanom. Struct.* **1994**, *12* (3), 1694.
- (91) Nania, M.; Matar, O. K.; Cabral, J. T. Frontal Vitrification of PDMS Using Air Plasma and Consequences for Surface Wrinkling. *Soft Matter* **2015**, *11* (15), 3067–3075.
- (92) Tian, C.; Ji, H. P.; Zong, C. Y.; Lu, C. H. Controlled Fabrication of Hierarchically Microstructured Surfaces via Surface Wrinkling Combined with Template Replication. *Chinese Chem. Lett.* **2015**, *26* (1), 15–20.
- (93) Bowden, N.; Huck, W. T. S.; Paul, K. E.; Whitesides, G. M. The Controlled Formation of Ordered, Sinusoidal Structures by Plasma Oxidation of an Elastomeric Polymer. *Appl. Phys. Lett.* **1999**, *75* (17), 2557–2559.

- (94) Yang, S.; Khare, K.; Lin, P. C. Harnessing Surface Wrinkle Patterns in Soft Matter. *Adv. Funct. Mater.* **2010**, *20* (16), 2550–2564.
- (95) Yin, J.; Han, X.; Cao, Y.; Lu, C. Surface Wrinkling on Polydimethylsiloxane Microspheres via Wet Surface Chemical Oxidation. *Sci. Rep.* **2014**, *4*, 5710.
- (96) Lentz, B. R.; Barenholz, Y.; Thompson, T. E. Fluorescence Depolarization Studies of Phase Transitions and Fluidity in Phospholipid Bilayers. 2 Two-Component Phosphatidylcholine Liposomes. *Biochemistry* **1976**, *15* (20), 4529–4537.
- (97) Burgess, N. K.; Dao, T. P.; Stanley, A. M.; Fleming, K. G. Beta-Barrel Proteins That Reside in the Escherichia Coli Outer Membrane in Vivo Demonstrate Varied Folding Behavior in Vitro. *J. Biol. Chem.* **2008**, *283* (39), 26748–26758.
- (98) Davis, J. H.; Clair, J. J.; Juhasz, J. Phase Equilibria in DOPC/DPPC-D62/Cholesterol Mixtures. *Biophys. J.* **2009**, *96* (2), 521–539.
- (99) Juhasz, J.; Sharom, F. J.; Davis, J. H. Quantitative Characterization of Coexisting Phases in DOPC/DPPC/Cholesterol Mixtures: Comparing Confocal Fluorescence Microscopy and Deuterium Nuclear Magnetic Resonance. *Biochim. Biophys. Acta - Biomembr.* **2009**, *1788* (12), 2541–2552.
- (100) Nagle, J. F. Introductory Lecture: Basic Quantities in Model Biomembranes. *Faraday Discuss.* **2013**, *161*, 11–29.
- (101) Attwood, S. J.; Choi, Y.; Leonenko, Z. Preparation of DOPC and DPPC Supported Planar Lipid Bilayers for Atomic Force Microscopy and Atomic Force Spectroscopy. *Int. J. Mol. Sci.* **2013**, *14* (2), 3514–3539.
- (102) Blosser, M. C.; Starr, J. B.; Turtle, C. W.; Ashcraft, J.; Keller, S. L. Minimal Effect of Lipid Charge on Membrane Miscibility Phase Behavior in Three Ternary Systems. *Biophys. J.* **2013**, *104* (12), 2629–2638.
- (103) Kaasgaard, T.; Leidy, C.; Crowe, J. H.; Mouritsen, O. G.; Jørgensen, K. Temperature-Controlled Structure and Kinetics of Ripple Phases in One- and Two-Component Supported Lipid Bilayers. *Biophys. J.* **2003**, *85* (1), 350–360.



- (104) Heimburg, T. *Thermal Biophysics of Membranes*; Wiley-VCH, 2007.
- (105) Nagle, J. F.; Tristram-Nagle, S. Structure of Lipid Bilayers. *Biochim. Biophys. Acta - Rev. Biomembr.* **2000**, *1469*, 159–195.
- (106) Cremer, P. S.; Boxer, S. G. Formation and Spreading of Lipid Bilayers on Planar Glass Supports. *J. Phys. Chem. B* **1999**, *103* (13), 2554–2559.
- (107) Bruker. PeakForce QNM Calibration Webinar - 17/2/2015 <https://vimeo.com/user15273673/review/119890124/ec51c428e4> (accessed Dec 19, 2018).
- (108) Avanti Polar Lipids Inc. Phase Transition Temperatures for Glycerophospholipids - Reference Sheet.
- (109) Benesch, M. G. K.; Lewis, R. N. a H.; McElhaney, R. N. A Calorimetric and Spectroscopic Comparison of the Effects of Cholesterol and Its Immediate Biosynthetic Precursors 7-Dehydrocholesterol and Desmosterol on the Thermotropic Phase Behavior and Organization of Dipalmitoylphosphatidylcholine Bilayer Membrane. *Chem. Phys. Lipids* **2015**, *191*, 123–135.
- (110) Furuya, K.; Mitsui, T. Phase Transitions in Bilayer Membranes of Dioleoyl-Phosphatidylcholine/Dipalmitoyl-Phosphatidylcholine. *J. Phys. Soc. Jpn* **1979**, *46* (611).
- (111) Marsh, D. *Handbook of Lipid Bilayers*, Second Edi.; CRC Press, 2013.
- (112) Demetzos, C. Differential Scanning Calorimetry (DSC): A Tool to Study the Thermal Behavior of Lipid Bilayers and Liposomal Stability. *J. Liposome Res.* **2008**, *18* (3), 159–173.
- (113) Jensen, M.; Mouritsen, O. G. Lipids Do Influence Protein Function - The Hydrophobic Matching Hypothesis Revisited. *Biochim. Biophys. Acta - Biomembr.* **2004**, *1666*, 205–226.
- (114) Needham, D.; Nunn, R. S. Elastic Deformation and Failure of Lipid Bilayer Membranes Containing Cholesterol. *Biophys. J.* **1990**, *58*, 997–1009.
- (115) Das, C.; Sheikh, K. H.; Olmsted, P. D.; Connell, S. D. Nanoscale

- Mechanical Probing of Supported Lipid Bilayers with Atomic Force Microscopy. *Phys. Rev. E* **2010**, 82 (4), 041920.
- (116) Jensen, M. H.; Morris, E. J.; Simonsen, A. C. Domain Shapes, Coarsening, and Random Patterns in Ternary Membranes. *Langmuir* **2007**, 23 (12), 8135–8141.
- (117) Crane, J. M.; Tamm, L. K. Role of Cholesterol in the Formation and Nature of Lipid Rafts in Planar and Spherical Model Membranes. *Biophys. J.* **2004**, 86 (5), 2965–2979.
- (118) Kaizuka, Y.; Groves, J. T. Structure and Dynamics of Supported Intermembrane Junctions. *Biophys. J.* **2004**, 86 (2), 905–912.
- (119) Burns, A. R.; Frankel, D. J.; Buranda, T. Local Mobility in Lipid Domains of Supported Bilayers Characterized by Atomic Force Microscopy and Fluorescence Correlation Spectroscopy. *Biophys. J.* **2005**, 89 (2), 1081–1093.
- (120) Schoch, R. L.; Barel, I.; Brown, F. L. H.; Haran, G. Lipid Diffusion in the Distal and Proximal Leaflets of Supported Lipid Bilayer Membranes Studied by Single Particle Tracking. *J. Chem. Phys.* **2018**, 148 (12), 123333.
- (121) Baumgart, T.; Hess, S. T.; Webb, W. W. Imaging Coexisting Fluid Domains in Biomembrane Models Coupling Curvature and Line Tension. *Nature* **2003**, 425, 821–824.
- (122) Tayebi, L.; Ma, Y.; Vashaee, D.; Chen, G.; Sinha, S. K.; Parikh, A. N. Long-Range Interlayer Alignment of Intralayer Domains in Stacked Lipid Bilayers. *Nat. Mater.* **2012**, 11 (12), 1074–1080.
- (123) Knoll, W.; Frank, C. W.; Heibel, C.; Naumann, R.; Offenhäusser, A.; Rühle, J.; Schmidt, E. K.; Shen, W. W.; Sinner, A. Functional Tethered Lipid Bilayers. *J. Biotechnol.* **2000**, 74 (3), 137–158.
- (124) Jackman, J.; Knoll, W.; Cho, N.-J. Biotechnology Applications of Tethered Lipid Bilayer Membranes. *Materials (Basel)*. **2012**, 5 (12), 2637–2657.
- (125) Tanaka, M.; Sackmann, E. Polymer-Supported Membranes as Models

of the Cell Surface. *Nature* **2005**, 437 (7059), 656–663.

- (126) Honerkamp-Smith, A. R.; Veatch, S. L.; Keller, S. L. An Introduction to Critical Points for Biophysicists; Observations of Compositional Heterogeneity in Lipid Membranes. *Biochim. Biophys. Acta - Biomembr.* **2009**, 1788 (1), 53–63.
- (127) McKiernan, A. E.; Ratto, T. V.; Longo, M. L. Domain Growth, Shapes, and Topology in Cationic Lipid Bilayers on Mica by Fluorescence and Atomic Force Microscopy. *Biophys. J.* **2000**, 79 (5), 2605–2615.
- (128) Motegi, T.; Yamazaki, K.; Ogino, T.; Tero, R. Substrate-Induced Structure and Molecular Dynamics in a Lipid Bilayer Membrane. *Langmuir* **2017**, 33 (51), 14748–14755.
- (129) Harb, F. F.; Tinland, B. Effect of Ionic Strength on Dynamics of Supported Phosphatidylcholine Lipid Bilayer Revealed by FRAPP and Langmuir-Blodgett Transfer Ratios. *Langmuir* **2013**, 29 (18), 5540–5546.
- (130) Tamm, L. K.; McConnell, H. M. Supported Phospholipid Bilayers. *Biophys. J.* **1985**, 47 (1), 105–113.
- (131) Ali, S.; Minchey, S.; Janoff, A.; Mayhew, E. A Differential Scanning Calorimetry Study of Phosphocholines Mixed with Paclitaxel and Its Bromoacylated Taxanes. *Biophys. J.* **2000**, 78 (1), 246–256.
- (132) Naumann, C.; Brumm, T.; Bayerl, T. M. Phase Transition Behavior of Single Phosphatidylcholine Bilayers on a Solid Spherical Support Studied by DSC, NMR and FT-IR. *Biophys. J.* **1992**, 63 (5), 1314–1319.
- (133) Lewis, R. N.; Mannock, D. A.; McElhaney, R. N. Differential Scanning Calorimetry in the Study of Lipid Phase Transitions in Model and Biological Membranes: Practical Considerations. In *Methods Mol. Biol.*; 2007; Vol. 400, pp 171–195.
- (134) Giocondi, M. C.; Yamamoto, D.; Lesniewska, E.; Milhiet, P. E.; Ando, T.; Le Grimellec, C. Surface Topography of Membrane Domains. *Biochim. Biophys. Acta - Biomembr.* **2010**, 1798 (4), 703–718.
- (135) Bao, P.; Cartron, M. L.; Sheikh, K. H.; Johnson, B. R. G.; Hunter, C. N.;

- Evans, S. D. SI - Controlling Transmembrane Protein Concentration and Orientation in Supported Lipid Bilayers. *Chem. Commun.* **2017**, 53 (30), 4250–4253.
- (136) Richter, R. P.; Escarpit, R. R.; Cedex, P. Formation of Solid-Supported Lipid Bilayers : An Integrated View. *Langmuir* **2006**, 22 (8), 3497–3505.
- (137) Lei, S. B.; Tero, R.; Misawa, N.; Yamamura, S.; Wan, L. J.; Urisu, T. AFM Characterization of Gramicidin-A in Tethered Lipid Membrane on Silicon Surface. *Chem. Phys. Lett.* **2006**, 429 (1–3), 244–249.
- (138) Mao, Y.; Shang, Z.; Imai, Y.; Hoshino, T.; Tero, R.; Tanaka, M.; Yamamoto, N.; Yanagisawa, K.; Urisu, T. Surface-Induced Phase Separation of a Sphingomyelin/Cholesterol/Ganglioside GM1-Planar Bilayer on Mica Surfaces and Microdomain Molecular Conformation That Accelerates A $\beta$  Oligomerization. *Biochim. Biophys. Acta - Biomembr.* **2010**, 1798 (6), 1090–1099.
- (139) McMahon, H. T.; Boucrot, E. Membrane Curvature at a Glance. *J. Cell Sci.* **2015**, 128 (6), 1065–1070.
- (140) Zimmerberg, J.; Kozlov, M. M. How Proteins Produce Cellular Membrane Curvature. *Nat. Rev. Mol. Cell Biol.* **2006**, 7 (1), 9–19.
- (141) Subramaniam, A. B.; Lecuyer, S.; Ramamurthi, K. S.; Losick, R.; Stone, H. A. Particle/Fluid Interface Replication as a Means of Producing Topographically Patterned Polydimethylsiloxane Surfaces for Deposition of Lipid Bilayers. *Adv. Mater.* **2010**, 22 (19), 2142–2147.
- (142) Parthasarathy, R.; Yu, C.; Groves, J. T. Curvature-Modulated Phase Separation in Lipid Bilayer Membranes. *Langmuir* **2006**, 22 (11), 5095–5099.
- (143) Hovis, J. S.; Boxer, S. G. Patterning Barriers to Lateral Diffusion in Supported Lipid Bilayer Membranes by Blotting and Stamping. *Langmuir* **2000**, 16 (3), 894–897.
- (144) Hovis, J. S.; Boxer, S. G. Patterning and Composition Arrays of Supported Lipid Bilayers by Microcontact Printing. *Langmuir* **2001**, 17 (11), 3400–3405.

- (145) Stubbington, L.; Arroyo, M.; Staykova, M. Sticking and Sliding of Lipid Bilayers on Deformable Substrates. *Soft Matter* **2017**, *13* (1), 181–186.
- (146) Hillborg, H.; Tomczak, N.; Olàh, A.; Schönherr, H.; Vancso, G. J.; Ola, A.; Scho, H.; Vancso, G. J. Nanoscale Hydrophobic Recovery: A Chemical Force Microscopy Study of UV / Ozone-Treated Cross-Linked Poly ( Dimethylsiloxane ). *Langmuir* **2004**, *20* (3), 785–794.
- (147) Owen, M. J.; Smith, P. J. Plasma Treatment of Polydimethylsiloxane. *J. Adhes. Sci. Technol.* **1994**, *8* (10), 1063–1075.
- (148) Hillborg, H.; Sandelin, M.; Gedde, U. W. Hydrophobic Recovery of Polydimethylsiloxane after Exposure to Partial Discharges as a Function of Crosslink Density. *Polymer (Guildf)*. **2001**, *42* (17), 7349–7362.
- (149) Hillborg, H.; Ankner, J. F.; Gedde, U. W.; Smith, G. D.; Yasuda, H. K.; Wikstro, K. Crosslinked Polydimethylsiloxane Exposed to Oxygen Plasma Studied by Neutron Reflectometry and Other Surface Specific Techniques. *Polymer (Guildf)*. **2000**, *41*, 6851–6863.
- (150) Staykova, M.; Holmes, D. P.; Read, C.; Stone, H. A. Mechanics of Surface Area Regulation in Cells Examined with Confined Lipid Membranes. *Proc. Natl. Acad. Sci.* **2011**, *108* (22), 9084–9088.
- (151) Feriani, L.; Cristofolini, L.; Cicuta, P. Soft Pinning of Liquid Domains on Topographical Hemispherical Caps. *Chem. Phys. Lipids* **2014**, *185*, 1–10.
- (152) Gilmore, S. F.; Nanduri, H.; Parikh, A. N. Programmed Bending Reveals Dynamic Mechanochemical Coupling in Supported Lipid Bilayers. *PLoS One* **2011**, *6* (12), 1–8.
- (153) Sanii, B.; Smith, A. M.; Butti, R.; Brozell, A. M.; Parikh, A. N. Bending Membranes on Demand: Fluid Phospholipid Bilayers on Topographically Deformable Substrates. *Nano Lett.* **2008**, *8* (3), 866–871.
- (154) Blachon, F.; Harb, F.; Munteanu, B.; Piednoir, A.; Fulcrand, R.; Charitat, T.; Fragneto, G.; Pierre-Louis, O.; Tinland, B.; Rieu, J. P. Nanoroughness Strongly Impacts Lipid Mobility in Supported

Membranes. *Langmuir* **2017**, 33 (9), 2444–2453.

- (155) Vasilca, V.; Sadeghpour, A.; Rawson, S.; Hawke, L. E.; Baldwin, S. A.; Wilkinson, T.; Bannister, D.; Postis, V. L. G.; Rappolt, M.; Muench, S. P.; et al. Spherical-Supported Membranes as Platforms for Screening against Membrane Protein Targets. *Anal. Biochem.* **2018**, 549, 58–65.
- (156) Faysal, K. M. R.; Park, J. S.; Nguyen, J.; Garcia, L.; Subramaniam, A. B. Lipid Bilayers Are Long-Lived on Solvent Cleaned Plasma-Oxidized Poly(Dimethyl)Siloxane (Ox-PDMS). *PLoS One* **2017**, 12, e0169487.
- (157) Morra, M.; Occhiello, E.; Marola, R.; Garbassi, F.; Humphrey, P.; Johnson, D. On the Aging of Oxygen Plasma-Treated Polydimethylsiloxane Surfaces. *J. Colloid Interface Sci.* **1990**, 137 (1), 11–24.
- (158) Thibault, C.; Séverac, C.; Mingotaud, A. F.; Vieu, C.; Mauzac, M. Poly(Dimethylsiloxane) Contamination in Microcontact Printing and Its Influence on Patterning Oligonucleotides. *Langmuir* **2007**, 23 (21), 10706–10714.
- (159) Eddington, D. T.; Puccinelli, J. P.; Beebe, D. J. Thermal Aging and Reduced Hydrophobic Recovery of Polydimethylsiloxane. *Sensors Actuators, B Chem.* **2006**, 114 (1), 170–172.
- (160) Lenz, P.; Ajo-Franklin, C. M.; Boxer, S. G. Patterned Supported Lipid Bilayers and Monolayers on Poly(Dimethylsiloxane). *Langmuir* **2004**, 20 (25), 11092–11099.
- (161) Lawton, R. A.; Price, C. R.; Runge, A. F.; Doherty, W. J.; Saavedra, S. S. Air Plasma Treatment of Submicron Thick PDMS Polymer Films: Effect of Oxidation Time and Storage Conditions. *Colloids Surfaces A Physicochem. Eng. Asp.* **2005**, 253 (1–3), 213–215.
- (162) Trantidou, T.; Elani, Y.; Parsons, E.; Ces, O. Hydrophilic Surface Modification of PDMS for Droplet Microfluidics Using a Simple, Quick, and Robust Method via PVA Deposition. *Microsystems Nanoeng.* **2017**, 3 (16091).
- (163) Goksu, E. I.; Hoopes, M. I.; Nellis, B. A.; Xing, C.; Faller, R.; Frank, C. W.; Risbud, S. H.; Satcher, J. H.; Longo, M. L. Silica Xerogel/Aerogel-

Supported Lipid Bilayers: Consequences of Surface Corrugation. *Biochim. Biophys. Acta - Biomembr.* **2010**, 1798 (4), 719–729.

- (164) Goksu, E. I.; Vanegas, J. M.; Blanchette, C. D.; Lin, W.-C.; Longo, M. L. AFM for Structure and Dynamics of Biomembranes. *Biochim. Biophys. Acta* **2009**, 1788 (1), 254–266.
- (165) Werner, J. H.; Montan, G. A.; Garcia, A. L.; Zurek, N. A.; Akhadov, E. A.; Lopez, G. P.; Shreve, A. P. Formation and Dynamics of Supported Phospholipid Membranes on a Periodic Nanotextured Substrate Formation and Dynamics of Supported Phospholipid Membranes on a Periodic Nanotextured Substrate. *Langmuir* **2009**, No. 25, 2986–2993.
- (166) Xing, C.; Faller, R. Interactions of Lipid Bilayers with Supports: A Coarse-Grained Molecular Simulation Study. *J. Phys. Chem. B* **2008**, 112 (23), 7086–7094.
- (167) Davis, R. W.; Flores, A.; Barrick, T. A.; Cox, J. M.; Brozik, S. M.; Lopez, G. P.; Brozik, J. A. Nanoporous Microbead Supported Bilayers: Stability, Physical Characterization, and Incorporation of Functional Transmembrane Proteins. *Langmuir* **2007**, 23 (7), 3864–3872.
- (168) Rädler, J.; Strey, H.; Sackmann, E. Phenomenology and Kinetics of Lipid Bilayer Spreading on Hydrophilic Surfaces. *Langmuir* **1995**, 11 (11), 4539–4548.
- (169) Ngamsaad, W.; May, S.; Wagner, A. J.; Triampo, W. Pinning of Domains for Fluid–fluid Phase Separation in Lipid Bilayers with Asymmetric Dynamics. *Soft Matter* **2011**, 7 (6), 2848.
- (170) Leonenko, Z. V.; Finot, E.; Ma, H.; Dahms, T. E. S.; Cramb, D. T. Investigation of Temperature-Induced Phase Transitions in DOPC and DPPC Phospholipid Bilayers Using Temperature-Controlled Scanning Force Microscopy. *Biophys. J.* **2004**, 86 (6), 3783–3793.
- (171) Garcia-Manyes, S.; Oncins, G.; Sanz, F. Effect of Temperature on the Nanomechanics of Lipid Bilayers Studied by Force Spectroscopy. *Biophys. J.* **2005**, 89 (6), 4261–4274.
- (172) Feng, Z. V.; Spurlin, T. a; Gewirth, A. a. Direct Visualization of Asymmetric Behavior in Supported Lipid Bilayers at the Gel-Fluid Phase

- Transition. *Biophys. J.* **2005**, *88* (3), 2154–2164.
- (173) Charrier, A.; Thibaudau, F. Main Phase Transitions in Supported Lipid Single-Bilayer. *Biophys. J.* **2005**, *89* (2), 1094–1101.
- (174) Yang, J.; Appleyard, J. The Main Phase Transition of Mica-Supported Phosphatidylcholine Membranes. *J. Phys. Chem. B* **2000**, *104* (34), 8097–8100.
- (175) Baumgart, T.; Hammond, A. T.; Sengupta, P.; Hess, S. T.; Holowka, D. A.; Baird, B. A.; Webb, W. W. Large-Scale Fluid/Fluid Phase Separation of Proteins and Lipids in Giant Plasma Membrane Vesicles. *Proc. Natl. Acad. Sci.* **2007**, *104* (9), 3165–3170.
- (176) Yethiraj, A.; Weisshaar, J. C. Why Are Lipid Rafts Not Observed in Vivo? *Biophys. J.* **2007**, *93* (9), 3113–3119.
- (177) Machta, B. B.; Papanikolaou, S.; Sethna, J. P.; Veatch, S. L. Minimal Model of Plasma Membrane Heterogeneity Requires Coupling Cortical Actin to Criticality. *Biophys. J.* **2011**, *100* (7), 1668–1677.
- (178) Ehrig, J.; Petrov, E. P.; Schwille, P. Near-Critical Fluctuations and Cytoskeleton-Assisted Phase Separation Lead to Subdiffusion in Cell Membranes. *Biophys. J.* **2011**, *100* (1), 80–89.
- (179) Fischer, T.; Vink, R. L. C. Domain Formation in Membranes with Quenched Protein Obstacles: Lateral Heterogeneity and the Connection to Universality Classes. *J. Chem. Phys.* **2011**, *134* (5).
- (180) McCarthy, N. L. C.; Ces, O.; Law, R. V.; Seddon, J. M.; Brooks, N. J. Separation of Liquid Domains in Model Membranes Induced with High Hydrostatic Pressure. *Chem. Commun.* **2015**, *51*, 8675–8678.
- (181) Chiantia, S.; London, E. Acyl Chain Length and Saturation Modulate Interleaflet Coupling in Asymmetric Bilayers: Effects on Dynamics and Structural Order. *Biophys. J.* **2012**, *103* (11), 2311–2319.
- (182) Bennett, W. F. D.; Maccallum, J. L.; Hinner, M. J.; Marrink, S. J.; Tieleman, D. P. Molecular View of Cholesterol Flip-Flop and Chemical Potential in Different Membrane Environments. *J. Am. Chem. Soc.* **2009**, *131* (35), 12714–12720.



- (183) Bruker Webinar: The AFM Probe - Fundamentals, Selection, and Applications [https://www.bruker.com/fileadmin/user\\_upload/8-PDF-Docs/SurfaceAnalysis/AFM/Webinars/AFM\\_Probes-Fundamentals\\_selection\\_and\\_applications-Webinar\\_Oct29-2013\\_.pdf](https://www.bruker.com/fileadmin/user_upload/8-PDF-Docs/SurfaceAnalysis/AFM/Webinars/AFM_Probes-Fundamentals_selection_and_applications-Webinar_Oct29-2013_.pdf) (accessed Nov 27, 2018).
- (184) Bruker AFM Probes [www.brukerafmprobes.com](http://www.brukerafmprobes.com) (accessed Nov 27, 2018).
- (185) Thermo Fisher Scientific <https://www.thermofisher.com/order/catalog/product/T1395MP> (accessed Nov 27, 2018).
- (186) Malvern Instruments Ltd. MicroCal VP-DSC system - Operating Instructions <https://www.malvernpanalytical.com/en/support/product-support/microcal-range/microcal-dsc-range/microcal-vp-dsc> (accessed Nov 17, 2018).
- (187) Bao, P.; Cartron, M. L.; Sheikh, K. H.; Johnson, B. R. G.; Hunter, C. N.; Evans, S. D. Controlling Transmembrane Protein Concentration and Orientation in Supported Lipid Bilayers. *Chem. Commun.* **2017**, 53 (30), 4250–4253.